Aerobatic Racing Aircraft Design

Design an aircraft fit to compete in the Red Bull Air Race World Championship 2017 and beat Red Bull in its own competition.

N.T. Andriesse	4132947	T. Hendrikx	4168925
R.J. Baaij	4013867	G.R. Poeran	4101766
J.A. Bellekom	4139410	M.A. Robijns	4088018
A.M. Berkel	4146492	I. van Teeseling	4122216
I.A. Gennissen	4014316	B.M. Verhagen	4149580

Final Report

Design Synthesis Excercise

FLASH
corporation

TUDelft
Delft
University of
Technology

Aerospace Engineering

Aerobatic Racing Aircraft Design

Design Synthesis Exercise

Group 15

Supervisor: Ir. S. Shroff

Coaches: Dr. Ir. B.F. Santos, Ir. M.F.M. Hoogreef

Core Team Coaches: Prof. Dr. A. Rothwell, Ir. D. Barazanchy

June 24, 2014

Preface

This is the final report in a series of four reports of the Design Synthesis Exercise (DSE) at the faculty of Aerospace Engineering of Delft University of Technology. The DSE is the final exercise of the Bachelor, in which ten students work on a design project for eleven weeks. This project describes the theoretical development of an aerobatic racing aircraft, designed to win the Red Bull Air Race in 2017.

The organization of the project was established in the project plan, which was the first report in this series. The baseline report dealt with the requirements and exploration of the project. In the midterm report, a conceptual design was given. In this final report, the detailed design of the aerobatic racing aircraft is presented.

We would especially like to thank Ir. S. Shroff, Dr. Ir. B.F. Santos, Ir. M.F.M. Hoogreef, Ir. D. Barazanchy, and Prof. Dr. A. Rothwell for their professional assistance and supervision.

We would also like to thank Dr. Ir. G. La Rocca, Dr. A. Gangoli Rao, Ir. L.M.M. Boermans, and Frank Versteegh for their assistance during the project.

Summary

The FX-15 is a modular aerobatic race aircraft designed to win the 2017 Red Bull Air Race Championship, a race characterized by spectacular maneuvers up to 10g and speeds up to 360 km/h. The FX-15 aims to undercut the finish times of all opponents by accelerating much faster due to the inherently lower drag of the streamlined fuselage.

The preliminary design process consists of several iteration loops containing class I weight estimations, class II weight estimations, drag estimations and initial subsystem sizing. Class II weight estimation methods predict an empty mass of 612 kg and a maximum take-off weight of 850 kg. However, the race will be flown at a mass of 698 kg because it is neither necessary to fly a race with full fuel nor maximum payload. The preliminary design lays the groundwork for a proper detail design.

A well performing aerobatic race aircraft wing has a maximum lift coefficient, $C_{L_{max}}$, sufficiently high to meet performance requirements while minimizing drag and retaining good-natured stall characteristics. This was achieved by using a custom-made airfoil, the NACA 0011-61MOD, and an optimized wing planform. The 9.3 m^2 of wing area generate a $C_{L_{max}}$ of 2.07. Drag is kept to a minimum by virtue of a high aspect ratio wing with a span of 8.5 m. Root stall, which is typically associated with benign stall characteristics, is enforced with a taper ratio of 0.6. The wing contains large ailerons spanning more than half of the wing to achieve a roll rate of 440 °/s. The aerodynamic loads are carried by a carbon fiber laminate spar filled with Divinycell HT131 foam. The laminate is a custom design made of HexPly 8552 with 65% IM7 fiber. The wing structure has a mass of merely 60 kg due to to precise geometric optimization by a sophisticated algorithm.

The innovative location of the engine, just above the main spar behind the cockpit, results in a fuselage with its heaviest and bulkiest components in the center section. This enables a highly smooth and streamlined fuselage shape with a zero-lift drag coefficient, C_{D_0}, of 0.0063. The loads on the fuselage are carried by a truss structure made of AISI 410S stainless steel tubes. The truss structure has a mass of 49 kg and does not fail despite loads of up to $\pm$12g, as confirmed by FEM analysis.

The ability to commence a $\pm$12g turn within a quarter second is assured by the horizontal stabilizer and its elevator with an area of 2.1 m^2 and horizontal tail volume coefficient, $S_h l_h / S\bar{c}$, of 0.68. The vertical stabilizer and its rudder are designed to allow safe cross-wind landings and to ascertain fast recovery from spins. The vertical tail has an area of 1.7 m^2 and a volume coefficient, $S_v l_v / Sb$, of 0.07.

The undercarriage consists of two main gears and a small tail wheel in a taildragger configuration. The shape of the two main gear struts is optimized by an advanced algorithm yielding both a low weight and low drag. The main landing gear with struts made of aluminum 2014-T6 contribute 19 kg to the total mass of the FX-15. The contribution of the landing gear to C_{D_0} is a mere 0.0031 as a result of struts shaped as NACA 64-020 airfoils.

The unconventional engine location requires a reliable system to transmit the engine power along the cockpit to the 3-bladed Hartzell 7690 composite propeller. A system of shafts, chains, and sprockets turned out to be the lightest, simplest, and most durable solution. A combination of shafts made of AISI 4130 steel, aluminum 6061-T6 sprockets, and Triathlon HT chains guarantees a reliable transmission of the 315 hp generated by the Lycoming Thunderbolt AEIO-540-D engine. The engine is supplied with air for cooling and combustion through air inlets conveniently located in the wing roots. This keeps cooling and intake drag to a minimum. The power output of the engine can optionally be increased to 350 hp by means of a turbocharger from Hartzell Engine Technologies.

Performance analysis shows that all performance requirements are met. The maximum speed is 456 km/h, slightly over the required speed of 450 km/h. The highest rate of climb is 25 m/s, well over the required rate of climb of 18 m/s. The FX-15 needs 145 meters of runway to get off the ground from stand still, well below the 500 required meters.

The FX-15 was designed to be an innovative and extraordinary aircraft, meant to show the world that thinking out of the box can be rewarding in the long run. It will inspire the next generation to come up with new ideas. New ideas that are needed for solutions to a more sustainable world.

Contents

List of Abbreviations

Abbreviation	Description
AC	Aerodynamic Center
AVL	Athena Vortex Lattice
CCT	Camera Control and Transmission
CFD	Computational Fluid Dynamics
CFRP	Carbon Fiber Reinforced Polymer
CG	Center of Gravity
CS	Certification Specifications
EAS	Equivalent Air Speed
EOM	Equations Of Motion
FEM	Finite Element Method
GFRP	Glass Fiber Reinforced Polymer
ISA	International Standard Atmosphere
LEMAC	Leading Edge at MAC
LG	Landing Gear
MAC	Mean Aerodynamic Chord
MIT	Massachusetts Institute of Technology
MOI	Moment Of Inertia
MTOW	Maximum Take-Off Weight
NA	Not Applicable
NACA	National Advisory Committee for Aeronautics
OEW	Operational Empty Weight
PCA	Porcupine Curvature Analysis
Q-3D	Quasi Three Dimensional
RAMS	Reliability, Availability, Maintainability and Safety
ROC	Rate Of Climb
RBAR	Red Bull Air Race
SCA	Surface Curvature Analysis
SF	Safety Factor
SFC	Specific Fuel Consumption
SM	Safety Margin
TOP	Take-Off Parameter
USAF	United States Air Force

List of Symbols

Symbol	Unit	Description
a	$[m/s^2]$	Acceleration
b	$[m]$	Wing span
b_f	$[m]$	Fuselage width
b_{ref}	$[m]$	Reference span
c	$[m]$	Local chord
c	$[m/s]$	Climb rate
c_p	$[-]$	Specific fuel consumption
d_b	$[m]$	Fuselage base diameter
d_f	$[m]$	Fuselage maximum diameter
e	$[-]$	Oswald factor
g	$[m/s^2]$	Gravitational acceleration
h	$[m]$	Height
h_f	$[m]$	Fuselage height
i_w	$[°]$	Angle of incidence
k_s	$[-]$	Factor of proportionality from Torenbeek
k_w	$[-]$	Factor of proportionality from Torenbeek
l_f	$[m]$	Fuselage length
l_{fn}	$[m]$	Length from nose to LEMAC
l_h	$[m]$	Distance between wing and hor. stabilizer aerodynamic centers
l_v	$[m]$	Distance between wing and vert. stabilizer aerodynamic centers
m	$[kg]$	Mass
n	$[-]$	Load factor
n	$[-]$	Number of sprocket teeth
p	$[N/m]$	Stress flow
q	$[N/m]$	Shear flow
r	$[m]$	Radius
e	$[m]$	Resolution
r_f	$[-]$	Fuselage correction factor
r_{Re}	$[-]$	Reynolds correction factor
r_t	$[-]$	Empennage correction factor
r_{uc}	$[-]$	Undercarriage correction factor
r_w	$[-]$	Wing correction factor
s_{TO}	$[m]$	Take-off distance
s_{land}	$[m]$	Landing distance
t	$[m]$	Thickness
t/c	$[-]$	Chord to thickness ratio
w	$[N]$	Distributed load
x_{cg}	$[m]$	CG location from nose
x_{ac}	$[m]$	Aerodynamic center location from nose
y_D	$[m]$	Roll drag arm
y_i	$[m]$	Inner aileron location from mid wing
y_l	$[m]$	Vertical distance between LG and CG
y_o	$[m]$	Outer aileron location from mid wing
A	$[m^2]$	Area
A	$[-]$	Aspect ratio
A_v	$[-]$	Vertical stabilizer aspect ratio
$A_{v_{eff}}$	$[-]$	Effective vertical stabilizer aspect ratio
B_A	$[m^2]$	Element area
B_p	$[-]$	Number of propellor blades

Symbol	Unit	Description
C	$[m]$	Circumference
C_A/C	$[-]$	Aileron chord to wing chord ratio
C_d	$[-]$	2D drag coefficient
C_D	$[-]$	3D drag coefficient
C_{D_r}	$[-]$	Roll drag coefficient
C_{D_0}	$[-]$	3D zero-lift drag coefficient
C_{D_i}	$[-]$	3D induced drag coefficient
C_E/C_h	$[-]$	Elevator-to-tail chord ratio
C_f	$[-]$	Friction coefficient
C_l	$[-]$	2D lift coefficient
C_l	$[-]$	X axis moment derivative
C_L	$[-]$	3D lift coefficient
C_{L_α}	$[-]$	3D lift gradient
C_{L_h}	$[-]$	Horizontal stabilizer lift coefficient
C_m	$[-]$	2D moment coefficient
C_M	$[-]$	3D moment coefficient
$C_{M_{\alpha_f}}$	$[-]$	Pitching moment coefficient
C_{n_β}	$[-]$	Static directional stability derivative
C_p	$[-]$	Pressure coefficient
C_r	$[-]$	Root chord
C_t	$[-]$	Tip chord
C_X	$[-]$	X force derivative
C_{Y_β}	$[-]$	Sideforce sideslip coefficient slope
C_Z	$[-]$	Z force derivative
D_t	$[m]$	Tire diameter
D_p	$[m]$	Propellor diameter
E	$[Pa]$	Young's modulus
E	$[s]$	Endurance
E	$[J]$	Energy
F	$[N]$	Force
G	$[Pa]$	Shear modulus
I	$[m^4]$	Moment of area
J	$[m^4]$	Polar moment of inertia
K_X^2	$[-]$	Non-dimensional radius of gyration about the X axis
K_Y^2	$[-]$	Non-dimensional radius of gyration about the Y axis
K_Z^2	$[-]$	Non-dimensional radius of gyration about the Z axis
L	$[N]$	Lift
L	$[m]$	Span of one wing
L_A	$[Nm]$	Aileron roll moment
L_{h_L}	$[-]$	Dimensionless distance tail AC and wing AC
M	$[-]$	Mach number
M	$[Nm]$	Moment
M_{ff}	$[-]$	Fuel Fraction
N	$[N]$	Normal force
N_e	$[-]$	Number of engines on top of the wing
N_{SR}	$[Nm]$	Moment requiered for spin recovery
P	$[W]$	Engine power
P_{br}	$[W]$	Brake horse power
P_{ss}	$[°/s]$	Roll rate
R	$[m]$	Turn radius
R	$[m]$	Range
RC	$[m/s]$	Rate of climb
Re	$[-]$	Reynolds number
$\dot{R}_{SR}$	$[rad/s^2]$	Required yaw acceleration for spin recovery
S	$[m^2]$	Wing area
S_f	$[m^2]$	Total fuselage area

Symbol	Unit	Description
S_{fp}	$[m^2]$	Projected fuselage area
T	$[N]$	Thrust
T	$[°C]$	Temperature
T	$[Nm]$	Torque
V	$[m/s]$	Velocity
V_h/V	$[-]$	Tail volume ratio
W	$[N]$	Weight
W_i	$[N]$	Weight at mission phase
$W_{battery}$	$[Wh]$	Battery capacity
Z_w/Z	$[-]$	Relative wing z-location
α	$[°]$	Angle of attack
α_0	$[°]$	Angle of attack at zero lift
γ	$[°]$	Flight path angle
δ	$[-]$	Power setting
δ_a	$[°]$	Aileron deflection
δ_e	$[°]$	Elevator deflection
δ_{max}	$[m]$	Max deflection
δ_r	$[°]$	Rudder deflection
ϵ	$[°]$	Downwash
η	$[-]$	Panel efficiency factor
η_j	$[-]$	Propulsive efficiency factor
η_p	$[-]$	Propeller efficiency factor
θ	$[rad]$	Pitch angle
$\ddot{\theta}$	$[rad/s^2]$	Pitch acceleration
κ_v	$[-]$	Coefficient for side force derivative
λ	$[-]$	Taper ratio
μ	$[°]$	Bank angle
μ	$[kg/ms]$	Dynamic viscosity
μ_b	$[-]$	Relative density, assymetric motion
μ_c	$[-]$	Relative density, symetric motion
μ_{TO}	$[-]$	Take-off friction coefficient
μ_{Land}	$[-]$	Landing friction coefficient
ρ	$[kg/m^3]$	Air density
σ	$[Pa]$	Stress
τ	$[-]$	Aileron angle of attack effectiveness parameter
τ	$[Pa]$	Shear stress
υ	$[-]$	Poisson's ratio
ω	$[°/s]$	Angular velocity
$\Delta_i C_{n_\beta}$	$[-]$	Wing fuselage interference effect
Λ	$[°]$	Sweep angle
$\Lambda_{0.25}$	$[°]$	Quarter chord sweep angle
$\Lambda_{0.5}$	$[°]$	Half chord sweep angle
Λ_{LE}	$[°]$	Leading edge sweep angle

1 Introduction

This report is the last report in a series of four reports detailing the process of designing an aerobatic racing aircraft with the mission to win the Red Bull Air Race World Championship 2017. This final report will describe the detailed design phase of the FX-15.

The project objective statement for this project is: *"Design an aircraft fit to compete in the Red Bull Air Race World Championship 2017 and beat Red Bull in its own competition."*

The mission need statement for this project is: *"Design an aircraft that can win the Red Bull Air Race World Championship 2017. The aircraft shall have a total cost lower than 275 000 euro. It shall comply with the CS23 regulations, as well as the Red Bull Air Race regulations. Furthermore, it shall be home-built and disposable in a sustainable manner."*

From the mission need statement the key requirements can be deduced, which will drive the design process. The most important requirement is that the aircraft should be able to win the Red Bull Air Race World Championship 2017. As mentioned in the mission need statement, it should also have a unit cost lower than €275 000, it should comply with the CS23 and Red Bull Air Race regulations, and it shall be home-built and disposable in a sustainable manner. Important requirements concerning performance include: the aircraft shall have a maximum load factor of at least ±12g, the aircraft shall have a minimum race mass of at least 698 kg before the flying session, and the aircraft have a service ceiling of 5 000 m. Important operational requirements include: The aircraft shall be longitudinally stable, the aircraft shall be controllable and the aircraft shall be able to fly a knife-edge attitude.

The project was carried out and documented in four phases: planning, baseline, conceptual design and detailed design. During the project planning phase the project was organized. The requirements were set up and a planning was made. During the baseline phase, functional analyses were performed and work packages were divided. During the conceptual design trade-offs were performed and the final concept was selected. In the detailed design phase the subcomponents were designed in detail, of which the process and results are presented in this final report.

In this report, a track analysis is performed in chapter 2 and the preliminary design of the FX-15 is reviewed in chapter 3. After this, the wing, fuselage, and tail detail design are presented in chapters 4 to 6. In chapters 7 and 8, the landing gear and propulsion detail design are discussed. The performance analysis will be discussed in chapter 9 before the final design is presented in chapter 10. Hereafter, sustainability will be elaborated on in chapter 11 followed by the project design and development logic in chapter 12. Finally the conclusion and discussion is presented in chapter 13.

2   Track Analysis

The core mission of the FX-15 is to fly the Red Bull Air Race (RBAR) with a duration of approximately one minute. The FX-15 has to demonstrate all of its abilities in this short amount of time. It is therefore of utmost importance to analyze all events in this single minute.

The race track is constrained by pairs of vertical poles. Participating aircraft have to fly through all gates as fast as possible. Touching a gate is punished by a time penalty and maneuvers at a load factor higher than 10 are not permitted. The track of the 2017 Red Bull Air Race Championship has not been determined at this time of writing. The 2008 London City track, as illustrated in fig. 2.1 will for that reason be used as a testbed. Among the maneuvers performed in the 2008 London City track are the Knife-Edge, the high-g turn, the slalom, and the Half Cuban Eight. The Knife-Edge maneuver has been excluded by Red Bull from all race tracks as of 2014.
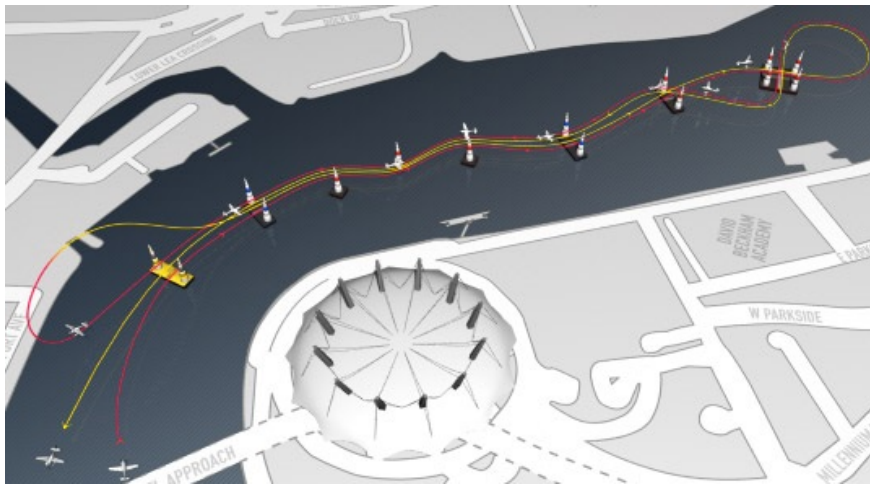
Figure 2.1: RBAR London track

A fictional Red Bull Air Race track included in a paper on trajectory optimization was analyzed during the preliminary design phase of the FX-15 [1]. The following recommendations were made:

1. A significant advantage can be obtained by achieving fast acceleration. The key to fast acceleration is minimizing drag as modifications to propulsion are prohibited. Drag minimization has a large influence on the finish time and is therefore of critical importance to win a race.

2. A high roll rate is not as important as previously thought. Aerobatic aircraft and race aircraft belong to a different class and are subject to different requirements. A race aircraft does not necessarily benefit from a high roll rate as remarked by aerobatic pilot Frank Versteegh.

3. The ability to fly turns at the maximum allowable load factor of 10g results in the lowest possible finish time.

4. Dangerous stall characteristics should be avoided as a stall in ground proximity can be fatal.

3 Preliminary Design

The preliminary design of the FX-15 has been described in the midterm report [2]. However, some parameters of the FX-15 have been altered after presenting the report to FlashCo. and many figures as presented in the midterm report have been improved. This chapter will explain the preliminary design process and will establish consensus over the FX-15 parameters.

First, an overview of the preliminary design method is described in section 3.1. The class I weight estimation is discussed in section 3.2, after which the drag polar is presented in section 3.3. The wing and power loading of the FX-15 are elaborated in section 3.4. Once this is done, a preliminary wing planform can be designed in section 3.5, a preliminary design of the propulsion system is discussed in section 3.6 and a preliminary design of the fuselage is given in section 3.7. Initial estimates of the aircraft drag and the Oswald factor are presented in section 3.8. After this, the class II weight estimation is performed in section 3.9. An improved drag estimation of the aircraft components is given in section 3.11. The chapter is concluded by discussing the optimization for the race in section 3.12.

3.1 Preliminary Design Method

The parameters of the FX-15 up to the detail design phase have been altered and updated throughout the project due to necessary iterations in the design process. Figure 3.1 shows the process of the preliminary design phase. This section will present the determined parameters on basis of the sequence from figure 3.1. In this process two iteration loops are used, indicated in the graph as loop 1 and loop 2. The reported input and output values and figures are based on the final iteration. At the end of each loop the change of the parameters over the iterations is reported.
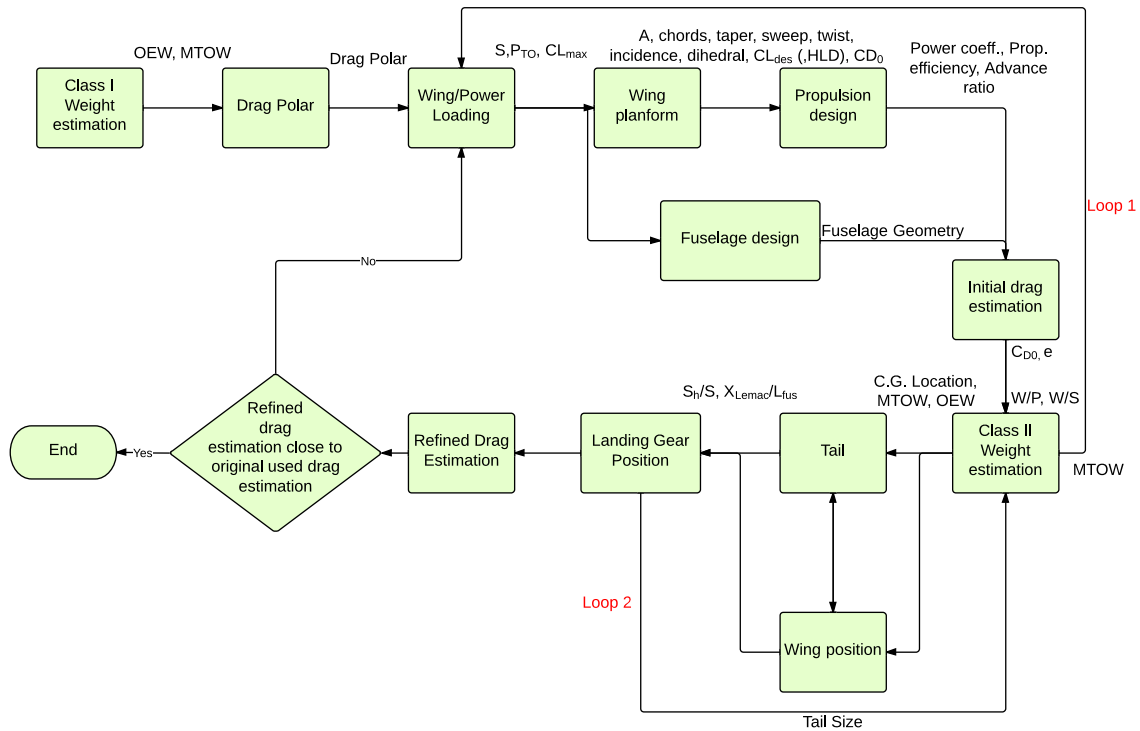
Figure 3.1: Preliminary design process

3

3.2 Class I Weight Estimation

The class I weight estimation is the first estimation of the weight of the FX-15. Input for the class I weight estimation is statistical data from comparable aircraft. Outputs are operational empty weight (OEW) and maximum take-off weight (MTOW). The statistical data needed as input consists of OEW and MTOW.

3.2.1 Method

Eq. (3.1) is used to calculate the MTOW. In order to calculate the MTOW, the right side of the equation must be written as function of the MTOW. For 39 reference aircraft the OEW is plotted versus the MTOW, see fig. 3.2, appendix C. This results in the statistical relation as given by eq. (3.2).

$$MTOW = OEW + W_F + W_{PL} + M_{tfo} \cdot OEW \qquad (3.1)$$

$$OEW = 0.6255 MTOW + 582.44 \qquad (3.2)$$
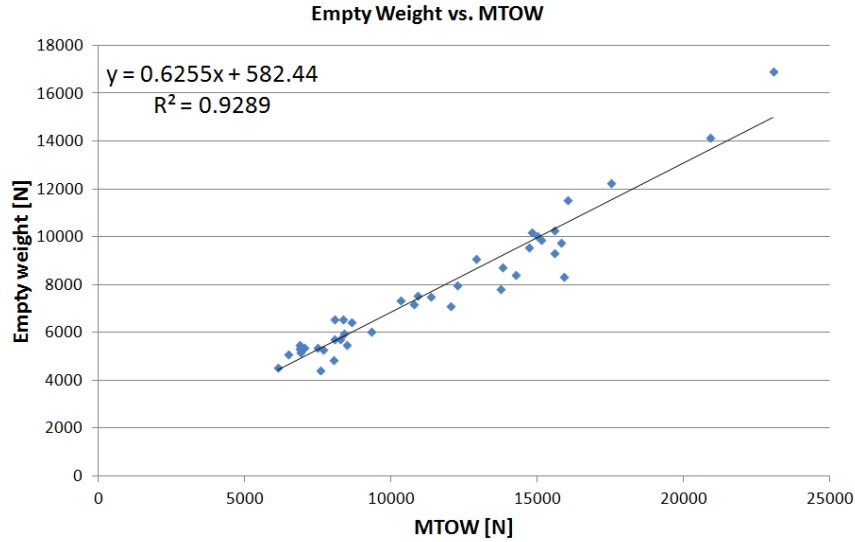
Figure 3.2: Statistical relation between MTOW and OEW based on reference aircraft

The fuel weight as function of the MTOW can be computed using eq. (3.3) [3].

$$W_F = (1 - M_{ff}) MTOW \qquad (3.3)$$

In this equation, M_{ff} is the total fuel fraction of the entire mission profile, which consists of the product of the fuel fractions of every phase of the mission profile. The reserve fuel has to be accounted for in the mission profile, fig. 3.3. For most of these phases the fractions can be taken from statistics (except for the fuel intensive phases). These phases are cruise, loiter, and performing the race. The cruise and loiter fuel fractions can be determined using Breguet's range and endurance equations [3]:

$$R = \left(\frac{\eta_p}{g c_p} \right)_{cruise} \left(\frac{L}{D} \right)_{cruise} \ln \left(\frac{W_i}{W_{i+1}} \right) \qquad (3.4)$$

$$E = \left(\frac{\eta_p}{V_{loiter} g c_p} \right)_{loiter} \left(\frac{L}{D} \right)_{loiter} \ln \left(\frac{W_i}{W_{i+1}} \right) \qquad (3.5)$$

In this equation, R is the range, E is the endurance, η_p is the propeller efficiency, g is the gravitational acceleration, c_p is the specific fuel consumption, L is the lift, D is the drag, V_{loiter} is the loiter velocity,

W_i is the weight at the beginning of the mission phase, and W_{i+1} is the weight at the end of the mission phase.

Figure 3.3: Mission profile of the FX-15

In the mission profile it can be seen that there are two cruise phases and two loiter phases. The range is equal for both cruise phases. The endurance for the first loiter phase is 5 min. The endurance for the second loiter phase is 30 min, in accordance with CS23.25 [4]. This loiter phase accounts for the reserve fuel that is needed.

The fuel fraction for the race phase of the mission, $M_{ff,r}$, is determined by dividing the weight at the end of the race W_{er} by the weight at the beginning of the race W_{br}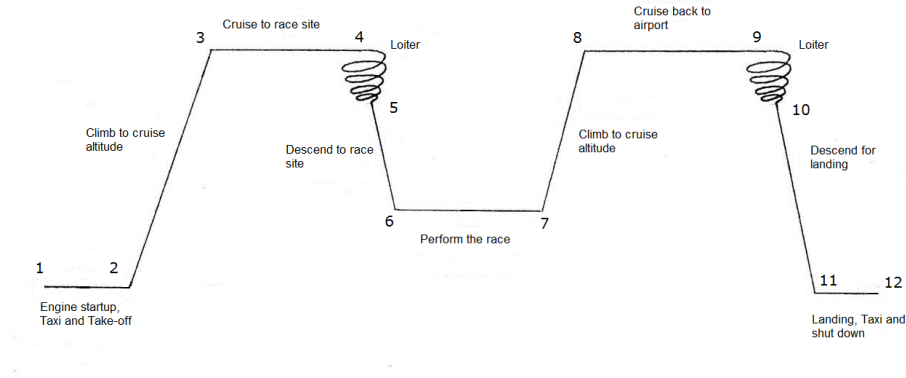. W_{br} can be determined by multiplying the total fuel fraction up to the race phase ($M_{ff,1}$) with MTOW. W_{er} is determined by subtracting the used fuel mass during the race from W_{br}.

The consumed fuel mass during the race is determined by eq. (3.6). In this equation, SFC is the specific fuel consumption, retrieved from [1] with a value of 0.303 L/hp/hr, P_{br} is the engine power, 315 hp [5], ρ is the density of aviation Gasoline 100LL [5] (0.718 kg/l [6]), and t is the time the aircraft is racing. The time the aircraft is racing is taken to be 2 min [1]. This is slightly more than the official race times because the aircraft starts accelerating before the official race time starts. The fuel mass burnt during a race, $W_{F,r}$ is thus 2.3 kg.

$$W_{fuel,race} = SFC \cdot P_{br} \cdot t \cdot \rho = 0.303 \cdot 315 \cdot \frac{120}{3600} \cdot 0.718 = 2.3 kg \tag{3.6}$$

$M_{ff,r}$ can now be determined using the following equation:

$$M_{ff,r} = \frac{W_{er}}{W_{br}} = \frac{M_{ff,1}MTOW - 2.3}{M_{ff,1}MTOW} = 1 - \frac{2.3}{M_{ff,1}MTOW} \tag{3.7}$$

The total fuel fraction, M_{ff}, consists of the product of all fuel fractions except for the race ($M_{ff,2}$) multiplied with the fuel fraction for the race $M_{ff,r}$ (eq. (3.7)). Therefore the total fuel weight W_f can be expressed as follows:

$$W_f = (1 - M_{ff}) MTOW = \frac{2.3M_{ff,2}}{M_{ff,1}} + (1 - M_{ff,2}) MTOW \tag{3.8}$$

The result of eq. (3.8) is a fuel weight of 51.6 kg. The payload weight W_{PL} is 140 kg [7]. Ballast will be added to the payload weight in order to achieve an OEW of 555.7 kg and minimum race mass of 698 kg as stated by the RBAR regulations [5]. The minimum MTOW to comply with the minimum race mass can be approximated with:

$$MTOW_{min} = \frac{W_{min,start}}{M_{ff,1}} = \frac{698}{0.969} = 720 kg \tag{3.9}$$

The total ballast that is added is 46 kg. The total payload weight is thus 186 kg. The fraction of trapped fuels and oils M_{tfo} is taken to be 0.001 [3]. Substituting eq. (3.2), eq. (3.8), W_{PL} and M_{tfo} in eq. (3.1) result in:

$$MTOW = (0.6255MTOW + 582.44) + \left(\frac{2.3M_{ff,2}}{M_{ff,1}} + (1 - M_{ff,2})\, MTOW \right) + (186 \cdot 9.81) + (0.001MTOW) \tag{3.10}$$

Solving eq. (3.10) results in an MTOW of 794 kg. Substituting the value for MTOW in eq. (3.2) results in an OEW of 556 kg.

3.2.2 Results

The input values used for the analysis can be found in table 3.1. The range R is estimated to be 50 km. It is expected that the aircraft will not be flying this distance, especially not twice. However in exceptional cases the aircraft should be able to fly this distance twice. E_1 is the endurance for the first loiter phase, this value was also estimated. E_2 is the endurance for the second loiter phase.

The values for L/D were taken as high as possible within the given range, because the FX-15 will be a high performance aircraft. The same reasoning is applied to the specific fuel consumption c_p, only here the lowest possible value was chosen.

The subscripts in the fuel fraction symbols correspond to the numbers in fig. 3.3. For example, $M_{1,2}$ corresponds to the phase between numbers 1 and 2, thus being engine start-up, taxi and take-off.

The final outputs are given in table 3.2. As can be seen both MTOW and OEW exceed the minimum weights as prescribed in the RBAR regulations [5]. This means that the FX-15 will comply with the regulations according to this analysis. Therefore the values can be used in further analysis.

Table 3.1: Input values for class I weight estimation

Parameter	Value	Unit	Source	Description
R	50	$[km]$	Estimate	Range
E_1	300	$[s]$	Estimate	Loiter time 1
E_2	1800	$[s]$	[4]	Loiter time 2
$\left(\frac{L}{D}\right)_{cruise}$	10	$[-]$	[3]	Lift over drag ratio at cruise
$\left(\frac{L}{D}\right)_{loiter}$	12	$[-]$	[3]	Lift over drag ratio at loiter
$(\eta_j)_{cruise}$	0.8	$[-]$	[3]	Propulsive efficiency at cruise
$(\eta_j)_{loiter}$	0.7	$[-]$	[3]	Propulsive efficiency at loiter
c_p	$8.45(10^{-8})$	$[kg/J]$	[3]	Specific fuel consumption
V_{loiter}	45	$[m/s]$	Estimate	Loiter speed
$M_{1,2}$	0.990	$[-]$	[3]	Fuel fraction from phase 1 to 2
$M_{2,3}$	0.992	$[-]$	[3]	Fuel fraction from phase 2 to 3
$M_{5,6}$	0.993	$[-]$	[3]	Fuel fraction from phase 5 to 6
$M_{7,8}$	0.992	$[-]$	[3]	Fuel fraction from phase 7 to 8
$M_{10,11}$	0.993	$[-]$	[3]	Fuel fraction from phase 10 to 11
$M_{11,12}$	0.993	$[-]$	[3]	Fuel fraction from phase 11 to 12

Table 3.2: Output values for class I weight estimation

Parameter	Value	Unit	Description
MTOW	794	$[kg]$	Maximum take-off weight (output class I)
OEW	556	$[kg]$	Operative empty weight
Payload	140	$[kg]$	Payload weight
Ballast	46	$[kg]$	Ballast
W_f	51.6	$[kg]$	Fuel weight
$M_{3,4}$	0.995	$[-]$	Fuel fraction from phase 3 to 4
$M_{4,5}$	0.999	$[-]$	Fuel fraction from phase 4 to 5
$M_{8,9}$	0.994	$[-]$	Fuel fraction from phase 8 to 9
$M_{9,10}$	0.992	$[-]$	Fuel fraction from phase 9 to 10
$M_{ff,1}$	0.969	$[-]$	Fuel fraction from phase 1 to 6
$M_{ff,2}$	0.935	$[-]$	Total fuel fraction without the race phase
M_{ff}	0.933	$[-]$	Total fuel fraction

3.3 Drag Polar

For the first iteration, a preliminary zero drag coefficient can be calculated using statistical data with the following equations:

$$C_D = C_{D_0} + \frac{C_L^2}{\pi Ae} \tag{3.11}$$

Where:

$$C_{D_0} = C_{f_e} \frac{S_{wet}}{S} + \Delta C_{D_{0_{uc}}} \tag{3.12}$$

The values for $C_{f_e} = 0.0055$, $\frac{S_{wet}}{S} = 4$ and $\Delta C_{D_{0_{uc}}} = 0.02$ are obtained from Roskam [8]. $\Delta C_{D_{0_{uc}}} = 0.02$ is the increment of C_{D_0} due to the landing gear. The first estimate for C_{D_0} is 0.042, this estimate is used as input for the wing and power loading diagram at the first iteration. For later iterations a more accurate value for C_{D_0} is used that is calculated using the initial drag estimation.

3.4 Wing & Power Loading

The wing and power loading diagrams use the estimate of the MTOW to find the surface area of the wing (S) and the required engine power (P). These are used as input for the preliminary design of the wing planform and propulsion system of the FX-15. The wing vs. power loading diagram has been improved and is shown in figure fig. 3.5 and fig. 3.6. During the midterm calculations inaccurate statistical data was used to calculate the Take-Off Parameter (TOP). Fig. 3.4 shows the improved TOP as function of landing distance for reference aircraft, appendix C. With the required landing distance of 500 m, the TOP of 39 reference aircraft (appendix C) is used to size for landing distance.
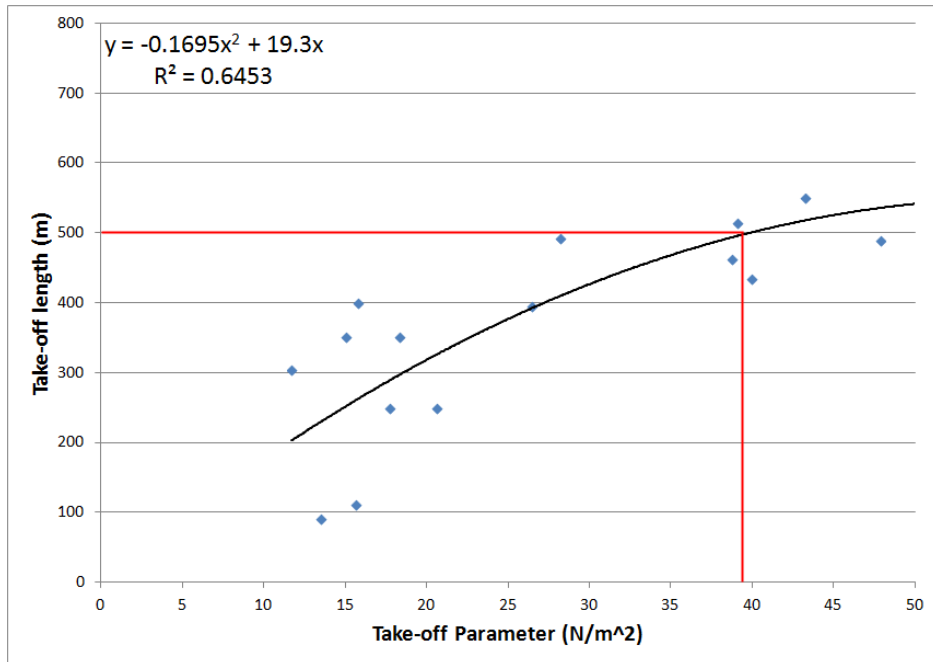
Figure 3.4: Take-off parameter vs. landing distance

In fig. 3.5, C_L values of 1.60, 1.80 and 2.00 are plotted that constrain the wing loading. Preliminary airfoil designs in collaboration with Ir. Loek Boermans show that section lift coefficients exceeding 2.1 are attainable. As a rule of thumb, the maximum wing lift coefficient for the aircraft can be estimated as 90% of the maximum section lift coefficient which results in a $C_{L_{max}}$ of 1.89 [9]. A $C_{L_{max}}$ of 1.80 should therefore suffice as a safe and conservative initial estimate.

The green area in fig. 3.5 shows the possible design area. Because a maximum wing loading is required to make efficient use of the wing area, it can be concluded that the design point, indicated by the red cross, has a wing loading of 744.2 N/m^2, as indicated by the red cross in the figure. From section 3.9 (at the last iteration), an MTOW of 849.6 kg was obtained. Using eq. (3.13) results in an wing area of 11.20 m^2.

$$S = \frac{W}{\left(\frac{W}{S}\right)} \tag{3.13}$$

Input values for the wing and power loading calculations can be found in table 3.3. Note that the input values of the last iteration are given.

Table 3.3: Input values for wing loading

Parameter	Value	Unit	Source	Description
ρ	1.225	$[kg/m^3]$	[10]	Density of air at sea level
V_{stall}	31.38	$[m/s]$	[11]	Stall speed
s_{TO}	500	$[m]$	[11]	Takeoff distance
s_{land}	500	$[m]$	[11]	Landing distance
M_{fuel}	51.6	$[kg]$	[11]	Fuel mass
C_{D_0}	0.0216	$[-]$	Section 3.8.3	Zero-lift drag coefficient
e	0.839	$[-]$	Section 3.8.3	Oswald factor
c	18.00	$[m/s]$	[12]	Climb rate
c/V	0.083	$[-]$	[4]	Climb gradient
η_j	0.86	$[-]$	[1]	Propulsive efficiency
TOP	39	$[-]$	Section 3.4	Take-off parameter
n_{max}	12	$[-]$	[12]	Maximimum load factor
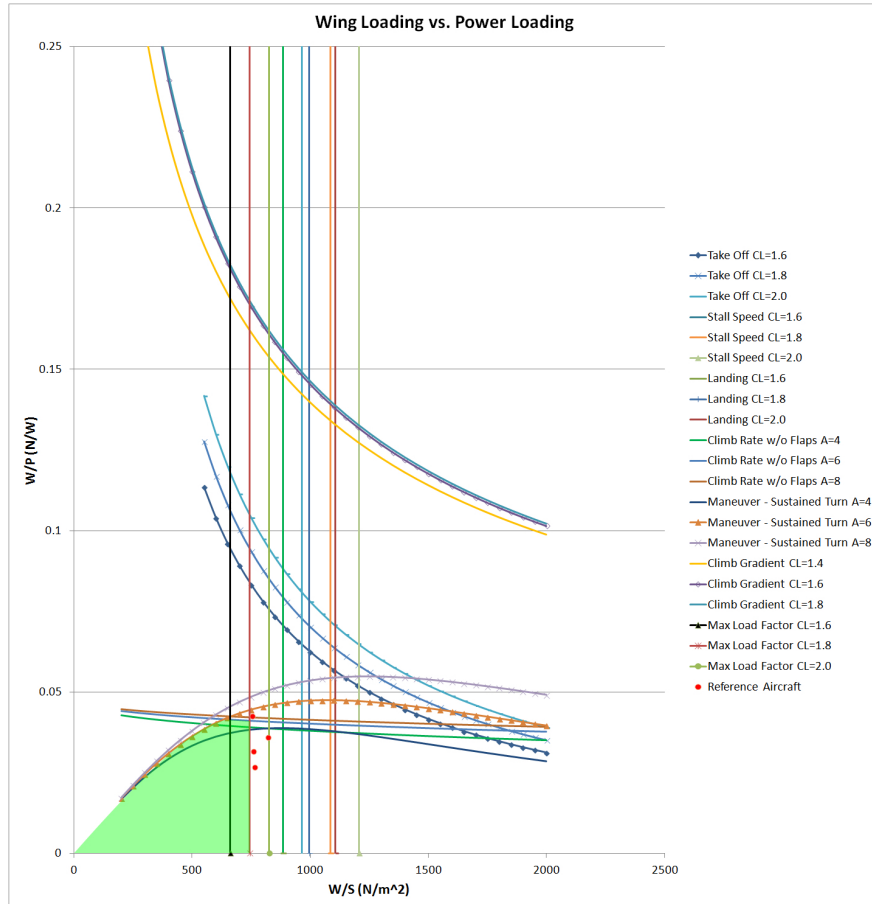
Figure 3.5: Wing vs. power loading diagram
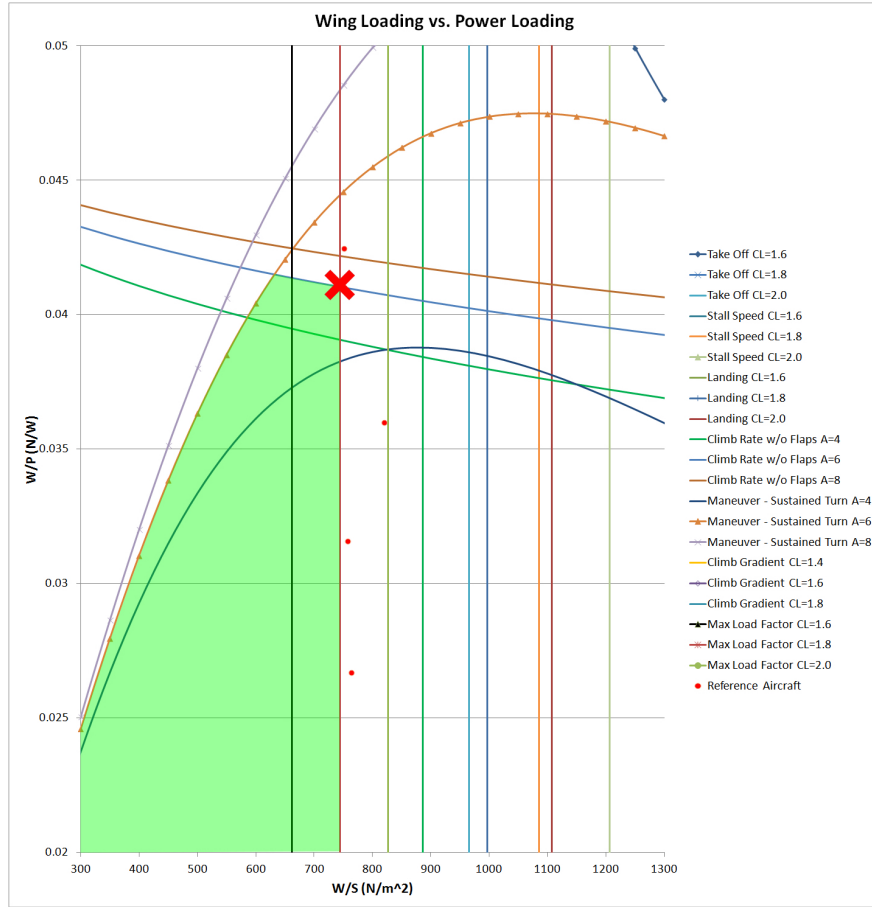
Figure 3.6: Wing vs. power loading diagram, zoomed on the possible design area

3.5 Preliminary Wing Planform

According to fig. 3.1, the next step in the iteration process is the sizing of the wing planform. In this section the design of the aspect ratio, taper ratio, sweep angle, and Mean Aerodynamic Chord (MAC) is discussed.

3.5.1 Aspect Ratio

The wing area (S) was determined to be 11.20 m^2 in section 3.4. The wing span (b) is regulated by the RBAR to be between 7.00 and 8.50 m [11][1]. Given the surface area and the span range, the aspect ratio can vary between 4.38 and 6.45. The benefits of a higher or lower aspect ratio are listed below. [13–15]

High aspect ratio
- Less induced drag
- A steeper C_L-α curve
- A higher climb rate
- A higher climb gradient

Low aspect ratio
- Lower moment of inertia (MOI)
- Less aerodynamic damping
- Lighter wing

The primary design goal is to minimize the drag [2] and a steeper C_L-α curve will allow the FX-15 to generate more lift at lower angles of attack. Furthermore in the midterm report it is analyzed that a reduction in drag is more beneficial than a reduction of weight. Therefore, the upper bound of the aspect ratios is preferred. The span is 8.50 m, hence the aspect ratio is 6.45.

---

[1]The RBAR 2010 regulations [5] and the FlashCo. requirements give a maximum span of 7.60 m, however the 2014 RBAR regulations give a maximum span of 8.50 m. It is recommended to use the new regulations as this will benefit the performance of the FX-15

3.5.2   Taper Ratio

As elaborated on in the midterm report [2], a single tapered planform is the optimal planform for the FX-15 due to the simplicity of the design and the minimal loss of efficiency. Even though the exact amount of sweep is not known at this point in the design process, the quarter chord sweep is approximated to be -2.5°, based on reference aircraft, appendix C. This results in a taper ratio of approximately 0.50, as can be seen in fig. 3.7.
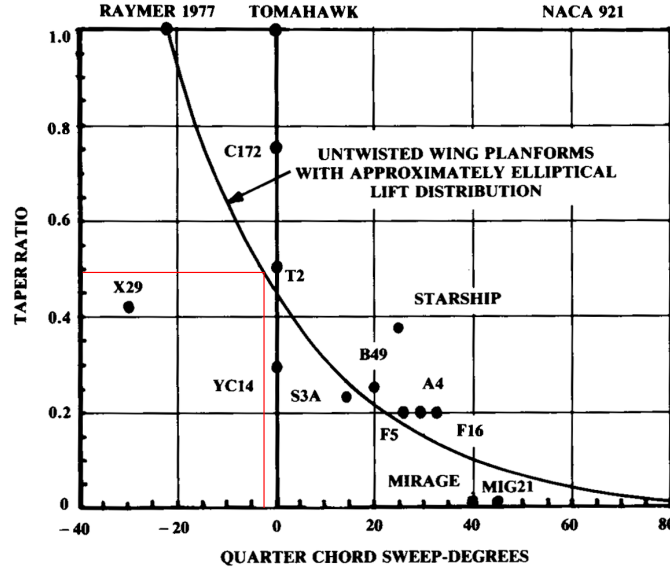
Figure 3.7: Optimal taper ratio vs. sweep angle [9]

3.5.3   Sweep

No sweep is required to reduce the flow velocity over the airfoil as the critical Mach number is approximately 0.57, 1.8 times the maximum Mach number of the FX-15. The critical Mach number has been determined using fig. 3.8 [14]. In the figure the $C_{p,cr}$ and the C_p of the NACA 0011-61MOD, which was selected in the midterm report, are plotted against the Mach number. The C_{p0} used to calculate the C_p of the airfoil is -1.270. This has been determined using JavaFoil in the International Standard Atmosphere (ISA) at a the maximum Mach number of 0.32 [16]. An unswept wing will induce root stall, which is a very mild and therefore beneficial type of stall. Like the Edge 540, which has proven itself by winning the RBAR since 2004, the FX-15 will have a straight leading edge and thus an unswept wing.
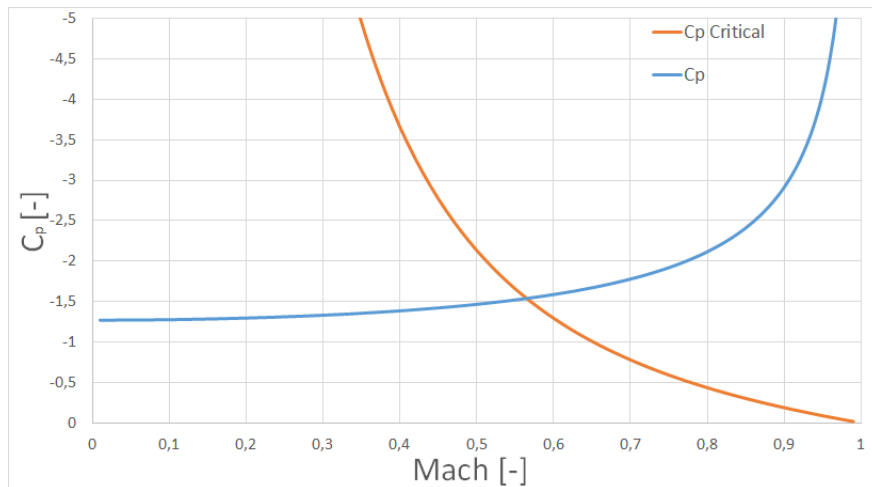
Figure 3.8: Pressure coefficient of the airfoil and the critical pressure coefficient plotted against the Mach number.

3.5.4 Mean Aerodynamic Chord

An estimation of the MAC for a trapezoidal wing can be made with eq. (3.14) [14].

$$\bar{c} = \frac{2}{3} \cdot C_r \cdot \left(\frac{1 + \lambda + \lambda^2}{1 + \lambda} \right) \tag{3.14}$$

3.5.5 Results

With a known surface area, span, sweep, and taper ratio, the wing planform can be determined using geometric relations. The quarter chord sweep is determined to be -1.48°, as this deviates only slightly from the initial guess of -2.5°, the taper ratio will remain at 0.50. The results are shown in table 3.5.

Table 3.4: Input for the wing planform design

Parameter	Value	Unit	Source	Description
S	11.20	$[m^2]$	Section 3.4	Wing area
b_{min}	7.00	$[m]$	[5]	Minimum wing span
b_{max}	8.50	$[m]$	[5]	Maximum wing span

Table 3.5: Output values for wing planform design

Parameter	Value	Unit	Description
b	8.50	$[m]$	Wing span
A	6.45	$[-]$	Aspect ratio
λ	0.50	$[-]$	Taper ratio
Λ_0	0.00	$[°]$	Leading edge sweep
$\Lambda_{0.25c}$	-1.48	$[°]$	Quarter chord sweep
$\Lambda_{0.50c}$	-2.96	$[°]$	Half-chord sweep
C_r	1.76	$[m]$	Root chord
C_t	0.88	$[m]$	Tip chord
$\bar{c}$	1.37	$[m]$	Length of MAC
$y_{\bar{c}}$	1.89	$[m]$	Spanwise location of MAC

3.6 Propulsion System

The propulsion system design is determined by the RBAR regulations [5]. The regulations stated that a Lycoming Thunderbolt AEIO-540-D engine should be used, together with a Hartzell 3-bladed 7690 structural composite propeller. The maximum power output (P) of the Lycoming engine is 315 hp. The MTOW is 849.6 kg, as determined in section 3.9. The maximum power loading can be calculated using equation eq. (3.15).

$$\frac{W}{P} = \frac{MTOW \cdot g}{P} = 0.0354 \tag{3.15}$$

With constraints on the maximum allowed power loading, and the updated value for C_{D_0} the wing loading vs. power loading plot can be updated, see fig. 3.9.
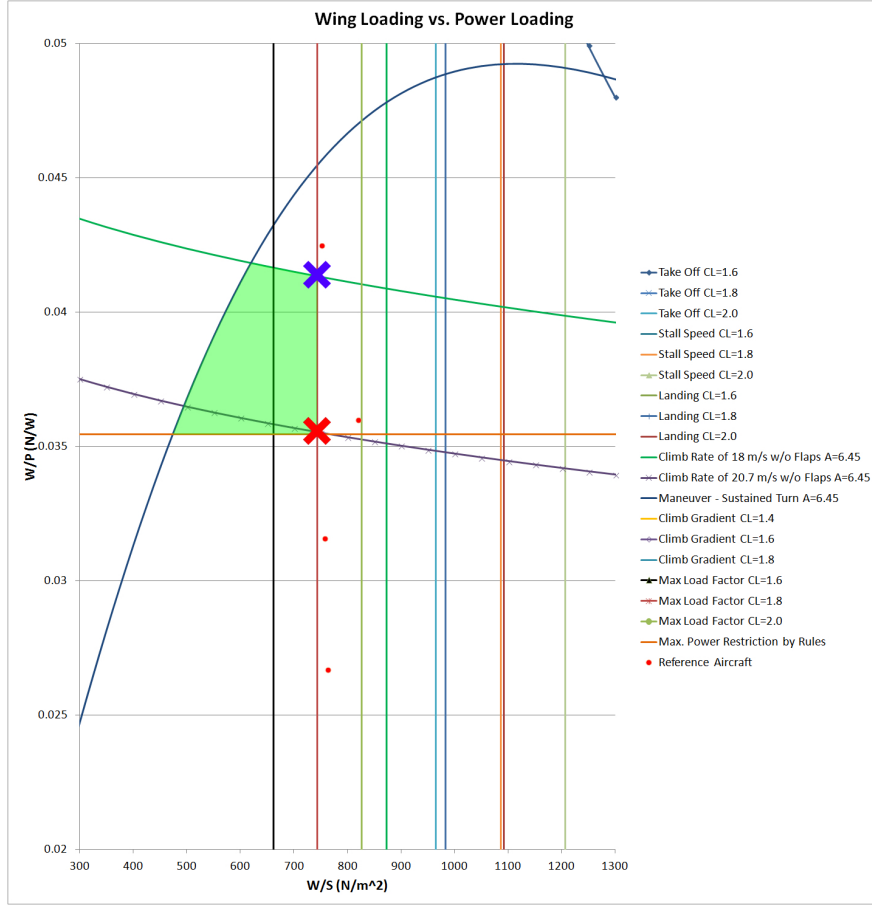
Figure 3.9: Wing vs. power loading diagram

In this figure are the constrains for the maximum power loading and the climb rate as function of the new aspect ratio plotted. The blue cross in this figure indicates the required power loading for all the maneuvers that the FX-15 should be able to perform. The red cross indicates the maximum power loading with the required engine from Red Bull. Therefore it can be concluded that the FX-15 has excessive power, so it can perform even better than required. For example, according to fig. 3.9, the FX-15 can obtain a climb rate of 20.7 m/s.

3.7 Preliminary Fuselage Design

The preliminary fuselage design was described in the midterm report [2]. The main goals of the fuselage design were to fit the payload and instruments in it, attach the lifting surfaces on it, and have a low drag coefficient. Fig. 3.10 shows the side view of the preliminary fuselage design. The width, height, and length of the fuselage are based on the dimensions of the instruments that have to fit inside, see table 3.6.

Table 3.6: Preliminary fuselage dimensions

Parameter	Value	Unit	Description
b_f	0.90	$[m]$	Fuselage width
h_f	1.25	$[m]$	Fuselage height
l_f	6.90	$[m]$	Fuselage length
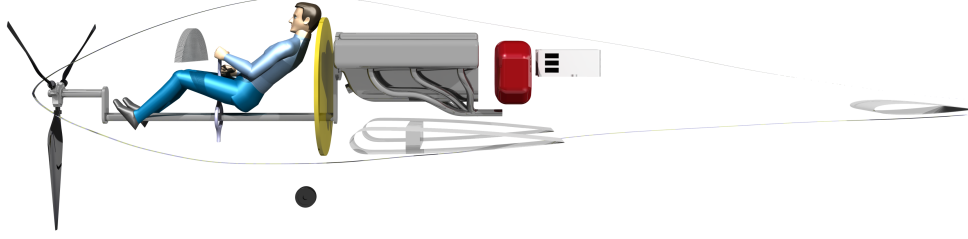
Figure 3.10: Side view render of the FX-15 fuselage

3.8 Initial Estimate of Aircraft Drag & Oswald Factor

The next step in the iteration process is to update the values for the zero-lift drag coefficient and the Oswald factor. These values will be used in the next iteration, as input for the wing and power loading diagrams.

3.8.1 Zero-lift Drag Coefficient

An initial estimate of C_{D_0} according to Torenbeek's method can be obtained by eq. (3.16) [15]. In this equation r_{Re} is the Reynolds number correction factor, r_{uc} the undercarriage drag penalty, r_t the tailplane contribution to the total drag, and $(C_{D_0} \cdot S)_j$ the zero-lift drag coefficient of the jth component times it's reference area. The input and output are shown in table 3.7 and table 3.8, respectively. Note that the input and output values for the final iteration are given.

$$C_{D_0} = \frac{1}{S} \cdot r_{Re} \cdot r_{uc} \left[r_t \left[(C_{D_0} \cdot S)_w + (C_{D_0} \cdot S)_f \right] + (C_{D_0} \cdot S)_{engine} \right] \tag{3.16}$$

The contribution of the wing is given by eq. (3.17). Where r_w is the wing correction factor, t/c the thickness over chord, $\Lambda_{0.25c}$ the quarter chord sweep, and S the wing surface area.

$$(C_{D_0} \cdot S)_w = 0.0054 \cdot r_w (1 + 3\frac{t}{c} cos(\Lambda_{0.25c})^2) S \tag{3.17}$$

The contribution of the fuselage is given by eq. (3.18). Where r_f is the fuselage correction factor, l_f the fuselage length, b_f the fuselage width, and h_f the fuselage height.

$$(C_{D_0} \cdot S)_f = 0.0031 \cdot r_f l_f (b_f + h_f) \tag{3.18}$$

The contribution of the engine is zero since the engine is located inside the fuselage, eq. (3.19).

$$(C_{D_0} \cdot S)_{engine} = 0 \tag{3.19}$$

3.8.2 Oswald Factor

The Oswald factor can be estimated using Howe's method [17]. Howe's equation eq. (3.20) is based on the Mach number (M), the taper ratio (λ), the aspect ratio (A), the airfoil thickness ratio (t/c), the quarter chord sweep ($\Lambda_{0.25c}$), and the number of engines on top of the wing (N_e). This function is valid for subsonic and transonic aircraft with a moderate to high aspect ratio ($A > 5$) [17].

$$e = \frac{1}{(1 + 0.12M^6) \left(1 + \frac{0.142 + f(\lambda)A(10\frac{t}{c})^{0.33}}{cos(\Lambda_{0.25c})^2} + \frac{0.1(3N_e+1)}{(4+A)^{0.8}} \right)} \tag{3.20}$$

$$f(\lambda) = 0.005 \cdot (1 + 1.5 \cdot (\lambda - 0.6)^2) \tag{3.21}$$

3.8.3 Results

The input values are stated in table 3.7. The resulting C_{D_0} and Oswald factor are given in table 3.8.

Table 3.7: Input for Torenbeek's initial estimation of airplane drag and Oswald factor

Parameter	Value	Unit	Source	Description
r_{Re}	1.31	$[-]$	[15]	Reynolds number correction factor
r_w	1.00	$[-]$	[15]	Wing correction factor
r_t	1.24	$[-]$	[15]	Tailplane contribution to the total drag
r_f	0.84	$[-]$	[15]	Fuselage correction factor
r_{uc}	1.25	$[-]$	[15]	Undercarriage drag penalty
$\Lambda_{0.25c}$	-1.48	$[°]$	Section 3.5.5	Sweep at quarter chord
l_f	6.90	$[m]$	Section 3.7	Fuselage length
b_f	0.90	$[m]$	Section 3.7	Fuselage width
h_f	1.25	$[m]$	Section 3.7	Fuselage height
N_e	0	$[-]$	[11]	Number of engines on the wing
λ	0.50	$[-]$	Section 3.5.5	Taper ratio
t/c	0.11	$[-]$	[2]	Maximum thickness w.r.t chord of the airfoil
A	6.45	$[-]$	Section 3.5.5	Aspect ratio
M	0.24	$[-]$	Section 3.5.3	Mach number at cruise of 80 m/s

Table 3.8: Output from Torenbeek's initial estimation of airplane drag and Oswald factor

Variable	Value	Unit	Description
C_{D_0}	0.0216	$[-]$	Zero-lift drag coefficient
e	0.839	$[-]$	Oswald factor

3.9 Class II Weight Estimation

Torenbeek's class II method is used to obtain a more accurate weight estimation of the FX-15 [15]. For the weight estimation of the equipment and safety systems are assumptions made:

1. The weight of the equipment is assumed to be 5% of the MTOW.

2. The weight of the safety systems is assumed to be 2% of the MTOW.

The class II weight estimation is the last step in the first iteration loop, see section 3.1. Five iterations were required to converge the MTOW to an deviation of 0%. The resulting class II weight estimation is shown in table 3.10. The input values for the class II weight estimation are given in table 3.9 and the change of the output values over the iterations is given summarized in table 3.10.

Table 3.9: Input values for Class II weight estimation

Variable	Value	Unit	Source	Description
W_{to}	849.6	$[kg]$	Section 3.9	Maximum take-off weight, output of the previous iteration
k_s	0.447	$[-]$	[15]	Factor of proportionality from Torenbeek
n_{ult}	12	$[-]$	[5]	Maximum load factor
b_f	0.90	$[m]$	Section section 3.7	Fuselage width
h_f	1.25	$[m]$	Section 3.7	Fuselage height
l_f	6.90	$[m]$	Section 3.7	Fuselage length
k_w	$4.90(10^{-3})$	$[-]$	[15]	Factor of proportionality from Torenbeek
b_{ref}	1.905	$[m]$	[15]	Reference span from Torenbeek
c_r	1.76	$[m]$	Section 3.5.5	Root chord
t/c	0.11	$[-]$	[2]	Maximum thickness w.r.t chord of the airfoil
S	11.20	$[m^2]$	Section 3.4	Wing surface area
b	8.50	$[m]$	Section 3.5.5	Wing span

$\lambda(0.5c)$	-2.96	[°]	Section 3.5.5	Half chord sweep	
S_h	1.77	[−]	Section 3.10	Horizontal tail surface area, output of the previous iteration	
S_v	1.39	[m^2]	[2]	Vertical tail surface area	
K_{wf}	0.23	[−]	[15]	Factor of proportionality Torenbeek	
V_D	96.0	[m/s]	[2]	Design dive speed, $1.2 \cdot$ cruise speed	
l_t	4.20	[m]	Section 3.7	Tail arm	
S_G	14.0	[m^2]	CATIA	Gross wetted area of the fuselage	
k_{uc}	1.00	[−]	[15]	Factor of proportionality from Torenbeek	
A	9.10	[−]	[15]	Factor of proportionality from Torenbeek	
B	0.082	[−]	[15]	Factor of proportionality from Torenbeek	
C	0.019	[−]	[15]	Factor of proportionality from Torenbeek	
k_{sc}	0.23	[−]	[15]	Factor of proportionality Torenbeek	
k_{pg}	1.16	[−]	[15]	Factor of proportionality Torenbeek	
P_{to}	315	[hp]	[5]	Power at take-off	
W_e	186	[kg]	[18]	Engine weight	

Table 3.10: Output values for Class II weight estimation

Component	Weight	Unit
Wing group	114	[kg]
Tail group	25	[kg]
Landing gear group	38	[kg]
Surface control group	21	[kg]
Propulsion group	255	[kg]
Fuselage group	100	[kg]
Equipment group	42	[kg]
Safety systems group	17	[kg]
Empty mass	612	[kg]
Fuel mass	51.6	[kg]
Payload mass	186	[kg]
MTOW	849.6	[kg]

Table 3.11: Change of parameters during iteration loop 1

Iteration	MTOW [kg]	% Difference	C_{D_0}	% Difference	Oswald factor	% Difference
1	794.0		0.0420		0.800	
2	835.2	10.3%	0.0218	-92.7%	0.838	0.1%
3	845.6	1.2%	0.0217	-0.5%	0.839	0.0%
4	848.9	0.3%	0.0217	-0.0%	0.839	0.0%
5	849.6	0.1%	0.0216	-0.5%	0.839	0.0%
6	849.6	0.0%	0.0216	-0.0%	0.839	0.0%
Iteration	Wing area	% Difference	Wing span	% Difference	Aspect ratio	% Difference
1	10.46		8.50		6.91	
2	11.00	4.9%	8.50	0%	6.57	-5.2%
3	11.15	1.4%	8.50	0%	6.48	-1.4%
4	11.18	0.3%	8.50	0%	6.46	-0.3%
5	11.20	0.2%	8.50	0%	6.45	-0.2%
6	11.20	0.0%	8.50	0%	6.45	-0.0%

3.10 Tail Sizing & Wing Location

Using the class II weight estimation the loading diagram is generated. The loading diagram shows the position of the wing against the range of the CG of the FX-15 during the RBAR. In order to size the horizontal stabilizer, this loading diagram is combined with the scissor plot. This scissor plot consists of two lines representing the controllability and stability limits by plotting S_h/S against the CG. The controllability curve is defined by eq. (3.22) and the stability curve is defined by eq. (3.23).

$$\bar{x}_{cg} = \bar{x}_{ac} - \frac{C_{m_{ac}}}{C_{L_{A-h}}} + \left(\frac{C_{L_h}}{C_{L_{A-h}}} \right) \frac{S_h l_h}{S \bar{c}} \left(\frac{V_h}{V} \right)^2 \tag{3.22}$$

$$\bar{x}_{cg} = \bar{x}_{ac} + \frac{C_{L_{\alpha_h}}}{C_{L_\alpha}} \left(1 - \frac{d\epsilon}{d\alpha}\right) \frac{S_h l_h}{S\bar{c}} \left(\frac{V_h}{V}\right)^2 - S.M. \tag{3.23}$$

The coefficients used to plot these curves are based on structural and aerodynamic properties of the aircraft. Most coefficients are calculated using aircraft parameters, but some are estimated using Torenbeek. Using the input values from table 3.12, the parameters of eq. (3.22) and eq. (3.23) can be determined using Torenbeek's method [15].

All the input parameters used for the calculation of the scissor plot are found in table 3.12.

Table 3.12: Input values for scissor plot calculations

Variable	Value	Unit	Source	Description
$(\bar{x}_{ac})_w$	0.25	[−]	[15]	Location of the aerodynamic center
$A_{tail,hor}$	5.00	[−]	Estimate	Tail aspect ratio
b_f	0.90	[m]	Section 3.7	Fuselage width
h_f	1.25	[m]	Section 3.7	Fuselage height
l_f	6.90	[m]	Section 3.7	Fuselage length
S	11.20	[m^2]	Section 3.5.5	Wing surface area
$\bar{c}$	1.37	[m]	Section 3.5.5	Length of the MAC
λ	0.50	[−]	Section 3.5.5	Taper ratio
b	8.50	[m]	Section 3.5.5	wing span
A	6.45	[m^2]	Section 3.5.5	Aspect ratio
M	0.32	[−]	Section 3.5.3	Maximum Mach number
η	0.95	[−]	[15]	Airfoil efficiency
$\Lambda_{0.25c}$	-1.48	[°]	Section 3.5.5	Sweep at quarter chord
$\Lambda_{0.5c}$	-2.96	[°]	Section 3.5.5	Sweep at half chord
$\Lambda_{0.5c_h}$	0.00	[°]	[15]	Sweep of the horizontal tail
ρ	1.225	[kg/m^3]	[10]	Density at sea level
P_{br}	315	[hp]	[5]	Engine power
W	849.6	[kg]	Section 3.9	MTOW
C_L	1.6	[−]	Section 3.4	Lift coefficient at cruise condition
$S.M.$	0.05	[−]	[15]	Stability Margin

Using the data from table 3.12, five iterations were performed to find the minimal horizontal stabilizer surface and optimal wing location. The results are shown in table 3.13.

Table 3.13: Change of parameters during iteration loop 2

	Input				Output				
Iteration	Tail mass	X_{LEMAC}	X_{cg}	Sh/s	X_{cg}/MAC_{min}	X_{cg}/MAC_{max}	X_{LEMAC}/L_{fus}	S_h	X_{LEMAC}
1	25.0	2.00	2.30	0.155	0.09	0.33	0.32	1.68	2.18
2	23.6	2.18	2.47	0.168	0.08	0.32	0.32	1.82	2.18
3	25.3	2.18	2.45	0.164	0.09	0.32	0.32	1.78	2.21
4	24.7	2.21	2.49	0.167	0.08	0.32	0.32	1.81	2.19
5	25.1	2.19	2.46	0.163	0.09	0.32	0.32	1.77	2.19

Using this iteration, the scissor plot as presented in the midterm report has been improved, resulting in fig. 3.11.
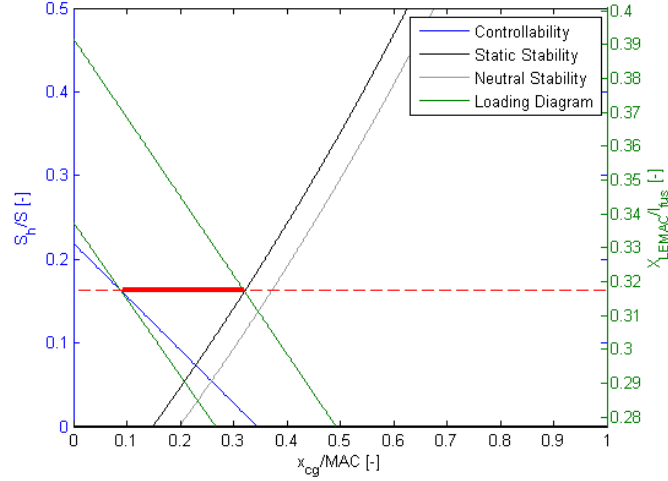
Figure 3.11: Improved scissor plot

3.11 Refined Drag Estimation

Before the detailed design of the subsystems can be performed, it is necessary to improve the drag estimation for the FX-15. This section describes the refined drag estimation. The drag contributions of the fuselage, wing, tail, and landing gear are predicted and added up, resulting in an accurate drag coefficient prediction for the entire aircraft. The refined drag estimation has been calculated using the methods from the master course AE3021 'Aircraft Design, Improved Drag Prediction' by Ir. Joris A. Melkert [19] with the input values given in table 3.14. Note that all drag coefficient values are for straight, symmetric flying conditions at ISA sea-level conditions and a speed of 80 m/s, which equals Mach 0.24 at ISA sea-level conditions.

3.11.1 Fuselage & Wing

The refined drag estimation for the fuselage is calculated with eq. (3.24) and eq. (3.25). $C_{D_{0,fus-base}}$ represents the fuselage zero-lift drag coefficient without base drag. The fuselage base-drag is given by $C_{D_{b,fus}}$. The induced drag of the fuselage is represented by $C_{D_{induced,fus}}$. Applying the refined drag calculation method results in the total fuselage drag coefficient $C_{D_{fus}}$ given in table 3.15.

$$C_{D_{0,fus-total}} = C_{D_{0,fus-base}} + C_{D_{b,fus}} \tag{3.24}$$

$$C_{D_{fus}} = C_{D_{0,fus-total}} + C_{D_{induced,fus}} \tag{3.25}$$

The refined drag estimation for the wing is based on eq. (3.26). Implementing the input values from table 3.14 into the refined drag calculation method results in the total wing drag coeficient, $C_{D,wing}$, given in table 3.15.

$$C_{D,wing} = C_{D_{0,wing}} + C_{D_{induced,wing}} \tag{3.26}$$

3.11.2 Empennage & Landing Gear

The refined drag estimation for the tail uses the same methodology and equations as for the wing [19]. The calculations will be performed seperately for the vertical and horizontal tailplane. The results of this are added up, giving the total tail drag coefficient. The input values for the tail refined drag estimation are stated in table 3.14. The resulting tail drag estimate is given in table 3.15. Note that whenever applicable, a Reynolds number of $2(10^6)$ and a Mach number of 0.24 were used.

The refiend drag estimation for the landing gear is based on eq. (3.27) [19]. Using this equation with the input values stated in table 3.14 results in the landing gear drag estimate given in table 3.15. Note that S_{gear} in eq. (3.27) is obtained by multiplying b_t and D_t.

$$C_{D_{gear}} = C_{D_{gear_{CL=0}}} \left(\frac{S_{gear}}{S} \right) \tag{3.27}$$

3.11.3 Results

The input values have been summarized in table 3.14 together with their description and source.

Table 3.14: Input values for refined drag estimation

Parameter	Value	Unit	Source	Description
$A_{tail,hor}$	5.00	[−]	Estimate	Tail aspect ratio
$A_{tail,vert}$	3.00	[−]	Estimate	Tail aspect ratio
A_{wing}	6.45	[−]	Section 3.5.5	Wing aspect ratio
b_t	0.1334	[m]	Estimate	Tire width (5.25 inch)
b_{tail}	2.35	[m]	[2]	Tail span
b_{wing}	8.50	[m]	Section 3.5.5	Wing span
C_{d_c}	1.21	[−]	[19]	Experimental steady state cross-flow drag
$C_{D_{gear_{CL=0}}}$	0.46	[−]	[19]	Main landing gear type 3 with fairing A, zero-lift drag coefficient
$C_{f,fus}$	$3.5(10^{-3})$	[−]	[19]	Fuselage friction coefficient
$C_{fw,tail}$	$6.0(10^{-3})$	[−]	[19]	Tail turbulent flat plate friction coefficient of the tail
$C_{fw,wing}$	$4.7(10^{-3})$	[−]	[19]	Wing turbulent flat plate friction coefficient of the wing
C_{L_0}	0.00	[−]	Estimate	Zero angle of attack lift coefficient
C_{L_α}	4.50	$[rad^{-1}]$	Estimate	Lift curve slope of aircraft
$C_{r,tail}$	0.63	[m]	Estimate	Tail root chord
$C_{r,wing}$	1.76	[m]	Section 3.5.5	Wing root chord
$C_{t,tail}$	0.31	[m]	Estimate	Tail tip chord
$C_{t,wing}$	0.88	[m]	Section 3.5.5	Wing tip chord
d_b	0.20	[m]	Estimate	Fuselage base diameter
d_f	1.25	[m]	Section 3.7	Maximum fuselage diameter
D_t	0.40	[m]	Estimate	Tire diameter (16 inch)
e	0.839	[−]	Section 3.8.3	Wing/Tail Oswald factor
l_f	6.90	[m]	Section 3.7	Fuselage length
L_{h_L}	3.48	[−]	Calculation	Dimensionless distance between tail AC and wing AC
$\bar{c}_{wing}$	1.37	[m]	Section 3.5.5	Wing MAC
$R_{ls,tail}$	1.08	[−]	[19]	Tail lifting surface correction factor
$R_{ls,wing}$	1.10	[−]	[19]	Wing lifting surface correction factor
$R_{wb,fus}$	1.05	[−]	[19]	Wing/fuselage interference factor
$R_{wb,tail}$	1.00	[−]	[19]	Tail/fuselage interference factor
$R_{wb,wing}$	1.01	[−]	[19]	Wing/fuselage interference factor
S	11.20	$[m^2]$	Section 3.5.5	Wing surface area
S_b	0.03	$[m^2]$	Estimate	Fuselage base area
S_{fus}	0.65	$[m^2]$	CATIA	Maximum fuselage frontal area
S_h	1.18	$[m^2]$	Section 3.10	Horizontal tail surface area
$S_{plf,fus}$	5.22	$[m^2]$	CATIA	Fuselage planform area
S_v	1.20	$[m^2]$	[2]	Vertical tail surface area
$S_{wet,fus}$	14.0	$[m^2]$	CATIA	Fuselage wetted area
t/c	0.11	[−]	[2]	Airfoil maximum thickness/chord ratio
V	80	$[m/s]$	[1]	Velocity
W	849.6	[kg]	Section 3.9	Aircraft mass
$x_{ac,wing}$	2.29	[m]	[2]	Wing AC location
x_{cg}	2.46	[m]	Section 3.10	Aircraft CG location
x_h	6.2	[m]	[2]	Tail AC location
x_t	0.1	[m]	[2]	Airfoil location of maximum thickness
η	0.66	[−]	[19]	Finite cylinder to infinite cylinder drag ratio
ρ	1.225	$[kg/m^3]$	[10]	Sea level air density

The output values for all drag predictions are given in table 3.15. In this table the individual drag coefficient contributions are stated, as well as the total zero-lift, induced and complete drag coefficients. Note that for the induced drag, straight, symmetric flying conditions at sea level and a speed of 80 m/s were assumed.

Table 3.15: Output values for refined drag estimation

Subsystem	Drag coefficient	Value
Fuselage	$C_{D_{0,fus-base}}$	$5.40(10^{-3})$
	$C_{D_{b,fus}}$	$0.90(10^{-3})$
	$C_{D_{0,fus-total}}$	$6.30(10^{-3})$
	$C_{D_{induced,fus}}$	$0.00(10^{-3})$
	$C_{D_{fus}}$	$6.30(10^{-3})$
Wing	$C_{D_{0,wing}}$	$13.1(10^{-3})$
	$C_{D_{induced,wing}}$	$1.40(10^{-3})$
	$C_{D_{wing}}$	$14.5(10^{-3})$
Tail	$C_{D_{0,tail}}$	$3.10(10^{-3})$
	$C_{D_{induced,tail}}$	$0.00(10^{-3})$
	$C_{D_{tail}}$	$3.10(10^{-3})$
Landing gear	$C_{D_{0,gear}}$	$2.20(10^{-3})$
	$C_{D_{induced,gear}}$	$0.00(10^{-3})$
	$C_{D_{gear}}$	$2.20(10^{-3})$
Total	C_{D_0}	$24.7(10^{-3})$
	$C_{D_{induced}}$	$1.40(10^{-3})$
	C_D	$26.1(10^{-3})$

3.12 Optimization for the Race

According to section 3.9, the MTOW of the FX-15 is 849.6 kg. The minimum required race mass, as given by Red Bull is 698 kg [11]. So, even though the output from the Class II weight estimation complies with the regulations, it is not optimal and the FX-15 will be optimized for the RBAR. To optimize the FX-15, the race mass at the start gate should be as close as possible to the 698 kg.

During the preliminary design process, a fuel mass of 51.6 kg and a payload mass of 186 kg were used to comply with the regulations, section 3.9. However, for the RBAR a fuel mass of 36 kg and a payload mass of 88.5 kg (pilot and parachute) are used. The race mass then becomes 735.5 kg [2], while the OEW remains unchanged.

The wing will be sized on the MTOW of 735.5 kg to increase the performance of the FX-15 during the race. With a wing loading of 744.2 N/m^2, the aircraft can fly all the required maneuvers according to section 3.4. Designing a wing based on the race mass requires a wing surface area of 9.70 m^2.

The FX-15 should still be able to fly the mission profile (except the race) as mentioned in section 3.2 with the updated MTOW of 849.6 kg. The wing loading as result of the MTOW and a wing area of 9.70 m^2 is 852.1 N/m^2. The wing loading at landing, which is the next constraint after the maximum load factor, may not be higher than 866 N/m^2, as shown in fig. 3.6. Therefore, this requirement is still met and the FX-15 can still fly the mission profile (except the race) within it's MTOW. The design of the lifting surfaces and propulsion system will be based on the race configuration, while the landing gear has to be sized for the MTOW.

To conclude the preliminary design the race mass, OEW, fuel weight and payload weight for the original and race configuration are summarized in table 3.16. All output values of the preliminary design phase are summarized in appendix D.

Table 3.16: Output values for the preliminary design phase

Parameter	MTOW Configuration	Race Configuration	Unit	Description
OEW	612	612	[kg]	Operative Empty Weight
Fuel weight	51.6	36	[kg]	Fuel weight
Payload weight	186	88.5	[kg]	Payload weight
Weight	849.6	735.5 [2]	[kg]	MTOW / Optimized weight for race

---

[2] A take-off mass of 849.6 kg was obtained from the class II weight estimation and was used to size the wing area at 11.2 m^2. However, during the race the aircraft does not fly at the maximum take-off mass but at race mass. This race mass was calculated to be 735.5 kg. Using this race mass, the wing area was sized at 9.7 m^2. This wing area should have been used in the class II weight estimation again, but it was not. This resulted in a weight of 735.5 kg being used as input for the detailed design, instead of the correct weight of 729.4 kg. The implications of this error are small since the error is smaller than 1%.

4   Wing Detail Design

This chapter outlines the design process of the wing. First, the aerodynamic design will be described in section 4.1. Second, the control surfaces will be designed in section 4.2. Finally, the structural design of the wing will be discussed in section 4.3.

4.1   Aerodynamics

This section concerns the aerodynamic design process of the FX-15's wing. The problem will be defined, the method will be outlined, and the results will be described. Particular attention will be devoted to the optimization of various geometry parameters.

4.1.1   Problem Analysis

Wing design is an important task because the wing will either make or break the performance of the aircraft. The key to the design of a well performing aerobatic race aircraft wing is to attain a $C_{L_{max}}$ sufficiently high to meet stall speed and turn performance requirements while minimizing drag and retaining good-natured stall characteristics.

Requirements and Constraints

The following requirements and constraints are directly applicable to the design of the wing:

- The wing shall have a symmetric airfoil [11]

- The wing shall have a span between 7.00 and 8.50 meters [11]

- The aircraft shall be able a turn at a load factor of 12, an equivalent airpseed (EAS) of 90 m/s, and a weight of 735.5 kg [2, 12]

- The aircraft shall have a stall speed of at most 61 knots at MTOW [11]

Assumptions

The following assumptions apply:

1. Viscous drag is independent of angle of attack. *Constant viscous drag results in a less accurate drag polar because the transition point will shift which results in a different value of viscous drag.*

2. The lift that would otherwise be generated by the fuselage is compensated by the part of the wing modeled inside the fuselage. *This results in a less accurate maximum lift coefficient because it is difficult to determine the lifting capabilities of the fuselage*

3. The horizontal stabilizer and the elevator generate a downforce with a magnitude of 10% of the lift force of the wing. *A downforce of 10% results in a larger wing area than required because 10% is a conservative estimate.*

4. Stall starts when the local C_l exceeds local $C_{l_{max}}$ anywhere along the span of the wing. *This results in a lower $C_{L_{max}}$ because it only accounts for the linear part of the C_L–α curve.*

4.1.2   Method

The method consists of two parts: 2D aerodynamic analysis and 3D aerodynamic analysis. Two additional methods are necessary to fill in shortcomings of the 3D aerodynamic analysis tool: a technique to compute $C_{L_{max}}$ and an approach to determine the drag polar.

2D Aerodynamic Coefficients

The aerodynamic coefficients of the two dimensional wing sections were determined by means of the XFOIL software package [20]. XFOIL was developed by Mark Drela at MIT and it has become the de facto standard for airfoil design and analysis. An initial airfoil selection was performed in the preliminary design stage of the FX-15 [2]. The initially selected airfoil was subsequently improved in close collaboration with Ir. Loek Boermans at Delft University of Technology.

3D Aerodynamic Coefficients

The aerodynamic coefficients of the three dimensional wing were obtained by means of the Quasi-3D Aerodynamic Solver (Q-3D AeroSolver) developed and validated by Dr. Ali Elham at Delft University of Technology [21]. Elham's Q-3D AeroSolver conveniently runs inside MATLAB and uses AVL, XFOIL, VGK, and MSES at its core, thereby creating a synergy of multiple powerful aerodynamic solvers.

Although accurate and usable for a wide range of flow conditions, Elham's Q-3D AeroSolver does not determine the maximum lift coefficient of a wing and is unable to compute viscous drag for complex geometries or at large angles of attack.

The Iteration Loop

An iteration loop is required because wing area is dependent on $C_{L_{max}}$ and vice versa. $C_{L_{max}}$ is dependent on wing area because different wing areas result in different aspect ratios at equal wing span. In the first iteration, wing area is calculated based on a $C_{L_{max}}$ of 1.80 as estimated in the preliminary design phase. Elham's Q-3D AeroSolver subsequently computes a new $C_{L_{max}}$ which in turn enables the computation of a refined wing area. A flowchart of this loop is shown in fig. 4.1.

Wing Maximum Lift Coefficient

The $C_{L_{max}}$ of the wing may be estimated from the assumption that this lift coefficient is reached when the local section lift coefficient C_l at any any position along the span is equal to the local maximum lift coefficient $C_{l_{max}}$ of the wing at the corresponding section [22]. The value of C_L at this point is the $C_{L_{max}}$ of the wing. An illustration of this method is shown in fig. 4.2.
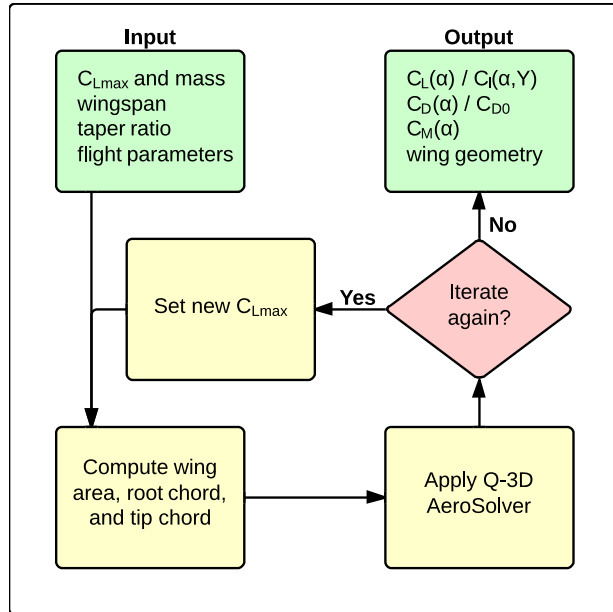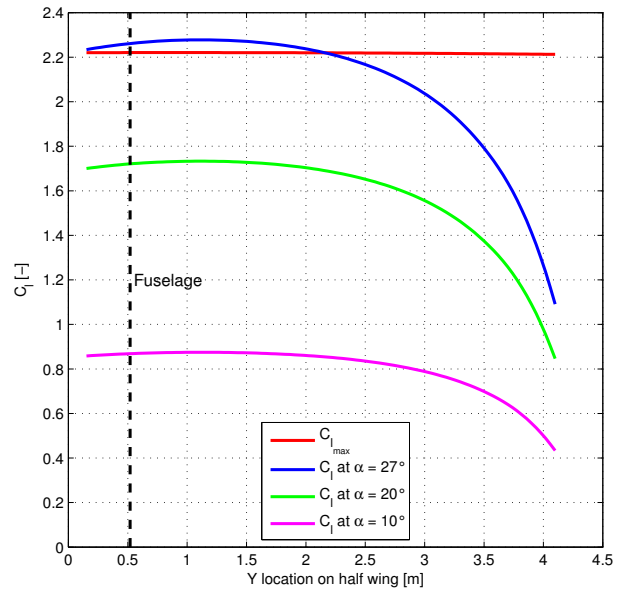

Figure 4.1: Iteration loop flowchart

Figure 4.2: Method to determine $C_{L_{max}}$ based on comparing local C_l against local $C_{l_{max}}$

A secondary benefit of this method is that it perfectly lends itself to determination of stall behavior. It shows at a glance the spanwise location where the wing begins to stall. Examples of tip and root stall of a generic wing are shown in fig. 4.3 and fig. 4.4, respectively. Tip stall is typically associated with dangerous stall characteristics while root stall is associated with benign stall characteristics because it allows the pilot to retain roll control in the event of a stall.
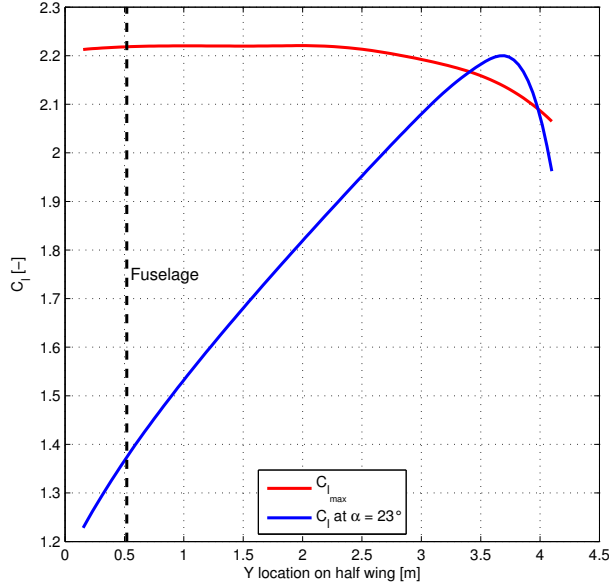

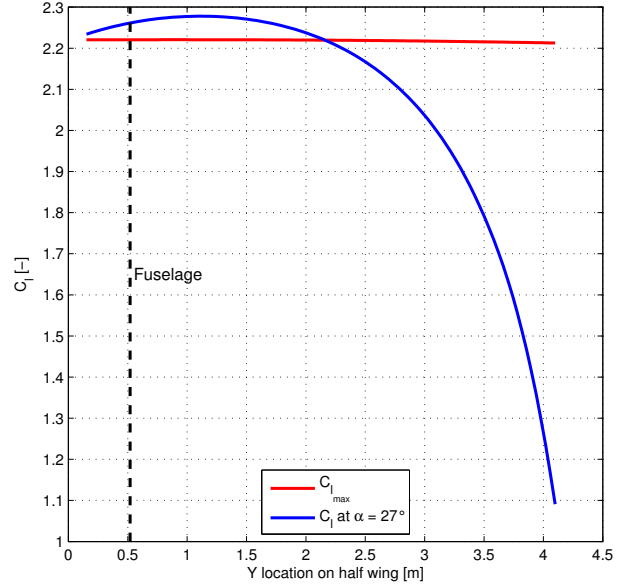Figure 4.3: C_l distribution at tip stall

Figure 4.4: C_l distribution at root stall

The value of spanwise local $C_{l_{max}}$ is dependent on both the Reynolds number and the section thickness. An overview of the $C_{l_{max}}$ of the improved airfoil as a function of Reynolds number and section thickness is shown in table 4.1. The aforementioned method of comparing C_l against $C_{l_{max}}$ requires some means of computing $C_{l_{max}}$ as function of an arbitrary Reynolds number and section thickness. Cubic interpolation is applied on the data in table 4.1 to determine an interpolant which enables $C_{l_{max}}$ to be computed as function of any Reynolds number and section thickness. This method is illustrated in fig. 4.5.

Table 4.1: Overview of $C_{l_{max}}$ as function of Reynolds number and thickness in % of chord length

		Reynolds number							
		$3 \cdot 10^6$	$4 \cdot 10^6$	$5 \cdot 10^6$	$6 \cdot 10^6$	$7 \cdot 10^6$	$8 \cdot 10^6$	$9 \cdot 10^6$	$10 \cdot 10^6$
Thickness	**8%**	1.63	1.65	1.69	1.76	1.77	1.78	1.80	1.81
	9%	1.68	1.71	1.72	1.73	1.77	1.82	1.83	1.84
	10%	1.76	1.77	1.78	1.80	1.81	1.83	1.84	1.85
	11%	2.10	2.16	2.19	2.21	2.22	2.22	2.22	2.22
	12%	2.07	2.12	2.16	2.18	2.18	2.17	2.14	2.10

Wing Drag Polar

A widely accepted equation to construct the drag polar of a wing is given by eq. (4.1).

$$C_{D_{wing}} = C_{D_{0_{wing}}} + \frac{C_L^2}{\pi e A} = C_{D_{0_{wing}}} + C_{D_{i_{wing}}} = \text{viscous drag} + \text{induced drag} \qquad (4.1)$$

Elham's Q-3D AeroSolver is used to obtain $C_{D_{0_{wing}}}$ by viscous analysis while forcing C_L to a value of 0. Values of $C_{D_{i_{wing}}}$ can subsequently be computed in the non-viscous mode by varying the value of α across its domain. The polar is then constructed by adding the values of $C_{D_{i_{wing}}}$ to $C_{D_{0_{wing}}}$. This approach is necessary because Elham's Q-3D AeroSolver does not converge in viscous mode at large angles of attack.
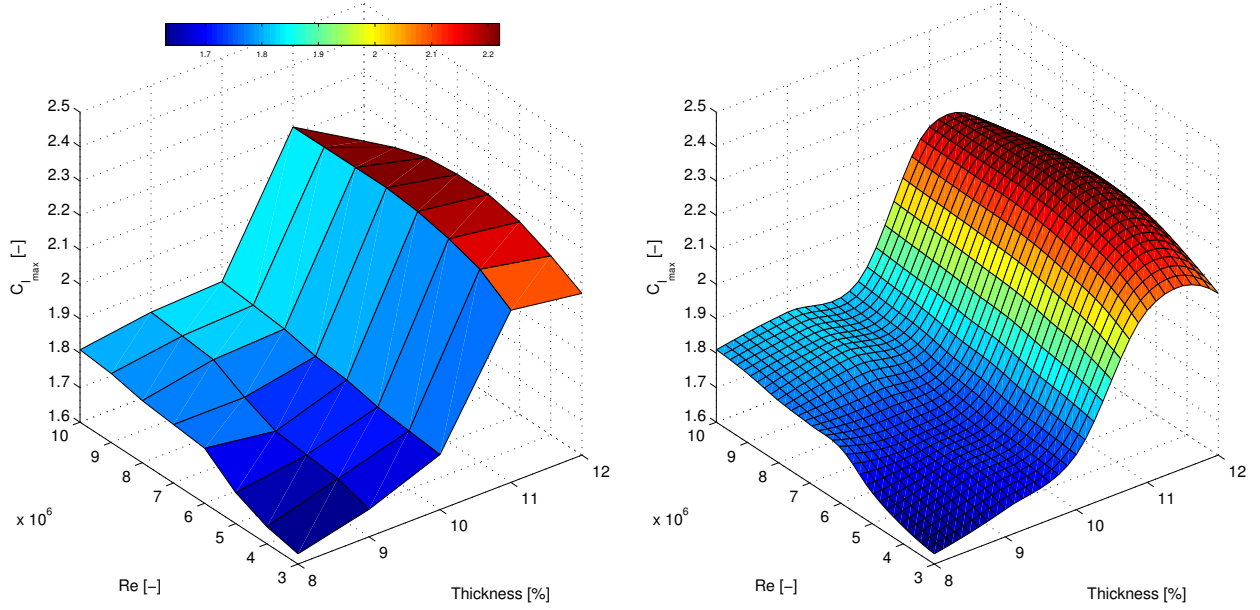
Figure 4.5: Cubic interpolation of $C_{l_{max}}$ showing raw data (left) and interpolated data (right)

4.1.3   Results

The results consist of one part describing the selected airfoil, multiple parts outlining the influence of various geometry parameters, and one part detailing the iteration loop. The parts outlining the influence of airfoil thickness, span, taper, and sweep serve the purpose to determine which value is optimal. These particular results were obtained after a single iteration with the following inputs, varying parameters where necessary: $C_{L_{max}} = 1.80$, $b = 8.50$ m, $\lambda = 0.40$, $\Lambda_{LE} = 0°$, $m = 735.5$ kg, $V = 90$ m/s, and an identical airfoil at root and tip. A velocity of 90 m/s is used as input because this is the velocity at which the maximum load factor is attained in flight [1]. The optimum values were used as inputs for the final wing sizing iteration loop.

Airfoil Selection

The NACA 0011-61 selected in the preliminary design stage was developed into the NACA 0011-61MOD in close collaboration with Ir. Loek Boermans. The geometry of the NACA 0011-61MOD is shown in fig. 4.6. Among the improvements of the NACA 0011-61MOD over the NACA 0011-61 are a significantly larger $C_{l_{max}}$ and vastly superior stall characteristics. The shape of the NACA 0011-61MOD was finetuned to achieve trailing edge stall because, according to Ir. Loek Boermans, an airfoil displaying trailing edge stall is not plagued by hysteresis. Pressure coefficients of the NACA 0011-61MOD at various angles of attack match those of a generic airfoil displaying trailing edge stall, as can be seen in fig. 4.9. The C_l–α curve and the drag polar of the NACA 0011-61MOD are shown in fig. 4.7 and fig. 4.8, respectively.
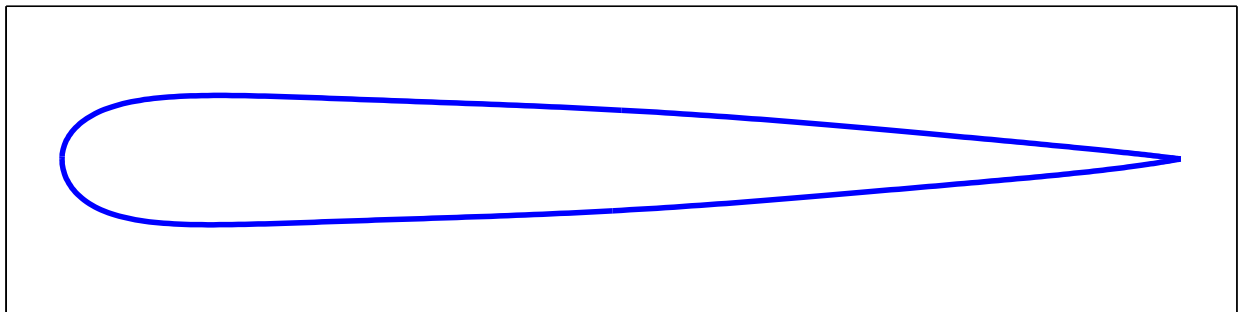
Figure 4.6: Geometry of the NACA 0011-61MOD
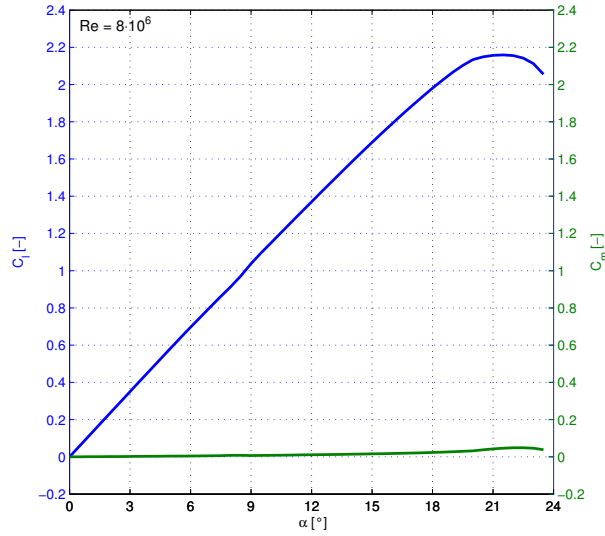
Figure 4.7: Lift curve of the NACA 0011-61MOD
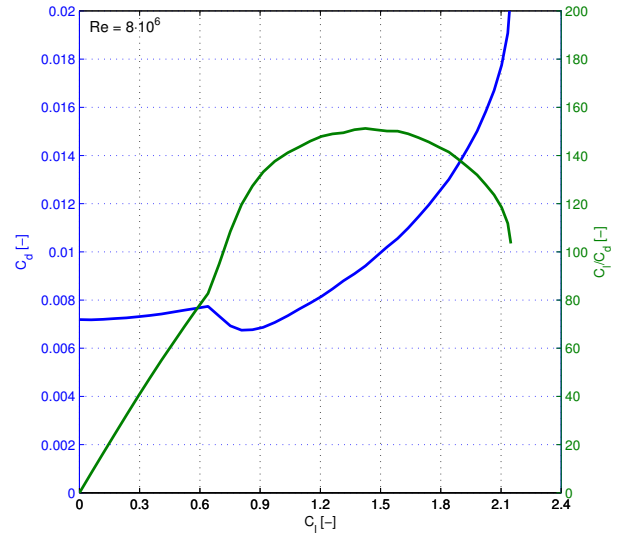
Figure 4.8: Drag polar of the NACA 0011-61MOD
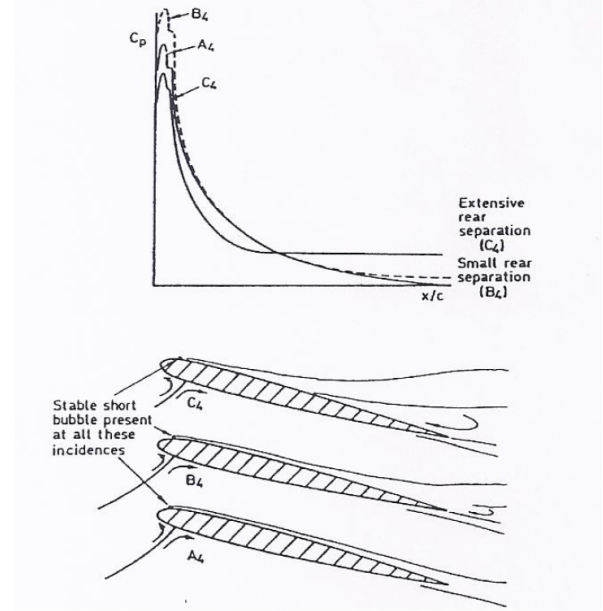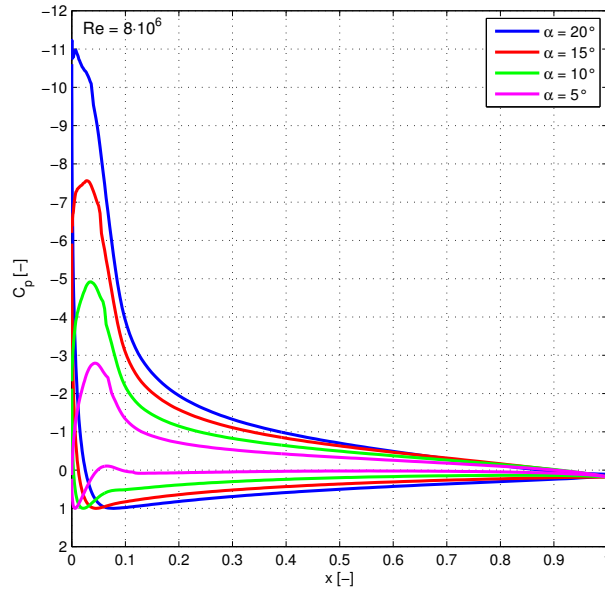
Figure 4.9: C_p distribution of the NACA 0011-61MOD (lift) compared to the typical C_p distribution of a generic airfoil during trailing edge stall (right)

Influence of Airfoil Thickness

The values of $C_{L_{max}}$ and C_L/C_D at $C_{L_{design}}$ for different combinations of root and tip airfoil thickness are shown in table 4.2. C_L/C_D at $C_{L_{design}}$ is the only meaningful way to compare C_D because it is dependent on α. Furthermore, C_L/C_D is a number that has a more meaningful context than a plain C_D. The design lift coefficient was set at 0.3, as determined in the preliminary design phase. However, $C_{L_{des}}$ is recomputed in every iteration because it is slightly dependent on wing area and mass. All airfoils are scaled versions of the NACA 0011-61MOD. The foremost reason for selecting a thinner root airfoil is to enforce root stall. However, in this case any combination of a smaller root than tip thickness results in vastly inferior performance compared to performance with an invariant thickness of 11%. It was therefore decided to set section thickness to a constant 11%. Root stall will be enforced by other means.

24

Table 4.2: Influence of different combinations of root and tip airfoil thickness in % of chord length on $C_{L_{max}}$ and C_L/C_D at $C_{L_{design}}$ (marked gray) of the wing

		Tip Airfoil Thickness				
		8%	9%	10%	11%	12%
Root Airfoil Thickness	8%	1.66	1.72	1.68	1.65	1.65
		28.0	27.8	27.6	27.3	27.2
	9%	1.72	1.69	1.65	1.66	1.68
		27.0	27.5	27.3	26.3	26.3
	10%	1.67	1.65	1.70	1.80	1.83
		26.9	25.8	27.0	25.5	25.4
	11%	1.65	1.68	1.88	2.06	2.07
		25.6	26.2	26.2	26.4	25.6
	12%	1.67	1.76	2.04	2.04	2.01
		25.7	25.3	26.7	26.3	26.1

Influence of Wing Span

The values of $C_{L_{max}}$ and C_L/C_D at $C_{L_{design}}$ for different values of wing span are displayed in table 4.3. It is clear that a wing span of 8.50 m prevails over a smaller span. This result is in line with expectations because a larger aspect ratio results in a decreased induced drag and a larger $C_{L_{max}}$. The wing span was therefore set to 8.50 m.

Table 4.3: Influence of wing span on the aerodynamic characteristics of the wing

b [m]	$C_{L_{max}}$ [−]	C_L/C_D at $C_{L_{design}}$ [−]	A [−]
7.00	2.02	23.3	4.58
7.50	2.04	24.4	5.26
8.00	2.05	25.5	5.98
8.50	2.06	26.4	6.76

Influence of Sweep Angle

The values of $C_{L_{max}}$ and C_L/C_D at $C_{L_{design}}$ as well as the stall location for different values of leading edge sweep angle are displayed in table 4.4. A leading edge sweep angle of 0° is clearly the best compromise between $C_{L_{max}}$, C_L/C_D, and stall characteristics. This reconfirms observations in the preliminary design phase. Leading edge sweep was set to an angle of 0° resulting in a wing with a straight leading edge.

Table 4.4: Influence of sweep angle on the aerodynamic characteristics of the wing

Λ_{LE} [°]	$C_{L_{max}}$ [−]	C_L/C_D at $C_{L_{design}}$ [−]	Stall Location [−]
-30	1.81	26.5	Root
-15	1.99	26.5	Root
0	2.06	26.4	Root
15	2.04	26.5	Center
30	2.00	26.6	Tip

Influence of Taper Ratio

The values of $C_{L_{max}}$ and C_L/C_D at $C_{L_{design}}$ as well as the stall location for different values of taper ratio are displayed in table 4.5. A taper ratio of 0.50 results in optimal aerodynamic coefficients, as foreseen in the preliminary design phase. However, in this case the requirement for root stall drives the choice of taper. The taper ratio was set to 0.60 because a wing with this taper ratio enforces root stall at a minimum cost of $C_{L_{max}}$.

Table 4.5: Influence of taper ratio on the aerodynamic characteristics of the wing

λ [−]	$C_{L_{max}}$ [−]	C_L/C_D at $C_{L_{design}}$ [−]	Stall Location [−]
0.30	2.03	26.4	Tip
0.40	2.07	26.4	Tip
0.50	2.08	26.4	Center
0.60	2.06	26.4	Root
0.70	2.03	26.4	Root

Wing Sizing

All values required to start the wing sizing iteration loop have now been determined and are summarized in table 4.6. Stall speed is omitted in the input table because the turn requirement is critical of the two, as is shown in fig. 3.5. The stall speed requirement is automatically met as soon as the turn performance requirement is met.

Table 4.6: Input values for wing sizing

Parameter	Value	Unit	Source	Description
$C_{L_{max}}$	1.80	[−]	Section 3.4	Initial value of $C_{L_{max}}$ in the iteration loop
b	8.50	[m]	Section 4.1.3	Wing span
λ	0.60	[−]	Section 4.1.3	Wing taper ratio
Λ_{LE}	0.00	[°]	Section 4.1.3	Wing leading edge sweep angle
m	735.5	[kg]	Section 3.12	Aircraft weight at design condition
V	90.0	[m/s]	[2]	Equivalent airspeed at design condition
ρ	1.225	[kg/m^3]	[10]	Air density at design condition
n_{design}	12	[−]	[12]	Design load factor

The values for wing area and $C_{L_{max}}$ converge to 9.30 m^2 and 2.07, respectively, as shown in fig. 4.10. The distribution of C_l in stall conditions is shown in fig. 4.11. Stall starts sufficiently close to the root for the pilot to retain roll control in the event of a stall. The requirement for good-natured stall characteristics has therefore been met.
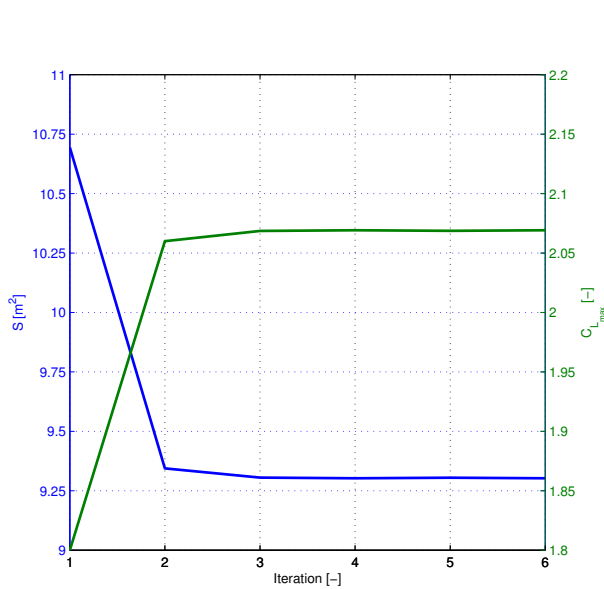
Figure 4.10: Values of S and $C_{L_{max}}$ during iteration
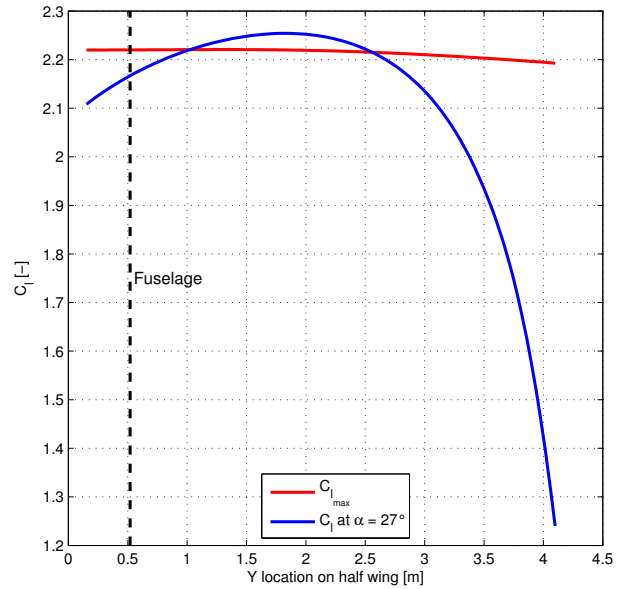
Figure 4.11: C_l distribution in stall conditions
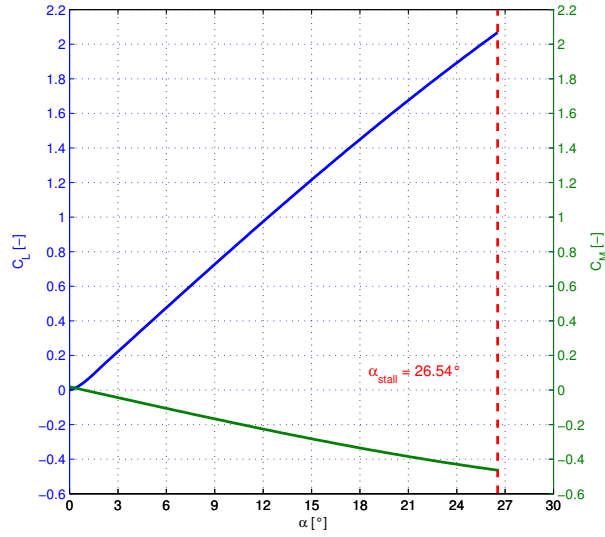
Figure 4.12: Wing C_L–α and C_M–α curves
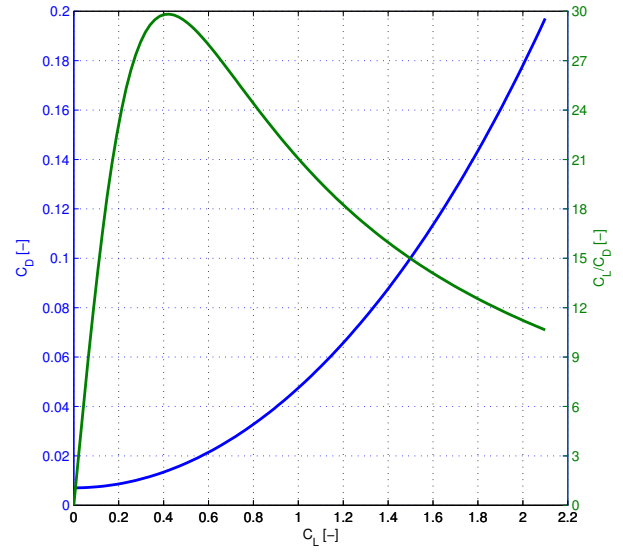
Figure 4.13: Wing drag polar

C_L–α and C_M–α curves of the wing are shown in fig. 4.12. The drag polar of the wing is displayed in fig. 4.13. A top view of the geometry of the wing is plotted in fig. 4.14. Principal parameters are included in the plot. A 3D view of the wing geometry is shown in fig. 4.15. The 3D view shows that the wing is neither twisted nor has a dihedral angle. The 3D view does not show the angle of incidence of the wing, which is the angle between the center line of the fuselage and the chord of the wing. The angle of incidence is set at an angle such that the wing generates its $C_{L_{design}}$ while the centerline of the fuselage is collinear with the flow velocity vector.
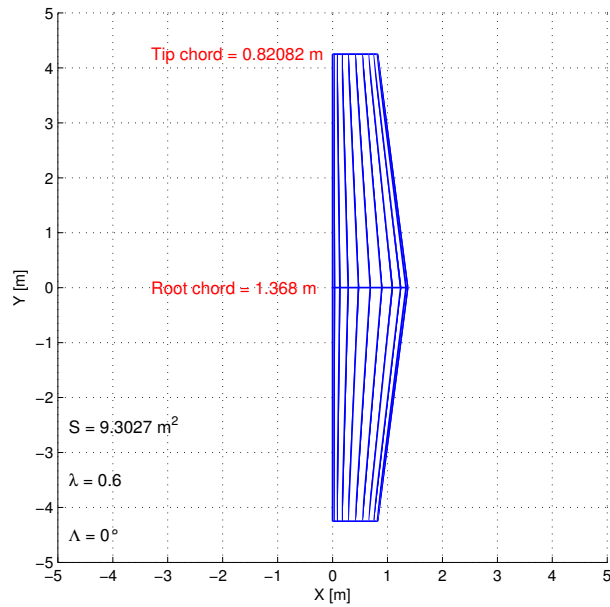
Figure 4.14: Top view of wing geometry
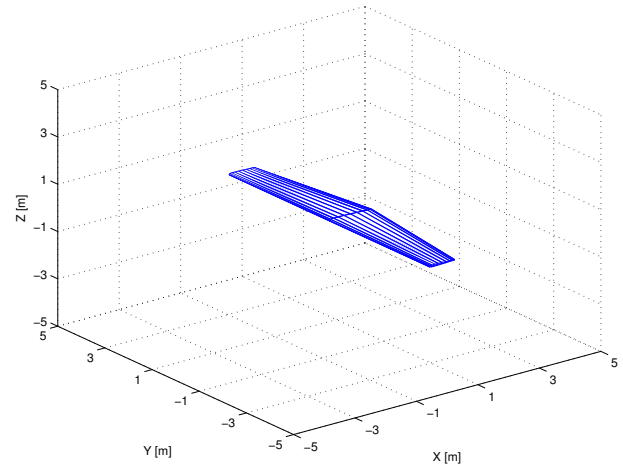
Figure 4.15: 3D view of wing geometry

The aerodynamic characteristics of the wing, the geometry of the wing, and any remaining output values of the aerodynamic wing design process are summarized in table 4.7.

27

Table 4.7: Output values for wing sizing

Parameter	Value	Unit	Description
$C_{L_{max}}$	2.07	$[-]$	Maximum lift coefficient of the wing
C_{L_α}	4.47	$[rad^{-1}]$	Wing lift slope
α_{stall}	26.5	$[°]$	Angle of attack of the wing at stall
$C_{L_{design}}$	0.31	$[-]$	Design lift coefficient of the wing
$C_{D_{0_{wing}}}$	$7.048(10^{-3})$	$[-]$	Zero-lift drag coefficient of the wing
e	0.836	$[-]$	Oswald factor
S	9.30	$[m^2]$	Wing area
C_r	1.37	$[m]$	Wing root chord
C_t	0.82	$[m]$	Wing tip chord
$\bar{c}$	1.12	$[m]$	Mean aerodynamic chord
b	8.50	$[m]$	Wing span
A	7.77	$[-]$	Wing aspect ratio
λ	0.60	$[-]$	Wing taper ratio
Λ_{LE}	0.00	$[°]$	Wing leading edge sweep angle
$\Lambda_{0.25c}$	-1.84	$[°]$	Wing quarter chord sweep angle
$\Lambda_{0.5c}$	-3.68	$[°]$	Wing half chord sweep angle
i_w	4.05	$[°]$	Angle of incidence of the wing

4.1.4 Verification & Validation

The wing area displayed in table 4.7 is used to check the C_L required to fly a turn at an airspeed of 90 m/s at a load factor of 12. The calculation is shown in eq. (4.2).

$$C_L = \frac{L}{\frac{1}{2}\rho V^2 S} = \frac{n \cdot W \cdot 1.1}{\frac{1}{2}\rho V^2 S} = \frac{n \cdot m \cdot g \cdot 1.1}{\frac{1}{2}\rho V^2 S} = \frac{12 \cdot 735.5 \cdot 9.81 \cdot 1.1}{\frac{1}{2} \cdot 1.225 \cdot 90^2 \cdot 9.3027} = 2.0636 \tag{4.2}$$

The resulting C_L is merely 0.25% less than the value given in table 4.7. Hence, the value of C_L shown in table 4.7 is correct. Conversely, the above calculation implies that the iteration script correctly calculates wing area based on C_L.

The wing lift slope is predicted in eq. (4.3) based on the estimation method given in [14]. The required compressibility factor β and the airfoil efficiency factor η are calculated in eq. (4.4) and eq. (4.5), respectively. The predicted wing lift slope is 8.87% larger than the lift slope shown in table 4.7, which is within a reasonable margin.

$$C_{L_\alpha} = \frac{2\pi A}{2 + \sqrt{4 + \left(\frac{A\beta}{\eta}\right)^2 \left(1 + \frac{\tan^2 \Lambda_{0.5c}}{\beta^2}\right)}} = \frac{2\pi \cdot 7.77}{2 + \sqrt{4 + \left(\frac{7.77 \cdot 0.964}{0.964}\right)^2 \left(1 + \frac{\tan^2(-3.683\pi/180)}{0.964^2}\right)}} = 4.862 \ rad^{-1} \tag{4.3}$$

$$\beta = \sqrt{1 - M_\infty^2} = \sqrt{1 - \left(\frac{90}{\sqrt{1.4 \cdot 287.05 \cdot 288.15}}\right)^2} = 0.964 \tag{4.4}$$

$$\eta = \frac{C_{l_\alpha}\beta}{2\pi} = \frac{2\pi \cdot 0.964}{2\pi} = 0.964 \tag{4.5}$$

The stall angle of the wing is estimated in eq. (4.6) based on the estimation method also given in [14]. The result is 4.56% smaller than the stall angle predicted by Elham's Q-3D AeroSolver. The difference is within a reasonable margin.

$$\alpha_{stall} = \frac{C_{L_{max}}}{C_{L_\alpha}} + \alpha_0 + \Delta\alpha_{C_{L_{max}}} = \frac{0.9 \cdot C_{l_{max}}}{C_{L_\alpha}} + \alpha_0 + \Delta\alpha_{C_{L_{max}}} = \frac{0.9 \cdot 2.2}{4.862 \cdot \pi/180} + 0 + 2 = 25.33° \tag{4.6}$$

The above results demonstrate that the wing design method indeed solves the right problem and produces correct results.

The Q-3D AeroSolver was validated by its author Dr. Ali Elham [21].

4.1.5 Conclusion & Discussion

The wing design meets performance requirements and displays excellent stall behavior. It thereby contributes to mission success and most importantly to safe operation of the aircraft.

Sensitivity Analysis

XFOIL is notorious for overestimating $C_{L_{max}}$ in some cases. Fortunately, two of the assumptions applied in the above method introduce a certain margin of safety. The first is the assumption that the wing stalls when the local C_l exceeds the local $C_{l_{max}}$ anywhere along the span of the wing. In reality this is merely the point at which the linear part of the C_L–α curve ends. C_L will continue to increase for a fair bit in the non-linear part of the C_L–α curve. The second is the assumption that the horizontal tail generates a downforce with a magnitude of 10% of the lift force of the wing. This downforce was calculated based on the requirement for a certain pitch-up radial acceleration. However, pitch-up radial acceleration is entirely unnecessary in near-stall conditions. The downforce will therefore in reality never reach 10% of the lift force. These two assumptions make the wing less susceptible to a perhaps erroneously calculated $C_{L_{max}}$ by XFOIL.

Winglets

The use of winglets is a proven method to decrease induced drag. Even a generic winglet design such as in fig. 4.16 is able to significantly reduce induced drag, as shown in fig. 4.17. However, Elham's Q-3D AeroSolver is unable to compute viscous drag for complex wing geometries. The value of C_{D_0} could therefore be significantly larger than that of a planar wing. It may be very well possible to improve the current wing by a winglet but a significant amount of time is required to contemplate an optimized winglet design. According to Prof. Mark Maughmer at The Pennsylvania State University it *"is certainly true that it is much easier to make an aircraft worse with winglets than it is to make it better"* [23]. The use of winglets will therefore be left as a recommendation for further design improvements.
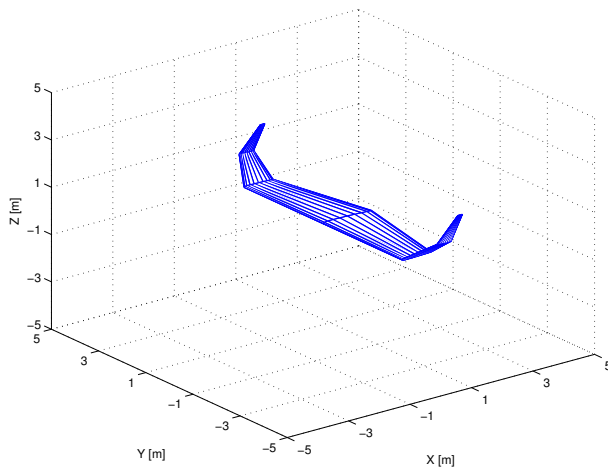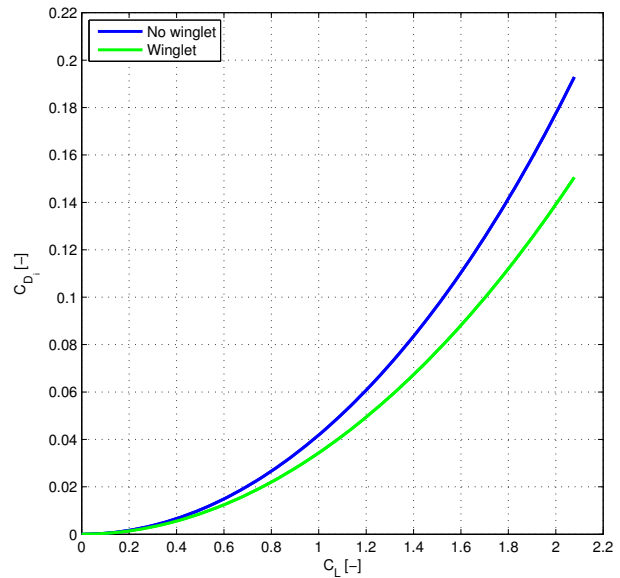

Figure 4.16: Geometry of a generic winglet

Figure 4.17: Influence of a winglet on C_{D_i}

4.2 Control Surfaces

The control surfaces of the wing solely consist of the ailerons. The ailerons are control surfaces that are placed on the wing to ensure that the pilot can control the roll angle of the aircraft. It goes without saying that the ailerons of the FX-15 are important for a successful RBAR performance, not having effective ailerons would mean that the pilot will not be able to fly the turns and slalom properly.

4.2.1 Problem Analysis

For designing the ailerons it is important to first look at the maneuverability and roll control requirements. The minimal roll rate for the FX-15 was already specified to be 440 °/s in the Baseline report [24].

The aileron design will consist of a location on the wing, span, chord length and maximum deflection angles of the ailerons. These parameters can all be determined using the requirement, FX-15 properties and some assumptions (as stated in the next paragraph).

In order to design the ailerons some simplifying and restricting assumptions have been applied:

1. Equal opposite aileron deflections. *The deflections of the ailerons are of equal magnitude, but in opposite direction.*

2. Steady state roll. *The roll requirement should be met at approach speed in a steady state (i.e. constant roll rate).*

3. No adverse yaw. *The effect of counter-yaw due to the roll rate on the roll rate is not taken into account (adverse yaw cannot be calculated accurately, flight tests should be executed to find the effect of this [25]).*

4. Wing tip clearance 0.25 m. *A 0.25 m clearance from the wing tips to the ailerons will be used for possible future usage of winglets (and/or wing tip wheels in case of future usage of single landing gear system).*

4.2.2 Method

To size the ailerons, a rolling flight will be simulated. As mentioned earlier the aileron parameters are aileron span, chord and maximum deflection angle. The best method for determining the aileron chord and deflection angles is by looking at the reference aircraft and using the same values. Then using the chord and deflection angles the span of the aileron can be optimized.

The complete derivations for how to obtain the roll rate will be left out of the report; for clarification one can look up the complete derivations in 'Aircraft Design: A Systems Engineering Approach' written by Mohammad Sadraey [26].
Eq. 4.7 describes the (steady state) roll rate at which moment equilibrium exists between elevator moment and roll drag moment.

$$P_{ss} = \sqrt{\frac{2 \cdot L_A}{\rho(S_w + S_{ht} + S_{vt})C_{D_R} \cdot y_D{}^3}} \tag{4.7}$$

The term C_{D_R} from equation 4.7 is an estimate for the coefficient of roll drag produced by the surface areas that are rolling. Sadraey [26] proposes a value of 0.9 as a reliable estimate. The term y_D describes the average arm for the rolling drag w.r.t. the fuselage center. It is assumed at 25 % of the wing span w.r.t. the center of the fuselage, as used in Sadraey [26].

Eq. 4.7 uses the rolling moment produced by the ailerons(L_A), see eq. (4.8). The rolling coefficient ($C_{l_{\delta A}}$) as used in eq. (4.8) can be found using eq. (4.9):

$$L_A = \frac{1}{2}\rho V_{app}{}^2 S C_l b \tag{4.8}$$

$$C_l = C_{l_{\delta A}} \delta_A \tag{4.9}$$

δ_A is the deflection angle of the ailerons. Now $C_{l_{\delta A}}$ can be found using:

$$C_{l_{\delta A}} = \frac{C_{L_{\alpha_w}} \tau C_r}{Sb} \int\limits_{y_i}^{y_o} Cy dy = \frac{C_{L_{\alpha_w}} \tau C_r}{Sb} \left[\frac{y^2}{2} + \frac{2}{3} \left(\frac{\lambda - 1}{b} \right) y^3 \right] \begin{matrix} y_0 \\ y_i \end{matrix} \qquad (4.10)$$

τ is the angle of attack effectiveness parameter, which can be extracted from figure 4.18.
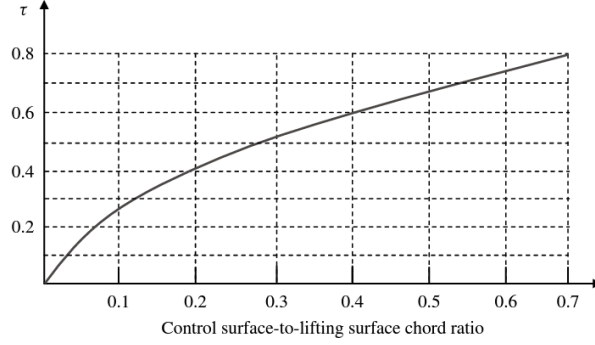
Figure 4.18: Angle of attack effectiveness against elevator-to-tail chord ratio (Source: [26])

y_o and y_i, the last unknowns, are the inner and outer locations of the ailerons. The outer aileron location was already assumed (close to the wing tip). Now all parameters and equations are known to solve for the inner aileron location, the last unknown for the aileron geometry.

4.2.3 Results

The used inputs for the calculations for the aileron sizing are shown in table 4.8.

Table 4.8: Input values for aileron sizing

Parameter	Value	Unit	Source	Description
P_{ss}	440	$[°/s]$	[24]	Required roll rate at steady state
ρ	1.225	$[kg/m^3]$	[10]	Air density at sea level
S_w	9.30	$[m^2]$	Section 4.1	Wing area, used value is from last iteration.
S_{vt}	1.65	$[m^2]$	Section 6.1	Vertical stabilizer area, used value is from last iteration.
S_{ht}	2.12	$[m^2]$	Section 6.1	Horizontal stabilizer area
C_{D_R}	0.90	$[-]$	[26]	Roll drag coefficient
y_D	2.13	$[m]$	[26]	Roll drag arm
V_{app}	33.17	$[m/s]$	[2]	Design speed
C_{L_α}	4.47	$[rad^{-1}]$	Section 4.1	Lift slope
δ_A	30	$[°]$	Appendix C	Max deflection elevator
C_A/C	0.25	$[-]$	Appendix C	(Aileron chord)/(wing chord)
C_r	1.37	$[m]$	Section 4.1	Rootchord
λ	0.60	$[-]$	Section 4.1	Taper ratio
y_o	4.0	$[m]$	Section 4.2.1	Outer aileron y-location

The outputs for the calculations from the aileron sizing are shown in table 4.9.

Table 4.9: Outputs values for aileron sizing

Parameter	Value	Unit	Description
$C_{l_{\delta A}}$	0.16	$[-]$	Roll moment derivative for aileron deflection
y_o	4.0	$[m]$	Outer aileron location (from mid wing)
y_i	1.84	$[m]$	Inner aileron location (from mid wing)
b_A/b	0.51	$[-]$	Aileron span over wing span
C_A/C	0.25	$[-]$	Aileron chord over wing chord
δ_A	30	$[°]$	Max deflection elevator

4.2.4 Verification & Validation

Verification of the approach has been done using a DATCOM simulation. DATCOM is a USAF stability and control prediction program. It's a widely used program that uses the aircraft geometry to estimate the stability and control coefficients and derivatives of aircraft. It has been used to check whether the calculated coefficient is approximately correct. DATCOM finds a $C_{l_{\delta_A}}$ of 0.20, while own calculations show 0.16. The difference of 20% is significant. It would mean that in case the DATCOM estimations would be more accurate, the ailerons would be even more powerful than calculated. The difference probably lies in the difference in assumptions regarding angle of attack effectiveness of the ailerons (τ), DATCOM probably estimates this parameter to be higher.

To validate the aileron design, it has been compared to the aileron designs of reference aircraft. Table 4.10 shows the table with the aileron geometry of reference aircraft (from C) compared to the aileron design for the FX-15.

Table 4.10: Verification & validation aileron design

Parameter	FX-15	MXS-R	Corvus 540	Extra 300L	Edge 540	Unit	Description
y_o	4.0	3.7	3.7	4.0	3.7	$[m]$	Aileron tip (from mid wing)
y_i	1.84	0.40	1.20	1.20	1.40	$[m]$	Aileron root(from mid wing)
b_A/b	0.51	0.88	0.67	0.70	0.60	$[-]$	(Aileron span)/(wing span)
C_A/C	0.25	0.25	0.28	0.20	0.25	$[-]$	(Aileron chord)/(wing chord)
δ_A	25	30	30	30	25	$[°]$	Max deflection elevator

The table clearly shows that the ailerons of the FX-15 are relatively small compared to its competitors, the ailerons of the FX-15 are smaller than all other reference aircraft. However, it can also be seen that the differences between the reference aircraft are also quite significant. Due to the comparison with reference aircraft, the question arises whether or not the ailerons are under-designed (i.e. not meet the roll requirement). Therefore it should be stated that the consequences of not meeting the roll requirement are not critical according to many (ex) RBAR pilots [27, 28].

4.2.5 Conclusion & Discussion

The design of the ailerons is pretty straight forward. Validation has shown that the ailerons are smaller than many reference aircraft, while verification suggests that the ailerons are even more powerful than calculated. Despite the reference aircraft ailerons being bigger, it is expected that the FX-15 ailerons will not underperform regarding roll rate.

Possible points of improvement for future aileron design or modifications:

- **Adverse yaw** If adverse yaw turns out to be significant during flight tests, a solution can and should be found. Possible solutions are: Differential deflections, Frise ailerons or rudder deflections.

- **Optimization for drag** Aileron deflections will produce lots of drag, optimization of the ailerons for drag reduction will prove to be complicated, but might yield better performance.

- **Optimization by analysis of all possible aileron-span, chord and deflection angles** The aileron span was optimized using one selected chord length and deflection angle range for the ailerons. Presumably the aileron geometry could be optimized by comparing all possible deflection angles and chord length combinations possible.

- **Spades** Spades have not been considered while designing the ailerons. Spades are aerodynamic balances on the ailerons that ensure that the pilot does not have to produce high stick forces. If it turns out that these are necessary, they can be placed on the ailerons. The design and production/assembly of spades are not complicated (it is a flat plate on a stick), therefore an off-the-shelf-solution can be used.

These improvements could yield lower drag and improved roll characteristics.

4.3 Structure

In the midterm report [2], it was decided to use a wing box type design. This section describes a MATLAB based optimization tool that has been created to design the wing structure in detail. With this tool, the main spar has been sized through an iterative process to get the optimal design.

This section describes the methodology behind the creation and the working of the MATLAB code, as well as the optimization results. First, the fundamentals on which the code is based will be explained. After that, the working method of the MATLAB tool is shown and clarified. The optimization results will be presented next. Continuing, the code will be verified after which a production version of the optimized design will be shown. Finally, the conclusions and remaining points of discussion will be stated.

4.3.1 Problem Analysis

This section will describe the design philosophy behind the chosen wing structure. Furthermore, the assumptions that were used in the calculations will be listed. Finally, the reference frame that was used for the calculations is shown.

Wing Structure Design Philosophy

The main spar will use a Carbon Fiber Reinforced Polymer (CFRP) skin. This will take up (nearly) all the shear stresses. The carbon fiber laminate thickness will be the same for all sides of a given cross-section of the main spar. It is difficult to vary the laminate thickness between different sides of a cross-section, because this will give weak points at the corners.

The cross-section of the main spar will be filled with a stiff foam, which will be attached to the carbon fiber skin by adhesive bonding. The foam will significantly improve buckling and deformation performance, at the cost of only a little extra weight.

Assumptions

Several assumptions have been made to simplify the code. The level of detail in the spar design is limited by the below mentioned assumptions.

Primary Assumptions

1. Rectangular cross-section. *In reality the front and rear spar will differ in height due to the shape of the airfoil, resulting in an asymmetrical cross-section. A rectangular beam will have lower internal stresses due to the symmetrical cross-section.*

2. No buckling. *Buckling is a major failure criterion for aerospace structures. For this design, the buckling of the carbon fiber skin is the critical buckling criterion of the entire spar. However, for now it is assumed that the carbon fiber skin does not fail due to buckling (because of the support of the foam). In reality, the adhesive bond between the carbon fiber skin of the spar and the foam with which it will be filled can fail, causing deformations and possibly buckling in the carbon skin.*

3. No drag. *Even though a wing is subjected to drag during flight, it is assumed to be negligible when compared to the other forces on the wing structure. This assumption could lower the effective loading of the wing.*

4. Main spar at aerodynamic center (AC). *The spar is located at the AC (to avoid torsion due to lift), and the AC is assumed to be at 0.25c. In reality, the location of the AC could be different. However, these differences - and thus the resulting torques - are expected to be negligible.*

5. No extra lift and/or control surfaces. *Extra lift and/or control surfaces can create significant forces and moments on the wing structure. For now, these forces are not taken into consideration. Taking these forces into consideration during later design stages will probably result in a heavier spar.*

6. Constant CFRP skin thickness. *The loads in the top, bottom and side CFRP plates are not necessarily the same and thus do not require the same thickness. Assuming the same thickness for all the CFRP*

skin panels in a cross-section will result in a slightly over-designed spar. However, for production purposes it is preferrable to have a constant thickness over a cross-section.

7. Thin-walled. *The thicknesses of the top, bottom and side plates are assumed to be much smaller than the overall dimensions of the wing box. With this assumption, higher order terms of t (t^2, t^3, etc.) can be neglected. The MOI - and thus the stresses - are influenced by this assumption.*

8. Shear force taken by carbon fibre skin only. *In reality, the foam will also take a fraction of the shear forces. That fraction however is very small and therefore the carbon fibre is designed to be able to take the entire shear force.*

Secondary Assumptions

9. Elliptical lift distribution. *The actual wing will have an almost perfect elliptical lift distribution (depending on the Oswald factor). Assuming a perfect elliptical lift distribution will cause a (minor) deviation in the loading of the spar. This deviation however is expected to be small.*

10. Subsystem weight varies with spar weight. *The weight of the (structural) subcomponents is modeled by multiplying the weight of each spar section with a certain factor. However, this means that it is assumed that the weight of the subcomponents varies in the same way as the spar weight. In reality this is not true, causing an error in the loading of the spar.*

11. All loads carried by the spar. *It is assumed that the main spar carries all loads that act on the wing. The skin only serves to maintain the aerodynamic shape of the wing.*

12. No subsystem attachment points. *Following from the previous assumption, attachment points of subsystems are not taken into account. This will lead to an underestimated main spar weight. The increase in weight is expected not to exceed 5%.*

Reference Frame

The reference frame that has been used for the calculations is depicted in fig. 4.19. The discretization of the spar runs from tip to root, as shown in the figure. The root chord line is taken at the center of the fuselage.
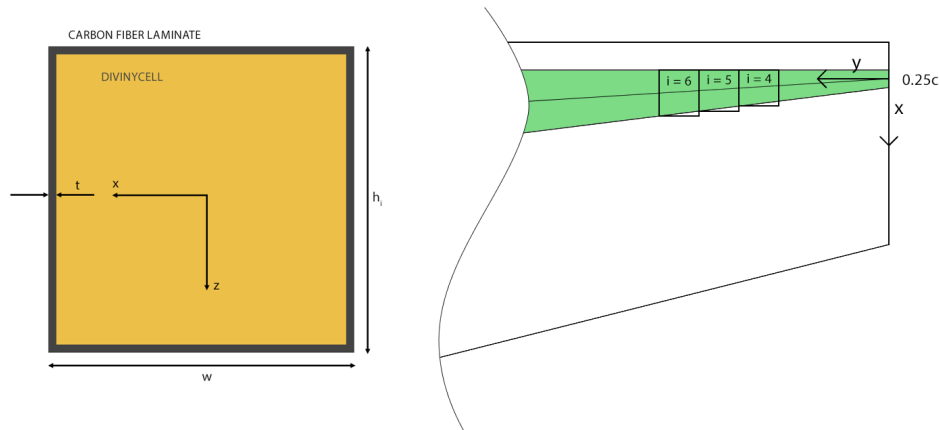
Figure 4.19: Reference frame used in the main spar optimization

4.3.2 Method

This section will describe the method that was used to optimize the wing structure. A MATLAB tool was used for the optimization process, and the general outline of the tool will be explained first. After that, the calculations that the code performs are explained.

The general outline of the MATLAB tool is given in fig. 4.20. The input values are explained in section 4.3.3.
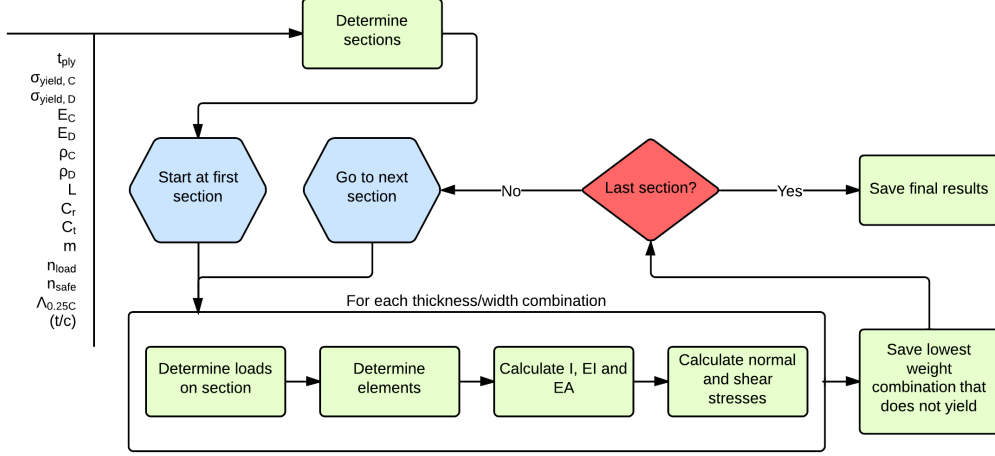
Figure 4.20: Flowchart describing the main spar optimization code

The MATLAB tool was designed according to the optimization conditions given in table 4.11. The objective is to design a spar with a minimal weight that does not yield (both the carbon fiber skin and divinycell core of the spar). The Von Mises stress in the carbon fiber skin is given by σ_c and the Von Mises stress in divinycell by σ_d. The yield stress of the carbon fiber skin is given by $\sigma_{yield,c}$ and the yield stress of divinycell by $\sigma_{yield,d}$.

The skin thickness is limited to be a multiple of the laminate thickness $t_{laminate}$, because the laminate will be symmetric and this way the mechanical properties stay the same. The width can be varied by the code between w_{min} and w_{max} in steps of w_{step}. Also, the thickness and width of the i'th wing section, t_i and w_i, must be equal to or larger than the thickness and width of the previous wing section (t_{i-1} and w_{i-1}).

Table 4.11: Optimization algorithm

Discription	Condition
Objective function	$f = min(mass)$
Constraints	$\sigma_c < \sigma_{yield,c}$
	$\sigma_d < \sigma_{yield,d}$
	$t_i = k \cdot t_{laminate}$
	$w_i = w_{min} \leq m \cdot w_{step} \leq w_{max}$
	$t_i \geq t_{i-1}$
	$w_i \geq w_{i-1}$

The code starts by discretizing the wing into n sections. For a given section, the code calculates the Von Mises stresses for every combination of the skin thicknesses and spar widths it has been given to use. Note that all the calculations have been based on the geometry given in fig. 4.19.

To get those stresses, the code first calculates the loads acting on a section. The total shear force is found with eq. (4.11). The lift on a section is given by L_i, the total weight of a section is denoted by W_i and the total force on the previous section is represented as $F_{z_{i-1}}$. The load factor of the aircraft is given by n_{load} and the safety factor by n_{safe}.

$$F_{z_i} = (-L_i + W_i)\, n_{load}\, n_{safe} + F_{z_{i-1}} \tag{4.11}$$

To calculate the right loads on a section, the weight of the wing needs to be modeled in stead of just the weight of the spar. This is done by multiplying the calculated spar weight with a factor (the expected wing weight from the class II weight estimation divided by the spar weight). The problem is that the spar weight is only known after the optimization process is finished. Therefore, an estimate of the spar weight is made beforehand and is used to calculate this margin. This estimate is updated until it converges to the actual spar weight. Eq. 4.12 shows how the total weight of a wing section W_i is calculated according to this method.

35

W_{spar_i} is the actual spar weight in a section and $W_{spar,estimate}$ the estimated total spar weight. The total wing weight is given by $W_{wing,total}$.

$$W_i = W_{spar_i} \frac{W_{wing,total}}{W_{spar,estimate}} \tag{4.12}$$

With the shear force known, the next step is to calculate the moments around the x- and y-axis using eq. (4.13) and eq. (4.14). dx and dy denote the x and y distances between the center points of two consecutive sections.

$$M_{x_i} = F_{z_i} dy + M_{x_{i-1}} \tag{4.13}$$

$$M_{y_i} = F_{z_i} dx + M_{y_{i-1}} \tag{4.14}$$

Also needed for the stress calculations are the moments of inertia of a section's cross-section. The moments of inertia are calculated using eq. (4.15) and eq. (4.16).

$$I_{xx_{total\,i}} = \left[\frac{1}{12} w h_i^3 \right]_{divinycell} + \left[\frac{1}{6} t h_i^3 + w t \frac{h_i}{2} \right]_{carbon} \tag{4.15}$$

$$I_{zz_{total\,i}} = \left[\frac{1}{12} h_i w^3 \right]_{divinycell} + \left[\frac{1}{6} t w^3 + h_i t \frac{h_i}{2} \right]_{carbon} \tag{4.16}$$

The spar is made out of two different types of materials so an equivalent bending stiffness has to be computed. This is calculated using eq. (4.17) and eq. (4.18).

$$EI_{xx} = (EI_{xx})_{carbon} + (EI_{xx})_{divinycell} \tag{4.17}$$

$$EI_{zz} = (EI_{zz})_{carbon} + (EI_{zz})_{divinycell} \tag{4.18}$$

Also, the equivalent compression stiffness has to be calculated with eq. (4.19).

$$(EA)_{total} = (EA)_{carbon} + (EA)_{divinycell} \tag{4.19}$$

The next step for the code is to find the bending plane of the cross-section. This is important since an inhomogeneous cross-section could result in asymmetrical bending of the spar. The vectors of the bending plane k_x and k_z and the strain ϵ due to a normal force are calculated by implementing the results of the previous calculations into eq. (4.20). S_x and S_x denote the orthogonal horizontal and vertical distance between a force and the normal force center. Given the fact that the normal force center coincides with the geometric centroid due to symmetry and that the forces are assumed to act through the shear center these terms are set to 0.

$$\begin{bmatrix} N \\ M_z \\ M_x \end{bmatrix} = \begin{bmatrix} EA & ES_x & ES_z \\ ES_x & EI_{zz} & EI_{xz} \\ ES_z & EI_{zx} & EI_{xx} \end{bmatrix} \begin{bmatrix} \epsilon \\ k_x \\ k_z \end{bmatrix} \tag{4.20}$$

With k_x, k_z and ϵ known it is now possible to calculate the strain at a location (x, z) in the cross-section of the spar using eq. (4.21).

$$\epsilon(x, z) = \epsilon + x k_x + z k_z \tag{4.21}$$

Finally, using Hooke's law the code can now calculate the bending stress with eq. (4.22). $E(x, z)$ represents the Young's modulus of the material at that (x, z) location.

$$\sigma(x, z) = E(x, z) \left(\epsilon + x k_x + z k_z \right) \tag{4.22}$$

However, in order to calculate the Von Misses stresses the shear stresses have to be known as well. Eq. 4.23 computes the shear flow in a cross-section that has been discretized using elements. B_A denotes the area of an element and the element location is given by x_b and z_b. The centroid coordinates are given by $\bar{x}$ and $\bar{z}$.

$$q_s = \sum \frac{I_{xx}F_x - I_{xz}F_z}{I_{xx}I_{zz} - I_{xz}^2} \cdot B_A \cdot (x_b - \overline{x}) - \sum \frac{I_{zz}F_z - I_{xz}F_x}{I_{xx}I_{zz} - I_{xz}^2} \cdot B_A \cdot (z_b - \overline{z}) \tag{4.23}$$

Adding to that shear flow is a shear flow resulting from torque loads. This torque M_y is present due to the sweep of the wing. The constant shear flow resulting from this torque is calculated using eq. (4.24).

$$M_y = 2A q_{const} \tag{4.24}$$

The final shear flow in the cross-section is found by adding the shear flow components.

$$q_{total} = q_s + q_{const} \tag{4.25}$$

Finally, the shear stress is calculated by implementing the total shear flow into eq. (4.26).

$$\tau = \frac{q_{total}}{t} \tag{4.26}$$

Now that the code has computed the bending and shear stresses for a skin thickness/spar width combination, the Von Mises stress can be calculated using eq. (4.27).

$$\sigma_{mises} = \frac{1}{\sqrt{2}} \sqrt{(\sigma_x - \sigma_y)^2 + (\sigma_y - \sigma_z)^2 + (\sigma_z - \sigma_x)^2 + 6\tau_{xy}^2 + 6\tau_{yz}^2 + 6\tau_{zx}^2} \tag{4.27}$$

When all the skin thickness/spar width combinations in a section have been evaluated the tool starts running a selection process according to the optimization algorithm in table 4.11. The optimal geometry is stored and the code continues to the next section repeating the calculations all over again.

4.3.3 Results

The results that were obtained in the main spar optimization process will be given in this section. The inputs that were used in the MATLAB tool will be presented first. After this, the optimization output - and thus the final design - will be shown.

The main spar of the FX-15 wing will be made out of a carbon fiber laminate. This carbon fiber laminate was designed using Kolibri [29], which is a tool that allows the user to get the properties of a laminate, if ply properties are known. The laminate will use a HexPly 8552 ply with 65% IM7 fiber, together with an epoxy resin and will have a [45, -45, 90, 0]s layup. The ply has been designed to be symmetric, to make sure it can be stacked without changing the laminate properties. The HexPly 8552 properties that were used in Kolibri to design the laminate are given in table 4.12. Note that all properties are given at an environment temperature of 25 °C.

Table 4.12: Properties of HexPly 8552

Parameter	Value	Unit	Source	Description
E_1	$164(10^9)$	$[Pa]$	[30]	Young's modulus in fiber direction
E_2	$12(10^9)$	$[Pa]$	[30]	Young's modulus in transverse direction
G_{12}	$5.2(10^9)$	$[Pa]$	Estimate	Shear modulus
ν_{12}	0.32	[-]	Estimate	Poisson's ratio
$\sigma_1^{(t)}$	$2724(10^6)$	$[Pa]$	[30]	Ultimate tensile strength in fiber direction
$\sigma_1^{(c)}$	$1690(10^6)$	$[Pa]$	[30]	Ultimate compressive strength in fiber direction
$\sigma_2^{(t)}$	$64(10^6)$	$[Pa]$	[30]	Ultimate tensile strength in transverse direction
$\sigma_2^{(c)}$	$1690(10^6)$	$[Pa]$	Assumed to be equal to $\sigma_1^{(c)}$	Ultimate compressive strength in transverse direction
τ_{12}	$114(10^6)$	$[Pa]$	[30]	Ultimate shear stress
t	$0.131(10^{-3})$	$[m]$	[30]	Cured ply thickness
ρ	1570	$[kg/m^3]$	[30]	Ply density

The carbon fiber laminate will be filled with Divinycell HT131 foam to improve buckling and deformation performance. The properties of both the laminate and Divinycell HT131 are given in table 4.13.

Table 4.13: Properties of materials used for the wing main spar

	Carbon fiber laminate	Divinycell HT131
Description	[45, -45, 90, 0]s layup with a HexPly 8552 ply (65% IM7 fiber) and an epoxy resin	Foam used to improve buckling and deformation performance
Source(s)	[29]	[31, 32]
Young's modulus $[Pa]$	$62.8(10^9)$	$0.145(10^9)$
Density $[kg/m^3]$	1570	130
Yield stress $[Pa]$	$364(10^6)$	$3.5(10^6)$
Thickness $[m]$	$1.048(10^{-3})$	Any thickness possible

Remaining input values that were required for the main spar optimization are given in table 4.14.

Table 4.14: Remaining input values for the wing main spar sizing

Parameter	Value	Unit	Source	Description
L	4.25	$[m]$	Section 4.1.3	Span of one wing
C_r	1.37	$[m]$	Section 4.1.3	Wing root chord
C_t	0.82	$[m]$	Section 4.1.3	Wing tip chord
m	735.5	$[kg]$	Section 3.12	Aircraft race mass
n_{load}	12	[-]	[5]	Design load factor
n_{safe}	1.5	[-]	[5]	Design safety factor
$\Lambda_{0.25c}$	-1.84	$[°]$	Section 4.1.3	Quarter chord wing sweep
(t/c)	0.11	[-]	Section 4.1.3	Maximum airfoil thickness to chord ratio

Using the input values stated in table 4.13 and table 4.14, and the assumptions mentioned in section 5.3.1, an optimized main spar design that weighs 28.53 kg is found (one wing).

The distribution of carbon fiber laminate thickness troughout the spar is shown in fig. 4.21. All thickness steps are multiples of the thickness of a single laminate, because this way the thickness can be increased without changing the laminate properties (since it is a symmetric laminate).

The spar width distribution is shown in fig. 4.22. The spar width was limited to vary between 0.05 and 0.25 m in steps of $5(10^{-4})$ m, to ensure that it fits with other subsystems (especially where the spar intersects with the fuselage) and to ensure that it is producable.

The distribution of spar weight is shown in fig. 4.23. As expected, the wing weight varies quadratically over the span.

Note that the structure is designed for a ±12g turn (the critical design point) with a safety factor of 1.5. Fig. 4.21 and fig. 4.22 both show a safety margin (S.M.), which is defined in eq. (4.28). In this equation, $\sigma_{VM,i}$ indicates the Von Mises stress on a section and σ_{yield} is the yield stress of the carbon fiber laminate. When the safety margin is 0, the Von Mises stress is equal to the yield stress (including safety factor of 1.5) and the spar is perfectly optimized. If the safety margin is close to 1, the spar is heavily overdesigned.

$$S.M. = \frac{\sigma_{yield} - \sigma_{VM,i}}{\sigma_{yield}} \tag{4.28}$$

The restrictions of the optimization code are clearly indicated in fig. 4.21 and fig. 4.22. The thickness can only increase in large steps (because the entire laminate has to be stacked) and the spar width can never decrease. Therefore, if an increase in spar width is not enough and an extra stack of laminate is needed, the stress margin suddenly increases significantly. How to address this issue is discussed further in section 4.3.6.

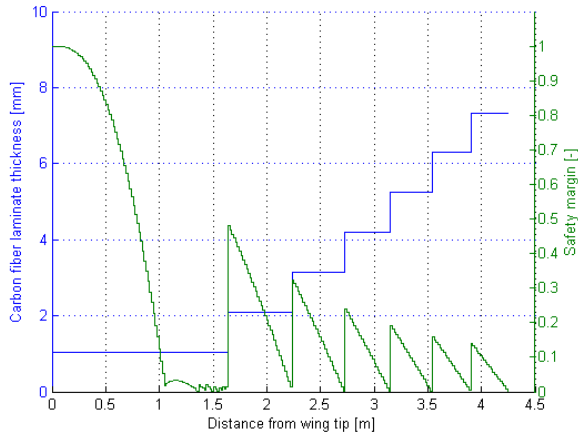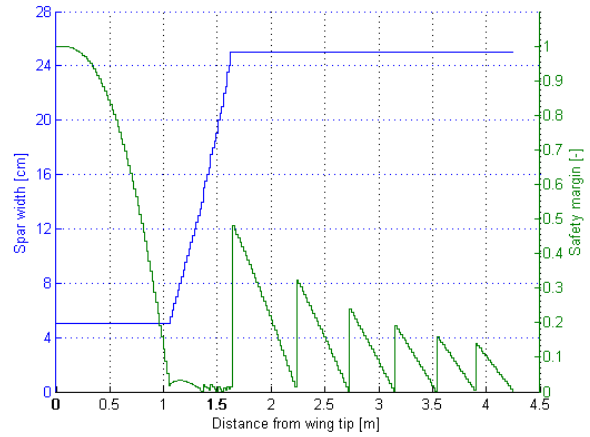Figure 4.21: Carbon fiber laminate thickness distribution
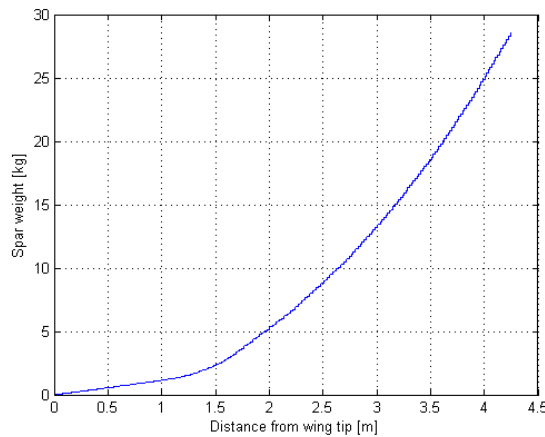

Figure 4.22: Spar width distribution

Figure 4.23: Spar weight distribution

4.3.4 Verification

This section describes the verification of the MATLAB code. The equations mentioned in section 8.1.3 have been verified first. After that, analytically calculated Von Mises stresses have been compared with the code output as an overall system test.

For the verification, the input values given in table 4.14 have been used. However, for simplicity, the thickness is set to a constant value of $5(10^{-3})$ m, the width is constant as well at a value of 0.25 m and the wing will be discretized into only two sections.

In table 4.15, the output values of the numerical and analytical calculations are summarized. τ_1, τ_2 and τ_3 represent the shear stresses due to a shear force. τ_{tot} is the summation of the previously stated shear stress and the constant shear stress due to torque.

All the stresses have been evaluated at the three points given in fig. 4.24.
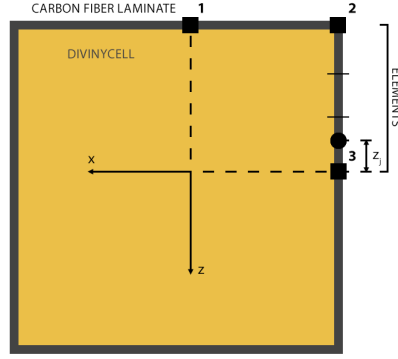
Figure 4.24: Spar cross-section

Table 4.15: Verification output values

	Section 1			Section 2		
	Analytical	**Numerical**	**Deviation**	**Analytical**	**Numerical**	**Deviation**
W $[kg]$	$2.07(10^1)$	$2.07(10^1)$	0.0 %	$4.56(10^1)$	$4.56(10^1)$	0.0 %
F $[N]$	$1.59(10^4)$	$1.59(10^4)$	0.0 %	$4.18(10^4)$	$4.18(10^4)$	0.0 %
M_x $[Nm]$	0.00	0.00	0.0 %	$8.71(10^2)$	$8.71(10^2)$	0.0 %
I_{xx} $[m^4]$	$4.00(10^{-5})$	$3.99(10^{-5})$	0.1 %	$9.24(10^{-5})$	$9.24(10^{-5})$	0.0 %
I_{zz} $[m^4]$	$1.76(10^{-4})$	$1.76(10^{-4})$	0.0 %	$2.30(10^4)$	$2.30(10^{-4})$	0.0 %
σ_1 $[Pa]$	0.00	0.00	0.0 %	$2.36(10^8)$	$2.36(10^8)$	0.0 %
σ_2 $[Pa]$	0.00	0.00	0.0 %	$2.36(10^8)$	$2.36(10^8)$	0.0 %
σ_3 $[Pa]$	0.00	0.00	0.0 %	0.00	$1.18(10^6)$	∞ %
τ_1 $[Pa]$	0.00	$2.93(10^4)$	∞ %	0.00	$4.46(10^4)$	∞ %
τ_2 $[Pa]$	$2.94(10^6)$	$2.93(10^6)$	0.1 %	$4.45(10^6)$	$4.46(10^6)$	0.1 %
τ_3 $[Pa]$	$3.63(10^6)$	$3.63(10^6)$	0.0 %	$5.86(10^6)$	$5.86(10^6)$	0.0 %
$\tau_{tot,1}$ $[Pa]$	0.00	$2.93(10^4)$	∞ %	$2.21(10^6)$	$2.26(10^6)$	1.9 %
$\tau_{tot,2}$ $[Pa]$	$2.94(10^6)$	$2.93(10^6)$	0.1 %	$6.67(10^6)$	$6.67(10^6)$	0.0 %
$\tau_{tot,3}$ $[Pa]$	$3.63(10^6)$	$3.63(10^6)$	0.1 %	$8.07(10^6)$	$8.07(10^6)$	0.0 %
$\sigma_{VM,1}$ $[Pa]$	0.00	$5.08(10^4)$	∞ %	$1.67(10^8)$	$1.67(10^8)$	0.0 %
$\sigma_{VM,2}$ $[Pa]$	$5.08(10^6)$	$5.08(10^6)$	0.0 %	$1.67(10^8)$	$1.67(10^8)$	0.0 %
$\sigma_{VM,3}$ $[Pa]$	$6.28(10^6)$	$6.28(10^6)$	0.0 %	$1.40(10^7)$	$1.66(10^8)$	91.6 %

There are 6 points of discussion in the comparison between the numerical and the analytical solutions. Deviations are present at τ_1, $\tau_{tot,1}$ and $\sigma_{VM,1}$ in section 1 and at σ_3, τ_1 and $\sigma_{VM,3}$ in section two. In section 1, the deviations in $\tau_{tot,1}$ and $\sigma_{VM,1}$ are a consequence of the deviation in τ_1. In section 2, the deviation in $\sigma_{VM,3}$ is a consequence of the deviation in σ_3 and τ_1.

For both sections, the deviation in τ_1 can be explained by looking at eq. (4.23). In this equation, the analytical solution of the shear flow equals 0 if the point lies on the z-axis. However, elements have been used for the numerical solution where the distance to the z-axis is measured from the center of the element. Therefore, there will always be a distance z_j or x_j to the center of the element closest to the neutral line and it is impossible to get 0 as a solution out of eq. (4.23).

The same explanation holds for σ_3 in section 2, which is calculated with eq. (4.22). Also, in this equation, the high value of the Young's modulus will result in large bending stress values due to the use of elements. This deviation does not occur in section 1 as there is no moment present in that section and thus the bending stress is equal for both the numerical and the analytical solutions.

The deviations can be reduced to negligible proportions by increasing the number of elements. Overall, it can be concluded that the code functions correctly according to the method used.

4.3.5 Production

The optimal main spar design that was found can not be produced perfectly in reality. There are two main aspects to address to find a producable design; the variation in laminate thickness and the variation in spar width.

The laminate varies from one stack to seven stacks. This is in principle not a problem for production, but for safety the location where there is an increase in thickness will always be rounded down (so for example the increase in thickness at 1.65 m will be rounded down to 1.6 m).

The spar width varies per section in the optimized design (see fig. 4.22). For production purposes, it has been decided to keep the spar width constant at 0.05 m for the first 1 m, let it vary linearly to 0.25 m at 1.5 m and keep it constant at 0.25 m for the remainder of the wing.

Because of these simplifications, the final spar design will weigh more than the predicted weight of the optimized spar. It is expected that the actual spar weight will be 30 kg (one wing).

A graphical representation of the final main spar design is given in fig. 4.25.
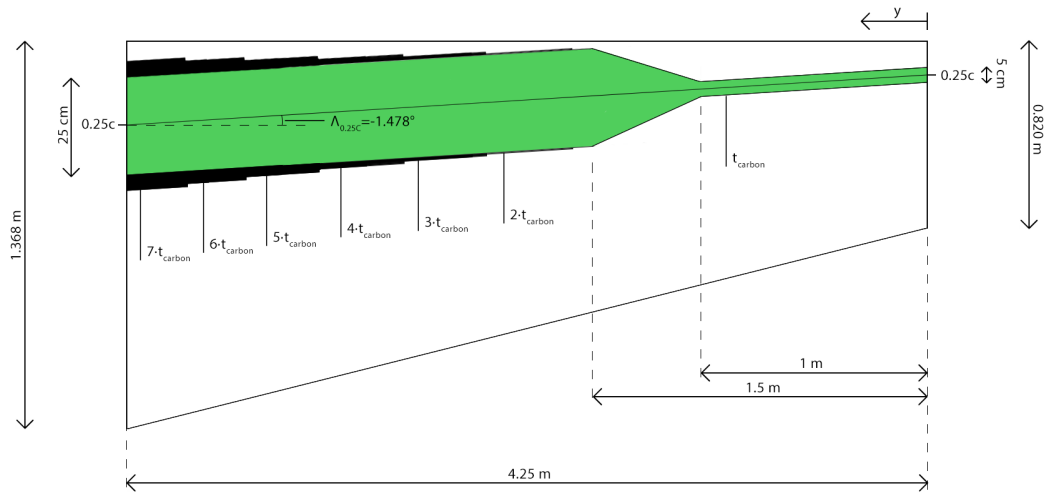
Figure 4.25: Final design of the wing main spar

4.3.6 Conclusion & Discussion

The optimized main spar design has a width that varies from 0.05 m at the tip to 0.25 m at the root. The center of the spar is located at 0.25c because it is assumed the lift acts there (and thus does not cause a torsion if the spar is located there). The main spar uses a custom carbon fiber laminate that was designed in Kolibri [29]. This laminate uses a HexPly 8552 ply with 65% IM7 fiber, together with an epoxy resin and has a [45, -45, 90, 0]s layup. The carbon fiber laminate thickness varies from $1.048(10^{-3})$ m at the tip (one stack) to $7.336(10^{-3})$ m at the root (seven stacks). The entire spar will weigh an estimated 30 kg (one wing).

Points of improvement for the future are:

- Change the spar geometry to avoid stress concentrations. Currently, the locations where the spar starts and stops tapering in width will have stress concentrations and will likely be the location where the spar fails. Also, the points where the laminate thickness changes will have stress concentrations and

are likely points of failure. It would be best to vary the laminate thickness by adding or removing plies in stead of stacking the entire laminate.

- Take failure of the adhesive bond layer between the foam and the carbon fiber laminate into account. Currently it is assumed that the adhesive bond does not fail.

- Take the effects of extra lift and/or control surfaces into account. These surfaces can create significant forces and moments on the wing structure.

- Take drag into account. Drag can influence the wing structure design, especially in the case of special maneuvers.

- Take the fact that the spar will not have a rectangular cross-section into account. The spar will actually be shaped according to the airfoil curvature. This can influence the stresses on the spar.

- Optimization of the fiber layout of the laminate. Fig. 4.21 and fig. 4.22 show that the spar is overdesigned for most sections. The carbon fiber laminate thicknesses are very restricted because they have to be multiples of the single stack thickness. Optimization of the laminate fiber layout - and thus the mechanical properties - as well as the panel thickness is advised to allow for an even more optimized design.

The RAMS characteristics of the wing structure are:

- **Reliability.** A very similar carbon fiber laminate found in EduPack 2013 has excellent durability properties for fresh and salt water and good durability properties for UV radiation. Therefore, the laminate is expected to perform well under the environmental conditions in which the FX-15 will fly. The fatigue strength at 10^7 cycles of the carbon fiber laminate found in EduPack 2013 is 247 - 422 MPa, so unless there is direct damage to the main spar it should last throughout the aircraft lifetime.

- **Availability.** The HexPly 8552 ply required for the carbon fiber laminate can be ordered at Hexcel in Germany. The Divinycell HT131 foam can be ordered at DIAB in Germany. Both materials are available and the main spar can be assembled at TU Delft in the Netherlands.

- **Maintainability.** The carbon fiber laminate is not easily repairable. In the case that there is major damage to the main spar, it will likely have to be replaced. If there is a problem with the Divinycell HT131 foam, it can be repaired depending on the location of the problem in the spar.

- **Safety.** According to EduPack 2013, a carbon fiber laminate that is very similar to the custom designed one has an impact strength between 96 and 123 kJ/m^2. Furthermore, the wing structure is designed to handle a ±12g turn with a safety factor of 1.5. Since the aircraft is limited to and only is allowed to fly a 10g turn, the wing structure can be considered very safe.

Because the main goal of the FX-15 is to win the Red Bull Air Race 2017, performance is the main design goal. However, this does not mean that sustainability can not be taken into account. For the wing structure, the main sustainability aspect is the material choice.

For the carbon fiber laminate there are two options:

- Replace the fibers by natural fibers. *The IM7 fibers can be partially recycled using pyrolysis at end of life [33]. However, if natural fibers are used, the fibers can be fully biodegradable. Traditionally though, natural fibers are weaker than normal carbon fibers [34]. Because performance is critical, and the use of natural fibers would have a large negative impact on performance, it is chosen to use IM7 fiber.*

- Replace the epoxy by biodegradable resin. *A biodegradable resin that could be used is polylactic acid [35]. The use of this resin in stead of an epoxy should be investigated in the future.*

According to DIAB, "Divinycell HT is good environmental selection due to its excellent strength-to-weight ratio and high performance over time" [36]. Therefore, the choice of foam can be considered sustainable.

5 Fuselage Detail Design

This chapter describes the process of designing the fuselage. First, the component locations are described in section 5.1. Using these locations, the aerodynamic hull is designed in section 5.2. Finally, the structure of the fuselage is designed in section 5.3.

5.1 Subsystem Locations

The locations of all the subcomponents in the fuselage are given in this section. Once the location and shape of the subcomponents are known, the center of gravity (CG) and total MOI of the FX-15 can be determined. These CG locations and the MOI are necessary to determine the stability derivatives. The determination of the subcomponent CG locations and the shape of the aerodynamic hull is an iterative process, of which the final step is presented in this section.

5.1.1 Method

In the midterm report, preliminary CG locations of the subcomponents have been determined [2]. These locations are used in the first iteration of the design of the fuselage.

All components are modeled in CATIA according to their actual dimensions and weights. The locations of the different subsystems are iterated together with the aerodynamic hull, and the results are shown in the next section.

5.1.2 Results

The resulting subcomponent locations are shown in fig. 5.1. The origin of the axis system in this model is located at the CG location of the propeller blades.
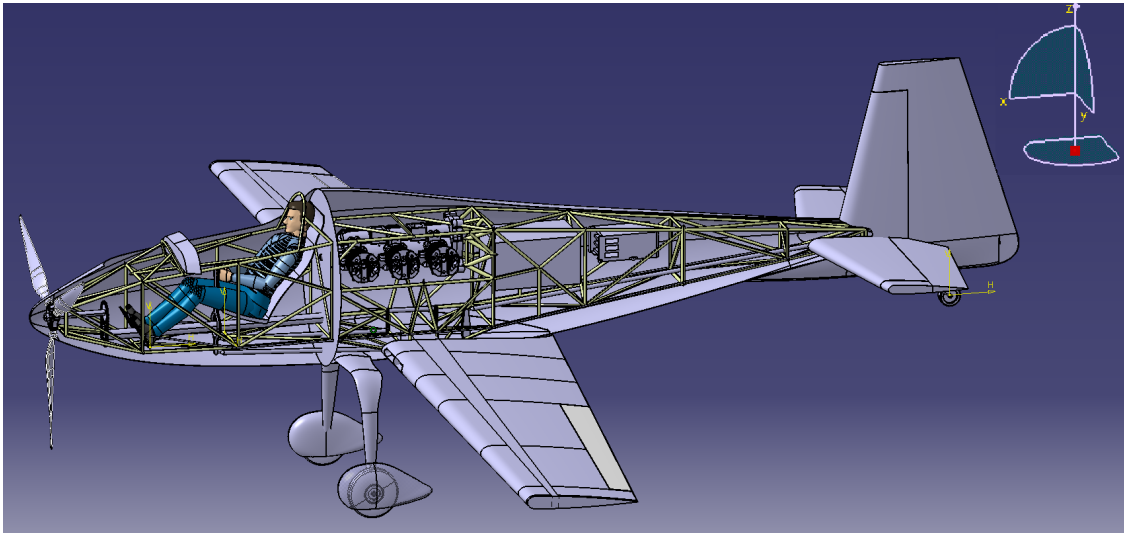
Figure 5.1: CATIA model of the FX-15

The masses are taken from the class II weight estimation in section 3.9, unless an updated mass is available. The mass of the control surfaces is distributed over the mass of the wing and the empennage. Furthermore the fuel tank weight is the weight of the fuel tank including 50 liter of fuel (the minimum amount of fuel stated by the RBAR regulations [5]). Complex components such as the wing, empennage and fuselage are

modeled only as the skin and are given the weight of the entire component. This approach gives an indication of the mass moment of inertia of the wing, empennage and fuselage.

The results are shown in table 5.1. It can be seen that the mass moments of inertia of the payload are low and symmetric. This is the result of the payload mass being modeled as a point mass.

Note that the masses that were modeled in CATIA are the exact masses as stated in the mass budget in section 10.2. Slight differences occur because small parts are not modeled in CATIA.

Table 5.1: Subcomponent locations and mass moments of inertia

Parameter	Mass [kg]	X_{cg} [m]	Y_{cg} [m]	Z_{cg} [m]	I_x [kgm²]	I_z [kgm²]	I_z [kgm²]	Source
Wing	129	2.85	0	-0.36	666.3	13.7	679.4	Section 3.9
Empennage	31	6.18	0	0.27	41.0	14.8	39.6	Section 3.9
Landing gear	19	1.96	0	-0.86	2.8	3.7	1.0	Section 7.8
Propulsion	249	2.20	0	0.25	16.1	201.6	207.2	Section 8.2.4
Fuselage	77	2.61	0	0.09	18.6	208	206.0	Section 5.3
Equipment	42	2.99	0	-0.05	13.9	72.5	79.5	Section 3.9
Safety systems	17	2.02	0	0.14	0.6	0.35	0.2	Section 3.9
Fueltank	45	3.43	0	0.18	1.5	2.5	2.8	Section 8.6.2
Payload	89	1.45	0	0.13	0.2	0.2	0.2	Section 3.9
FX-15	**697.2**	**2.56**	**0.00**	**0.05**	**807.5**	**1111**	**1715**	

5.2 Aerodynamics

In this section, the aerodynamic shape of the fuselage is determined by fitting the hull around all the subcomponents (mentioned in the previous section) in such a way that drag is minimized. The profile drag of the fuselage is compared to that of a symmetric airfoil to ensure that the fuselage is designed properly.

5.2.1 Method

In the midterm report [2], the preliminary CG locations of the different components have been determined. These locations are taken as a starting point for the fuselage design and are updated to fit properly inside the fuselage skin. A clearance of at least 40 mm is present in all cases between the components and the fuselage skin to make sure that both the components and the truss structure will fit.

Two main design principles were used to minimize drag: minimizing the frontal area while taking into account the above mentioned clearance and minimizing changes in surface curvature. The changes in curvature are minimized because changes in curvature induce pressure changes, which in turn cause drag.

The design of the fuselage is performed in CATIA, as shown in fig. 5.2. The model is built up from 5 longitudinal lines, crossing 13 sections. The fuselage hull is smoothed out using the Porcupine Curvature Analysis (PCA) tool and the Surface Curvature Analysis (SCA) tool in CATIA. The PCA tool is used to analyze the curvature of a line and the SCA tool is used (as the name suggest) to analyze the curvature of a surface.

To ensure that the fuselage has been designed properly, a 2D analysis will be performed in XFOIL on the fuselage hull and a symmetric NACA 4-digit airfoil with a comparable t/c ratio. As the fuselage will be in the wake of the propeller, there will be no laminar flow over the profile. To simulate this lack of laminar flow, the transition point is forced to be at the leading edge for both profiles.
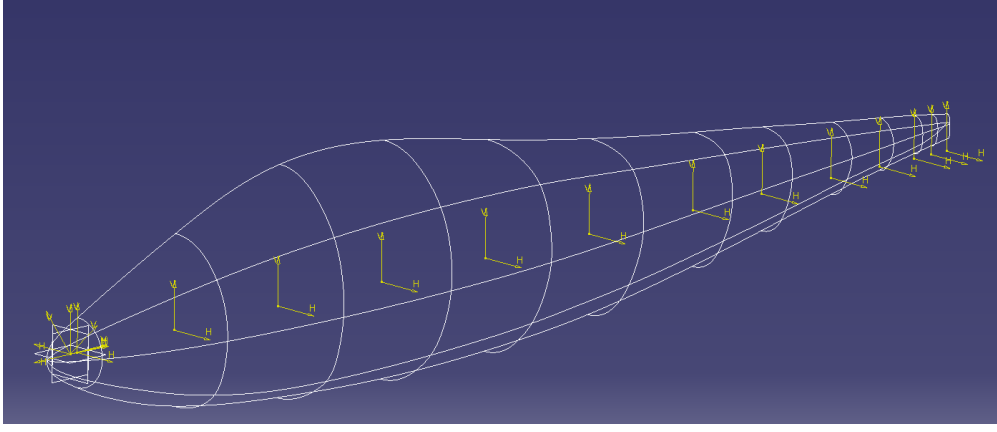
Figure 5.2: The wire frame used to construct and design the fuselage skin

5.2.2 Results

The resulting fuselage hull is shown in fig. 5.3. The color range that is shown gives the radius of the surface curvature and the figure shows that the change in curvature has been minimized. An area with higher curvature can be seen near the upper-mid section of the fuselage. This slight extrusion is due to the width of the engine. If the fuselage were to be fully smoothed out, the width and the height of the fuselage would increase significantly.

In addition to the surface curvature analysis, the porcupine analysis tool can be seen at the top and bottom outline of the hull. As expected, the curvature of the nose cone is high compared to the remaining fuselage. A higher curvature can also be seen at the cockpit, which is gradually straightened out. This curvature on the fuselage is due to the height and the visibility of the pilot. The resulting geometrical data is shown in table 5.2.
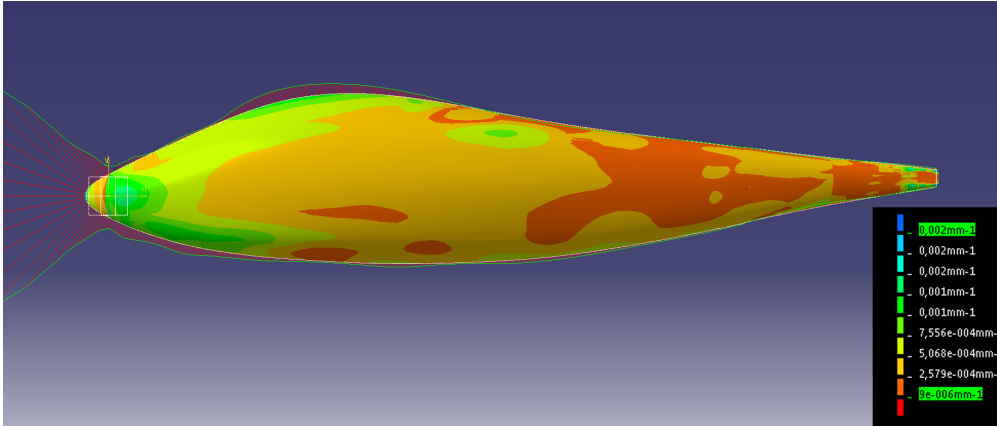
Figure 5.3: The resulting fuselage hull including the curvature analysis

Table 5.2: Final fuselage geometrical data

Parameter	Value	Unit	Description
L_f	7.14	$[m]$	Fuselage length
b_f	1.04	$[m]$	Maximum fuselage width
h_f	1.30	$[m]$	Maximum fuselage height
t/c	0.20	$[-]$	Thickness over chord ratio of the fuselage
S_{fp}	5.40	$[m^2]$	Projected area of the fuselage
S_f	16.0	$[m^2]$	Total surface area of the fuselage

Since the length of the fuselage is known, the Reynolds number at design conditions can be calculated to be

$35(10^6)$. At these conditions, the 2D profile of the fuselage is compared to a NACA 0020 airfoil. For a fair comparison and convergence in XFOIL, the vertical aft of the fuselage is closed like an airfoil. The input profile is shown in fig. 5.4 and the resulting drag polar is shown in fig. 5.5. Both analyses were done at a transition point of 0.10 as XFOIL was not able to converge with lower transition point locations. It can be seen that the fuselage profile has a laminar drag bucket, which is caused by the fact that the turbulent flow behind the propeller is not modeled in XFOIL. Since the flow is turbulent, an approximation is indicated by the red line in the figure. This approximation will be used for the conclusions of this analysis.

In the figure it can be seen that the NACA 0020 airfoil has a C_D value of 0.0068 and that the fuselage profile has a C_D value of 0.0070. The C_D of the airfoil is slightly lower, but the airfoil has to be modified such that the tail section can be attached at the correct location, which will likely increase the C_D. Considering this together with the fact that the difference in C_D is only 2.9%, it can be said that the aerodynamic hull is designed properly. It should be noted that these C_D values are not representative for the drag of the fuselage and can only be used for this comparison.
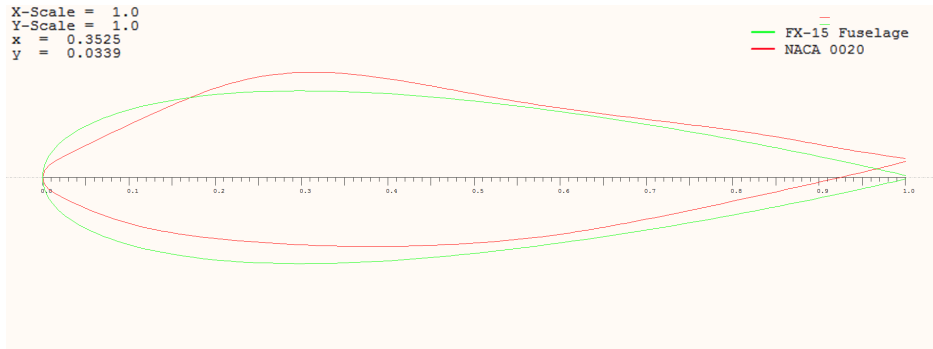
Figure 5.4: The 2D profile of the aerodynamic hull and a NACA 0020 airfoil
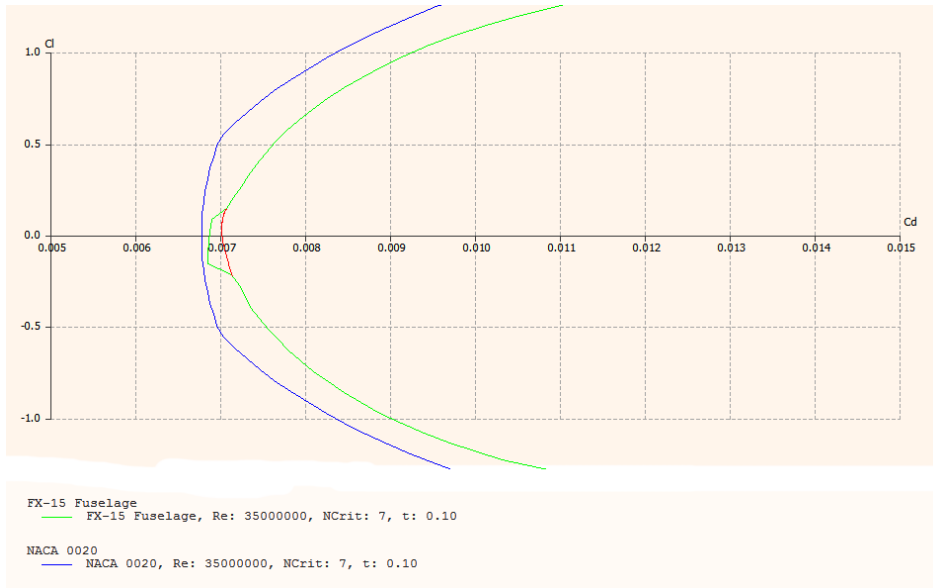
Figure 5.5: The resulting drag polars for the aerodynamic hull and a NACA 0020 airfoil

Material

The fuselage skin will be made out of CFRP, since it will result in a lower skin weight than the traditionally used Glass Fiber Reinforced Polymer (GFRP) [2]. In addition to the lower weight, CFRP provides the opportunity to use the skin as a load-carrying component. As will be explained in section 10.2, there is enough margin in the cost budget to use CFRP, even though it is more expensive than GFRP. It is reasonable to estimate that the CFRP will have a thickness of $1(10^{-3})$ m. Using this estimate, together with the fact that the density of CFRP is 1760 kg/m^3 [2], it is calculated that the total skin mass will be

28.2 kg. It is a known safety issue that a CFRP skin will shatter upon impact, so to ensure the safety of the pilot a layer of Kevlar will be applied to the inside of the cockpit hull. The increase in weight caused by this Kevlar lining can not be determined yet, because it is not known what amount of Kevlar is needed to ensure safety.

5.2.3 Conclusion & Discussion

The fuselage hull has a smooth airfoil-like surface curvature and a drag coefficient comparable to that of a NACA 0020 airfoil. The hull will be made out of CFRP with an estimated thickness of $1(10^{-3})$ m, which will result in higher cost but lower weight. The mass of the aerodynamic hull is estimated to be 28.2 kg, but this is without the Kevlar lining of the cockpit. If this is included, the weight is expected to increase slightly.

Points of improvement for the future are:

- Perform a CFD analysis. *When a CFD analysis is performed, the critical points in the design of the fuselage can be identified and drag can be reduced more effectively. In addition, an accurate drag estimation can be obtained which can then be used to accurately approximate the actual performance of the FX-15.*

- Design junction between the fuselage and subcomponents. *Properly designed junctions between the fuselage and the wing, landing gear, and empennage can significantly lower the drag of the FX-15.*

The RAMS characteristics of the aerodynamic hull are:

- **Reliability.** As discussed in section 4.3.6, a CFRP laminate has excellent durabillity properties. The critical points of the skin will be the connection to the structure.

- **Availability.** The CFRP that is required for the skin is widely available and can be supplied by multiple companies, such as Hexcel.

- **Maintainability.** The CFRP laminate is not easily repairable. In case of major damage, the CFRP hull part that is damaged has to be replaced. In case of a slight crack, the part can be repaired by adding an extra CFRP layer.

- **Safety.** Under normal operating conditions, the CFRP skin is considered to be safe. However, upon impact the CFRP will likely shatter with the potential to seriously injure the pilot. As stated before, it is recommended to protect the pilot using a layer of Kevlar on the inside of the cockpit.

5.3 Structure

In this section, a description of the fuselage structure of the FX-15 will be given. The design is a continuation on the midterm report, in which a hollow, steel-tubed truss structure was selected as the best fuselage structure design option [2].

First, the problems regarding the truss structure design are analyzed. After that, the method used to create the structure is explained. Next, the final results of the design process are shown. Finally, the conclusions and remaining points of discussion are stated.

5.3.1 Problem Analysis

In this section, the problems regarding the truss structure design are analyzed. The loads the fuselage has to handle are discussed first. After this the assumptions are stated. Finally, the design constraints (including the fuselage subcomponents the truss has to fit around and the accessibility and modularity aspects of the fuselage structure design) are investigated.

Loads

The fuselage can be seen as a beam on which multiple loads are acting. For the fuselage structure the following main loads have been identified [37]:

- Engine thrust. *The power unit is attached to the fuselage, which makes the fuselage the 'towing line' of the entire aircraft. The thrust can be significant and must be taken into account.*

- Torque. *Torques act on the fuselage due to the angular momentum of the subcomponents when they have an angular acceleration. The propulsion unit creates torque with its rotating parts (propeller, engine shaft, main transmission shaft etc) when they are accelerating due to an increase/decrease of the throttle. Also, a constant torque caused by friction on the rotating parts in the power system is present. When a roll acceleration of the entire aircraft is present, the fuselage has to enforce an angular momentum on the subcomponents in order to get them to accelerate with the rest of the aircraft. The required size of this angular momentum is given by eq. (5.1). α represents the angular acceleration and I_m the mass moment of inertia. The total angular momentum is given by M.*

$$M = I_m \alpha \tag{5.1}$$

- Body forces. *The body forces are the general loads that act on the body of the fuselage. This includes subcomponents weights, aerodynamic forces and landing gear forces. Important for the aerodynamic loads is to identify the lift forces generated by the wing and the tail. For the landing gear it is important to identify the most extreme landing situation as the fuselage must be able to withstand those loads.*

- Repetitive loading. *Besides torque, the propulsion system also causes vibrations. An engine that does not run smoothly or an engine shaft that is not perfectly aligned will cause major vibrations. The two most important problems caused by vibrations are that they increase the maximum amplitude of the torques and that they have a large negative impact on the fatigue life of the structure. It is very important that the vibrations are kept to a minimum and that they are taken into consideration during a future stress analysis of the structure.*

Assumptions

1. Skin carries no loads. *In reality, the skin will carry (at least some) loads and a conscious decision can even be made in the future to design it as load carrying. As a consequence, all loads are transferred to the fuselage truss structure through the spar.*

2. No repetitive loading. *Even though these loads are very important, for simplicity vibrations are not taken into account during this design stage. It is expected that leaving out the vibrations will lead to an underdesigned fuselage of which the fatigue life is uncertain. Vibrational loads will be included in future design updates.*

3. No torques. *Again for simplicity, angular momentum of the subcomponents and thus the resulting torques are not taken into account. Again, it is expected that this will also lead to an underdesigned fuselage.*

Design Constraints

The positions of all subcomponents are illustrated in fig. 5.1 and table 5.1. The truss structure has to fit between the fuselage skin and the subcomponents. Also, the truss structure must leave enough free space between the trusses and the subcomponents for fixing brackets en control mechanisms.

Three subcomponents require additional attention. It has to be possible to remove the wing and empennage from the structure, to make sure the aircraft can be transported in an efficient manner. Furthermore, the engine has to be easily accessible and removable from the structure in order to minimize downtime during maintenance or engine failure.

5.3.2   Method

The section describes the method that was applied to design the structure of the fuselage. The general design principles are discussed. After this, the actual FEM implementation is outlined. Finally, the method used to check for buckling and yielding is presented.

Design Principles

There are two main design principles that were used throughout the truss structure design. These design principles are listed below.

- The truss structure was designed in such a way that all tubes fit with the fuselage subsystems.

- In a truss structure, it is very important to dissipate forces as quickly as possible. This is what the diagonal bars are used for.

The driving factors for the precise locations and directions of the trusses are the loads caused by the weights of the subcomponents and the aerodynamic forces. At locations where heavy loads act upon the fuselage, trusses are added to distribute the load.

The design point for the fuselage is a steady ±12g turn with a safety factor of 1.5. The aerodynamic tail loads are calculated by assuming an equilibrium situation around the CG.

The landing gear is yet to be designed. Therefore, it has not been incorporated into the current fuselage design. According to requirements, the aircraft must be able to withstand a 3g landing [38]. The landing gear will be placed in the proximity of the wing where the fuselage is able to cope with the high performance ±12g maneuvers. It is therefore expected that the loads that occur during landing will not pose any problems.

FEM

A wire frame of the truss structure is created in CATIA. For the FEM analysis the wire frame is broken down into sections of 0.5 mm. In the FEM workbench, a constant cross-section is defined which, in combination with the given material properties, is used for a 1D FEM analysis. This 1D analysis is based upon the Timoshenko beam theory [39].

The wire frame is clamped at the location where the main spar is connected to the fuselage structure. All loads acting upon the structure are defined with respect to this location. In the FEM analysis trusses have to be selected as the point of action for the loads. Therefore, if the CG of a subcomponent is located a significant distance from the nearest truss, a corresponding moment will be added.

Buckling & Yielding

Before a given truss design can be evaluated, it has to be checked if the longest member of the structure will buckle or yield first. The load used to calculate the buckling is the largest compression force given by the FEM analysis. The equation that is used to calculate the stress required for buckling is eq. (5.2), in which k is 0.50 because all truss structure members are clamped.

$$F_{buckle} = \frac{\pi^2 EI}{(kL)^2} \quad \rightarrow \quad \sigma_{buckle} = \frac{F_{buckle}}{A} \tag{5.2}$$

If σ_{buckle} is higher than the yield stress of the material, the structure will yield before it buckles.

5.3.3 Results

The results that were obtained by following the design principles and FEM method discussed in section 8.1.3 are presented in this section.

Material Choice

According to references, the Zivko Edge 540, the Corvus CA-41 and the Extra 300S [40–43] all use hollow steel tubes in their fuselage truss structures. The reasons for this are listed below [44].

- Hollow steel tubes have very high specific strength.

- Hollow steel tubes are easy to fabricate (they can be welded easily).

- Hollow steel tubes are easy to repair.

For the reasons stated above, it has been chosen to use hollow steel tubes for the fuselage truss structure. The steel that is used for the tubes is AISI 410S stainless steel, tempered at 233 °C [45], because it has a high yield stress and is designed to handle the temperatures that are found around the engine (expected to be approximately 200 °C). The properties of this steel are stated in table 5.3.

Table 5.3: AISI 410S stainless steel properties

Parameter	Value	Unit	Source	Description
E	$200(10^9)$	$[Pa]$	[45]	Young's modulus
σ_{yield}	$1005(10^6)$	$[Pa]$	[45]	Yield stress
ρ	7800	$[kg/m^3]$	[45]	Density
T_{max}	705	$[°\ C]$	[45]	Maximum continuous service temperature, air

The tubes used for the truss structure have an outer radius of $10(10^{-3})$ m and an inner radius of $9(10^{-3})$ m. This design has a high MOI over weight ratio and is easy to produce.

Truss Structure Layout

The side view of the truss structure is given in fig. 5.6 and the top view of the truss structure is given in fig. 5.7. The sides of the truss structure are completely symmetrical, to avoid an unsymmetrical bending plane. The top and bottom of the truss structure are designed such that the bending plane will be as symmetric as possible. However, due to the constraints imposed by some of the fuselage subsystems it was not possible to do this perfectly.

The points of interest in fig. 5.6 and fig. 5.7 are listed below.

- There is no diagonal bar at the engine location because it does not fit with the engine. Of course the fuselage could have been made wider to fit the truss structure around the engine, but the amount the width would have had to increase was considered too much. Instead, it was chosen to use the support of the diagonals of the main spar structure to avoid deformations at the engine location.

- The main spar slot is suspended below the rest of the truss structure. This is done because it is the only way the spar will fit with the rest of the fuselage subsystems. This results in a vertical wing postions of -0.325 m with respect to the CG of the propeller.

- There is no truss at the location of the pilot.

- A roll bar is present to protect the pilot from impact.
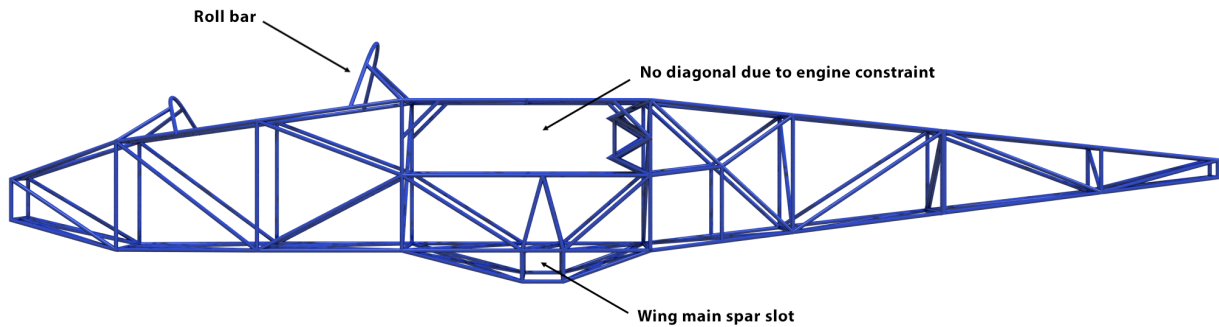
Figure 5.6: Fuselage truss structure side view
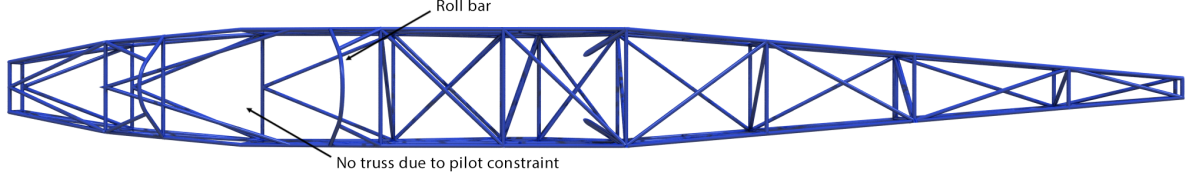
Figure 5.7: Fuselage truss structure top view

Stresses & Displacements

The inputs for the FEM analysis are given in table 5.4. The loads applied consists of the masses of the subcomponents, the aerodynamic forces required for equilibrium and the engine and propeller forces at $\pm 12g$ with a safety factor of 1.5. The locations of the applied loads are clarified in fig. 5.8. Three main load types can be identified in the table and figure. Forces acting on a specific location, Moments at a specific location, and a distributed force acting through a larger part of the fuselage. The weight of the fuselage is modelled to act on the entire structure, and the drag force is modelled to act on the aft section of the fuselage.

Table 5.4: Input values for the FEM Analysis

Parameter	Value	Unit	Acting Location	Source	Description
$w_{Fuselage}$	-15221	$[N]$	Whole structure	Section 5.1.2	Distributed force due to fuselage weight
F_{Tail}	-4238	$[N]$	Aft end	Section 5.1.2	Force due to tail weight
$F_{Propeller}$	-4874	$[N]$	Front end	Section 5.1.2	Force due to propeller weight
$M_{Propeller}$	-292	$[Nm]$	Front end	Section 5.1.2	Moment due to propeller thrust
$F_{Landing\ gear}$	-9341	$[N]$	Mid section	Section 5.1.2	Force due to landing gear weight
$w_{Driveshaft}$	-1589	$[N]$	Front $\rightarrow$ mid	Section 5.1.2	Distributed force due to driveshaft weight
F_{Engine}	-37453	$[N]$	Engine support	Section 5.1.2	Force due to engine weight
M_{Engine}	-22472	$[Nm]$	Engine support	Section 5.1.2	Moment due to engine weight
F_{CCT}	-706	$[N]$	Aft section	Section 5.1.2	Force due to CCT weight
F_{Safety}	-610	$[N]$	Mid section	Section 5.1.2	Force due to weight of safety systems
$F_{Payload}$	-14480	$[N]$	Cockpit section	Section 5.1.2	Force due to payload weight
$F_{Fuel\ tank}$	-10153	$[N]$	Behind engine	Section 5.1.2	Force due to fuel tank (and fuel) weight
$w_{Control\ system}$	-4467	$[N]$	Cockpit $\rightarrow$ aft	Section 5.1.2	Distributed force due to control system weight
F_{Thrust}	3600	$[N]$	Front end	Section 5.1.2	Force due to propeller thrust
w_{Drag}	-3600	$[N]$	Aft section	Section 5.1.2	Distributed force due to drag
$F_{Elevator}$	4740	$[N]$	Aft end	Section 5.1.2	Force due to elevator deflection
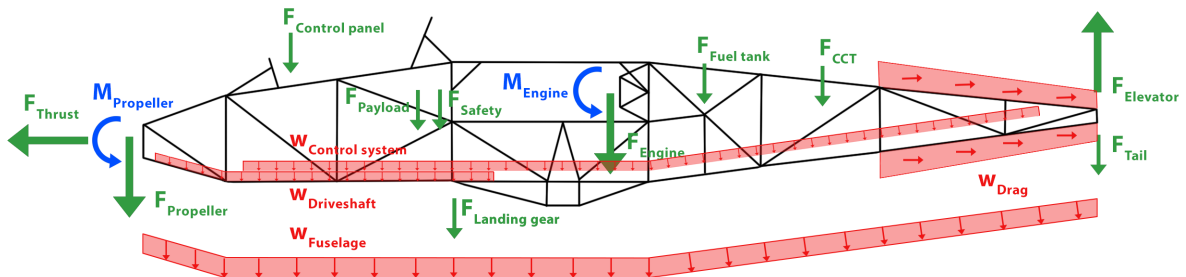
Figure 5.8: Locations of the applied loads

The displacement results of the FEM analysis are shown in fig. 5.9 and the stress locations are shown in fig. 5.10. The maximum and minimum stresses and the maximum displacement of the truss are given in table 5.5.
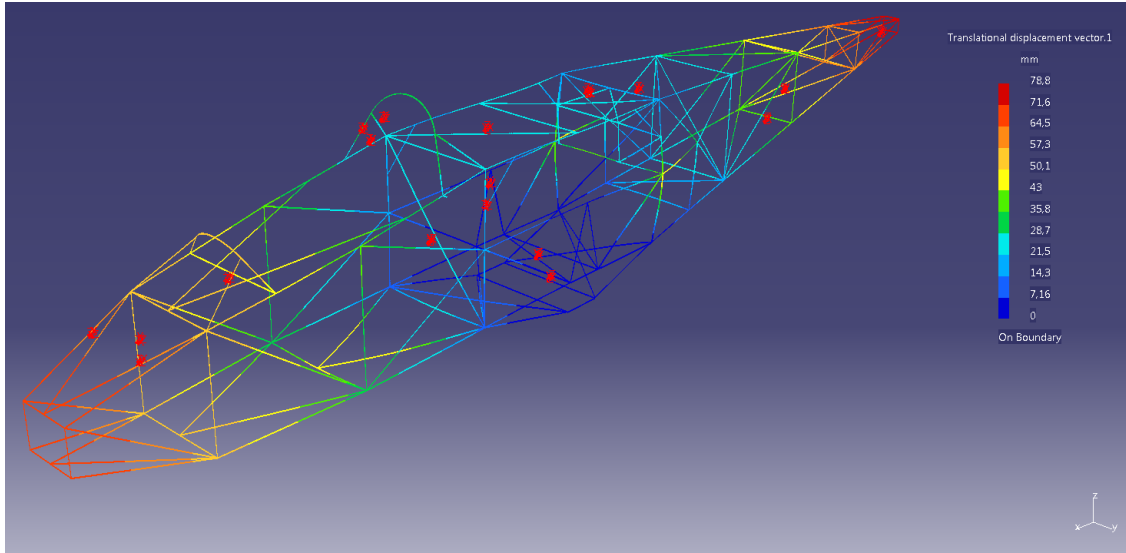
Figure 5.9: Displacement of the truss structure under a load of 12g with safety factor of 1.5
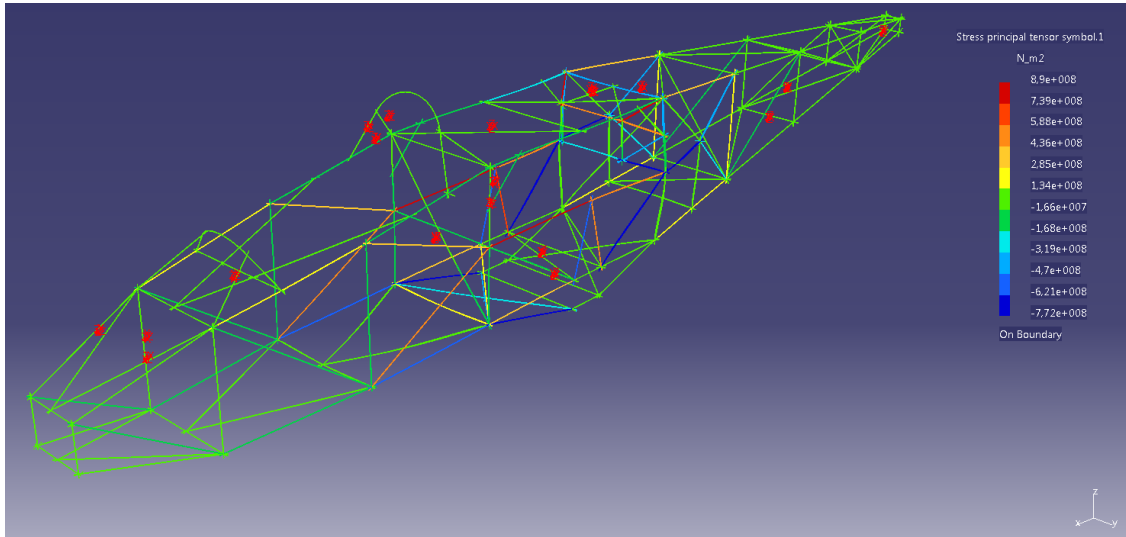
Figure 5.10: Load distrubution in the truss structure under a load of 12g with safety factor of 1.5

Table 5.5: Output values for the material choice analysis

Parameter	Value	Unit
σ_{max}	$890(10^6)$	$[Pa]$
σ_{min}	$-772(10^6)$	$[Pa]$
δ_{max}	$7.88(10^{-2})$	$[m]$

According to this analysis, the fuselage truss structure will weigh 48.8 kg. Since the skin was calculated to weigh 28.2 kg in section 5.2.2, the entire fuselage structure will weigh 77.0 kg.

Buckling & Yielding

The longest member in the truss structure has a length of 0.896 m. According to eq. (5.2), the required stress for buckling is therefore $80.6(10^9)$ Pa. The yield stress of 410S stainless steel is $1.005(10^9)$ Pa (table 5.3). Therefore the structure will yield before it buckles and buckling does not have to be considered.

5.3.4 Conclusion & Discussion

The fuselage truss structure uses hollow steel tubes and weighs 48.8 kg. It can handle the loads that act on the fuselage at the critical design point with a safety margin of 1.5 without yielding or buckling. The maximum displacement under these conditions is 7.88 cm. As the weight of the skin is 28.2 kg, the weight of the fuselage truss structure including the skin is 77.0 kg.

Points of improvement for the future are:

- Investigate including the skin as a load bearing component. *If the skin is included as a load bearing component, the truss will have to carry less loads and can be made even lighter. The skin is needed anyway for aerodynamic reasons, so it makes sense to also use it as a load carrying structure.*

- Include vibrations in the truss structure analysis. *Considering vibrations and the fatigue life of the structure will have a significant impact on the design of the truss.*

The RAMS characteristics of the fuselage structure are:

- **Reliability.** Most reference aircraft also have steel truss structures in their fuselages, and these structures are highly reliable. However, as mentioned before vibrations have not been taken into account yet. These vibrations can have a significant impact on the reliability of the fuselage structure and should be investigated in the future. Note that the P-63 King Cobra [46] also has a mid-mounted engine configuration and was operated with great success. Therefore, it is expected that if vibrations are investigated and the design is adapted to handle vibrational loads, the fuselage structure will be very reliable.

- **Availability.** The truss structure is built using AISI 410S stainless steel. This steel is widely available and can be ordered at several suppliers. The truss structure can be assembled at TU Delft.

- **Maintainability.** The structure has been designed with maintainability in mind. The steel that is used for the truss structure is easily repairable, both the wing and the engine can easily be removed for maintenance and all fuselage subsystems are easily accessible.

- **Safety.** The structure has been designed for a ±12g turn (the critical design point) with a safety factor of 1.5. Furthermore, the truss structure is a proven design for aerobatic racing aircraft fuselages. The design is therefore expected to be very safe.

The sustainability options for the fuselage structure can be split into several parts. The first and most obvious part is the production. The production options are:

- Produce the fuselage structure in The Netherlands if possible. This will reduce the environmental impact of transporting the fuselage.

- Produce the energy that is used for the production of the steel tubes in a sustainable manner.

Another important part is end-of-life. The end-of-life options are:

- Melt and re-use the steel for other purposes. The steel can be fully recycled this way. However, pollutants are emitted during the melting process.

- Place the fuselage truss structure in the ocean as an artificial reef. This way, the steel can be re-used in a non-polluting way.

6 Tail Detail Design

During the conceptual design, preliminary sizing of the horizontal and vertical stabilizer was performed. These designs will be used as a starting point for the detailed design of the empennage. First the detailed horizontal tail will be designed after which the vertical tail and its control surfaces will be designed.

The planforms of the horizontal and vertical tails are described in section 6.1. After this, the tail control surfaces are designed in section 6.3. The system with which these control surfaces are operated is outlined in section 6.4. Finally, the aircraft flight dynamics are discussed in section 6.5.

6.1 Horizontal Stabilizer

This section will elaborate on the detail design procedure of the horizontal stabilizer. First the problem will be analyzed and assumptions will be stated, then the used methods for design will be explained, after which the results will be presented.

6.1.1 Problem Analysis

The main function of the horizontal tail is to provide longitudinal stability and control. It should be kept as small as possible, because a larger surface will result in more drag. When the tail surface has been determined, the other tail planform parameters must be selected. The main goal of the planform selection is to improve controllability and minimize drag. This section describes the methods used to size and shape the horizontal stabilizer, after which the results will be presented, verified and validated.

For the sizing of the horizontal stabilizer, the scissor plot method is used as described by Torenbeek [15]. Torenbeek uses a number of assumptions, the most important ones are summarized here:

1. Stability margin is 5%. *The stability margin is assumed to be 5% of the MAC. This margin might seem small, but it is better to have the aircraft be close to neutrally stable or even unstable, rather than to be very stable. This is due to the fact that high stability means low controllability.*

2. SF of 1.5 on aerodynamic moment. *The aerodynamic moment coefficient of the aircraft is assumed to have a safety factor of 1.5, in order to ensure full controllability during the entire mission.*

6.1.2 Method

The first design step is to update the scissor plot, in order to create a solid baseline for the detailed design. The second step is selecting a planform and airfoil for the horizontal stabilizer, after which the tail configuration will be determined.

Scissor Plot Update

During the preliminary design, a scissor plot was created (section 3.10) in order to find an initial tail size. After the preliminary design it was assumed that a safety factor of 1.5 must be added to the controllability curve. Using the results of the new scissor plot, the rest of the planform of the wing will be designed. This will be done using Sadraey's method [26]. First, the design tail lift coefficient needs to be determined. This will be done by rewriting the trim equation from eq. (6.1) to eq. (6.2).

$$0 = C_{m_{\alpha_f}} + C_{L_{A-h}}(\bar{x}_{ac} - \bar{x}_{cg}) + C_{L_h} \frac{S_h l_h}{S\bar{c}} \left(\frac{V_h}{V} \right)^2 \tag{6.1}$$

$$C_{L_h} = \frac{C_{m_{ac}} + C_{L_{A-h}}(\bar{x}_{cg} - \bar{x}_{ac})}{\frac{S_h l_h}{S\bar{c}} \left(\frac{V_h}{V} \right)^2} \tag{6.2}$$

For the lift coefficient of the wing ($C_{L_{A-h}}$) the design lift coefficient will be used. The value for the fuselage contribution to the pitching moment ($C_{M_{\alpha_f}}$) can be found using eq. (6.3) which is described by Raymer [9].

$$C_{M_{\alpha_f}} = \frac{K_f b_f^2 l_f}{\bar{c} S} \tag{6.3}$$

When the horizontal tail required lift coefficient, described by eq. (6.2), has been found, the rest of the tail can be designed.

Horizontal Tail Planform

The next step is to select a planform. The parameters needed are: aspect ratio, taper ratio and sweep angle. The aspect ratio of the horizontal tail will be designed using the following criteria:

- The span of the horizontal stabilizer should be larger than the diameter of the propeller, so that a significant part of the stabilizer will be out of the wake of the propeller.

- The aspect ratio of the horizontal stabilizer should be kept as small as possible, because the higher the aspect ratio, the higher the bending moments during elevator deflection, which will result in a heavier structure.

The taper ratio for the wing is used to create an elliptical lift distribution but this is not a requirement for the tail. Therefore, the taper ratio should be selected to reduce weight by decreasing the bending moment. The sweep of the aircraft should be selected such that the hinge of the control surface is perpendicular to the aircraft center-line. This improves the stall characteristics (relative to the forward swept main wing) and allows for easier construction of the hinge.

Horizontal Tail Airfoil

Parallel to the selection of the planform, an airfoil must be selected. The airfoil selected should produce enough lift for the aircraft to be stable, and the drag should be minimized. When the airfoil and planform parameters are selected, the lift generated by the 3D-horizontal tail can be calculated using the same software used for the wing (section 4.1). This generates a $C_L - \alpha$ plot, from which the desired horizontal stabilizer angle of attack (α_h) during cruise flight can be found.

Horizontal Tail Configuration

The vertical position of the the horizontal stabilizer has been determined by constructing a linear regression between the vertical location of the wing and the vertical difference between the wing and the horizontal stabilizer. This linear regression has been constructed using 21 reference aircraft from section 3.2. The R^2 value for this regression is 0.86 and the height of the horizontal stabilizer with respect to the wing position equals 0.40 m.

In order to find the inclination angle of the horizontal stabilizer i_h, the angle of attack of the tail needs to be combined with the downwash angle and the angle of attack of the fuselage. The downwash angle is found using eq. (6.4) as described by Sadraey [26].

$$\epsilon = \epsilon_0 + \frac{d\epsilon}{d\alpha} \alpha_w \tag{6.4}$$

Here, the α_w describes the angle of attack of the wing, and the downwash slope $\frac{d\epsilon}{d\alpha}$ has been calculated before during the preliminary design (section 3.10).The equation for the downwash at zero angle of attack (ϵ_0) is given by Sadraey [26] and is described by eq. (6.5).

$$\epsilon_0 = \frac{2 \cdot C_{L_w}}{\pi \cdot A_w} \tag{6.5}$$

Here, C_{L_w} describes the wing lift coefficient and A_w the wing aspect ratio. The tail setting angle will then be calculated using eq. (6.6).

$$i_h = \alpha_h - \alpha_f + \epsilon \tag{6.6}$$

Where α_h and α_f represent the angles of attack of the horizontal stabilizer and the fuselage respectively. With this the size, shape, airfoil and setting of the tail are known, which concludes the design of the horizontal stabilizer.

Stability

In order to check whether the tail provides enough stability, the aircraft static longitudinal stability derivative should be checked. It is determined as follows:

$$C_{m_\alpha} = C_{L_{\alpha_f}} + C_{L_{\alpha_w}}(\bar{x}_{cg} - \bar{x}_{ac}) - C_{L_{\alpha_h}}\eta_h\frac{S_h}{S}\frac{l}{\bar{c}}(1 - \frac{d\epsilon}{d\alpha}) \tag{6.7}$$

This value will be checked with simulation data during the verification process.

6.1.3 Results

The input values used for the scissor plot remain the same, but a safety factor is added. Most input values have been changed due to iterations in the design. They are shown in table 6.1. The input values that remain unchanged can be found in table 3.12.

Table 6.1: Input values for horizontal stabilizer sizing

Variable	Value	Unit	Source	Description
Fuselage parameters				
l_f	7.14	$[m]$	Section 5.2.2	Fuselage length
b_f	1.04	$[m]$	Section 5.2.2	Fuselage width
h_f	1.30	$[m]$	Section 5.2.2	Height of fuselage
α_f	0.00	$[°]$	Estimate	Fuselage angle of attack
K_f	$1.3(10^{-2})$	$[-]$	[9]	Empirical pitching moment factor
l_{fn}	2.26	$[m]$	CATIA	Length from nose to LEMAC
Wing parameters				
$(\bar{x}_{ac})_w$	0.25	$[-]$	Estimate	AC as % of MAC
S	9.30	$[m^2]$	Section 4.1.3	Wing surface
A	7.77	$[m^2]$	Section 4.1.3	Wing aspect ratio
$\bar{c}$	1.12	$[m]$	Section 4.1.3	Wing MAC
λ	0.60	$[-]$	Section 4.1.3	Wing taper ratio
$\Lambda_{0.25c}$	-1.84	$[°]$	Section 4.1.3	Wing sweep at 25% chord
$\Lambda_{0.5c}$	-3.68	$[°]$	Section 4.1.3	Wing sweep at 50% chord
Misc.				
S.F.	1.5	$[-]$	[5]	Safety factor
W	735.5	$[kg]$	Section 3.12	Aircraft race mass
$C_{L_{des}}$	0.31	$[-]$	Section 4.1.3	Design lift coefficient
$(V_h/V)^2$	0.85	$[-]$	[15]	Tail-to-wing velocity ratio (squared)

The revised scissor plot is shown in fig. 6.1. With the S_h found, the required C_{L_h} is determined. Due to the low value of C_{L_h} the NACA 0009 is selected. The most important characteristics of the airfoil are shown in table 6.2.

Table 6.2: NACA 0009 airfoil characteristics [26]

$C_{d_{min}}[-]$	$C_{l_{max}}[-]$	$C_{l_\alpha}[rad^{-1}]$	$(t/c)max$
0.005	1.3	6.7	9%
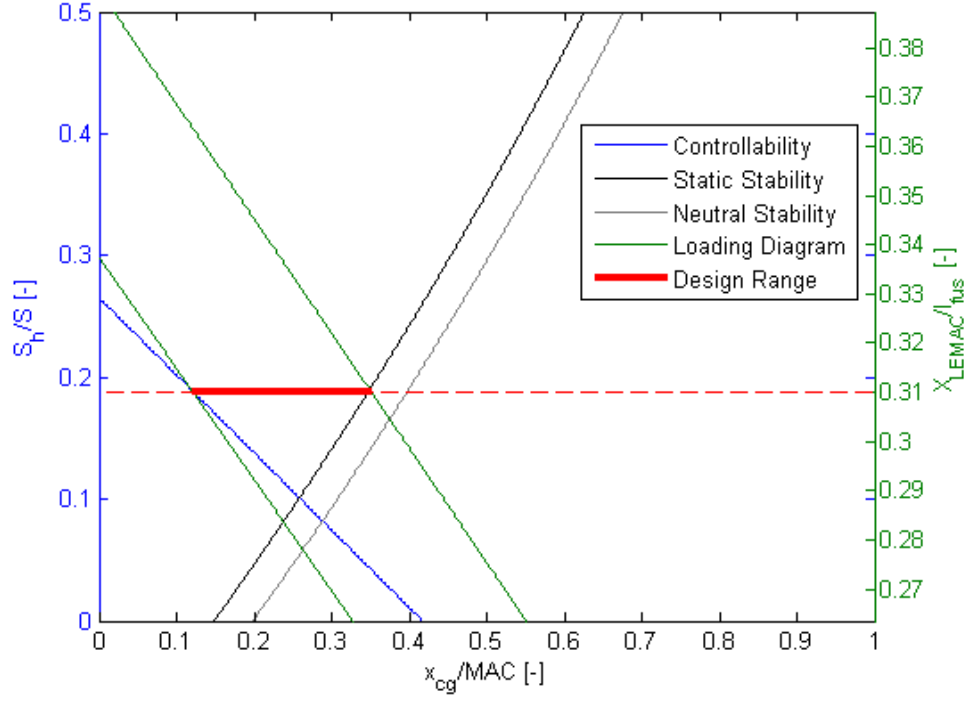
Figure 6.1: Revised scissor plot including safety factor for $C_{m_{ac}}$

Combining the parameters from table 6.2 with the planform as shown in table 6.3, the Q-3D AeroSolver (explained in detail in section 4.1.2) produces the $C_l - \alpha$ curve shown in fig. 6.2b.

(a) α_h from 0 to 25
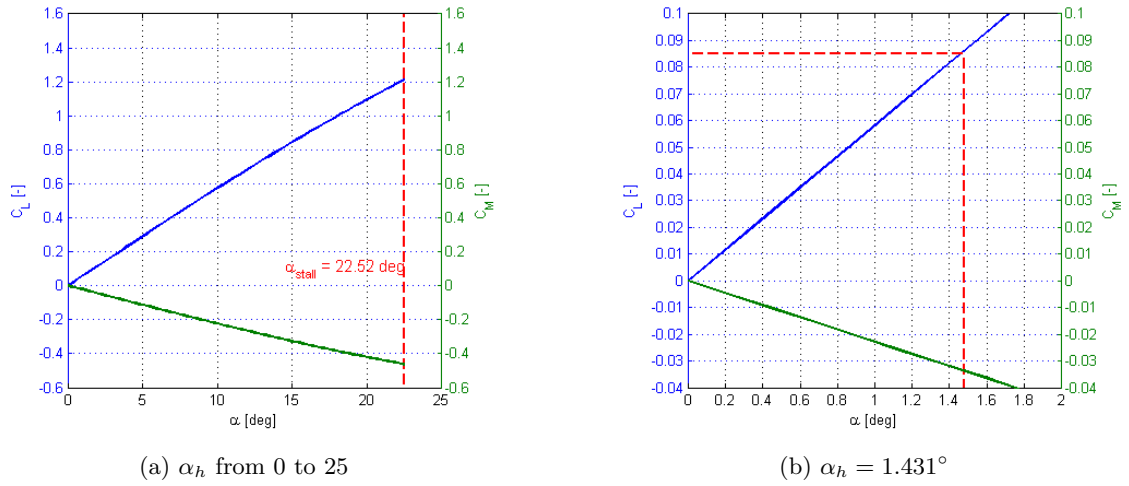
(b) $\alpha_h = 1.431°$

Figure 6.2: $C_l/C_m - \alpha$ curve for the NACA 0009 airfoil

Using the angle of attack ($\alpha_h = 1.431°$) resulting from fig. 6.2b, the incidence angle can be calculated using eq. (6.6), which concludes the design of the horizontal stabilizer.

Table 6.3: Output values for horizontal stabilizer design

Variable	Value	Unit	Description
S_h/S	0.23	[−]	Horizontal stabilizer-to-wing surface ratio
S_h	2.12	[m^2]	Horizontal stabilizer surface
x_{LEMAC}	2.14	[m]	Distance nose to LEMAC
x_{cg}	2.56	[m]	Distance nose to CG
x_{ac}	2.41	[m]	Distance nose to AC
C_{L_h}	0.085	[−]	Horizontal stabilizer design lift coefficient
A_h	3.00	[−]	Horizontal stabilizer aspect ratio
λ_h	0.55	[−]	Horizontal stabilizer taper ratio
$\Lambda_{h_{0.25c}}$	8.98	[°]	Horizontal stabilizer sweep at 25% chord
b_h	2.52	[m]	Horizontal stabilizer span
c_{h_r}	1.09	[m]	Horizontal stabilizer root chord
c_{h_t}	0.58	[m]	Horizontal stabilizer tip chord
α_h	1.43	[°]	Horizontal stabilizer design angle of attack
i_h	4.51	[°]	Horizontal stabilizer incidence angle

6.2 Vertical Stabilizer

The vertical tail is a means to ensure lateral stability for the aircraft. A preliminary design was proposed in the midterm report [2]. The used method to find the preliminary design in the midterm was the Torenbeek method [15]. The preliminary design will be used as a starting point for the detail design. This section will elaborate on the detailed design process and results of the vertical stabilizer sizing.

6.2.1 Problem Analysis

The design of the vertical stabilizer as proposed in the midterm report will be analyzed to check whether the design is sufficient to ensure laterally stable flight and whether the tail can be improved. The initial design of the vertical stabilizer consists of an Aspect Ratio, taper ratio, sweep angle and span area. For optimizing the vertical stabilizer each of these will be kept constant except for the vertical stabilizer span and surface area, these will be adjusted if needed for optimizing the design.

For the sizing of the vertical stabilizer, some assumptions have been made:

1. C_{n_β} must be over 0.06. *It is assumed that the yawing moment derivative (C_{n_β}) should at least be 0.06 for stable and safe aircraft operating properties as stated by Torenbeek [15].*

2. V_v is equal to V_h. *The flow velocity over vertical tail is assumed equal to the velocity over the horizontal tail as used in section 6.1.*

6.2.2 Method

As mentioned in the sizing. The required yawing moment derivative (C_{n_β}) for the aircraft is known from the assumptions. The yawing moment derivative for side-slip consists of contributions of the different aircraft subsystem: fuselage ($C_{n_{\beta_f}}$), wing ($C_{n_{\beta_w}}$), propulsion ($C_{n_{\beta_p}}$) and vertical tail ($C_{n_{\beta_v}}$). The sum of all the C_{n_β} should be bigger than 0.06 as stated earlier:

$$0.06 \leq C_{n_\beta} = C_{n_{\beta_f}} + C_{n_{\beta_p}} + C_{n_{\beta_w}} + C_{n_{\beta_v}} \tag{6.8}$$

For each contributor to C_{n_β} the individual contribution will be calculated, filling these in eq. (6.8) will results in the required contribution from the vertical stabilizer ($C_{n_{\beta_v}}$), which will be used to size the vertical stabilizer planform.

An estimate for the fuselage contribution can be made using the fuselage geometry following Torenbeeks [15], see eq. (6.9) (and eq. (6.10)):

$$C_{n_{\beta f}} = -K_\beta \frac{S_{fs} l_f}{Sb} \left(\frac{h_{f1}}{h_{f2}}\right)^{\frac{1}{2}} \left(\frac{b_{f2}}{b_{f1}}\right)^{\frac{1}{3}} \qquad (6.9) \qquad\qquad K_\beta = 0.3\frac{l_{cg}}{l_{lf}} + 0.75\frac{h_{fmax}}{l_f} - 0.105 \qquad (6.10)$$

The contribution of the propulsion can also be found using Torenbeeks [15] method:

$$C_{n_{\beta p}} = -0.053 B_p \sum \frac{l_p D_p^2}{Sb} \qquad (6.11)$$

The wing and horizontal tail contribution towards the C_{n_β} are obviously zero since the airfoils and planforms are symmetrical (no dihedral). The interaction between the fuselage and the wing, however, does influence the yawing moment coefficient. Torenbeek [15] proposes a positive effect of 0.024 in case of low mounted wings.

Now all the contributions except from the vertical tail itself are known. The required contribution to C_{n_β} from the vertical stabilizer can be expressed in terms of side-force derivative ($C_{y_{\beta v}}$) and moment arm. Rewriting equation 6.8 yields equation 6.12.

$$C_{n_{\beta v}} = C_{n_\beta} - (C_{n_{\beta f}} + C_{n_{\beta p}} + \Delta_i C_{n_\beta}) = C_{y_{\beta v}} \frac{l_v}{b}\left(\frac{V_v}{V}\right)^2 \qquad (6.12)$$

Note that the term $\Delta_i C_{n_\beta}$ represents the interaction between wing and fuselage. The sideforce derivative, $C_{y_{\beta v}}$, can be found using equation 6.13 from Roskam's 'Airplane Design Part 6 - Preliminary Calculation of Aerodynamic, Thrust and Power Characteristics' [47].

$$C_{Y_{\beta v}} = -\kappa_v C_{L_{\alpha v}}\left(1 + \frac{d\sigma}{d\beta}\right)\eta_v\left(\frac{S_v}{S}\right) \qquad (6.13)$$

κ_v (an empirical factor) can be extracted from figure 10.12 on page 385 in Roskam part six [47]; its value is 0.8. The rest of equation 6.13 can be solved using equations 6.14 and 6.17.

The DATCOM method for lift gradient (it can be found in Roskam part six as well [47]) has been used to find an estimate $C_{L_{\alpha v}}$ (the lift slope of the vertical stabilizer), see equations eqs. (6.14) and (6.15).

$$C_{L_{\alpha v}} = \frac{2\pi A_{v_{eff}}}{2 + \sqrt{4 + \left(\frac{A_{v_{eff}}\beta}{\eta}\right)^2 \left(1 + \frac{\tan^2 \Lambda_{0.5C}}{\beta^2}\right)}} \qquad (6.14)$$

$$\beta = \sqrt{1 - M_\infty^2} \qquad (6.15)$$

For eq. (6.14) an estimate of the effective aspect ratio ($A_{v_{eff}}$) is needed, Roskam uses the following equation for that:

$$A_{v_{eff}} = \frac{A_v(f)}{A_v} A_v \qquad (6.16)$$

Where $\frac{A_v(f)}{A_v}$ can be extracted from figure 10.14 from page 388 in Roskam part six [47]; its value is 1.6.

An estimate for the term $\left(1 + \frac{d\sigma}{d\beta}\right)\eta_v$ (which represents the changed angle of sideslip on the vertical stabilizer due to aerodynamic effects of the aircraft) can be found using equation 6.17. Again this is from Roskam [47].

$$\left(1 + \frac{d\sigma}{d\beta}\right)\eta_v = 0.724 + 3.06\frac{\left(\frac{S_v}{S}\right)}{1 + \cos\Lambda_{.25c}} + 0.4\left(\frac{Z_w}{Z_f}\right) + 0.009A \qquad (6.17)$$

Equation 6.13 can now be solved for S_v, the vertical tail surface.

A suitable airfoil needs to be selected for the vertical stabilizer as well. A rule of thumb that can be used when selecting an airfoil is that the thickness ratio is 12% [15]. The used method for finding an airfoil is to

look into the standard NACA0012 profiles, and than adjusting (increasing) the nose radius until the desired angle of attack range is reached. In this case the required stall angle is 15 ° (angle of attack on the lifting surface); crosswind-landing yaw angle as required by CS-23 [4] including safety factor of 1.5 for gusts.

6.2.3 Results

The used inputs for the vertical stabilizer sizing can be found in tab 6.4

Table 6.4: Input values for vertical stabilizer sizing

Variable	Value	Unit	Source	Description
Wing geometry				
S	9.30	$[m^2]$	Section 4.1	Wing surface area
b	8.50	$[m]$	Section 4.1	Wing span
A	7.77	$[-]$	Section 4.1	Wing aspect ratio
$\Lambda_{0.25c}$	-1.84	$[°]$	Section 4.1	Wing quarter chord
$\Delta_i C_{n_\beta}$	0.024	$[rad^{-1}]$	[15]	Wing-fuselage interference effect
Fuselage geometry				
S_{fs}	5.40	$[m^2]$	CATIA	Wetted area fuselage
$h_{f_{max}}$	1.30	$[m]$	CATIA	Max fuselage height
h_{f_1}	1.29	$[m]$	CATIA	Height at quarter length fuselage
h_{f_2}	0.47	$[m]$	CATIA	Height at three quarter lentgh fuselage
b_{f_1}	1.00	$[m]$	CATIA	Width at quarter length fuselage
b_{f_2}	0.31	$[m]$	CATIA	Width at three quarter length fuselage
l_f	7.14	$[m]$	Section 5.2	Fuselage length
l_v	3.21	$[m]$	CATIA	Vertical stabilizer location from CG
CG	2.56	$[m]$	Section 6.1.3	CG location from nose
Propulsion data				
B_p	3	$[-]$	[48]	Number of propeller blades
l_p	2.56	$[m]$	CATIA	Distance between CG and propeller
D_p	1.98	$[m]$	[48]	Propeller diameter
Miscellaneous				
$(V_v/V)^2$	0.85	$[-]$	Section 6.1	Vertical stabilizer velocity
M_∞	0.24	$[-]$	Section 3.11	Aircraft Mach number
κ_v	0.80	$[-]$	[47]	Coefficient for side force derivative (yaw)
Z_w/Z_f	0.67	$[-]$	[47]	Relative wing z-location (see Roskam)
$A_{v(f)}/A_v$	1.60	$[-]$	[47]	Ratio for finding A_{veff}
η	0.95	$[-]$	[47]	Airfoil efficiency
Preliminary planform design				
$\Lambda_{v_{0.5c}}$	0.00	$[°]$	[24]	Half chord sweep angle vertical stabilizer
A_v	1.50	$[-]$	[24]	Aspect ratio vertical stabilizer
S_v	1.20	$[m^2]$	[24]	Surface area vertical stabilizer
λ	0.40	$[-]$	[24]	Vertical stabilizer taper ratio

The results from the calculations and estimations as described in the methods section can be found in table 6.5. The results include the planform geometry and yaw derivatives.

Table 6.5: Output values for vertical stabilizer sizing

Parameter	Value	Unit	Description
Airfoil	NACA 0012-93	$[-]$	Airfoil of the vertical stabilizer
$C_{n_{\beta_{fus}}}$	-0.076	$[rad^{-1}]$	Yaw derivative due to sideslip contribution fuselage
$C_{n_{\beta_{prop}}}$	-0.020	$[rad^{-1}]$	Yaw derivative due to sideslip contribution propulsion
$C_{n_{\beta_v}}$	0.132	$[rad^{-1}]$	Yaw derivative due to sideslip contribution vert. stab
$C_{Y_{\beta_v}}$	-0.417	$[rad^{-1}]$	Sideforce sideslip coefficient slope vertical stabilizer
$C_{n_{\beta_{tot}}}$	0.600	$[rad^{-1}]$	Aircraft yawing moment coefficient due to sideslip
S_v	1.20	$[m^2]$	Surface area vertical stabilizer
A_v	1.50	$[-]$	Aspect ratio vertical stabilizer
b_v	1.34	$[m]$	Aspect ratio vertical stabilizer
$\Lambda_{0.5}$	0.00	$[°]$	Half chord sweep angle vertical stabilizer
λ	0.40	$[-]$	Vertical stabilizer taper ratio

It can be seen in table 6.5 that the midterm design, by chance (the wing surface has been changed in mean time, changing the tail volume), already was exactly the required tail size.

6.3 Control Surfaces

This section will discuss the design both the rudder and elevator. First the elevator design process will be explained, followed by the rudder design.

6.3.1 Elevator

The elevator is needed for control in pitch direction. The parameters designed for during the elevator design are the span, chord and deflection angles. The design process will be explained in this section.

The most critical flight condition for pitch control in general aviation is during low-speed operations such as take-off and landing. Of course, during aerobatic flight, a different set of requirements will need to be met. This means that the different aerobatic maneuvers during the RBAR must be analyzed and that a set of requirements must be built from this analysis. Knowing these requirements, the elevator can be designed.

The assumption used during the elevator design is: When analyzing the critical flight condition, the moment due to thrust is assumed equal to the moment due to drag. *The pitching moment might differ slightly from the calculated value.*

Method

The design of the elevator starts by finding the design requirements. When it is known what is required from the elevator, the different forces and pitching moments on the aircraft under critical flight conditions are analyzed. This will give the necessary information to find the span and chord-ratio of the elevator. This will then be used to calculate the elevator effectiveness derivatives.

The first step in this design process is to find the maximum amount of lift that has to be generated by the horizontal stabilizer during flight operations. The two critical conditions that will ultimately size the elevator are the ability to generate $\pm 12g$. Using the trajectory optimization master thesis of C. Liem, it can be seen that the aircraft needs to generate a 10g load within a fraction of a second [1]. This fraction of a second is from no on noted as pitching time, t_θ. As the aircraft needs to be designed for $\pm$ 12g, this is extrapolated up to 12g. The 12g lift is generated when the wing of the aircraft reaches an angle of attack α_w. Using the eq. (6.18), the requirement for the angular pitch acceleration $\ddot{\theta}$ can be found, with θ the amount of pitch that needs to be generated to achieve the necessary angle of attack.

$$\theta = \alpha_{w_{\min/\max}} - \alpha_{w_{\text{cruise}}} = \frac{1}{2}\ddot{\theta}t_\theta^2 \tag{6.18}$$

Knowing the MOI around the Y-axis I_{yy}, the necessary pitching moment to reach the pitching acceleration $\ddot{\theta}$ can be found using eq. (6.19).

$$I_{yy} \cdot \ddot{\theta} = M = M_{\alpha_f} + T \cdot x_T + D \cdot x_D + W \cdot x_W + L_w \cdot x_{L_w} + L_h \cdot x_{L_h} \qquad (6.19)$$

The pitching moment can be found by adding the force contributions multiplied with their arm, which is how the force needed by the tail can be found. The tree contributions recognized are:

- W, the weight of the aircraft.
- L_w, the lift generated by the wing under critical flight conditions.
- L_h, the lift generated by the tail under critical flight conditions.

The arms under which these forces work are described as follows:

- x_W, the distance between the working arm of the aircraft weight and the CG, which are at the same location. It's value is therefor equal to zero.
- x_{L_w}, the horizontal distance between the AC of the wing and the CG.
- x_{L_h}, the horizontal distance between the AC of the horizontal stabilizer and the CG.

Next to the forces working on the aircraft, the fuselage contributes a pitching moment, M_{α_f}. It can be found using the dimensionless pitching moment coefficient $C_{m_{\alpha_f}}$ according to eq. (6.20).

$$M_{\alpha_f} = \frac{1}{2}\rho V_c^2 C_{m_{\alpha_f}} S \bar{c} \qquad (6.20)$$

The required horizontal stabilizer lift can be found by varying L_h and finding the value for which $|I_{yy}\ddot{\theta}| < |M|$ holds. When this value L_h is found, the two values for required C_{L_h} can be found using eq. (6.21)

$$C_{L_h} = \frac{2L_h}{\rho V_c^2 S_h} \qquad (6.21)$$

In order to find the elevator-to-tail chord ratio, the angle of attack effectiveness needs to be determined. This can be done using eq. (6.22).

$$\tau_e = \frac{\alpha_h + (C_{L_h}/C_{L_{\alpha h}})}{\delta_{E_{\max}}} \qquad (6.22)$$

If the angle of attack effectiveness is greater than 1, the tail size should be increased to decrease C_{L_h}. Then for the smaller C_{L_h}, the angle of attack effectiveness should be recalculated. Then, fig. 4.18 can be used to determine the required elevator-to-tail chord ratio. If the elevator-to-tail chord ratio is larger than 0.5, an all-moving tail, also called stabilator, should be selected. If not, the elevator can be sized using the resulting C_h/C_E.

Results

The inputs for the elevator design can be found in table 6.6. The output generated by the elevator design process is shown in table 6.7.

Table 6.6: Input values for elevator sizing

Parameter	Value	Unit	Source	Description
Horizontal stabilizer parameters				
X_{ac_h}	6.00	[m]	Section 6.1	Horizontal stabilizer AC
S_h/S	0.23	[−]	Section 6.1	Horizontal stabilizer-to-wing surface ratio
$(V_h/V)^2$	0.85	[−]	Section 6.1	Horizontal stabilizer-to-wing airspeed
λ_h	0.55	[−]	Section 6.1	Horizontal stabilizer taper ratio
A_h	3.00	[−]	Section 6.1	Horizontal stabilizer aspect ratio
$\Lambda_{0.25_h}$	9.00	[°]	Section 6.1	Horizontal stabilizer sweep at 25% chord
$C_{l_{\alpha_h}}$	6.70	[rad^{-1}]	Section 6.1	Horizontal stabilizer lift gradient
η_h	0.98	[−]	Section 6.1	Horizontal stabilizer efficiency
l_h	3.44	[m]	Section 6.1	Horizontal stabilizer arm
Wing parameters				
S	9.30	[m^2]	Section 4.1.3	Wing surface area
$\bar{c}$	1.12	[m]	Section 4.1.3	Wing MAC
$C_{L_{des}}$	0.31	[−]	Section 4.1.3	Wing design lift coefficient
A	7.77	[−]	Section 4.1.3	Wing aspect ratio
e	0.839	[−]	Section 4.1.3	Wing oswald factor
α_w	2.00	[°]	Section 4.1.3	Wing design angle of attack
$\Lambda_{0.25_w}$	-1.84	[°]	Section 4.1.3	Wing sweep at 25% chord
b	8.50	[m]	Section 4.1.3	Wing span
$C_{L_{\alpha_w}}$	4.47	[rad^{-1}]	Section 4.1.3	Wing lift gradient
Fuselage parameters				
$C_{m_{\alpha_f}}$	0.011	[−]	Section 6.1	Pitching moment coefficient due to fuselage
Misc.				
$d\epsilon/d\alpha$	0.671	[−]	Section 3.10	Downwash gradient
ρ	1.225	[kg/m^3]	[10]	Air density
V_c	80.00	[m/s]	[1]	Design velocity
x_{cg}	2.56	[m]	Section 6.1.3	Distance nose to CG
x_{ac}	2.41	[m]	Section 6.1.3	Distance nose to AC
x_{LEMAC}	2.14	[m]	Section 6.1.3	Distance nose to LEMAC
I_{yy}	1111	[kgm^2]	Section 5.1.2	Mass moment of inertia around Y-axis
θ_{max}	22.52	[°]	[1]	Maximum pitch angle for 12g
θ_{min}	-22.52	[°]	[1]	Minimum pitch angle for -12g
t_θ	0.25	[s]	Figure 4.18	Time to achieve pitch angle for ± 12g

Table 6.7: Output values for elevator sizing

Parameter	Value	Unit	Description
$C_{L_{h_{min}}}$	-0.567	[−]	Minimum horizontal stabilizer lift
$C_{L_{h_{max}}}$	0.786	[−]	Maximum horizontal stabilizer lift
τ_{max}	0.597	[−]	Maximum angle of attack effectiveness
C_E/C_h	0.40	[−]	Elevator-to-tail chord ratio

6.3.2 Rudder

The rudder needs to be designed such that it offers sufficient directional control in all flight conditions. This means that also for the rudder, the most critical flight condition at which rudder must be applied should be identified and analyzed in the problem analysis. The methods subsection will focus on the critical flight condition and will present the method for rudder sizing. The results will be presented in the subsection thereafter.

Problem Analysis

In general it can be stated that two flight situations are critical for the rudder design; cross wind landing and spin recovery. Sadraey [26] states that for aerobatics aircraft the spin recovery requirement is the critical

requirement (for an explanation on what a spin is and does see [26]). Therefore the rudder will be sized accordingly.

CS23 states rules for the spinning motion of aircraft as follows [4]:

The aircraft should be able to recover from the spin in not more than one additional turn or three seconds after the first control surface deflection applied for recovery.

An important assumption for the vertical tail regarding the spin motion is:

- Vertical stabilizer velocity $(V_h/V)^2 = 0.95$. *The squared velocity over the vertical stabilizer is $0.95 \cdot V_\infty^2$ (which is higher than normal conditions), due to the angles of sideslip and attack which cause less disturbances from the fuselage to the vertical stabilizer.*

Method

To find the required rudder chord, a steady state spin will be analyzed. The steady state spin means that the aircraft is in forces and moment equilibrium, to recover from the spin a moment around the yaw axis is needed. The moment required to recover from the spin can be stated as follows (from Sadraey [26]):

$$N_{SR} = \left(\frac{I_{xx_w} I_{zz_w} - I_{xz_w}{}^2}{I_{xx_w}} \right) {}_w \overset{\bullet}{R}_{SR} \tag{6.23}$$

The required yaw acceleration can be found by using a maximum typical spin rate of 240 $°/s$ [26] and the required spin recovery time of three seconds as stated in [4]. Hence a yaw acceleration of 80 $°/s^2$ (1.4 rad/s^2) for recovery. The moments of Inertia needed for eq. (6.23) are known for the body fixed axis system, however, during the spin motion it is required that they are used in the wind-axis system. The assumed angle of attack is a typical spin angle of 45 $°$ [26]. The transformation can be done using:

$$\begin{bmatrix} I_{xx_w} \\ I_{yy_w} \\ I_{xz_w} \end{bmatrix} = \begin{bmatrix} \cos^2\alpha & sin^2\alpha & -\sin 2\alpha \\ sin^2\alpha & \cos^2\alpha & \sin 2\alpha \\ \frac{1}{2}\sin 2\alpha & -\frac{1}{2}\sin 2\alpha & \cos 2\alpha \end{bmatrix} \begin{bmatrix} I_{xx_b} \\ I_{yy_b} \\ I_{xz_b} \end{bmatrix} \tag{6.24}$$

The standard procedure for spin recovery is PARE: Power idle, Ailerons neutral, Rudder full deflected in opposite direction, Elevator through neutral (when spinning rate is zero). This procedure affects the yaw moment in two ways: the propulsion to idle makes sure that the thrust produces a less negative moment and the rudder deflection generates a positive moment, see eq. (6.26).

The yawing moment required to recover and how this moment is composed of the pilots actions (power idle, rudder deflected) can be found in eq. (6.25) and eq. (6.26).

$$N_{SR} = \frac{1}{2}\rho V_s{}^2 SbC_n \tag{6.25} \qquad\qquad C_n = \beta \cdot C_{n_{\beta_p}} + C_{n_{\delta_r}} \cdot \delta_r \tag{6.26}$$

The used yaw moment derivative for sideslip from the propulsion $(C_{n_{\beta_p}})$ is already known from section 6.2. The rudder control derivative as used in eq. (6.26) is defined by:

$$C_{n_{\delta_r}} = -C_{L_{\alpha V}} \cdot \frac{l_v S_{v-eff}}{bS} \cdot \left(\frac{V_v}{V} \right)^2 \cdot \tau_r \cdot \frac{b_{r-eff}}{b_v} \tag{6.27}$$

The terms S_{v-eff} and b_{r-eff} stand for the effective surface area and span during the spinning motion. Because the stalled horizontal stabilizer causes a wake of 45 $°$, the surface area and span of the vertical stabilizer in the wake are assumed not to contribute to the rudder control derivative $C_{n_{\delta_r}}$. The effective surface and span have been found using CATIA drawings, see fig. 6.3 for an example.

All parameters are now known to solve eq. (6.27) for τ_r, then from fig. 4.18 in section 4.2 the required chord ratio can be extracted using the found τ_r, completing the rudder design.

Results

The input values for the calculations are given in table 6.8:

Table 6.8: Input values for rudder sizing

Parameter	Value	Unit	Source	Description
l_v	3.21	$[m]$	Section 6.2	Vertical tail arm (from cg to ac vert tail)
δ_r	30.00	$[°]$	Appendix C	Max deflection angle rudder
S_v	1.20	$[m^2]$	Section 6.2	Surface area rudder
S	9.30	$[m^2]$	Section 4.1	Surface area wing
b	8.50	$[m]$	Section 4.1	Wing span
$C_{n_{\beta_p}}$	-2.018(10^{-2})	$[rad^{-1}]$	Section 6.2	Aircraft yaw derivative wrt sideslip due to propulsion
$\dot{R}_{SR}$	80.00	$[°/s^2]$	[4]	Required yaw acceleration for spin recovery
ρ	1.225	$[kg/m^3]$	[10]	Air density at sea level
V_{spin}	31.38	$[m/s]$	[4]	Spin velocity
I_{xx_b}	807.50	$[kgm^2]$	Chapter 5	Aircraft MOI around x-axis
I_{zz_b}	1715.00	$[kgm^2]$	Chapter 5	Aircraft MOI around z-axis
I_{xz_b}	43.90	$[kgm^2]$	Chapter 5	Aircraft MOI around xz-axis
α_{spin}	45.00	$[°]$	[26]	Spin angle of attack
β_{spin}	20.00	$[°]$	[26]	Sideslip during spin
$S_{v_{eff_{spin}}}$	0.45	$[m^2]$	CATIA	Effective vertical tail area under spin
$b_{r_{eff_{spin}}}$	0.56	$[m]$	CATIA	Effective rudder span under spin

The calculations for the rudder requirements on spin recovery, using the inputs from table 6.8, showed that the vertical tail, as was designed in section 6.2, will not be able to ensure the required spin recovery, regardless of the chosen rudder-chord. Due to the selected relative locations of the horizontal and vertical stabilizer, the wake of the horizontal stabilizer during spin would affect the vertical stabilizer so much that spin recovery is not possible. It has become clear that the vertical stabilizer design needs to be revised in order to ensure that the FX-15 is able to recover from a spin. After an iterative process of resizing the vertical a suitable design has been found, the results for vertical tail planform and for rudder properties can be found in table 6.9 and visualized in fig. 6.3.
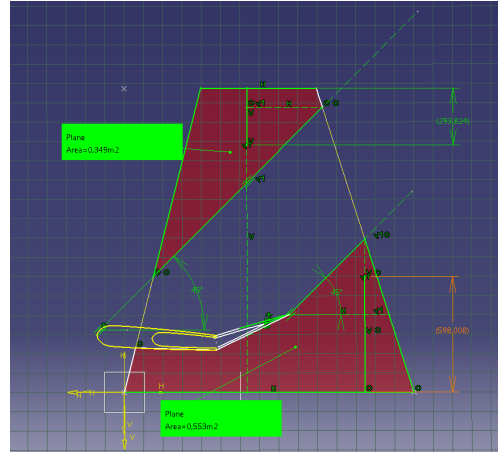
Figure 6.3: Vertical tail planform for spin

Fig. 6.3 shows the revised vertical stabilizer and rudder design including the wake by the horizontal stabilizer. The rudderchord is high and the top of the vertical tail is even made fully movable for maximum rudder effect (many reference aircraft use this as well [7, 49–51]. This effect translates into a bigger τ_r (the average is taken from the fully movable part and the normal rudder part using the span ratio between the two, the value for τ_r is extrapolated from fig. 4.18 since it lies out of range).

Table 6.9: Output values for rudder sizing and vertical tail redesign

Parameter	Value	Unit	Description
$C_{n_{SR}}$	0.03	$[-]$	Yawing moment coefficient for rudder spin recovery
τ_r	0.79	$[-]$	Angle of attack effectiveness parameter rudder
Redesigned vertical stabilizer and rudder geometry			
A_v	1.50	$[-]$	Aspect ratio (remained the same)
b_v	1.58	$[m]$	Vertical stabilizer span
S_v	1.65	$[m^2]$	Vertical stabilizer surface
$\Lambda_{0.5C}$	0.00	$[°]$	Vertical stabilizer half chord sweep angle
λ	0.40	$[-]$	Vertical stabilizer taper ratio
C_{r_v}	1.50	$[m]$	Vertical stabilizer root chord
$C_{n_{\beta_v}}$	0.13	$[-]$	Yaw derivative due to sideslip contribution vert. stab (normal condition)
$C_{n_{\beta_{tot}}}$	0.14	$[-]$	Aircraft yaw derivative (normal condition)
S_{eff_s}	0.90	$[m^2]$	Effective vertical stabilizer surface during spin
b_{eff_s}	0.89	$[m]$	Effective vertical stabilizer span during spin
δ_r	30.0	$[°]$	Maximum rudder deflection
C_{rudder}/C	0.60	$[-]$	Rudder hinge line

6.4 Control System

The control surfaces that have been designed above are controlled by the control system. The layout of the control system is shown in fig. 6.4. In this figure the aileron controls are indicated in yellow, the elevator controls (section 4.2) are shown in green and the rudder controls are shown in blue. The aileron and elevator controls consist of a system of push/pull rods whereas the rudder is controlled using two cables.

To control the ailerons the stick is translated in a sideways motion, which will rotate push/pull rod 1. This rotation will translate rod 2 sideways, which in turn will transfer the movement to rod 3. The forward/aft translation of rod 3 will deflect the aileron. A bypass is necessary in rod 1 due to the spar which is present at this location.

The elevator will be controlled by pushing/pulling the stick forward or aft. This will translate rod 4. The translation of rod 4 is transferred through a hinge to rod 5. This these push/pull rods are split up to guide the movement through the FX-15 and to increase the buckling strength of the rods. Rod 5 will be connected to the elevator with a hinge to deflect the control surface.

The pedals will be directly connected to the rudder through the cables displayed. These cables will be guided through the structure using pulleys.

The CS23 regulations do not require a failsafe system, therefore the control system will be designed using the safe life principles [4]. All comparable RBAR aircraft have a similar control system, so it is expected the system can be designed properly [40–43]. When it is necessary to reduce the required stick force, spades will be attached to the ailerons. For the rudder and elevator the same could be accomplished by the use of horns.
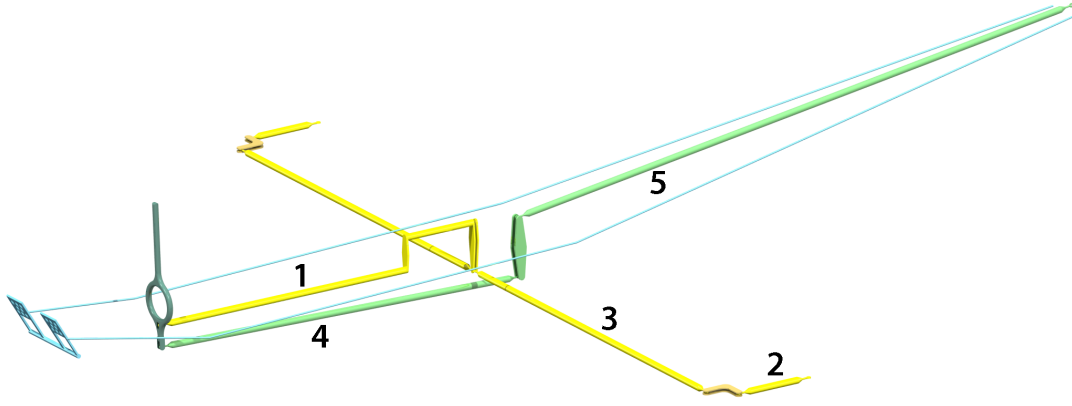
Figure 6.4: The control system used to control the ailerons and the elevator

6.5 Aircraft Flight Dynamics

The control surfaces and empennage have been designed for controllability and stability. A lack of control would translate in an underperforming aircraft during the race. A lack of stability, however, is unsafe and could potentially cause fatal accidents. Therefore the eigenmodes of the aircraft should be analyzed.

6.5.1 Problem Analysis

In this section, the Equations Of Motion (EOM) of a number of motions for the aircraft are analyzed. This is necessary for the eigenvalue computation, which is described in the next section.

Short Period

The short period eigenmode is the effect of a strong but short elevator step input on the aircraft. The reaction of the aircraft is a quick pitch up and down motion. The aircraft should be able to damp out the motion quickly. Some assumptions are made in order to find the eigenvalues of the motion;

1. The initial flight condition is level. *This means $\gamma_0 = 0$ and $C_{X_0} = 0$.*

2. The airspeed remains constant. *This means $\bar{u} = 0$.*

The EOM of the motion can be set up and simplified using the assumptions (for reference see section 4.4 from the lecture notes of the Flight Dynamics course [25]). The following set of equations needs to be solved:

$$
\begin{bmatrix} C_{Z_\alpha} + (C_{Z_{\dot\alpha}} - 2\mu_c)D_c & C_{Z_q} + 2\mu_c \\ C_{m_\alpha} + C_{m_{\dot\alpha}} - 2D_c & C_{m_q} - 2\mu_c K_Y^2 D_c \end{bmatrix} \begin{bmatrix} \alpha \\ \frac{q\bar{c}}{V} \end{bmatrix} = 0
\tag{6.28}
$$

The parameters for these EOM are explained in section 6.5.3.

Phugoid

The phugoid eigenmode is the effect of a small but long elevator step input on the aircraft. The reaction of the aircraft should be a periodical oscillating pitch up and pitch down motion. Some assumptions are made in order to find the eigenvalues of the motion:

1. The angle of attack remains constant. *This means $\alpha = 0$ and $\dot\alpha = 0$.*

2. The motion started from steady flight conditions. *This means $C_{X_0} = 0$.*

3. There is no acceleration around the y-axis. *This means $\dot\theta = 0$.*

Using the same method that has been used for the short period, the eigenvalues are determined. The EOM that these eigenvalues are based on are described in eq. (6.29) [25].

$$
\begin{bmatrix}
C_{X_u} - 2\mu_c D_c & C_{Z_0} & 0 \\
C_{Z_u} & 0 & 2\mu_c \\
0 & -D_c & 1
\end{bmatrix}
\begin{bmatrix}
\hat{u} \\
\theta \\
\frac{q\bar{c}}{V}
\end{bmatrix} = 0
\tag{6.29}
$$

Aperiodic Roll

The aperiodic roll motion is the roll motion due to an aileron input. The moment the aileron is released the roll motion should stop due to the resistance of the wings. Also for the aperiodic roll, it is assumed that there only is a rolling motion. This means that $\beta = 0$ and $r = 0$. The EOM used for the aperiodic roll are described in eq. (6.30) [25]:

$$
\left[C_{l_p} - 4\mu_b K_X^2 D_b \right] \left[\frac{pb}{2V} \right] = 0
\tag{6.30}
$$

Dutch Roll

The Dutch roll is a periodic motion in which the aircraft sideslips, yaws and rolls. The motion is initiated with an input on the rudder and should damp out after some time. Some assumptions are made in order to find the eigenvalues of the motion:

1. The rolling motion is negligible. *This means $\phi = 0$ and $p = 0$.*

2. $C_{Y_{\dot\beta}}$ and $C_{n_{\dot\beta}}$ are negligible.

3. $4\mu_b \gg C_{Y_r}$. *This means C_{Y_r} can be neglected.*

4. There is only yaw rotation. *This means that the airplane's CG moves along a straight line and the course trajectory χ is constant.*

The EOM used for the Dutch roll are described in eq. (6.31) [25].

$$
\begin{bmatrix}
C_{n_\beta} & C_{n_r} - 4\mu_b K_Z^2 D_b
\end{bmatrix}
\begin{bmatrix}
\beta \\
\frac{pb}{2V}
\end{bmatrix} = 0
\tag{6.31}
$$

Spiral

The spiral motion is the only unstable eigenmotion of the aircraft. The motion is initiated with an input on the aileron and the roll angle should keep increasing. Some assumptions will be made in order to find the eigenvalues of the motion:

1. Due to the slow nature of this motion, all linear and angular accelerations can be neglected. *This means that for all terms $D_b = 0$.*

2. C_{Y_r} and C_{Y_p} are negligible.

The EOM used for the Dutch roll are described in eq. (6.32) [25].

$$
\begin{bmatrix}
C_{Y_\beta} & C_L & 0 & -\mu_b \\
0 & -\frac{1}{2}D_b & 1 & 0 \\
C_{l_\beta} & 0 & C_{l_p} & C_{l_r} \\
C_{n_\beta} & 0 & C_{n_p} & C_{n_r}
\end{bmatrix}
\begin{bmatrix}
\beta \\
\phi \\
\frac{pb}{2V} \\
\frac{rb}{2V}
\end{bmatrix} = 0
\tag{6.32}
$$

6.5.2 Method

From the EOM described in the previous sections, the characteristic equation can be found by substituting D_c with λ_c. This can be done because it is assumed that the equation for any variable is $f(x) = Ae^{\lambda_c \frac{V}{c}t}$ and we know that $D_c m = \frac{\bar{c}}{V}\frac{d}{dt}$. This gives $D_c f(t) = \frac{\bar{c}}{V}\frac{d}{dt}(Ae^{\lambda_c \frac{V}{c}t}) = \lambda_c f(t)$. Substituting λ_c and setting the determinant equal to zero gives eq. (6.33).

$$\begin{vmatrix} C_{Z_\alpha} + (C_{Z_{\dot\alpha}} - 2\mu_c)\lambda_c & C_{Z_q} + 2\mu_c \\ C_{m_\alpha} + C_{m_{\dot\alpha}} - 2\lambda_c & C_{m_q} - 2\mu_c K_Y^2 \lambda_c \end{vmatrix} = 0 \tag{6.33}$$

The eigenvalues are calculated by determining the characteristic equation $(A \cdot \lambda_c^2 + B \cdot \lambda_c + C = 0)$ from the EOM. The values for A, B and C for each equation are shown in table 6.10.

Table 6.10: Input values for characteristic equation

	Short period	Phugoid	Aperiodic roll	Dutch roll	Spiral
A	$-2\mu_c K_Y^2(C_{z_{alpha}} - 2\mu_c)$	$-4\mu_c^2$	0	$-2\mu_b K_Z^2$	0
B	$C_{m_q}(C_{z_{\dot\alpha}} - 2\mu_c) - 2C_{z_\alpha}\mu_c K_Y^2 + 2(C_{z_q} + 2\mu_c)$	$2\mu_c C_{X_u}$	$-4\mu_b K_X^2$	$\frac{1}{2}C_{n_r}$	$-\frac{1}{2}C_{Y_\beta}C_{l_p}C_{n_r}$
C	$C_{z_\alpha}C_{m_q} - (C_{z_q} + 2\mu_c)(C_{m_\alpha} + C_{m_{\dot\alpha}})$	$C_{Z_0}C_{Z_u}$	C_{l_p}	$-C_{n_\beta}$	$C_L C_{l_r}C_{n_\beta}$

6.5.3 Results

The coefficients shown in table 6.10 are estimated following the method described in the Flight Dynamics reader [25]. All used parameters are obtained in non-dimensional coefficients. The results from these estimations are shown in table 6.11.

Table 6.11: Input values for eigenmode analysis

Parameter	Value	Unit	Source	Description
K_X^2	0.015	$[-]$	[25]	Non-dimensional radius of gyration about X-axis
K_Y^2	0.021	$[-]$	[25]	Non-dimensional radius of gyration about Y-axis
K_Z^2	0.032	$[-]$	[25]	Non-dimensional radius of gyration about Z-axis
μ_b	8.27	$[-]$	[25]	Relative density, assymetric
μ_c	62.90	$[-]$	[25]	Relative density, symmetric
C_{m_q}	-7.88	$[-]$	[25]	Moment derivative about Y-axis due to angular velocity about the Y-axis
$C_{m_{alpha}}$	-0.22	$[-]$	[25]	Moment derivative about Y-axis due to angle of attack
$C_{m_{\dot\alpha}}$	-4.83	$[-]$	[25]	Moment derivative about Y-axis due to change in angle of attack
C_{X_u}	-0.05	$[-]$	[25]	Force derivative about X-axis due to velocity along the X-axis
C_{Z_α}	-4.48	$[-]$	[25]	Force derivative about Z-axis due to angle of attack
$C_{Z_{\dot\alpha}}$	-1.57	$[-]$	[25]	Force derivative about Z-axis due to change in angle of attack
C_{Z_0}	-0.02	$[-]$	[25]	Dimensionless force about Z-axis in steady flight
C_{Z_u}	-0.60	$[-]$	[25]	Force derivative about Z-axis due to velocity along the X-axis
C_{Z_q}	-3.69	$[-]$	[25]	Force derivative about Z-axis due to angular velocity about the Y-axis
$C_{L_{des}}$	0.31	$[-]$	[25]	Design Lift coefficient
C_{l_p}	-0.35	$[-]$	[25]	Moment derivative about X-axis due to angular velocity about the X-axis
C_{l_r}	0.10	$[-]$	[25]	Moment derivative about X-axis due to angular velocity about the Z-axis
C_{n_β}	0.12	$[-]$	[25]	Moment derivative about Z-axis due to sideslip angle
C_{n_r}	-0.08	$[-]$	[25]	Moment derivative about Z-axis due to angular velocity about the Z-axis
C_{Y_β}	-0.63	$[-]$	[25]	Force derivative about Y-axis due to sideslip angle

Table 6.12: Output values for eigenvalues

Motion	Eigenvalue(s)
Short period	$-1.872 \pm 1.251i$
Phugoid	$-2.146(10^{-4}) \pm 8.439(10^{-4})i$
Aperiodic roll	-0.705
Dutch roll	$-0.0576 \pm 0.5850i$
Spiral	0.4082

6.6   Verification & Validation

For verification and validation of the empennage design two methods have been used. To verify that the calculations have been performed correctly, the found values will be compared to found values from digital simulations and to reference aircraft. No large deviations should be found, if they do, the methods will be revised. The validation will be done by comparing with reference aircraft. A possible risk is that the design of the horizontal and vertical stabilizer is designed for non-critical situations. If this is the case, this will be found during validation.

Verification

Verification of the calculations regarding longitudinal stability and control have been done using available coefficients of other aircraft. The calculated C_{m_α} has been compared to many reference aircraft C_{m_α}'s of reference aircraft it turned out that the calculated C_{m_α} was within the expected range.

For lateral coefficients DATCOM has been used for verification. DATCOM provides the possibility to calculate the moment coefficients of individual components to some extent, therefore individual contributions can be verified. Table 6.13 presents the coefficients as calculated and also as simulated by DATCOM.

Table 6.13: Verification tail

	DATCOM	Calculations	Difference
$C_{n_{\beta_{wingfus}}}$	-0.073	-0.051	43%
$C_{n_{\beta_{tot}}}$	0.1438	0.120	19.8%

The differences between the estimates of the coefficients are significant. When looking at the wing fuselage yaw derivative one might notice that the difference between the two is very close to the wing-fuselage interaction. Possibly the explanation for the difference is that DATCOM does not account for wing fuselage interaction the same way as Torenbeek does (or does not account wing fuselage interaction at all).

An important conclusion is that both results show a lateral and longitudinal stable aircraft. For both methods the calculated surface areas of the vertical and horizontal stabilizers are sufficient.

Validation

In case the reference aircraft use completely different values for their stabilizer designs, it is possible that something is off. In that case the stabilizers would possibly be designed following the wrong requirements or using a wrong method. Table 6.14 shows the stabilizer parameters of some of the reference aircraft compared to the FX-15 stabilizers (reference aircraft data from chapter C). In case important parameters deviate significantly, the method for designing the stabilizer should be revised. The surfaces of the horizontal stabilizer are clearly shown to be in line with the reference aircraft. The most deviating value is the tail volume, $S_h l_h / S\bar{c}$, which is 7% higher than the second highest value of the Extra 300L. This is not a strange number, as the aircraft is designed to have a higher controllability than its competition.

For the validation of the vertical stabilizer, the most important deviation to notice is the vertical stabilizer surface. The FX-15 surface is bigger than any other vertical stabilizer. The main reason for this is known: spin recovery. Another reason is that the vertical stabilizers of the reference aircraft have more overflow onto the fuselage than the FX-15 (the fuselage of the FX-15 is kept as small as possible for drag reduction), their actual effective vertical stabilizer surfaces (including the overflow in the fuselage) would be close to the surface area of the FX-15.

Table 6.14: Reference aircraft tail data compared to the FX-15

	MXS-R	Corvus Racer 540	Extra 300L	Zivko Edge 540	FX-15	Unit
S_h	1.830	2.060	2.560	2.040	2.120	$[m^2]$
$S_h l_h / S\bar{c}$	0.452	0.601	0.637	0.462	0.684	$[-]$
S_h / S	0.193	0.231	0.239	0.207	0.228	$[-]$
S_v	1.210	1.300	1.390	1.300	1.656	$[m^2]$
$S_v l_v / Sb$	0.061	0.069	0.057	0.060	0.067	$[-]$
S_v / S	0.130	0.150	0.130	0.130	0.180	$[-]$

6.7 Conclusion & Discussion

Looking at the design of the complete empennage it might be concluded that w.r.t. the reference aircraft the design has become pretty straightforward. Only the vertical tail design turned out to be a slight setback for the FX-15 design, it turned out bigger than expected and desired in order to be able to recover from a spin. This is the unexpected price to be paid for having the mid-engine configuration. For future design the tail could be improved by implementing some improvements:

- Improved coefficient estimates: Many of the estimated aerodynamic coefficients are estimates. Flight tests for example would improve the accuracy decreasing the margins kept when optimizing the design.

- Become an experimental aircraft: Not having to comply with CS23 [4] would abolish the need for spin recovery. After all, the FX-15 is made for RBAR flying, all operations are at low altitudes meaning that spin recovery within 3 seconds would not be sufficient to prevent a crash. Therefore designing the aircraft for stable spin might be unnecessary.

7 Landing Gear Detail Design

This chapter discusses the landing gear design. First, the location of the landing gear is determined in section 7.1. The single and double landing gear concepts from the midterm are compared in section 7.2. Section 7.3 presents the curvature optimization of the selected design and 7.4 present the dimensional optimization. Hereafter the aerodynamic optimization is discussed in section 7.5. Next the equipment and final lay-out are discussed in sections 7.6 and 7.7. Finally the conclusion and discussion are presented in section 7.8.

7.1 Landing Gear Location

The first step in the design of the landing gear is to determine the location of the landing gear. The position was determined using the book of Raymer [9]. The requirements for the location of the landing gear are visualised in fig. 7.1. Note that the requirements apply to a taildragger configuration, as selected in the midterm report [2].

"The c.g. (most forward and most aft) should fall between 16-25 deg back from vertical measured from the main wheel location. If the c.g. is too far forward the aircraft will tend to nose over, and if it is too far back it will tend to groundloop" [9]. This is the first requirement set by Raymer. To determine the location eqs. (7.1) and (7.2) were established.

$$x_{LG,aft} = x_{CG,for} - h_{LG} \tan(\alpha_1) \qquad (7.1) \qquad\qquad x_{LG,for} = x_{CG,aft} - h_{LG} \tan(\alpha_2) \qquad (7.2)$$
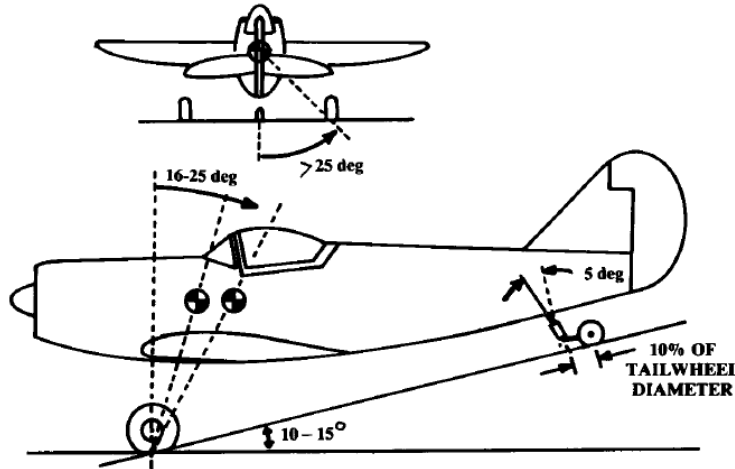
Figure 7.1: Visualised requirements for the location of the landing gear [9]

In these equations α_1 is the angle between the vertical and the most forward CG and has a value of $16°$, α_2 is the angle between the vertical and the most aft CG and has a value of $25°$. $x_{CG,aft}$ is the most aft location of the CG with respect to the nose which is 2.78 m, $x_{CG,for}$ is the most forward location of the CG with respect to the nose which is 2.55 m, $x_{LG,for}$ is the most forward location of the landing gear, $x_{LG,aft}$ is the most aft location of the landing gear, and h_{LG} is the height from the CG to the ground. Note that the CG locations might change during the design process due to iterations. For the location of the landing gear, no iterations will be conducted.

The landing gear will be located such that it complies with both angle requirements at the same time. This means that $x_{LG,aft} = x_{LG,for}$. Now eqs. (7.1) and (7.2) can be combined to obtain:

$$h_{LG} = \frac{x_{CG,aft} - x_{CG,for}}{\tan(\alpha_2) - \tan(\alpha_1)} \qquad (7.3)$$

Using this equation, h_{LG} was determined to be 1.28 m. Using eq. (7.1) or eq. (7.2), x_{LG} was determined to be 2.18 m.

The propeller needs enough clearance with the ground when the aircraft is standing on its landing gear at a leveled attitude as seen in fig. 7.1. The clearance of the tip of the propeller with the ground for the chosen position is 0.27 m. This is more than sufficient.

The second requirement from Raymer is as follows: "*To prevent the aircraft from overturning the main wheels should be laterally separated beyond a 25 deg angle off the c.g., as measured from the rear in a tail-down attitude*" [9]. Using trigonometry the lateral separation distance $x_{LG,lsd}$ between the two wheels was determined to be 1.20 m. The lateral distance between the CG and one wheel is 0.60 m, and will be called x_l. From CATIA, the vertical length of the landing gear y_l was determined to be 0.80 m.

The third and last requirement from Raymer is as follows: "*The tail-down angle should be about 10-15 deg with the gear in the static position*" [9]. From CATIA this angle proved to be 13° for the FX-15.

Tab. 7.1 and table 7.2 show the input and output values for the positioning of the landing gear.

Table 7.1: Input values for the position of the landing gear

Parameter	Value	Unit	Source	Description
$x_{CG,aft}$	2.78	[m]	CATIA	Most aft CG location
$x_{CG,for}$	2.55	[m]	CATIA	Most forward CG location

Table 7.2: Output values for the position of the landing gear

Parameter	Value	Unit	Description
h_{LG}	1.28	[m]	Distance from CG to ground
x_{LG}	2.18	[m]	Location of landing gear
c_{prop}	0.27	[m]	Propellor clearance at leveled attitude
x_l	0.60	[m]	Lateral length of the landing gear
y_l	0.80	[m]	Vertical length of the landing gear

7.2 Single Landing Gear vs. Double Landing Gear

In this section a trade-off is made between the single and double landing gear concepts. First the trade-off method will be discussed, followed by the mass and drag determination. In addition, the RAMS characteristics of both concepts are explained. This section concludes with the trade-off and the selection of one of the landing gear concepts.

7.2.1 Method

This section describes the method used to compare the single and double landing gear. The trade-off method is given, after which the method to compute mass is presented. Finally, the method to compute drag is discussed.

Trade-off Method

In order to compare both concepts, the same curvature was used as a baseline. The curvatures of the landing gears of reference aircraft are approximately a quarter circle. Therefore, a quarter circle with a radius of 0.80 m was used for a comparison between a single and a double landing gear. A quantitative trade-off will be performed based on mass and drag since they influence the race time [2]. Furthermore, a qualitative trade-off will be performed based on RAMS.

Mass

This section will describe the method used to find the minimum mass for the single and double landing gear concepts.

The applied load on the landing gear is given by eq. (7.4), where n_{LG} is the load factor at landing for which the landing gear should be designed [38], M_{ff} is the fuel fraction for the mission profile, and n is the number of struts for the two concepts.

$$F = \frac{MTOW \cdot n_{LG} \cdot M_{ff} \cdot 9.81}{n} \tag{7.4}$$

The struts are discretized using angle $\Delta\theta$ as shown in figs. 7.2 and 7.3. The force on each element is composed of a normal and a shear force, eqs. (7.5) and (7.6) respectively. The moment on each element is given by eq. (7.7).

$$F_{ax_i} = F(\theta_i) \tag{7.5}$$

$$F_{per_i} = F\sin(\theta_i) \tag{7.6}$$

$$M_i = FR(1 - \cos(\theta_i)) \tag{7.7}$$

The geometric properties of each element are constant. The length and MOI are given by eqs. (7.8) and (7.9), and the cross-sectional area of each element is calculated. The radius of the curvature R, equals the height of the landing gear.
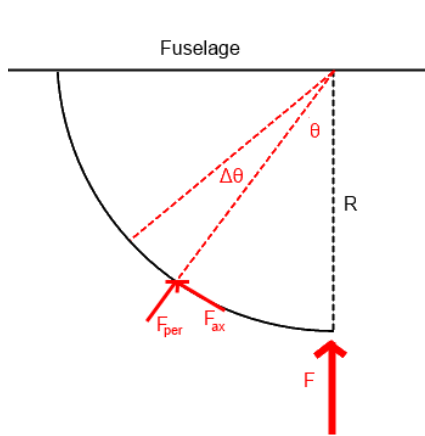
Figure 7.2: Schematic image of the side view of the FX-15 with a single landing gear
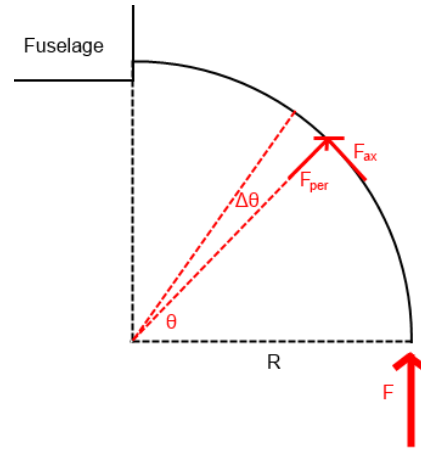
Figure 7.3: Schematic image of the front view of the FX-15 with a double landing gear

$$l_i = R \cdot \Delta\theta \tag{7.8}$$

$$I_i = \frac{1}{4}\pi r_i^4 \tag{7.9}$$

For each cross-section the maximum Von Mises stress is calculated using eq. (7.10). The Von Mises stress consists of the bending stress, normal stress, and the shear stress, eq. (7.12), eq. (7.13), and eq. (7.14) respectively. The maximum bending stress occurs at the maximum distance from the neutral line, in case of a circular cross-section the maximum distance is equal to the radius. The local radius r_i is increased until the maximum Von Mises stress in the cross-section is equal to or lower than the yield stress of the material.

$$\sigma_{y_i} = \sqrt{\sigma_{x_i}^2 + 3\tau_i^2} \tag{7.10}$$

$$\sigma_{x_i} = \sigma_{x_{bending_i}} + \sigma_{x_{axial_i}} \tag{7.11}$$

$$\sigma_{x_{bending_i}} = \frac{M_i(r_i)}{I_i} \qquad (7.12) \qquad \sigma_{x_{axial_i}} = \frac{F_{ax_i}}{A_i} \qquad (7.13) \qquad \tau_i = \frac{F_{per_i}}{A_i} \qquad (7.14)$$

The minimum mass of one strut is given by eq. (7.15), where n is the number of elements in the discretization. Aluminum 2024-O is used as material, which has a density ρ of 2770 kg/m^3.

$$m = \sum_{i=1}^{n} m_i = \sum_{i=1}^{n} (A_i \cdot l_i \cdot \rho) \qquad (7.15)$$

Drag

In the midterm report, the influence of drag on the race time was analyzed. This resulted in a time increase of 2.02 s for one count increment of C_{D_0} [2]. The drag of a landing gear is purely parasitic, so it should be minimized. Both concepts were compared on drag using XFLOW [52]. The C_D values are calculated using the wing as reference area. The C_D values obtained from the CFD analysis are large in comparison to realistic values, due to the circular cross-section which has a large frontal area. The quantitative trade-off is based on time loss due to drag and weight. To make an unbiased trade-off both the drag and weight should have a realistic value, in accordance with the contribution that they would have on the aircraft drag and weight. For this reason the drag coefficient is scaled to a realistic value according to the refined drag estimation in section 3.11.

7.2.2 Results

The results that were obtained by following the methods discussed in section 7.2.1 are presented in this section.

Mass

Table 7.3 and table 7.4 show the input and output values for the mass calculation of both landing gear concepts.

Table 7.3: Input values for mass calculation for comparison of landing gear concepts

Parameter	Value	Unit	Source	Description
$MTOW$	849.6	$[kg]$	Section 3.9	Maximum take-off weight
n_{LG}	3	$[-]$	[38]	Load factor at landing
M_{ff}	0.933	$[-]$	Section 3.2	Total fuel fraction
ρ	2770	$[kg/m^3]$	[53]	Density of Aluminum 2024-O
σ_y	$96(10^6)$	$[Pa]$	[53]	Yield stress of Aluminum 2024-O
R	0.80	$[m]$	Section 7.1	Height of the struts
n_{single}	1	$[-]$		Number of struts for single landing gear
n_{double}	2	$[-]$		Number of struts for double landing gear

Table 7.4: Output values for mass calculation for comparison of landing gear concepts

Parameter	Value	Unit	Description
m_{single}	28.98	$[kg]$	Mass of single landing gear
m_{double}	23.55	$[kg]$	Mass of double landing gear
$r_{begin,single}$	$12(10^{-3})$	$[m]$	Radius at location of applied load
$r_{end,single}$	$55(10^{-3})$	$[m]$	Radius at fuselage
$r_{begin,double}$	$6(10^{-3})$	$[m]$	Radius at location of applied load of one strut
$r_{end,double}$	$43(10^{-3})$	$[m]$	Radius at fuselage of one strut

Drag

The input values used for the CFD analysis in XFLOW are given in table 7.5. The results are presentend in table 7.6.

Table 7.5: Input values for the drag determination of both landing gear concepts

Parameter	Value	Unit	Source	Description
r	$0.05(10^{-3})$	$[m]$		Resolution of the used mesh during the CFD
S	9.30	$[m^2]$	Section 4.1.3	Wing surface area
V	80.00	$[m/s]$	[1]	Average speed during the race
μ	$1.79(10^{-5})$	$[Pa\ s]$	[10]	Dynamic viscosity at sea level
ρ	1.225	$[kg/m^3]$	[10]	Fluid density at sea level
T	288.15	$[K]$	[10]	Temperature at sea level

Table 7.6: Output values for the drag determination of both landing gear concepts

Parameter	Single landing gear	Double landing gear
C_D	$9.1(10^{-3})$	$9.6(10^{-3})$
Scaled C_D	$2.6(10^{-3})$	$2.7(10^{-3})$

RAMS

A comparison of the RAMS characteristics of the single and double landing gear are presented below.

1. **Reliability.** A single landing gear is less reliable than a double landing gear because a single landing gear is unstable by nature. The aircraft will tip over once the aircraft has landed. Unless measures are taken to protect the wings at tip over, damage will occur. The measures that have to be taken add weight and drag to the aircraft. A double landing gear will not encounter these problems, as it is naturally stable. Therefore, on reliability, the single landing gear performs less than the double landing gear.

2. **Availability & Maintainability.** The layers of protection would need intensive inspection to make sure the wings do not get damaged. This would mean more maintenance time and costs. If protection wears off, replacement would have to occur. This would mean more down time, less availability, and higher cost. The double landing gear has its standard maintenance, but does not have to worry about protection layers or replacement of them. Therefore, the inspection hours will be less, as well as maintenance hours and costs. Thus it can be concluded that the single landing gear also performs less on availability and maintenance. It has to be noted that if the protection layers are designed well, they would not need frequent replacement, thereby making the availability and maintainability not much worse for the single landing gear than for the double landing gear.

3. **Safety.** The safety of a single landing gear with respect to the double landing gear is not much worse. The best pilots will be flying the aircraft and will be able to safely land the aircraft, also with only one landing gear. In flight the single landing gear might act as a vertical stabilizer, causing problems. However, when designing a single landing gear, one could optimize the design such that this problem does not occur, or the effect is minimized. In conclusion, the single landing gear can be considered just as safe as the double landing gear.

Furthermore, the single landing gear is unconventional for this type of aircraft. That would mean that designing it would take more time and cost more. Furthermore, it would be more difficult to comply with all regulations. Therefore increasing the complexity in the design process.

Final Comparison

The results obtained in the comparison between the single and the double landing gear are presented in this section. The input values used for the analysis are given in table 7.7. Using the analysis from the midterm report, a relation can be made between between the mass and drag expressed in race time [2].

Table 7.7: Mass and drag coefficient for both landing gear concepts

Parameter	Value	Unit	Source	Description
C_{D_1}	$2.6(10^{-3})$	$[-]$	Section 7.2.1	Scaled drag coefficient for single landing gear
C_{D_2}	$2.7(10^{-3})$	$[-]$	Section 7.2.1	Scaled drag coefficient for double landing gear
m_1	28.98	$[kg]$	Section 7.2.1	Mass for the single landing gear
m_2	23.55	$[kg]$	Section 7.2.1	Mass for the double landing gear

The first part of table 7.8 contains the time loss due to drag and mass for the single and double landing gear, according to the analysis presented in this section. The second part of table 7.8 contains the qualitative trade-off. As criteria reliability, availability, maintainability, and safety are used. The qualitative values that can be given are catastrophic, bad, normal, good, and excellent. The double landing gear scores normal on all criteria because it is used as the baseline. The single landing gear scores bad on all criteria except safety, on this it scores normal. The reasoning behind this trade-off can be found in section 7.2.2.

Table 7.8: Trade-off table between sinlge and double landing gear

Parameter	Single landing gear	Double landing gear
Time loss due drag [s]	5.2	5.5
Time loss due mass [s]	2.9	2.4
Total time loss [s]	8.1	7.8
Reliability	Bad	Normal
Availability	Bad	Normal
Maintainability	Bad	Normal
Safety	Normal	Normal

It can be concluded from the results that a single landing gear is not preferable over a double landing gear. In terms of drag the single landing gear performs better, but in terms of weight it performs worse. In terms of total time, the double landing gear performs better than the single landing gear. The qualitative analysis also proves that the double landing gear performs better. It has to be concluded that, in contrast with the conclusion in the midterm report [2], a double landing gear is preferable over a single landing gear. Therefore, a double landing gear will be designed in detail for the FX-15.

7.3 Curvature Optimization

This section guides the reader through the curvature optimization of the double landing gear concept. The curvature optimization is performed using a structural and drag optimization.

7.3.1 Problem Analysis

The curvature optimization consists of multiple elements. First the structure of different curvatures will be optimized to withstand the loads, making a comparison on weight for different curvatures. Next, the curvatures will be compared on drag using CFD simulations. Finally, the optimal combination between drag and weight will be determined by comparing the curvatures on time loss on the race track. The result will be an optimal curvature, that is fastest around the track.

7.3.2 Method

This section describes the method that was used to perform the curvature optimization of the landing gear. It contains the methods for the structural and drag optimization, and concludes with the method used to find the optimum.

Structural

This section will describe the method used to find the optimal structure for different curvatures of the landing gear. First the general outline of the MATLAB code used will be explained, after which the equations that are used will be explained.

The general outline of the MATLAB code is given in fig. 7.4. The objective of the MATLAB code is to find the cross-sectional dimensions for different curvatures of the landing gear, such that it will not yield. Furthermore it should also provide the masses of the different landing gears. Note that the code only analyzes one strut of the landing gear, since the landing gear is symmetrical.

The equation that is used to optimize the structure can be found in eq. (7.16), where m is the power which will be varied to obtain different curvatures. This equation makes sure the function covers the correct lateral and vertical length of the landing gear, x_l and y_l respectively, as determined in section 7.1.

$$y = y_l - \frac{x^m}{x_l^m} y_l \tag{7.16}$$
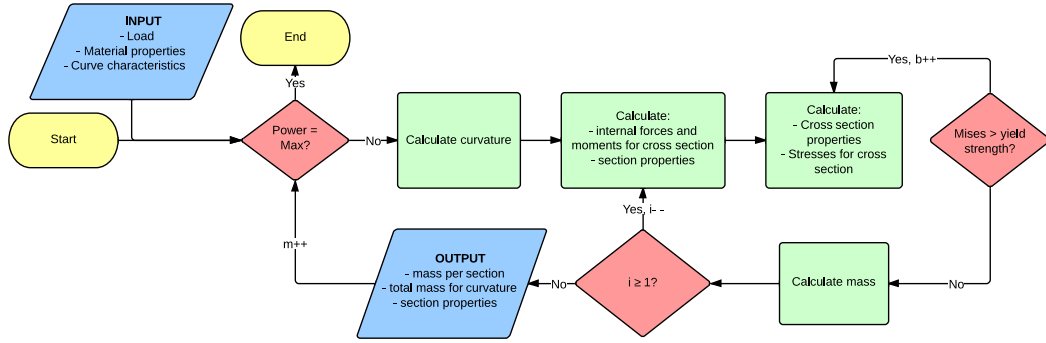
Figure 7.4: Flowchart describing the structural optimization for different curvatures

The load on one strut of the landing gear is determined using eq. (7.4). The landing gear is discretized into i sections, for each of which the angle θ_i, the length l_i, the normal and shear force F_{ax_i} and F_{per_i}, and the moment M_i (eq. (7.17)) are calculated.

$$M_i = M_{i+1} + F_{per_i} \cdot l_i \tag{7.17}$$

With the forces and moments known, the stresses can be determined. First, the cross-sectional properties are determined. The height h_i is determined using the width of the cross-section and the ratio $b_i/h_i = 5$. This ratio is chosen because most airfoils have approximately this ratio. Since in the end an airfoil will be fitted around the structure, this ratio is a good preliminary estimate to use. The width will be iterated until the cross-section is able to withstand the loads. The MOI I_i (eq. (7.18)) and area A_i of each cross-section (eq. (7.19)) are calculated.

$$I_i = \frac{b_i h_i^3}{12} \tag{7.18} \qquad\qquad A_i = b_i \cdot h_i \tag{7.19}$$

The stresses are determined using eqs. (7.11), (7.13), (7.14) and (7.20), after which the Von Mises stress is calculated using eq. (7.10).

$$\sigma_{x_{bending,i}} = \frac{M_i y_i}{I_i} = \frac{M_i \frac{h_i}{2}}{I_i} \tag{7.20}$$

The total mass is calculated using eq. (7.15). Once this is all done for one curvature the power m will be increased by 0.5 until m reaches 15. After the calculations for $m = 15$ the code stops.

Drag

The influence of drag on the curvature is also investigated. For six curvatures CATIA models are made, based on the dimensions as obtained from structural sizing, section 7.3.2. These models are compared on the drag coefficient using XFLOW [52].

Optimum

In the midterm report an increment in the mass and drag coefficient were related to losses in race time (eqs. (7.21) and (7.22)). Using the results from the structural and drag optimization in section 7.3.2, a relation between time loss, with respect to a baseline of $m = 1$, and the power m can be determined. The power with the lowest time loss will provide the optimal curvature for the landing gear.

$$t_{loss_{mass}} = 0.1m \qquad (7.21) \qquad\qquad t_{loss_{drag}} = 1000 \cdot 2.02 C_D \qquad (7.22)$$

7.3.3   Results

The results that were obtained by following the methods discussed in section 7.3.2 are presented in this section.

Structural

The input values for the analysis are given in table 7.9. The total mass of a landing gear curvature in relation with the power is visualised in fig. 7.5. It can be seen that the mass decreases with increasing power. However, this does not imply that a larger power is optimal, because the drag could increase with increasing power. Six curvatures will be investigated on drag. These are the curvatures with powers $m = 1$, $m = 2$, $m = 3$, $m = 6$, $m = 10$, and $m = 15$. Their masses are given in table 7.10, as well as the widths of four cross-sections. The six curvatures are visualised in fig. 7.6. The mass in table 7.10 is given for a single strut of the landing gear.

Table 7.9: Input values for structural curvature optimization

Parameter	Value	Unit	Source	Description
$MTOW$	849.6	$[kg]$	Section 3.9	Maximum take-off weight
n_{LG}	3	$[-]$	[38]	Load factor for landing gear
M_{ff}	0.933	$[-]$	Section 3.2.2	Total fuel fraction
n_{double}	2	$[-]$	Section 7.2.2	Number of struts for double landing gear
ρ_{Al-O}	2770	$[kg/m^3]$	[53]	Density of Aluminum 2024-O
x_l	0.60	$[m]$	Section 7.1	Lateral length of the landing gear
y_l	0.80	$[m]$	Section 7.1	Vertical length of the landing gear
$\sigma_{yield,Al-O}$	$96(10^6)$	$[Pa]$	[54]	Yield stress of Aluminum 2024-O

Table 7.10: Output values for structural curvature optimization

Power	Mass	b at $x = 0$	b at $x = 0.198$	b at $x = 0.397$	b at $x = 0.597$
m	$[kg]$	$[m]$	$[m]$	$[m]$	$[m]$
1	16.69	$223.7(10^{-3})$	$195.7(10^{-3})$	$155.9(10^{-3})$	$32.5(10^{-3})$
2	14.99	$222.9(10^{-3})$	$195.6(10^{-3})$	$156.0(10^{-3})$	$31.7(10^{-3})$
3	14.40	$222.9(10^{-3})$	$195.3(10^{-3})$	$156.0(10^{-3})$	$31.4(10^{-3})$
6	13.53	$222.9(10^{-3})$	$194.9(10^{-3})$	$155.8(10^{-3})$	$31.3(10^{-3})$
10	12.91	$222.9(10^{-3})$	$194.9(10^{-3})$	$155.3(10^{-3})$	$31.2(10^{-3})$
15	12.45	$222.9(10^{-3})$	$194.9(10^{-3})$	$155.0(10^{-3})$	$31.2(10^{-3})$
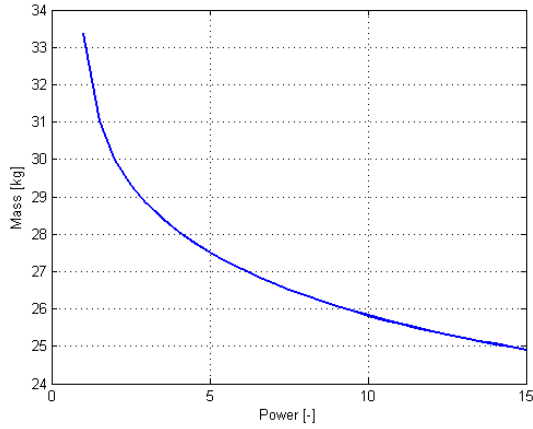
Figure 7.5: Mass of the landing gears with respect to power
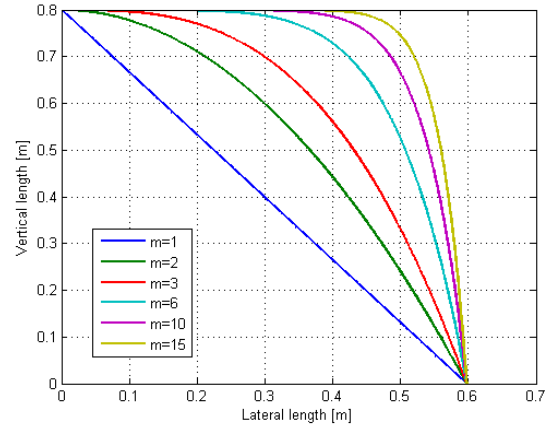
Figure 7.6: Different strut curvatures

Drag

Table 7.11 shows the input values used for the CFD simulation. Table 7.12 gives the results. Fig. 7.7 shows the C_D values as a function of the power of the curvature. A cubic spline is applied to get a continuous function. It can be seen that there is an optimum around a curvature with a power of 4.

Table 7.11: Input values for CFD for the comparison of different curves

Parameter	Value	Unit	Source	Description
S	9.30	$[m^2]$	Section 4.1	Wing surface
V	80.00	$[m/s]$	[1]	Average velocity during the race
μ	$1.79(10^{-5})$	$[Pa\ s]$	[10]	Dynamic viscosity of air at sea level
ρ	1.225	$[kg/m^3]$	[10]	Fluid density of air at sea level
T	288.15	$[K]$	[10]	Temperature at sea level
r	$0.05(10^{-3})$	$[m]$		Resolution of the used mesh during the CFD
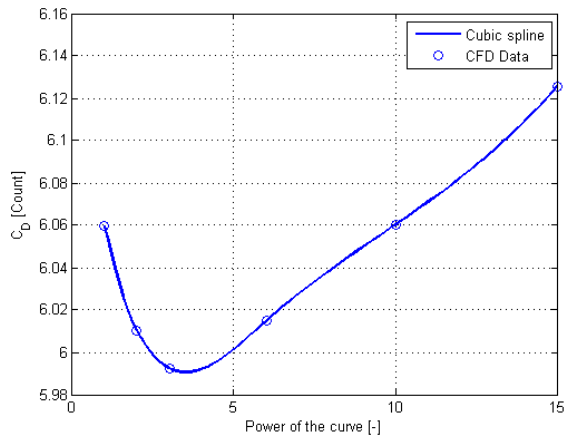
Figure 7.7: Drag vs. power of the curvature

Table 7.12: Output values for CFD simulation for the comparison of different curves

Power	C_D [-]
1	$6.06(10^{-3})$
2	$6.01(10^{-3})$
3	$5.99(10^{-3})$
6	$6.02(10^{-3})$
10	$6.06(10^{-3})$
15	$6.13(10^{-3})$

Optimum

Table 7.13 summarizes the results and relates them to the loss in race time. The time loss with respect to the curvature with power 1 is also given to make a better comparison. Fig. 7.8 shows the loss in race time versus the power with respect to the curvature with a power of 1. A cubic spline is used to interpolate the data. From this figure it can be concluded that a curvature with power of 4 has the lowest drag. However, the optimum curvature has a power of 9.96 as indicated in fig. 7.8.

Table 7.13: Effect of the power of the curvature on the race time

		Drag		Mass			Total	
P. $[-]$	C_D $[-]$	Time $[s]$	w.r.t. P. 1 $[s]$	Mass $[kg]$	Time $[s]$	w.r.t. P. 1 $[s]$	Time $[s]$	w.r.t. P. 1 $[s]$
1	$6.06(10^{-3})$	12.24	0.00	33.38	3.34	0.00	15.58	0.00
2	$6.01(10^{-3})$	12.14	-0.10	29.97	3.00	-0.34	15.14	-0.44
3	$5.99(10^{-3})$	12.11	-0.14	28.81	2.88	-0.46	14.99	-0.59
6	$6.02(10^{-3})$	12.15	-0.09	27.06	2.71	-0.63	14.86	-0.72
10	$6.06(10^{-3})$	12.24	0.00	25.82	2.58	-0.76	14.83	-0.76
15	$6.13(10^{-3})$	12.38	0.13	24.91	2.49	-0.85	14.87	-0.72
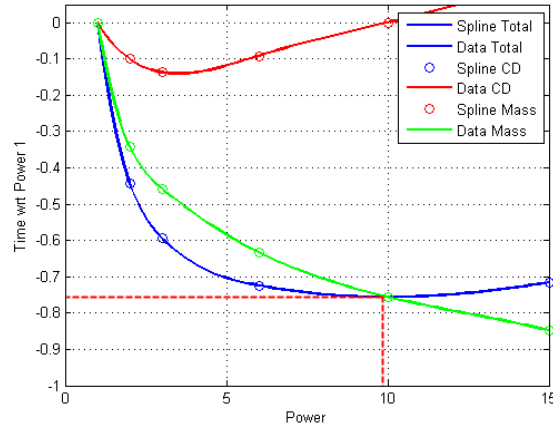
Figure 7.8: Change in race time with respect to power as function of the curvature of the landing gear

7.4 Dimensional Optimization

This section describes the process followed to conduct the dimensional optimization. The dimensional optimization is performed by conducting a structural optimization, followed by a drag optimization, and concludes by combining the structural and drag optimization to find the optimum between the two with respect to time loss.

7.4.1 Method

This section describes the method used to conduct the dimensional optimization. First the structural optimization method will be discussed, after which the drag optimization method is presented, concluded by the method that was used to find the optimum.

Structural

This section will describe the method used to find the optimal structure for different dimensions of the landing gear. Increasing the dimensions of the solid strut may reduce the weight because a hollow structure can be used.

Fig. 7.9 shows the flowchart of the MATLAB program used to determine the mass as a function of the dimension. The dimensions of the solid strut are multiplied with different scaling factors to get the outer dimensions of each cross-section.

The next step is the discretization of the strut and the calculation of the normal and shear forces and moments in each element according to the same method as explained in section 7.3.2. At this point in the flow the outer dimensions, forces, and moments for each cross-section are determined.
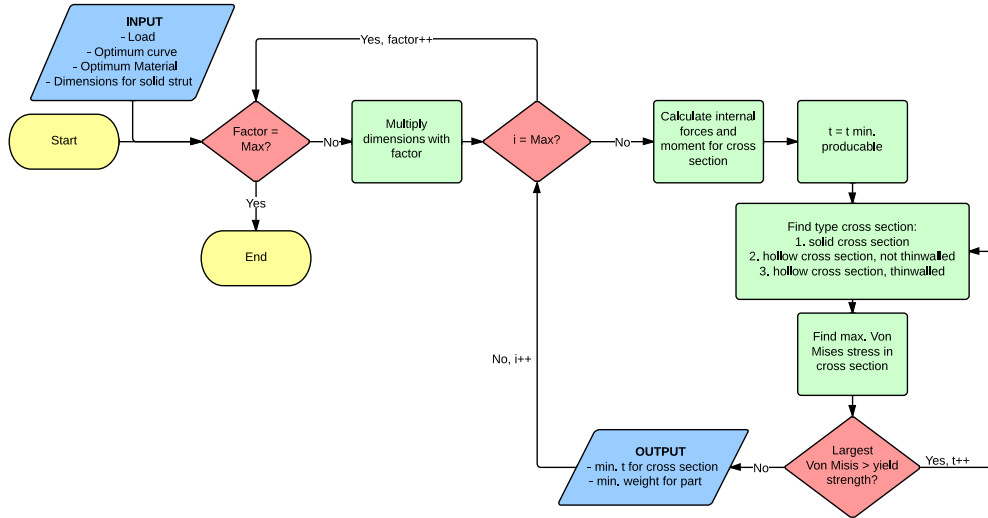
Figure 7.9: Flowchart for the structural dimension optimization of the landing gear

Subsequently the thickness of each cross-section is iterated to come to the minimum thickness at which the largest Von Mises stress in each cross-section is lower than the yield strength of the material according to the Von Mises criterion given in eq. (7.10). The minimum producible thickness is assumed to be $5(10^{-4})$ m. In this iteration three types of cross-sections are considered:

1: Solid Cross-section

The cross-section is considered to be solid if it meets the following criterion:

$$2t_{i,j} \geq h \tag{7.23}$$

In this case the MOI and area are given by eqs. (7.18) and (7.19) respectively. The normal stress, shear stress and bending stress are calculated using eqs. (7.13), (7.14) and (7.20). The maximum Von Mises stress occurs at $h/2$ because the normal and shear stresses are constant over the cross-section and the maximum bending stress occurs at $h/2$.

2: Hollow Cross-section, not Thin-walled

The cross-section is considered to be hollow, but not thinwalled if it meets the following criterion [55]:

$$\frac{t_i}{h_i} \geq 0.1 \tag{7.24}$$

In this case the area and MOI are given by eqs. (7.25) and (7.26) respectively.

$$A_i = 2t_i \cdot (b_i + h_i) - 4t_i^2 \tag{7.25} \qquad I_i = \frac{1}{12}b_i h_i^3 - \frac{1}{12}(b_i - 2t_i)(h_i - 2t_i)^3 \tag{7.26}$$

The normal stress, shear stress and bending stress are calculated using eqs. (7.13), (7.14) and (7.20). The maximum Von Mises stress occurs at $h/2$ because the normal and shear stresses are constant over the cross-section and the maximum bending stress occurs at $h/2$.

3: Thin-walled Cross-section

The cross-section is considered to be thin-walled if it meets the following criterion [55]:

$$\frac{t_i}{h_i} < 0.1 \tag{7.27}$$

In this case the area and MOI are also given by eq. (7.25) and eq. (7.26) respectively. For each cross-section the maximum Von Mises stress is determined. The normal stress, bending stress and shear stress are given by eqs. (7.13), (7.20) and (7.28). The highest Von Mises stress for the cross-section is compared to the yield stress according to the Von Mises criterion, eq. (7.10).

$$\tau_{i,j} = -\frac{S_y}{I_{xx}} \int_0^s tyds \tag{7.28}$$

The local thickness is increased until the maximum Von Mises stress of each cross-section is lower than the yield stress. According to fig. 7.9, the next step is saving the output values and proceed to the next element. After the minimum required thickness of each the elements is calculated, the scaling factor will be increased and the calculations are repeated.

Drag

The influence of the drag on the dimension is also investigated. For eight scaling factors CATIA models are made, based on the dimensions as obtained from structural sizing, see section 7.4.1. These models are compared on the drag coefficient using XFLOW [52]. A cubic spline is applied to obtain a continuous function.

Optimum

In the midterm report increments in the mass and drag coefficient were related to losses in race time (eqs. (7.21) and (7.22)). Using the results from the structural and drag optimization in section 7.4.1, a relation between time loss, with respect to a baseline of scaling factor 1, and the scaling factor can be determined. The scaling factor with the lowest time loss will be the optimal scaling factor to use for the landing gear.

7.4.2   Results

The results that were obtained by following the method described in section 7.4.1 are presented in this section.

Material

The weight of the structural landing gear design can be minimized by using the material with the highest specific strength. In table 7.14 the density, yield strength, and specific strength of commonly used materials are given [55]. Ti-6Al-4V has the highest specific strength, but is very expensive. Therefore Aluminum 2014-T6, which has the second highest specific strength, will be used for the design of the landing gear structure.

Table 7.14: Commonly used aerospace material properties

Material	Density $[kg/m^3]$	Yield strength $[Pa]$	Specific strength $[Pa/(kg/m^3)]$
Aluminum 2014-T6	2790	$4.140(10^8)$	$1.484(10^5)$
Aluminum 2024-O	2770	$9.600(10^7)$	$3.466(10^4)$
Aluminum 6061-T6	2710	$2.550(10^8)$	$9.410(10^4)$
Red Brass C83400	8740	$7.000(10^7)$	$8.009(10^3)$
Bronze C86100	8830	$3.450(10^8)$	$3.907(10^4)$
Am 1004-T61	1830	$1.520(10^8)$	$8.306(10^4)$
Structural steel A36	7850	$2.500(10^8)$	$3.185(10^4)$
Stainless steel 304	7860	$2.070(10^8)$	$2.634(10^4)$
Tool L2 Steel	8160	$7.030(10^8)$	$8.615(10^4)$
Ti-6Al-4V	4430	$9.240(10^8)$	$2.086(10^5)$

Structural

Table 7.15 shows the input values that were used for the MATLAB program.

Table 7.15: Input values for structural size optimization

Parameter	Value	Unit	Source	Description
$MTOW$	849.6	$[kg]$	Section 3.9	Maximum take-off weight
n_{LG}	3	$[-]$	[38]	Load factor for landing gear
M_{ff}	0.933	$[-]$	Section 3.2	Total fuel fraction
n_{double}	2	$[-]$	Section 7.2	Number of struts for double landing gear
ρ_{Al-T6}	2790	$[kg/m^3]$	[53]	Density of Aluminum 2014-T6
x_l	0.60	$[m]$	Section 7.1	Lateral length of the landing gear
y_l	0.80	$[m]$	Section 7.1	Vertical length of the landing gear
$\sigma_{yield,Al-T6}$	$414(10^6)$	$[Pa]$	[54]	Yield stress of Aluminum 2014-T6

Fig. 7.10 shows the mass of the two struts as a function of the scaling factor. From this figure it can be concluded that increasing the size allows for a hollow structure which reduces weight. The reason is that the moment is the most critical factor that determines the Von Mises stress. Material that is located at a larger distance from the neutral line is more efficient in carrying bending stresses than material close to the neutral line. It can also be observed that there is a minimum weight around a scaling factor of 2.9. At this dimension, the minimum producible thickness of $5(10^{-4})$ m is reached. Further increasing the size will not result in a smaller thickness.
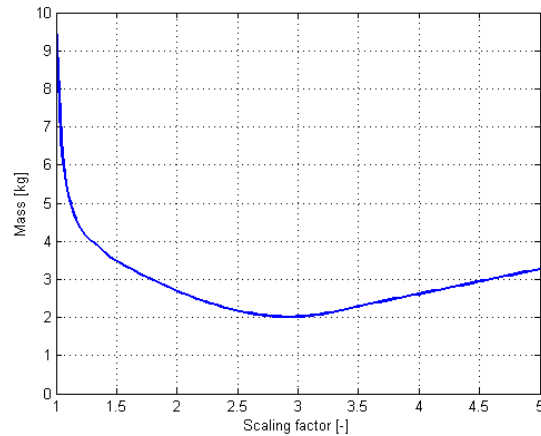
Figure 7.10: Mass vs. scaling factor

Drag

Table 7.16 shows the input values that were used for the CFD simulation. Table 7.17 gives the results. Fig. 7.11 shows the C_D values as a function of the scaling factor.

Table 7.16: Input values for CFD for the comparison of different curves

Parameter	Value	Unit	Source	Description
S	9.30	$[m^2]$	Section 4.1	Wing surface
V	80.00	$[m/s]$	[1]	Avarage velocity during the race
μ	$1.79(10^{-5})$	$[Pa\ s]$	[10]	Dynamic viscosity of air at sea level
ρ	1.225	$[kg/m^3]$	[10]	Fluid density of air at sea level
T	288.15	$[K]$	[10]	Temperature at sea level
r	$0.05(10^{-3})$	$[m]$		Resolution of the used mesh during the CFD
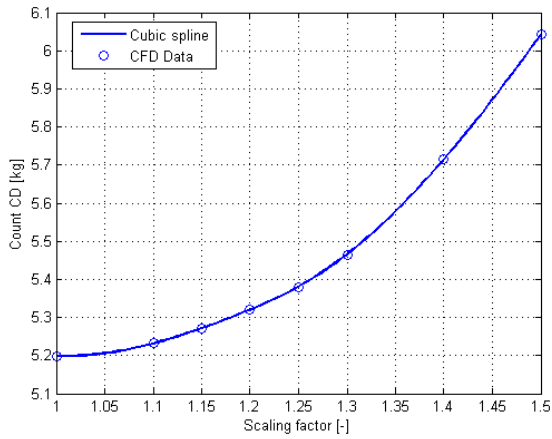
Figure 7.11: Drag vs. scaling factor

Table 7.17: Output values for CFD simulation for the comparison of different scaling factors

Scaling factor	C_D $[-]$
1.00	$5.20(10^{-3})$
1.10	$5.23(10^{-3})$
1.15	$5.27(10^{-3})$
1.20	$5.32(10^{-3})$
1.25	$5.38(10^{-3})$
1.30	$5.47(10^{-3})$
1.40	$5.71(10^{-3})$
1.50	$6.04(10^{-3})$

Optimum

The effect of mass and drag on different scaling factors has been determined in section 7.4.2. Fig. 7.12 shows the loss in race time versus the scaling factor with respect to the solid cross-section (scaling factor of 1). A cubic spline is used to interpolate the data. From this figure it can be concluded that a scaling factor of 1.085 is the optimum scaling factor. Fig. 7.13 shows the thickness as function of the lateral length for the optimum scaling factor. The mass for the chosen scaling factor is 5.18 kg, see fig. 7.10. Fig. 7.14 shows the dimensions of the final landing gear as a function of the lateral length.
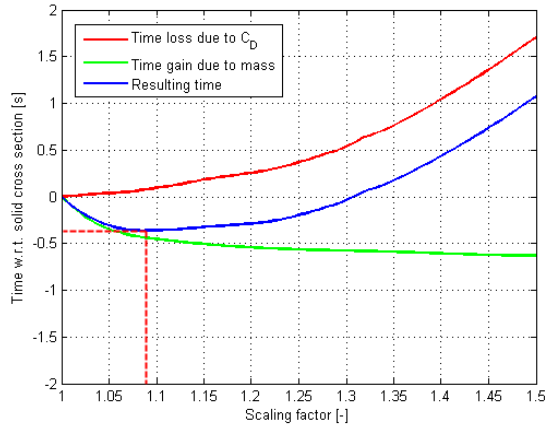
Figure 7.12: Change in race time with respect to the solid strut as function of the scaling factor of the landing gear
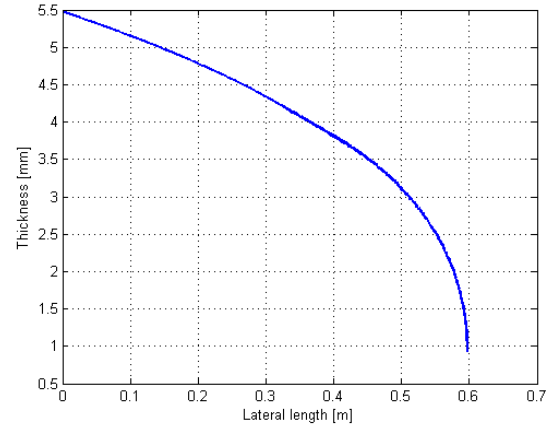
Figure 7.13: Thickness as function of the lateral length of the landing gear for a scaling factor of 1.085
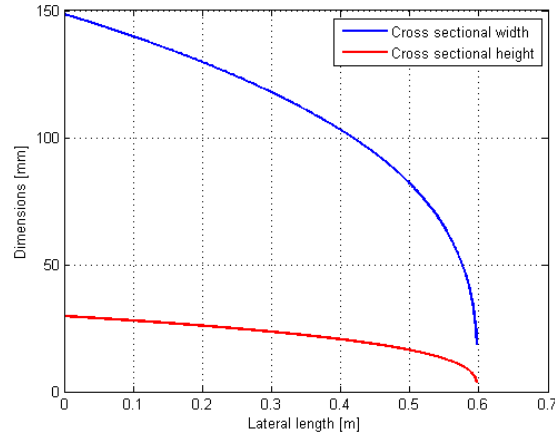
Figure 7.14: Dimensions of the final landing gear design as a function of the lateral length

7.5 Aerodynamic Optimization

The struts have the optimal curvature, material, and dimensions. However the C_D can be improved by using an airfoil as fairing over the strut. As explained in section 7.3.2 the ratio between the width and height of the cross-section is 5. Therefore an airfoil with a t/c of 0.2 has to be used to be able to fit the strut inside. Different NACA 6 serie airfoils are considered. The Reynolds number is varying over the strut because of the variation in dimensions. The C_D of the airfoils is compared at the minimum and maximum Reynolds number. The airfoil with the lowest C_D at zero lift has been selected as fairing. According to table 7.18, the NACA 64-020 has the lowest C_D at both the lowest and highest Reynolds number.

The C_D of the landing gear can also be improved by placing a fairing over the wheels. An asymmetrical fairing is used since it results in the lowest drag coefficient [19].

Table 7.18: C_D values for the considered airfoils at lowest and highest Reynolds number

		Wheel side	Fuselage side
	Airfoil chord [m]	$30.4(10^{-3})$	$263.5(10^{-3})$
	Re	$1.67 \cdot 10^5$	$1.44 \cdot 10^6$
C_D	**NACA 63-020**	$19.63(10^{-3})$	$12.10(10^{-3})$
	NACA 64-020	$19.62(10^{-3})$	$12.10(10^{-3})$
	NACA 65-020	$19.96(10^{-3})$	$12.28(10^{-3})$
	NACA 66-020	$21.86(10^{-3})$	$13.13(10^{-3})$

7.6 Equipment

The landing gear does not only exist of the structural component. It also includes tires, wheels, brakes, and a tail wheel. These components will be discussed in this section. Detailed design of these components is usually done by the manufacturers of the corresponding components. Therefore these components will not be designed in detail. However, the sizes will be determined and a manufacturer will be appointed that can supply the components.

The following equipment is chosen for the FX-15 based on reference aircraft [7, 49, 50].

- The main tires will be Goodyear 500-5" 6PR TT tires.

- The wheel kit will be the Grove Aircraft 50-201 kit. This includes the wheel and the brake system.

- The tail wheel kit will be the Grove Aircraft 06-00004 kit. This includes the 6" tire and the wheel.

A check needs to be done whether the chosen equipment can withstand the loads inflicted on them by the FX-15. The static load rating of the Grove Aircraft 50-201 kit is 583 kg per wheel [56]. Since the MTOW of the FX-15 is 849.6 kg, two wheels have enough static load rating to carry the weight of the aircraft. The limit load rating of the Grove Aircraft 50-201 kit is 2331 kg per wheel [56]. The limit load that the aircraft will apply on the landing gear is 2369 kg table 7.3. Thus, the wheels will never reach their limit load rating. The main tire has the same static and maximum load rating as the wheel kit, and can thus also sustain the loads inflicted on them [57].

The weight of the wheel kit is 2.77 kg per kit, the tires weigh 3.04 kg per tire, and the tail wheel weighs 2.15 kg [56–58]. The total weight of the equipment is 13.78 kg.

7.7 Landing Gear Layout

Fig. 7.15 shows the cross-section of the struts of the landing gear. It can be seen that the cross-section consists of the hollow strut with a NACA 64-020 airfoil fairing. Fig. 7.16 shows the main landing gear with the selected wheel kit and tires.
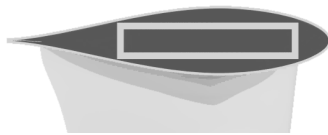
Figure 7.15: Cross-section of the landing gear strut
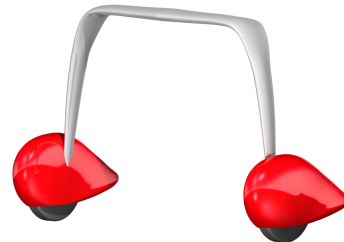
Figure 7.16: Main landing gear

7.8 Conclusion & Discussion

In this chapter a trade-off has been made between the single and double landing gear based on mass, drag, and RAMS. The double landing gear is selected. The double landing gear is optimized on its curvature, material, dimensions and aerodynamic properties. The results are a power m of 9.96, the material used is Aluminum 2014-T6, a scaling factor with respect to the solid strut of 1.085 and a NACA 64-020 airfoil is used as fairing for the strut. This results in a total mass of 5.18 kg for the strut and a C_D contribution of $1.8(10^{-3})$ for the FX-15.

The Grove Aircraft 50-201 wheel kit, the Goodyear 500-5" 6PR TT tires, and the Grove Aircraft 06-00004 tail wheel kit are used as equipment. The total weight of the equipment is 13.78 kg. An asymmetrical wheel fairing is used.

This results in landing gear with a mass of 18.96 kg and a C_D contribution of $3.1(10^{-3})$ for the FX-15.

Points of improvement for future research are:

- Do more elaborate CFD analyses. This will provide more detailed and reliable data on drag, thereby improving the design.

- Investigate the use of composites and other materials for the landing gear. This could further increase the efficiency of the design.

- Do more research on the stiffness of the landing gear. The spring behavior can be investigated, giving more insight in the behavior of the landing gear.

- The single landing gear could be designed in detail, to make a better comparison with the double landing gear. If designed well, the single landing gear could perform better than the double landing gear, leading to a more efficient design.

- Design the strut in the shape of an airfoil, instead of a rectangular strut with an airfoil fairing. This will further reduce the weight of the landing gear.

8   Propulsion Detail Design

In this chapter the propulsion system of the FX-15 is discussed. Included in this chapter is the design of the transmission system in section 8.1. The design of air intake and cooling system is performed next in section 8.2. The engine tuning will be discussed in section 8.3. Following is the design of an automatic pitch control system in section 8.4 and the electrical power sizing in section 8.5. Finally, the design of the fuel tank and firewall is shown in section 8.6.

8.1   Transmission System

In most aerobatic racing aircraft, the engine is placed in the front of the aircraft and the engine is connected directly to the propeller. However, in the FX-15, the engine is placed behind the pilot. This configuration requires an innovative solution for the transmission system.

This section describes the design of the transmission system. First a general trade-off will be performed to select the best transmission system. After that the fundamental problems of designing such a system will be analyzed and discussed. Resulting from the problem analysis is the main designing method used to design the transmission system. Next, the results of the design process will be summarized. The main points of discussions and RAMS are reported last.

8.1.1   Transmission System Trade-off

For the continuation of the design, first a transmission system has to be selected. Four options were considered for the transmission system which will be compared on: temperature, mass and complexity.

1. A V-belt transmission system, which consists of a V-belt and pulleys

2. A transmission system that uses two large gears between the two shafts on both sides

3. A cardan joint system which consists of multiple rods

4. A transmission system which consists of a chain and two sprockets on both sides

The V-belt transmission system is eliminated because it cannot withstand the temperature to which it will be exposed. For every $20°$ increase in ambient temperature above $30°$, the V-belt's life is reduced by 50%. So at $70°$ the life is only 25% of the belt's life at $30°$ [59]. The other three systems can handle the loads if designed properly. The most important factors which will decide which system is used, are the mass and the complexity of the transmission system. The system with two large gears is eliminated because the distance between the engine shaft and the transmission shaft is too large. The distance is 0.45 m which would result in using large and thus heavy gears which take up a lot of space in the fuselage. The cardan joint system can handle the loads and the high temperatures, however it consists of many parts because the operating angle should be less than $25°$ for good performance [60]. Another disadvantage of this system is that it would result in relatively high power losses due to friction. Having many joints would also result in a high mass. The chain system turned out to be the best option because it is light and can handle high loads and temperatures. The chain length can also be modified very easily in case the shaft is slightly moved for optimization or other reasons [61].

Now that a chain transmission system has been chosen, a suitable chain has to be found. This chain is a Wippermann triathlon HT chain with a pitch of $1.588(10^{-2})$ m, a breaking load of 27000 N and a weight of 0.91 kg/m [61]. This chain has been chosen because it is a light and simple chain, it also has a small pitch and the highest specific strength. The small pitch is needed to ensure smooth running at higher chain speeds [62].

8.1.2   Problem Analysis

In this section the assumptions used to design the transmission system are listed.

1. Frictionless transmission system. *Normally, there will be power loss due to friction. Assuming a frictionless transmission system will result in a higher loading and thus an overdesigned system.*

2. Connections are strong enough. *The connections between the shafts and sprockets are assumed to be strong enough to cope with the loads, if this would be not the case, the transmission system may fail at these connections.*

3. Chain margin of 0.001 m. *A margin of 0.001 m between the chain and sprocket is assumed to be sufficient to ensure smooth operation of the chain system, a too small margin will cause a slipping chain which has consequences on the chain wear.*

4. Load carrying teeth. *Half of the number of teeth of the sprocket are load carrying, if less teeth of the sprocket are load carrying, the stresses and strains of the sprocket teeth will increase.*

8.1.3 Method

First, the maximum torque of the engine has to be determined. A maximum power output of 350 hp has been assumed. This power will be reached at an rpm of 2700 (note that during the race the maximum output power will be limited to 315 hp [5]). Knowing this, the torque can be calculated using eq. (8.1).

$$T = \frac{P}{\omega} \cdot SF \tag{8.1}$$

Where, ω is the rotational speed of the shaft.

Now the chain speed can be calculated using eq. (8.2), where r_{final} is calculated with eqs. (8.3) to (8.6). This speed is required to determine the number of teeth n on a sprocket to ensure smooth running [62]. This determination is an iterative process because the radius of the sprocket is a variable input for both variables. Furthermore, the radius of the sprocket can only be a multiple of the chain pitch.

$$v = \omega \cdot r_{final} \tag{8.2}$$

$$C_{initial} = 2 \cdot \pi \cdot r_{initial} \tag{8.3}$$

$$n = round(\frac{C_{initial}}{pitch}) \tag{8.4}$$

$$C_{final} = n \cdot pitch \tag{8.5}$$

$$r_{final} = \frac{C_{final}}{2 \cdot \pi} \tag{8.6}$$

When the above iteration has been performed, the final sprocket radius is known. With this radius the force on the chain can be calculated using eq. (8.7).

$$F = \frac{T}{r_{final}} \tag{8.7}$$

Now it is possible to calculate the shear stress that the sprocket has to withstand with eq. (8.8), where the load bearing area of the sprocket is eq. (8.9).

$$\tau = \frac{F}{A} \tag{8.8}$$

$$A = floor(\frac{n}{2}) \cdot x \cdot b_{inner} \tag{8.9}$$

The shear stress has to be checked with the ultimate material shear stress, to ensure the material does not fail under the applied loads. Also, the displacement of the teeth due to the loads has to be checked to ensure smooth running. A margin of $1(10^{-3})$ m has been used when calculating the size of the teeth. Thus, a displacement of more than $1(10^{-3})$ m would require a more stiff material for the sprocket. The strain and displacement are calculated with eqs. (8.10) and (8.11), respectively.

$$\epsilon = \frac{\tau}{G} \qquad (8.10) \qquad\qquad \delta = \epsilon \cdot x \qquad (8.11)$$

Finally, the mass of the chain system is determined using eq. (8.12), where the component masses are calculated with eqs. (8.13) to (8.15). The required chain lengths are known so the chain mass can now be determined by multiplying this length with the chain mass per meter q. The sprocket mass has to be multiplied by 4, because 4 identical sprockets are used in the transmission system. There are two main reasons that all four sprockets have the same size and number of teeth. The most important reason is that on the front side of the aircraft, there is not enough space inside the fuselage to use different sprocket sizes. The current sprocket-chain setup just fits at the front of the FX-15. The second reason is the critical speed of the shaft. To decrease the torque, the shaft has to rotate faster. In the current setup, it has been determined that the shaft is already rotating close to its critical speed. Therefore, it is not worth the trouble to change the sprocket sizes because the torque and mass would not decrease significantly.

$$m_{chainsystem} = 4 \cdot m_{sprocket} + m_{enginechain} + m_{propchain} \qquad (8.12)$$

$$m_{sprocket} = V \cdot \rho \qquad (8.13)$$

$$m_{chain} = q \cdot (C_{final} + 2 \cdot \Delta) \qquad (8.14)$$

$$V = r_{final}^2 \cdot 2 \cdot \pi \cdot b_{inner} \qquad (8.15)$$

Next, the two transmission shafts are designed. The stresses can be determined using eq. (8.16), where the polar moment of inertia J is determined with eq. (8.17). As with the sprocket system, the shafts will have to cope with the same torque. Furthermore, a restriction for the outer radius of the main shaft has been set to 0.035 m because the shaft has to fit between the pilot's legs. The maximum outer radius of the propeller shaft has been set to 0.02 m in order to fit in the propeller hub.

$$\tau = \frac{T \cdot r}{J} \qquad (8.16)$$

$$J = \frac{\pi}{2} \cdot (r^4 - (r - t)^4) \qquad (8.17)$$

The angular deflections of the shafts can be found using eq. (8.18). A maximum deflection limit of 4° has been set to ensure smooth running of the propulsion system.

$$\theta = \frac{T \cdot L}{JG} \cdot \frac{180}{\pi} \qquad (8.18)$$

At this point it is possible to obtain the mass of the complete transmission system. This mass is calculated using eq. (8.19), where the mass of a shaft is calculated using eq. (8.20). The area of a shaft can be determined with eq. (8.21).

$$m_{transmissionsystem} = m_{chainsystem} + m_{mainshaft} + m_{propshaft} \qquad (8.19)$$

$$m_{shaft} = A_{shaft} \cdot L_{shaft} \cdot \rho_{shaft} \qquad (8.20)$$

$$A_{shaft} = (r_{shaft,outer}^2 \cdot \pi) - ((r_{shaft,outer} - t_{shaft})^2 \cdot \pi) \qquad (8.21)$$

8.1.4 Results

Now that the calculations have been performed, the input and output values of the transmission system are shown below in tables 8.1 and 8.2.

AISI 4130 Steel, normalized at 870°C, is used for the shafts for its high shear modulus. Aluminum 6061-T6 is used for the sprockets, because of its low weight.

Table 8.1: Input values for transmission system design

Variable	Value	Unit	Source	Description
rpm	2700	$[rpm]$	[18]	Rotational speed of the engine shaft
$r_{initial}$	$65(10^{-3})$	$[m]$	Estimate	Initial sprocket radius
P	350	$[hp]$	Estimate	Maximum output power of the (tuned) engine
$chainpitch$	$15.8(10^{-3})$	$[m]$	[61]	Pitch of the chain elements
b	$9.7(10^{-3})$	$[m]$	[61]	Inner width of a chain element (=tooth width)
d	$10.2(10^{-3})$	$[m]$	[61]	Roller diameter
$margin$	$1.0(10^{-3})$	$[m]$	Estimate	Safety margin to ensure smooth running
x	$4.7(10^{-3})$	$[m]$	[61]	Tooth length
g	$14.7(10^{-3})$	$[m]$	[61]	Height of the chain
q	0.91	$[kg/m]$	[61]	Specific weight of the chain
F_{max}	27000	$[N]$	[61]	Maximum load of the chain (breaking load)
Δ_{engine}	0.45	$[m]$	CATIA	Distance between engine shaft and main shaft
Δ_{prop}	0.17	$[m]$	CATIA	Distance between main shaft and propeller shaft
$\rho_{sprocket}$	2700	$[kg/m^3]$	[63]	Material density of the sprocket
$G_{sprocket}$	$26(10^9)$	$[Pa]$	[63]	G modulus of the sprocket material
$\tau_{maxsprocket}$	$207(10^6)$	$[Pa]$	[63]	Maximum shear strength of the sprocket material
SF	1.5	$[-]$	[11]	Safety factor
$L_{mainshaft}$	1.65	$[m]$	CATIA	Length of the main shaft
$L_{propshaft}$	0.3	$[m]$	CATIA	Length of the propeller shaft
$r_{mainshaft,outer}$	$35(10^{-3})$	$[m]$	Estimate	Outer radius of the main shaft
$r_{propshaft,outer}$	$20(10^{-3})$	$[m]$	[48]	Outer radius of the main shaft
$t_{mainshaft}$	$2(10^{-3})$	$[m]$	Estimate	Wall thickness of the main shaft
$t_{propshaft}$	$2(10^{-3})$	$[m]$	Estimate	Wall thickness of the propeller shaft
ρ_{shaft}	7850	$[kg/m^3]$	[64]	Material density of the shaft
G_{shaft}	$80(10^9)$	$[Pa]$	[64]	G modulus of the shaft material
$\tau_{maxshaft}$	$387(10^6)$	$[Pa]$	[64]	Maximum shear strength of the shaft material

Table 8.2: Output values for transmission system design

Variable	Value	Unit	Description
T_{engine}	923.08	$[Nm]$	Maximum torque of the (tuned) engine
n	26	$[-]$	Number of teeth of the sprocket
r_{final}	$65.7(10^{-3})$	$[m]$	Final radius of the sprocket
v_{chain}	18.57	$[m/s]$	Speed of the chain
F_{chain}	$21.08(10^3)$	$[N]$	Maximum applied force on the chain
τ_{tooth}	$39.8(10^6)$	$[Pa]$	Maximum applied shear stress on a sprocket tooth
$m_{sprocket}$	0.317	$[kg]$	Mass of a sprocket
$m_{enginechain}$	1.195	$[kg]$	Mass of the engine chain
$m_{propchain}$	0.687	$[kg]$	Mass of the propeller chain
$m_{chainsystem}$	3.148	$[kg]$	Mass of the chainsystem
$\tau_{mainshaft}$	$98.0(10^6)$	$[Pa]$	Maximum shear stress in the main shaft
$\tau_{propshaft}$	$320.4(10^6)$	$[Pa]$	Maximum shear stress in the propeller shaft
$\theta_{mainshaft}$	3.31	$[°]$	Maximum angular deflection of the main shaft
$\theta_{propshaft}$	3.44	$[°]$	Maximum angular deflection of the propeller shaft
$m_{mainshaft}$	5.53	$[kg]$	Mass of the main shaft
$m_{propshaft}$	0.56	$[kg]$	Mass of the propeller shaft
$m_{transmission\ system}$	9.24	$[kg]$	Mass of the complete transmission system
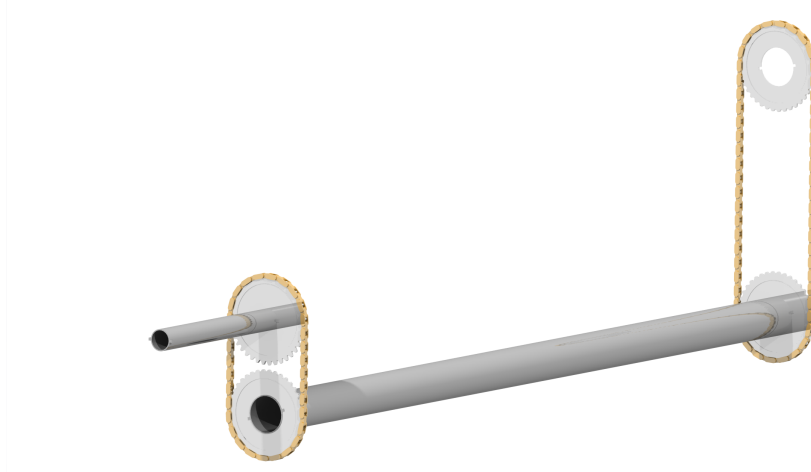
Figure 8.1: The chain-sprocket transmission system

8.1.5 Conclusion & Discussion

An innovative transmission design was needed for the mid-mounted engine configuration. The main criteria on the system were that it should be light, simple and durable (the system has to withstand high loads and temperatures). The chain-sprocket system fulfills all these requirements. The system consists of a transmission shaft, a propeller shaft, two chains that only differ in length and four identical sprockets. The total weight of the transmission system is 9.244 kg. The system can cope with the forces generated by a 350 hp engine, but the engine will only generate 315 hp during the race. Thus, it is expected that the system will perform well during the race.

The transmission system is sensitive to even small changes in the fuselage design, because it fits exactly in the small space that is available in the fuselage.

The RAMS characteristics of the transmission system are:

- **Reliability.** The chain-sprocket transmission system is used in many harsh industries such as mining and high performance systems such as motorcycles (which can reach more than 10000 rpm). The Triathlon HT chain is specifically designed to withstand high loads and high temperatures (up to 200 °). The parts are coated to be extremely wear-resistant. The calculations confirm that the chain is able to easily withstand the torque that a 350 hp generates and will thus have no problems with the 315 hp generated during the race. The sprocket is designed for chain speeds up to 30 m/s, while the actual chain speed will not exceed 18.57 m/s. The sprockets are made of aluminum, which is reliable and widely used. The shafts are made from steel because of its high Young's modulus. A special coating is applied to limit corrosion. The transmission system is designed with a safe life philosophy, so it can be used safely for a specific amount of time before it has to be replaced.

- **Availability.** The transmission system is always available, except during scheduled maintenance of the entire aircraft. The expected lifetime of a similar chain is 15 000 working hours [62]. Due to their similarity, the Wipperman is expected to also have a lifetime of approximately 15 000 working hours.

- **Maintainability.** The transmission system can and should (because it is a critical system) be checked for wear and damage when the aircraft is disassembled for transportation after a race. According to the manufacturer, the chain is practically maintenance free [61]. The sprockets and shafts are also designed for easy access and maintenance.

- **Safety.** This transmission system is not commonly used in aerobatic racing aircraft, so the safety has to be proven. The most important aspect is the safety of the pilot in case of transmission system failure. Failure of chain has been considered during design. This is a dangerous situation due to the speed of the chain. To avoid this scenario, the chain is placed as far as possible from the pilot and is inside a casing. This case also contains lubricant to ensure the system operates smoothly. The system uses an oil bath at the bottom of the case [62]. A structure is built to prevent lateral movement of the shaft due its rotation. The maximum load that occurs on the chain is 21077.7 N, so there is a 6000 N safety margin. Therefore it is expected that the chain will not break or deform to such an extent that

it cannot operate properly. However, no exact numbers could be found for the deformation of the used chain.

Note that the assumption of the frictionless transmission system is only valid for structural design. Performance-wise, there will be power losses due to the gear system. The efficiency of the power transmission of a single lubricated chain-sprocket system is 98 % [65], bringing the total transmission efficiency to 96.04 % (because 2 chain-sprocket systems are used). Thus 96.04 % of the engine power will be transferred to the propeller. This will have to be taken into account when analyzing the performance of the FX-15.

8.2   Engine Cooling & Air Intake

This section is the continuation of the air intake design that was performed in the midterm report in which a wing air intake was selected [2]. The problems regarding the design of the intake system will be discussed first. After that methodology and equations used for the design are shown followed by the resulting. Finally the RAMS and remaining points of discussions will be stated.

8.2.1   Problem Analysis

The air intake combines the cooling air and intake air in one intake, so the two single air intakes should provide cooling air as well as oxygen for the engine. Not all heat generated by the engine has to be cooled. The energy of the engine comes in the forms of work and heat. This heat consists of exhaust gases and radiant heat. This radiant heat is the only fraction that must be cooled. The exhaust heat is directly dumped into the atmosphere (= the heat sink).

The relative locations of the engine and wing are important for the design of the wing intake. There is a risk that the intake will be less effective due to this location difference. This risk is mitigated by guiding the air to the engine using ducts. These ducts run from the intakes to the engine air intake and the upper part of the engine block to cool the cylinders (which generate most radiant heat). This allows for more efficient cooling, because the tubes can be placed at an optimal position to cool the cylinders.

Note that just like the transmission system, the air intake and cooling are designed for a 350 hp engine. This allows the placement of a turbocharger to increase the power output and efficiency of the 315 hp engine during the race.

Assumptions

The assumptions that were made during the cooling and intake design are listed below.

1. The influence of other gases on the $c_{p\ exhaust}$ is neglected. *The actual value $c_{p\ exhaust}$ will have a deviation of approximately 0.5% This difference is insignificant and does not change any important parameters.*

2. The exhaust gas temperature is 1400° F (760° C). *If the actual value turns out to be higher, more energy will leave the exhaust and less cooling air will be required.*

3. The race condition is the critical cooling condition. *If there is another situation which requires more cooling, the intake will not be able to provide a sufficient amount of air.*

4. The air is incompressible. *This assumption is valid because at the top speed of the FX-15, the Mach number is 0.32.*

8.2.2   Method

The total mass flow through the engine is equal to eq. (8.22), where the fuel and intake mass flow are calculated with eqs. (8.23) and (8.24).

$$\dot{m}_{engine} = \dot{m}_{fuel} + \dot{m}_{intakeair} \tag{8.22}$$

$$\dot{m}_{fuel} = SFC \cdot (1/3600) \cdot P \cdot \rho_{fuel} \qquad (8.23) \qquad\qquad \dot{m}_{intakeair} = \dot{m}_{fuel} \cdot AFR \qquad (8.24)$$

The $c_{p\ exhaustgas}$ has been determined with eq. (8.25). In order to do this the composition of (petrol) exhaust gases has been analyzed [66] and the c_p's of the different elements are obtained from Cengel-Boles, 2010 [67].

Using the fuel mass flow and eq. (8.27), the amount of energy going into the engine per second can be determined. The used energy fractions are calculated with eqs. (8.26) to (8.28). The result of eq. (8.26) is the heat per time unit that needs to be cooled.

$$c_{p\ exhaustgas} = N_2 \cdot cp_{N_2} + CO_2 \cdot cp_{CO_2} + H_2O \cdot cp_{H_2O} + CO \cdot cp_{CO} \qquad (8.25)$$

$$E_{heat} = E_{total} - E_{exhaust} - E_{work} \qquad (8.26)$$

$$E_{total} = \dot{m}_{fuel} \cdot HV \qquad (8.27) \qquad\qquad E_{work} = P \cdot 745.7W \qquad (8.28)$$

$$E_{exhaust} = \dot{m}_{engine} \cdot c_{p\ exhaustgas} \cdot (T_{exhaust} - T_{intakeair}) \qquad (8.29)$$

A good way to check the above calculations is to calculate the efficiency using eq. (8.30). A normal efficiency for a (petrol) combustion engine is 0.3.

$$\eta = \frac{E_{work}}{E_{total}} \qquad (8.30)$$

Since the heat which has to be dissipated is known, the total mass flow can be calculated with eq. (8.31), where eq. (8.32) is the cooling mass flow.

$$\dot{m}_{total} = \dot{m}_{cooling} + \dot{m}_{intakeair} \qquad (8.31)$$

$$\dot{m}_{cooling} = \frac{E_{heat}}{dT \cdot c_{p_{air}}} \qquad (8.32)$$

The next step is to calculate the intake area that is required. This is done with eq. (8.33), where eq. (8.34) is the intake area and SF is the safety factor of 1.5. This safety factor should compensate for the losses in the ducts, outside air temperature variations and airflow under high angle of attack. The mass flow can be checked with eq. (8.35). Furthermore, the average race speed (v_{race}) of 80 m/s has been used [1].

$$A_{safe} = SF \cdot A \qquad (8.33)$$

$$A = \frac{\dot{m}_{total}}{\rho \cdot v_{race}} \qquad (8.34) \qquad\qquad \dot{m}_{safe} = A_{safe} \cdot v_{race} \cdot \rho \qquad (8.35)$$

The last variable which is determined is the exit temperature of the cooling air (eq. (8.36)). Just like the efficiency this is a sanity check for the calculations.

$$T_{exitcooling} = T_{intakeair} + dT \qquad (8.36)$$

8.2.3 Results

Input values are depicted in table 8.3 and table 8.4. The resulting output values are shown in table 8.5.

Table 8.3: Input values for exhaust c_p

Variable	Value	Unit	Source	Description
N_2	0.71	$[-]$	[66]	Fraction of N_2 in exhaust gas
CO_2	0.14	$[-]$	[66]	Fraction of CO_2 in exhaust gas
H_2O	0.13	$[-]$	[66]	Fraction of N_2O in exhaust gas
CO	0.015	$[-]$	[66]	Fraction of CO in exhaust gas
$Other\ gases$	0.005	$[-]$	[66]	Fraction of other gases in exhaust gas
$c_p\ N_2$	1039	$[J/(kg\ K)]$	[67]	Specific heat coefficient of N_2
$c_p\ CO_2$	846	$[J/(kg\ K)]$	[67]	Specific heat coefficient of CO_2
$c_p\ H_2O$	1872.3	$[J/(kg\ K)]$	[67]	Specific heat coefficient of H_2O
$c_p\ CO$	1040	$[J/(kg\ K)]$	[67]	Specific heat coefficient of CO

These inputs will lead to a $c_{p\ exhaust}$ of 1115 $J/kg \cdot K$.

Table 8.4: Input values for air intake and cooling system sizing

Variable	Value	Unit	Source	Description
SFC	0.303	$[l/(hp \cdot hr)]$	[1]	Specific fuel consumption
ρ_{fuel}	0.718	$[kg/m^3]$	[68]	Density of the fuel
HV	$44(10^6)$	$[J/kg]$	[68]	Heating value of the fuel
P	350	$[hp]$	Estimate	Maximum power output of the (tuned) engine
AFR	14.5:1	$[-]$	[69]	Stoichiometric air to fuel ratio
$T_{intakeair}$	288.15	$[K]$	[10]	Temperature of the intake air
$T_{exhaust}$	1033.2	$[K]$	Estimate	Temperature of the exhaust gases
ρ_{air}	1.225	$[kg/m^3]$	[10]	Density of the intake air
v_{race}	80	$[m/s]$	Estimate, [1]	Average airspeed during the race
dT	120	$[K]$	Estimate	Temperature increment of the cooling air
$c_{p\ air}$	1005	$[J/(kg\ K)]$	[67]	Specific heat coefficient of the intake air
SF	1.5	$[-]$	[11]	Safety factor

Table 8.5: Output values for air intake and cooling system sizing

Variable	Value	Unit	Description
$\dot{m}_{cooling\ required}$	3.29	$[kg/s]$	Required mass flow to cool the engine
$\dot{m}_{intake\ required}$	0.31	$[kg/s]$	Required mass flow to run the engine
$\dot{m}_{total\ required}$	3.60	$[kg/s]$	Total required mass flow to operate the engine
$\dot{m}_{total\ safe}$	5.40	$[kg/s]$	Total required mass flow to operate the engine (with safety factor)
$A_{required}$	$37(10^{-3})$	$[m^2]$	Required intake area
A_{safe}	$55(10^{-3})$	$[m^2]$	Required intake area with safety factor
$A_{safe,\ one\ intake}$	$2.75(10^{-2})$	$[m^2]$	Required safe intake area of one intake
$T_{cooling\ exit}$	408.15	$[K]$	Exit temperature of the cooling air
η	0.28	$[-]$	Engine efficiency
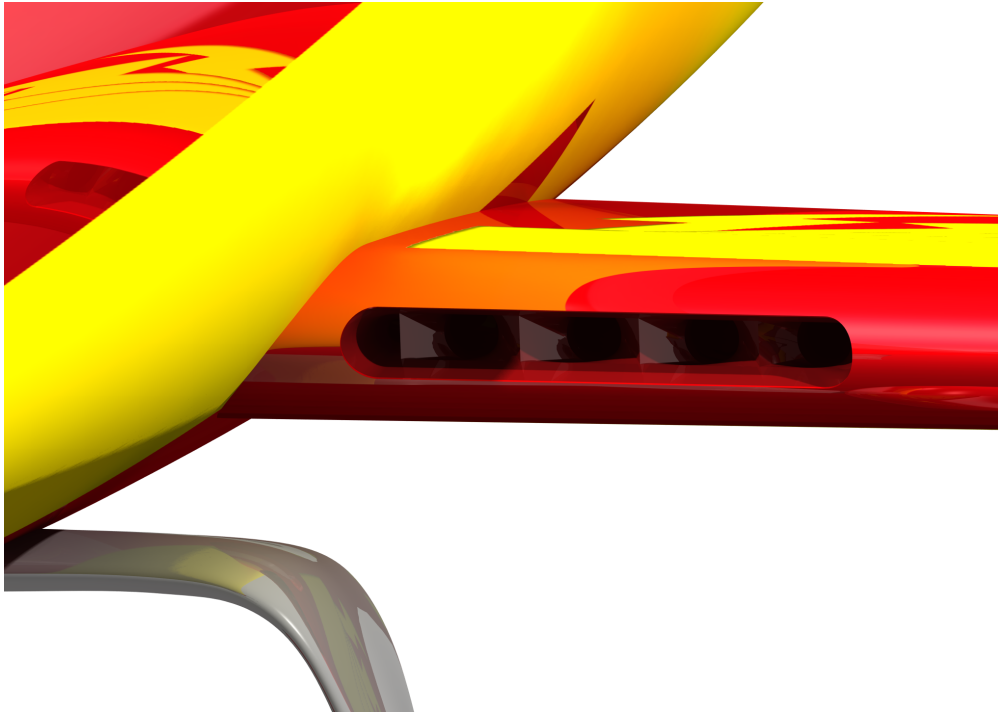
Figure 8.2: The intake of the FX-15

8.2.4 Conclusion & Discussion

The wing intake design will be able to provide cooling air and intake air to the engine. The air will be guided to the engine using ducts, these ducts are estimated to have a mass of 2 kg. The intake is integrated into the wing root, so a minimal amount of intake and cooling drag is generated. Furthermore, the lift and pitching moment characteristics of the wing are not significantly altered [70]. The cooling air will exit near the exhaust pipe. However, if the cooling air is not able to flow from intake to exit sufficiently, an air extractor could be placed on the upper half of the fuselage (behind the highest point of the fuselage, because there is a low pressure area there and the air extractor would create a suction effect that improves the flow of the cooling air without significantly affecting drag [71]). Note that the air extractor is only a recommendation for when cooling is insufficient.

The wing intake design is sensitive to changes of the relative wing and engine locations. This sensitivity is minimized by using ducts that run from the intake to the engine.

The RAMS characteristics of the wing intake design are:

- **Reliability**. The reliability of the intake system is expected to be very good, because each wing has an intake and thus there is redundancy. If one intake is blocked, the FX-15 can continue flying at reduced power and land. Furthermore, a standard air filter is mounted on the engine to ensure smooth running.

- **Availability**. When the wing is removed during races, the ducts that run from the intake to the engine will need to be detached. This will be a bit more time consuming compared to other intake designs.

- **Maintainability**. Maintenance will be performed in between races, when the ducts are detached.

- **Safety**. The wing intake is a proven design and there is redundancy. Therefore, the system is expected to be very safe.

8.3 Engine Tuning

The modification and optimization methods of the engine are described in this section. Note that it is not allowed to increase the engine power for the RBAR, so these modifications are only to show the power

and efficiency enhancement options for other purposes. However, for the RBAR there is a compulsory modification, which is to fit a smoke generator on the engine. This generator is connected to the exhaust, because the smoke oil is injected into the exhaust manifold [72].

8.3.1 Problem Analysis

The power output of the engine can be increased to improve the overall performance of the aircraft. For the midterm report only the use of a supercharger or turbocharger was taken into consideration. However, there are also other ways to improve the engine's performance. Another modification that can improve the performance of the engine is increasing the compression ratio.

The following assumption was made for the turbocharger.

1. The turbocharger adds 35 hp to the engine's power output [18]. *If the turbocharger adds less power, some performance requirements, such as the maximum design cruise speed, may not be met.*

8.3.2 Method

For the engine tuning, no calculations have been performed. The midterm report has been used to ensure that the important criteria were taken into account during the process of choosing suitable parts [2]. Furthermore, the components of the turbocharger are stock parts that are bought from Hartzell [73]. It was also not possible to determine the turbocharger dimensions very accurately. Therefore, these values were estimated and implemented into CATIA to see if the system would fit. The results can be seen in the next section.

8.3.3 Results

Modifications that significantly increase the compression ratio will increase the wear of the cylinders and is thus eliminated as an option for sustainability, reliability and safety reasons [74]. Another important change is that the choice has shifted from a supercharger to a turbocharger. After a discussion with G3Ignition (a company that supplies superchargers for Lycoming engines) the conclusion was drawn that it is not possible to install a supercharger on the mandatory Lycoming D-series engine, because the engine needs to be a vertical draft. This means that the induction cowl needs to be vertical [75]. However, this does not have a negative impact, because a turbocharger does the same as a supercharger, only in a different way. The turbocharger increases the air intake of the engine by recuperating the exhaust energy using a turbine and a compressor. The turbocharger system that will be used is supplied by Hartzell Engine Technologies and consists of five different parts; a turbocharger, a controller, a wastegate, a valve assembly and a scavenge pump [73]. This system costs € 18755. The prices of the individual components can be seen in table 8.6. The turbocharger dimensions have been estimated since no exact numbers could be found. The Lycoming engine data sheets were used for this estimation [18]. This was done by comparing the dimensions of a non-turbocharged engine with the turbocharged version of the same engine. The fuselage is designed in such a way that the turbocharger can be attached to the engine.

Table 8.6: Turbocharger Component Prices

Component	Price	Unit	Source
Turbocharger	4563	[€]	[73]
Controller	4630	[€]	[73]
Wastegate	4249	[€]	[73]
Valve assembly	2688	[€]	[73]
Scavenge pump	2624	[€]	[73]

8.3.4 Conclusion & Discussion

The engine is tuned by using a turbocharger from Hartzell Engine Technologies. The choice shifted to a turbocharger because it is not possible to fit a supercharger on Lycoming D-series engines [75]. The turbocharger is assumed to increase the engine power output by 35 hp [18]. Calculations were performed

that showed that an increment of one additional hp has a bigger impact on the track time than an increment of one kilogram extra weight.

The turbocharger is only sensitive to changes in the fuselage design, because there has to be enough space to mount the turbocharger on the engine.

The RAMS characteristics of the turbocharger are:

- **Reliability**. Turbochargers have been used for a long time. In the past they were not always reliable (due to improper cooling), but nowadays they are properly cooled and have direct injection. Therefore the turbocharger is expected to be reliable and last the lifetime of the vehicle [76].

- **Availability**. Due to the increase in turbocharger reliability over the past decades, the availability is expected to be the same as that of an aircraft without turbocharger.

- **Maintainability**. Maintenance of the engine will become more time consuming, because there is an extra subsystem. However, this increase is expected to be insignificant because turbochargers are not very complex.

- **Safety**. Modern turbochargers are not very prone to failure [76]. Also, failure of the turbocharger would not result in failure of the entire engine. The only difference would be a reduced power output.

The turbocharger can improve engine efficiency and is therefore important with respect to sustainability [77]. This increase in efficiency is possible because the additional air in the cylinder provided by the turbocharger will make the combustion of the fuel more complete and thus more efficient. This means that in comparison with the normally-aspirated engine, a turbocharged engine will use less fuel while obtaining the same output power.

8.4 Automatic Propeller Pitch Control & Electrical Power

This section describes the design of the automatic propeller pitch control system that will be used to optimally use the propeller during the race. Futhermore, the electrical power system that will power the electrical components of the FX-15 will be sized.

8.4.1 Problem Analysis

As a result of an interview with Frank Versteegh (former RBAR pilot), it was concluded that the pilot does not have the time to change the propeller pitch during the race. This is why an automatic propeller pitch control system is considered. This system will adjust the propeller pitch according to the airspeed, which will ensure that the propeller is always operating at its optimal efficiency. Because the Hartzell 3-bladed 7690 structural composite propeller is a variable pitch propeller, no modifications need to be made to the propeller. Only a servo and controller are needed to make this system operational. The blade pitch can be changed by sliding a rod forward/afterward through the propeller hub. Of course the electrical power that this system consumes needs to be included in the electrical power budget.

The systems of the FX-15 which consume or produce electrical power are:

- A CCT (Camera Control and Transmission) Box: consumes an estimated 250 W

- Instruments and radio: consumes an estimated 20 W [78]

- A servo to power the automatic pitch control system: determined to be 6 W [79]

- A racing battery: provides 96 Wh [80]

- A generator: provides enough power in order to power all electrical systems

The assumptions that were made during the automatic propeller pitch control system design are:

1. The force needed to change the blade pitch angle will not be higher than 50 N. *If the required force turns out to be higher, the servo might not be able to change the propeller pitch angle.*

2. The standard generator provides enough power for all electrical systems. *If the generator is not able to power all systems, the battery will have to provide the remaining power.*

3. The CCT box consumes 250 W of electrical power. *If the power consumption is higher, the operating time of the system decreases, but unless the power consumption increases by a factor 10, the CCT box will be able to record the entire race.*

8.4.2   Method

In order to make the automatic pitch control system work, it is clear that a servo and controller are needed. First, the controller will be looked into. This controller will need to relate airspeed (input) to a propeller blade pitch (output). This can be done with the advance ratio eq. (8.37).

$$J = \frac{v}{n_p \cdot D} \tag{8.37}$$

The optimal blade pitch can now be determined, with fig. 8.3. Note that fig. 8.3 is not for the Hartzell 3-bladed 7690 structural composite propeller, because this data could not be obtained from Hartzell. However, the shape of the figure will be similar. The controller will be recalibrated with the Hartzell propeller values when they are obtained. The controller will always strive for maximum propulsive efficiency.
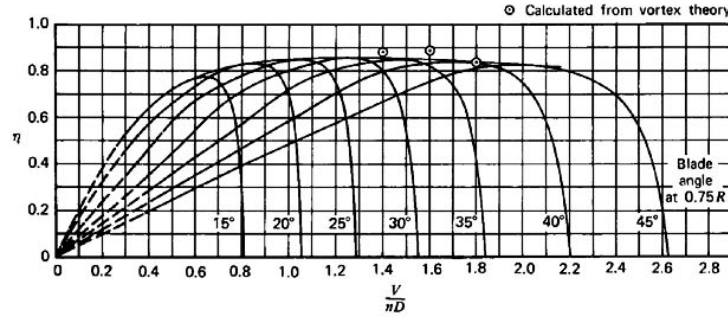
Figure 8.3: Propulsive efficiency vs. advance ratio for different pitch angles

The servo for the pitch control system can now be designed. A gear will be put on the servo, which drives the rod, which in turn changes the propeller pitch. This rod has notches that fit with the gear. The gear radius is set to 0.02 m. The torque that the servo needs to provide is calculated in eq. (8.38). This is used to select a suitable servo.

$$T = r_{servo\ gear} \cdot F \tag{8.38}$$

For the electrical power sizing the same battery has been used as in the Corvus CA-41: the Varley Red Top 8 [80]. This battery is designed to operate under high g loadings and racing conditions. With the power consumption of the subsystems and the battery capacity known, it can be calculated how long the aircraft can still fly safely in case the generator of the engine fails. Eq. 8.39 determines the time when all electrical systems are operational, eq. (8.40) determines the time when the CCT box is shut down and only the vital instruments are operational.

$$t_{all\ systems} = \frac{W_{battery}}{P_{CCT} + P_{servo} + P_{intruments\&comms}} \tag{8.39}$$

$$t_{vital\ systems} = \frac{W_{battery}}{P_{servo} + P_{intruments\&comms}} \tag{8.40}$$

8.4.3 Results

Table 8.7: Input values for automatic propeller pitch control system

Variable	Value	Unit	Source	Description
v	0 to 140	$[m/s]$	Speed range of the FX-15	Airspeed vector
n_p	2700	$[rpm]$	[18]	Propeller rotational speed
D	1.98	$[m]$	[48]	Propeller diameter

Finally, a relation between J and v is obtained as can be seen in fig. 8.4, from this the advance ratio can be determined and inserted in fig. 8.3 to obtain the propeller blade pitch.
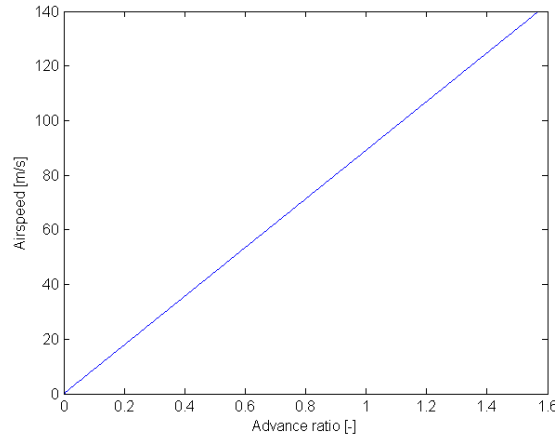
Figure 8.4: Airspeed vs. advance ratio

Table 8.8: Input values for electrical power sizing

Variable	Value	Unit	Source	Description
P_{CCT}	250	$[W]$	Estimate	Power of the CCT box
P_{servo}	6	$[W]$	[79]	Power of the servo
$P_{intruments\&comms}$	20	$[W]$	Estimate, [81]	Power of the instruments and communication devices
$W_{battery}$	96	$[Wh]$	[80]	Battery capacity

Table 8.9: Output values for electrical power sizing

Variable	Value	Unit	Description
$t_{all\ systems}$	20	$[min]$	Time that all systems can be powered by the battery (when generator fails)
$t_{vital\ systems}$	221	$[min]$	Time that only vital systems can be powered by the battery (when generator fails)

8.4.4 Conclusion & Discussion

The automatic propeller pitch control system will be simple and compact and can significantly improve the FX-15 performance, by ensuring that it always flies at the best possible propulsive efficiency. This implies that the fuel consumptions will drop slightly when not flying at the performance limits, which is beneficial for sustainability. The rotational speed of the servo is equal to 5.82 rad/s [79]. This gives a sliding rod speed of 0.12 m/s. Thus it is expected that the automatic propeller pitch control system will be able to adjust the pitch angle fast enough during the race. The power budget is almost not affected by the pitch control system, so the same battery as in the Corvus CA-41 can be used. The electrical subsystems will be discussed in more detail in section 8.5.

The RAMS characteristics of the automatic propeller pitch control system are:

- **Reliability**. The automatic pitch control system is simple, and only needs a small modification to be compatible with the existing pitch control system. The system is expected to be very reliable.

- **Availability**. The availability will be high, because the system is simple and maintenance can be performed quickly.

- **Maintainability**. The maintainability of the pitch control system and the electrical system will be good, because they are simple and easily accessible systems.

- **Safety**. In case the pitch control system should fail, the pilot will still be able to control the pitch manually and continue flying safely. If the generator fails, the aircraft will be able to continue flying for a decent amount of time. In case all electrical systems fail, there is still no direct threat to the pilot safety. All important instruments are analog. The only important electrical system is the communications system.

8.5 Electrical Subsystems

The FX-15 has several electrical systems. An overview of the interaction of these systems is shown in the diagram below.
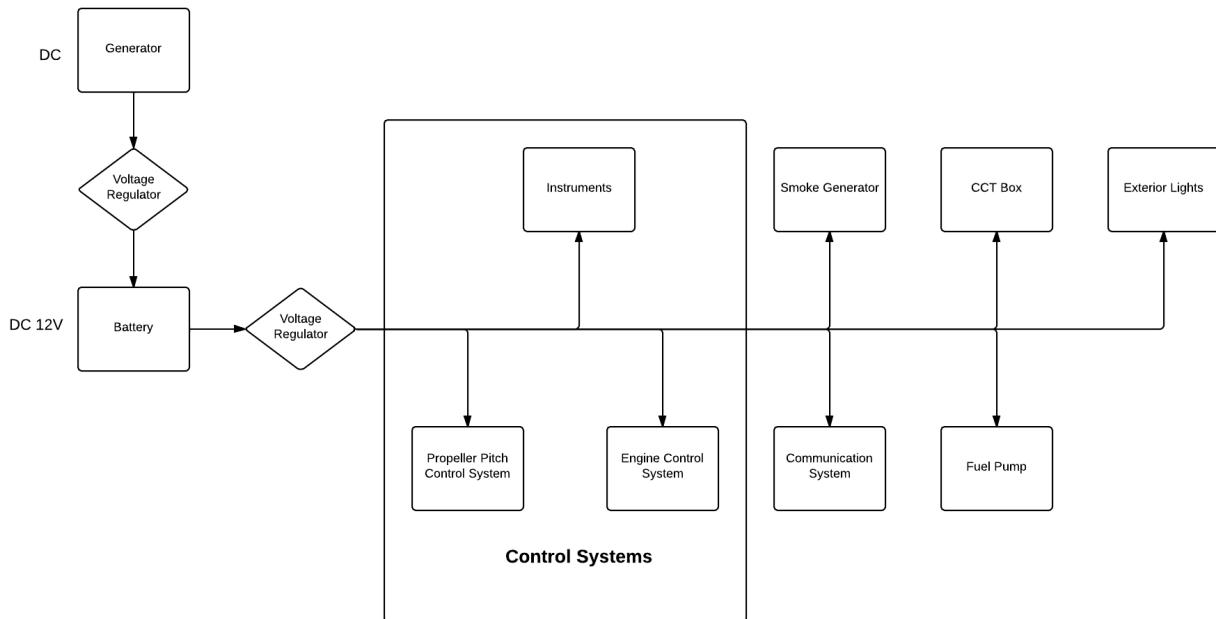
Figure 8.5: Electrical diagram

The FX-15 has an onboard communications system which consists of a radio. The system serves two purposes. The first is to enable the pilot to communicate with his technical staff during the race. The second is to communicate with air traffic control when he has to take off before the race and land the aircraft after the race.

The FX-15 has three subsystems that process data during the race. The first is the onboard camera which records the race and sends this data to the CCT box that is located in the back of the aircraft. This makes it possible to see the race from the pilot's point of view. The second subsystem is the GPS unit. This system exchanges data with satellites to obtain information regarding the current position of the aircraft. The third subsystem is the automatic pitch control system. The diagram below shows how the system controls the pitch angle of the propeller blades.
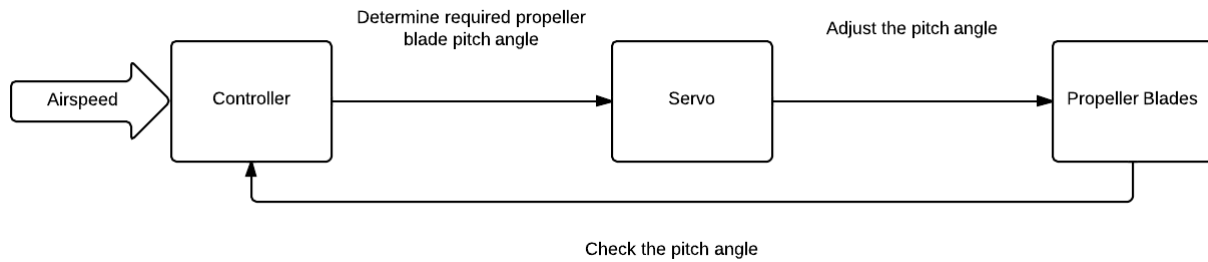
Figure 8.6: Automatic propeller pitch control diagram

8.6 Fuel Tank & Firewall

In this section the fuel tank and firewall subsystems will be discussed. The fuel tank for an aerobatics racer is different from other fuel tanks and imposes some additional challenges. The firewall is a safety system that protects the pilot in case of a fire or excessive heat production of the engine.

8.6.1 Problem Analysis

First, it has to be analyzed what the fuel tank and firewall need to be able to do, this is done here.

Fuel Tank

The fuel tank of an aerobatic aircraft has to withstand much higher loads than the fuel tanks of general aviation aircraft. For the RBAR, the FX-15 is required to have a 50 liter fuel tank. However, the aircraft should be able to divert to another airport in case of emergency, so the fuel tank size has increased to 83 liter (section 3.2). Two different options have been considered for the fuel tank design.

1. The first option is to use a single fuel tank with a capacity of 83 liter.

2. The second option is a combination of two tanks; one 50 liter tank for the race and one 33 liter tank for other purposes.

Fuel Tank: Trade-off The first option with a single fuel tank was chosen because it is less complex and also weighs less. In case of two fuel tanks, twice the amount of tubes would be needed and also another structural support for the fuel tank would have to be fitted inside the fuselage. This would result in more time-consuming maintenance.

Fuel Tank: Cost Analysis The fuel tank is a $1.6(10^{-3})$ m thick aluminum rectangular box, with a Kevlar reinforced bladder which is specifically designed for race purposes [82]. The dimensions in meters of the fuel tank are: $0.635 \cdot 0.432 \cdot 0.356$. The price of this tank is €1412,40 [83]. The mass of the fuel tank is 9.53 kg. In order to provide the engine with fuel when flying inverted, a flop tube system in used. Inside of the tank is a flexible hose (the flop tube) with a weight attached to the free end. The flop tube weighs approximately 0.5 kg and costs €80. When the plane is right side up the flop tube, rests on the bottom of the tank because of the weight and draws fuel from the bottom of the tank. When the plane is rolled to inverted, the weight causes the hose to flop to the top of the tank (which is the bottom now) and draw fuel from there [84].

Firewall

To ensure pilot safety, a firewall is place between the pilot and the engine. Also, some subsystems will need to be shielded from excessive engine heat and should be placed behind the firewall. The firewall can be made from different materials. Mass is a critical criterion, so the lightest material possible is chosen. The design of the firewall is more extensive, because more calculations have to be performed before one option can be eliminated.

1. The first option is to use a titanium sheet with a ceramic heat shield.

2. The second option is to use a sandwich structure of two aluminum sheets with aerogel placed in between the sheets.

Firewall: Trade-off The mass of the first option is calculated as follows. A titanium sheet with a thickness of $4 \cdot 10^{-4}$ m weighs 1.80 kg/m^2 and a ceramic heat shield with a thickness of $2.5 \cdot 10^{-4}$ m weighs 0.46 kg/m^2 [85, 86]. The cross-sectional area of the firewall is 1.032 m^2. This value has been determined with CATIA. Now the total mass of the firewall can be calculated. The total mass is calculated as follows: $1.032 \cdot (1.80 + 0.46) = 2.332 kg$. Now the mass of the second option will be calculated. Since aerogel is very light, the critical factor is the mass of the aluminum sheets [87]. The total aluminum area is twice the firewall area. This is equal to 2.064 m^2. The thickness is equal to $0.813(10^{-3})$ m. Now the mass is calculated with: $m = A \cdot t \cdot \rho$. This mass is equal to 4.5 kg. The density that was used for this calculation is 2700 kg/m^3. This is almost twice as heavy as the first option, therefore this option is eliminated.

Firewall: Cost Analysis The total price of the first option consists of two parts: The grade 5 titanium price and the ceramic heat shield price. The titanium costs approximately €220 per square meter [88]. The total titanium price is approximately €230. This price has been estimated by choosing multiple sheets that add up to approximately one square meter and rescaling the price for one square meter. The ceramic heat shield costs €240. This is because the heat shield is only sold in certain dimensions. Therefore three separate pieces have to be bought. This leads to a total firewall price of €470.

8.6.2 Conclusion & Discussion

The fuel tank system consists of a tank and a flop tube. The fuel tank that is chosen is designed by Aero Tec Laboratories. It is a simple rectangular box, which is placed behind the engine. The flop tube is bought separately and mounted inside the fuel tank to ensure a continuous fuel flow to the engine. The firewall subsystem is made from a titanium sheet with a ceramic heat shield. The titanium sheet would suffice as a firewall, but to give the pilot extra protection, the ceramic heat shield is added. The heat shield reduces surface temperatures up to 64% [86]. This turned out to be the lightest option available in this price class that gives such a high level of protection.

Both systems only depend on the cross-sectional area of the fuselage. The fuel tank is critical, so the fuselage is designed to properly fit the fuel tank. The firewall can easily be resized and does not significantly influence other systems.

The RAMS characteristics of the fuel tank and firewall are:

- **Reliability.** The chosen fuel tank is used in many different types of races and is thus considered highly reliable. The flop tube increases reliability even further because it ensures the engine receives fuel regardless of aircraft orientation. The titanium firewall with heat shield is considered very reliable. According to CS23 regulations, this firewall setup can be used without further testing (since it is a proven design).

- **Availability.** The fuel tank is very reliable, and therefore expected to always be available. The firewall is expected to perform during the entire aircraft lifetime. Only in the case of engine fire or failure of the cooling system, the firewall will need to be replaced.

- **Maintainability.** The fuel tank is a simple system and will be easily accessible. Therefore the fuel tank will be easy to maintain. It is expected that the firewall be virtually maintenance free. However, it will still be inspected during maintenance.

- **Safety.** The fuel tank is often used in racing environments and is considered safe for racing conditions. The firewall is a proven design according to CS23 and is considered a very safe design.

9 Performance Analysis

This chapter concerns the performance analysis of the FX-15. Here, values will be determined to see how well the aircraft will perform in a race. First, the problems regarding the analysis are investigated in section 9.1. After that, the method used for the investigation is explained in section 9.2. Finally, the results will be discussed in section 9.4 and some of these values will be compared to reference aircraft in order to see whether the FX-15 has a chance of beating the competition.

9.1 Problem Analysis

The most important aspect of the FX-15 is its performance. The FX-15 has been designed to win the RBAR, so having a superior performance compared to reference aircraft is crucial. From the midterm report it turned out that drag minimization is extremely important for the RBAR [2]. This minimization has been taken into account for each relevant subsystem in order to design a high performance aircraft such as the FX-15.

For the performance analysis the below listed assumptions have been made:

1. The runway friction coefficient at take-off is 0.05. *A higher coefficient will lead to an increase in take-off distance.*

2. The runway friction coefficient (with braking) at landing is 0.60. *A higher coefficient will lead to a decrease in landing distance.*

3. The aircraft mass is assumed to be constant. *This assumption will only have effect on the range calculation because this is the only situation where the total aircraft mass decreases notably (with 7.2%). This will have as a consequence that the range which is stated later will be slightly lower than the range in real life. During a race, the aircraft mass will only decrease with 0.4%.*

9.2 Method

The method that was used for the performance analysis is described in the midterm report [2]. This method is identical to the one used here so if more explanation is needed, please refer to the midterm report. The only addition to this performance analysis is the range calculation, which is described in eq. (9.1).

$$R = t \cdot v_{max} \tag{9.1}$$

Where,

$$t = \frac{V_{fuel} - 10l}{SFC \cdot P} \tag{9.2}$$

v_{max} is determined in fig. 9.2 (right graph). The range is calculated with the maximum (cruise) speed in order to approach the required cruise speed of 450 km/h as demanded by FlashCo. Note that 10 l of fuel is subtracted from the total fuel amount, as reserve fuel.

Furthermore the minimal aircraft race mass for the race is determined in section 10.2. The performance analysis is performed at this mass (=698 kg) because the FX-15 is designed to win the race instead of reaching a maximum range or endurance.

9.3 Results

The inputs for the following graphs are listed in table 9.1.
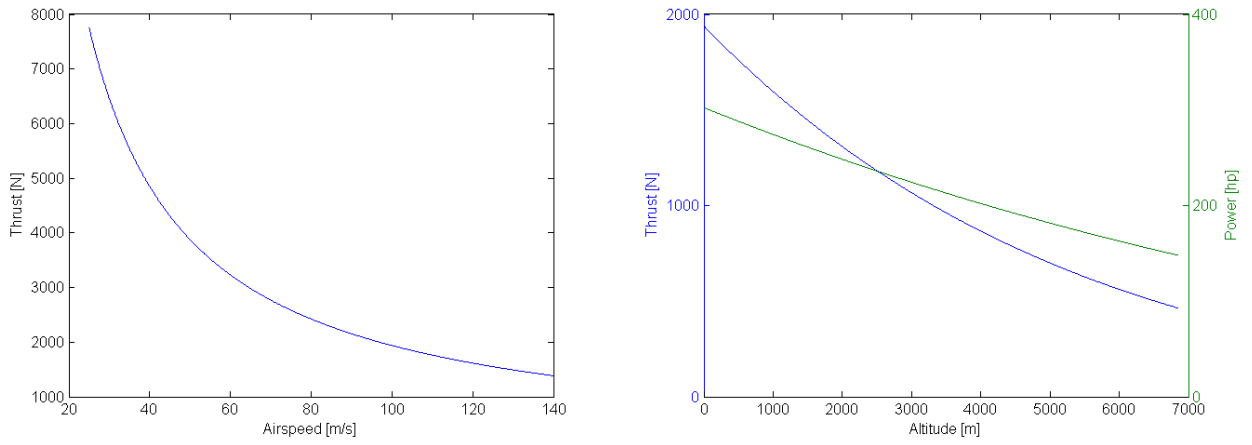
Figure 9.1: Thrust vs. airspeed at sea level and thrust and power vs. altitude at 100 m/s
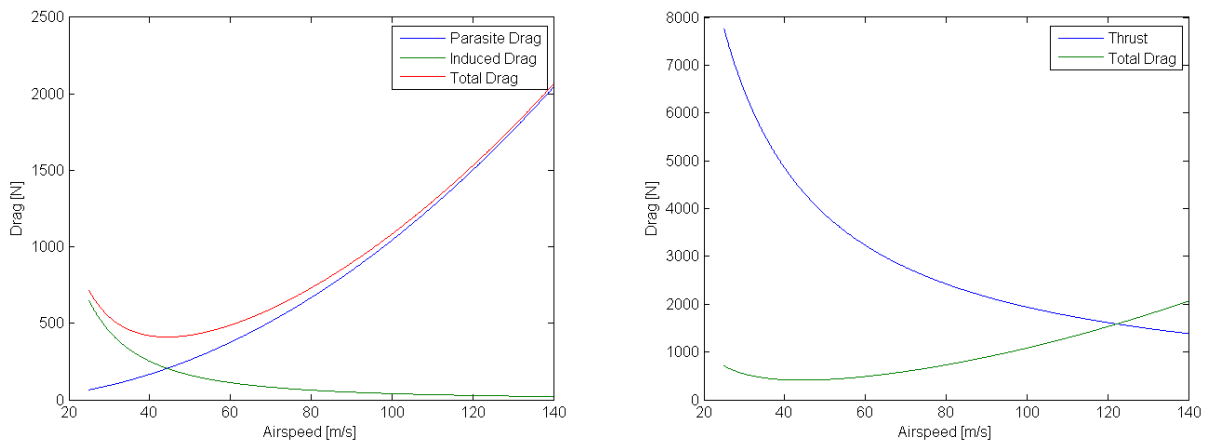
Figure 9.2: Drag at sea level and thrust vs. drag at sea level
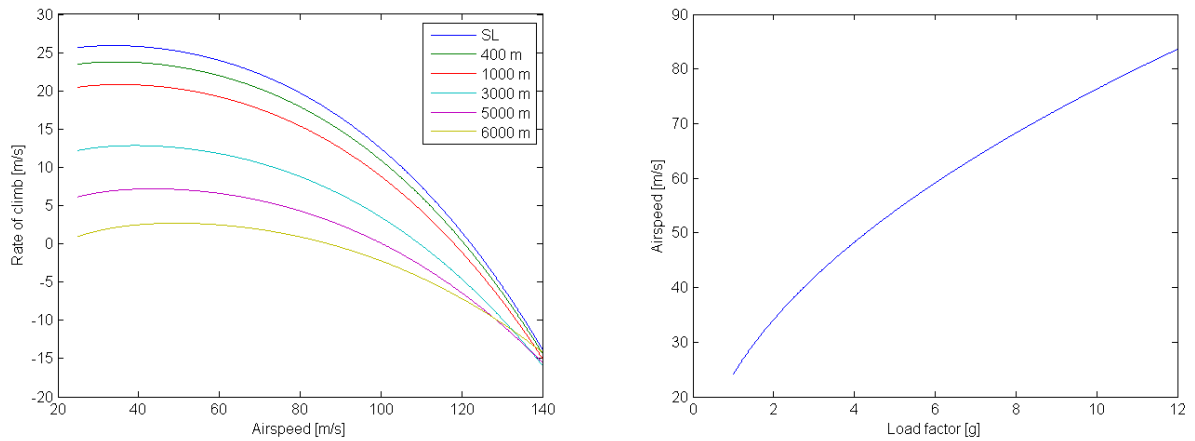
Figure 9.3: Maximum rate of climb and stall airspeed vs. load factor
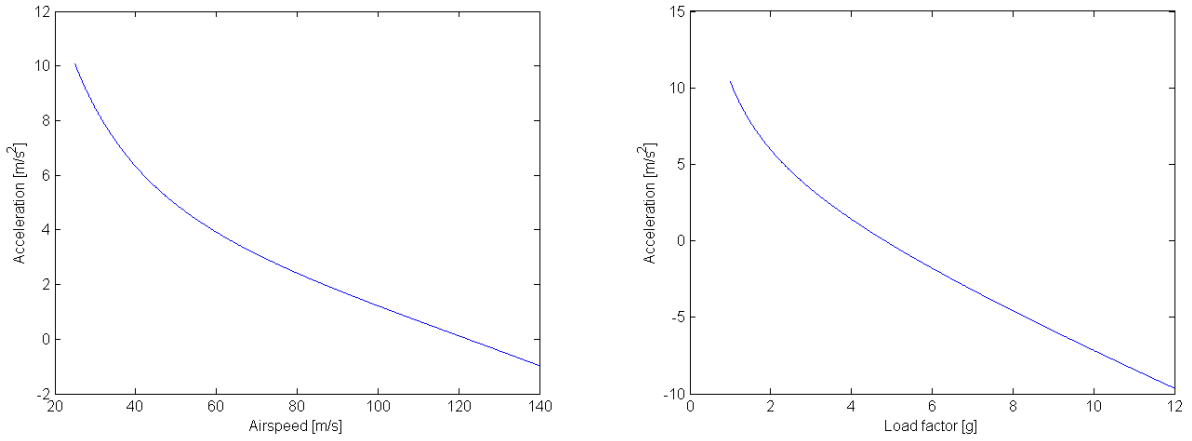
Figure 9.4: Max. acceleration vs. airspeed (at 1g) and max. acceleration vs. load factor at stall speed

The above graphs indicate the performance of the FX-15 with the 315 hp engine in order to comply with the RBAR regulations [5].

From fig. 9.1, it can be seen that the thrust is dependant on the airspeed (left graph). Furthermore, both engine power and thrust decrease with increasing altitude (right graph). Most of the performance analysis is done at sea level, where the race is flown. In fig. 9.2, the drag at sea level is plotted versus airspeed (left graph). If now the thrust is plotted together with the drag (right graph) the maximum airspeed can be obtained, which is the point where both graphs intersect. Finally, in fig. 9.3 the maximum rate of climb (left graph) is plotted for different altitudes. It can be seen that at 6000 m altitude the rate of climb is almost zero, which is also the maximum operating altitude for the engine. 6000 m can be concluded to be the service ceiling. The left graph of fig. 9.3 shows the stall speed versus the load factor, from which it can be concluded that the FX-15 has a sufficiently high $C_{L\ max}$ and will not stall during the RBAR when the fastest trajectory is flown [1]. In fig. 9.4 the accelerations are shown depending on airspeed and load factor (left graph and right graph respectively). The left graph is important for straight line speed during the race, the right graph is important for the high g turns. From this graph it can be seen that when the aircraft flies below 4.8g at its stall speed, it will be able to accelerate. When the FX-15 flies at a load factor higher than 4.8g, the aircraft will decelerate and will thus needs to decrease the load factor gradually during the turn in order to not stall.

When the 350 hp engine is used, the maximum speed is 126.8 m/s, the maximum rate of climb is 29.1 m/s at an airspeed of 33.7 m/s and the take-off distance is 138 m. All other variables will be the same as the ones which are provided in table 9.2.

Note that both landing and take-off distances are below 500 m, which means that the FX-15 complies with the landing and take-off requirements enforced by the RBAR [5].

Table 9.1: Input values for performance analysis

Parameter	Value	Unit	Source	Description
m	698.0	$[kg]$	Section 10.2	Aircraft mass
δ	1.0	$[-]$		Powersetting
η_j	0.86	$[-]$	[1]	Propulsive efficiency
P	315	$[hp]$	[5]	Engine power output
SFC	0.303	$[l/(hp\ hr)]$	[1]	Specific fuel consumption
$\eta_{transmission}$	0.96	$[-]$	Section 8.1	Transmission efficiency
ρ_{race}	1.225	$[kg/m^3]$	[10]	Air density at the race
S	9.30	$[m^2]$	Section 4.1	Wing surface area
A	7.77	$[-]$	Section 4.1	Aspect ratio
e	0.836	$[-]$	Section 4.1	Oswald factor
$C_{L_{max}}$	2.07	$[-]$	Section 4.1	Maximum lift coefficient
$C_{L_{TO}}$	0.6	$[-]$	Estimate	Lift coefficient at take-off
μ_{TO}	0.05	$[-]$	Estimate	Runway friction coefficient at take-off
μ_{land}	0.6	$[-]$	Estimate	Runway friction coefficient at landing
h_{scr}	10.7	$[m]$	[4]	Screen height
γ_{TO}	15	$[°]$	Estimate	Take-off slope
$\gamma_{landing}$	3	$[°]$	Estimate	Landing glide slope
n_{max}	12	$[-]$	[12]	Maximum load factor
$C_{D_0\ fuselage}$	$6.30(10^{-3})$	$[-]$	Section 3.11	Fuselage zero-lift drag coefficient
$C_{D_0\ wing}$	$7.05(10^{-3})$	$[-]$	Section 4.1	Wing zero-lift drag coefficient
$C_{D_0\ gear}$	$3.10(10^{-3})$	$[-]$	Section 7.8	Landing gear zero-lift drag coefficient
$C_{D_0\ horz.tail}$	$1.10(10^{-3})$	$[-]$	Section 3.11	Horizontal stabilizer zero-lift drag coefficient
$C_{D_0\ vert.tail}$	$7.40(10^{-4})$	$[-]$	Section 3.11	Vertical stabilizer zero-lift drag coefficient
C_{D_0}	$18.29(10^{-3})$	$[-]$		Total zero-lift drag coefficient

Table 9.2: Output values for performance analysis

Parameter	Value	Unit	Description
RC_{max}	25.9	$[m/s]$	Maximum rate of climb (at an airspeed of 33.7 m/s)
L/D_{max}	16.7	$[-]$	Maximum lift over drag ratio
v_{stall}	24.1	$[m/s]$	Stall airspeed
s_{land}	398	$[m]$	Landing distance
$s_{takeoff}$	145	$[m]$	Take-off distance
V_{max}	122.3	$[m/s]$	Maximum (cruise) speed
R_{50l}	184	$[km]$	Range with 50l of fuel (with 10 l reserve) at maximum cruise speed
R_{83l}	337	$[km]$	Range with 83l of fuel (with 10 l reserve) at maximum cruise speed

9.4 Conclusion & Discussion

It can be concluded that the FX-15 meets all of the performance related requirements. Only the design cruise speed of 450 km/h (=125 m/s) can not be flown with the 315 hp engine. However, the 350 hp engine is powerful enough to reach this speed. The load factor (of ±12g) that can be reached during the race is sufficient to fly the tight turns in order to achieve the fastest time, since only a maximum load factor of 10g is allowed during the race. Another interesting aspect is that the range with a 22 gallon (=83 l) fuel tank increases from 184 km to 337 km (these ranges do not include loiter, however 10 l of reserve fuel is included for safety). This significant range increase is beneficial for end-of-season purposes.

According to the RBAR regulations [11], the minimal race mass should be 698 kg. As can be seen in section 10.2, ballast will be added to achieve the minimal race mass of 698.0 kg. This means that practically the maximum possible performance is reached in a race session. Another interesting comparison to make is the maximum speed of the FX-15 compared to the already competing aircraft. The FX-15 has a top speed of 122.3 m/s while the Zivko Edge 540, the MSX-R and Corvus CA-41 all have a top speed of 118 m/s [49] [51] [7], indicating that the drag of the FX-15 is slightly lower. Thus it can be concluded that the FX-15 has a very decent chance to beat the competition and win the RBAR.

10 Final Design

There are many aspects involved in the development of an aircraft design. Extensively discussing all aspects in one chapter is hardly possible due to the extent of the project. This chapter, however, will summarize all main aspects. The topics that will be discussed concern the aircraft parameters such as: geometry, mass, costs and performance. The final design will be recapped in the first section. It will include illustrations and explanations regarding the complete aircraft design and the modularity of the design. The section that follows contains tables with the mass and cost breakdowns of the aircraft. It will give an insight in the performance and unit cost of the FX-15. The chapter will be concluded by checking whether the final design complies with the requirements as stated by FlashCo. (and other stakeholders).

10.1 Description of Final Design

The design of the FX-15 subsystems has extensively been discussed from chapter 4 to chapter 8. The assembly of all these subsystems forms the complete final design of the aircraft. This section will describe and illustrate the final design of the FX-15, it will include technical drawings and elaborate on the modularity of the aircraft. The complete aircraft design in terms of parameters can be found in appendix A.

10.1.1 Technical Drawings

Scaled drawings of the side and top view of the FX-15 can be found in appendix B. Fig. 10.1 shows the side view of the FX-15. The skin of the aircraft has been removed, exposing the locations and placing of the different subsystems. All major components and subsystems can be seen in the figure, the different colors depict the different subsystems: blue for the truss structure, grey for the propulsion group, yellow for the control system group, green for the fuel tank, and purple for the CCT box.
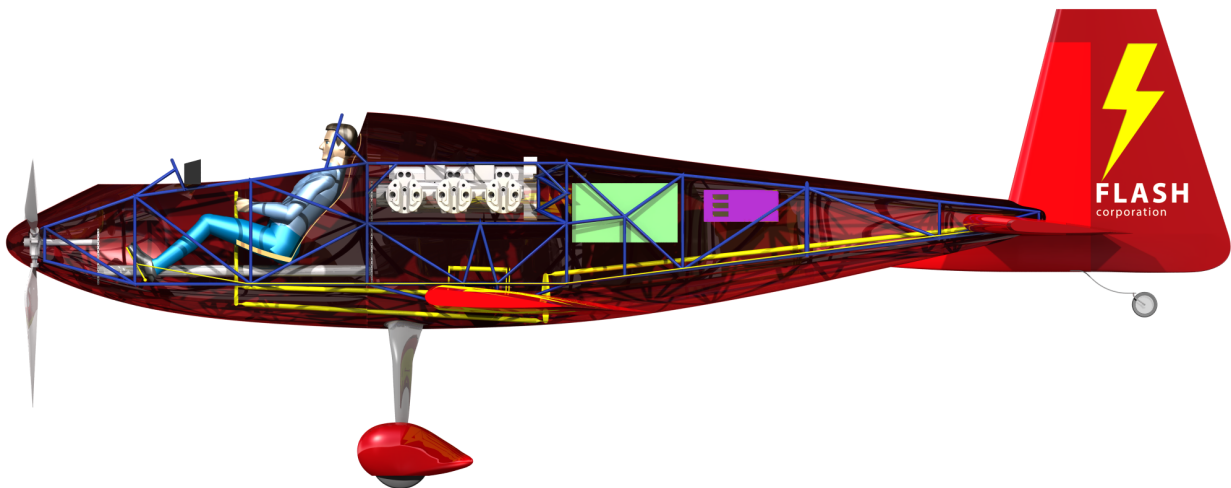
Figure 10.1: A side view of the FX-15 showing the major subcomponents

10.1.2 Modularity

The modularity of the FX-15 is an important aspect of the final design, it is needed for maintenance, transport and sustainability. In this section, the modularity of the aircraft will be discussed and illustrated using figures.

The entire wing will be taken out through the bottom of the fuselage for transportation. In fig. 10.2 the trusses that have to be removable for the modularity of the wing are highlighted. The main spar will be bolted to brackets on the truss structure. The ailerons will be easy to dismantle for quick maintenance.
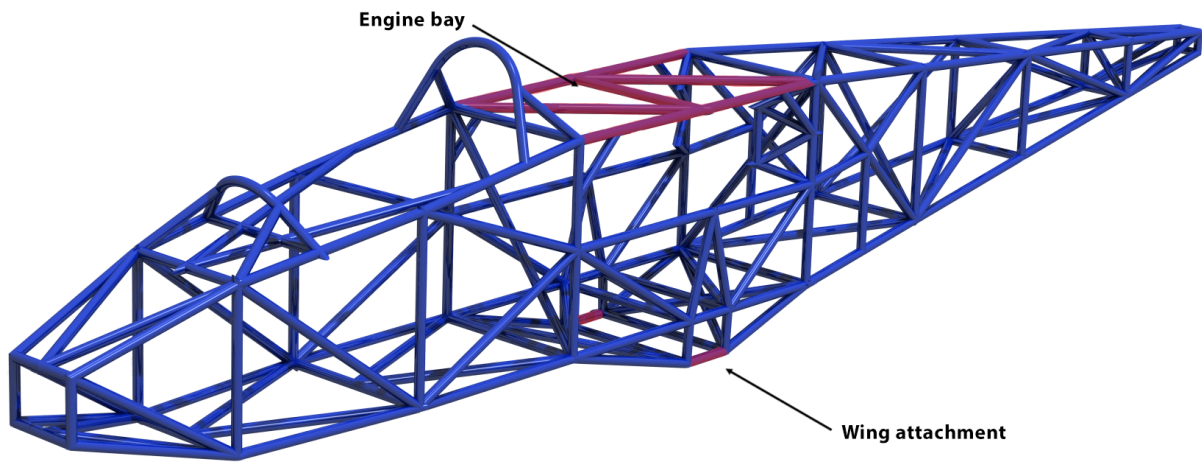
Figure 10.2: Removable trusses

The engine must be easy to access and replace. Therefore, the highlighted trusses in fig. 10.2 have to be removable. Fig.10.3 shows a possible connecting method for the removable trusses [89].
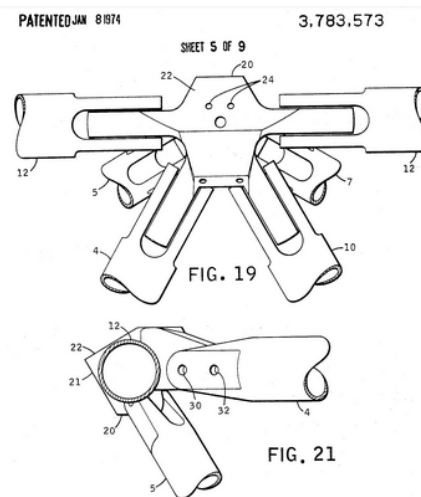
Figure 10.3: Truss joining method [89]

The horizontal and vertical tailplanes will be removed individually. The elevator and rudder do not have to be removed for transportation. However, they are easy to replace. The modular design of the empennage will be based on the Corvus CA-41 Racer as depicted in fig. 10.4 to fig. 10.7 included [7].
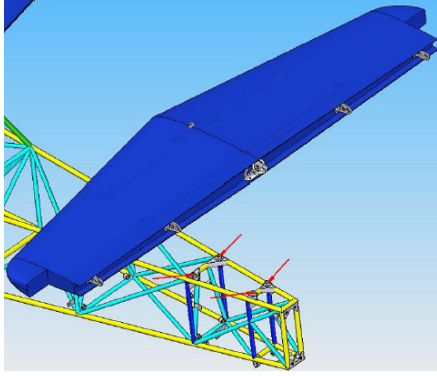
Figure 10.4: Modularity of horizontal tailplane
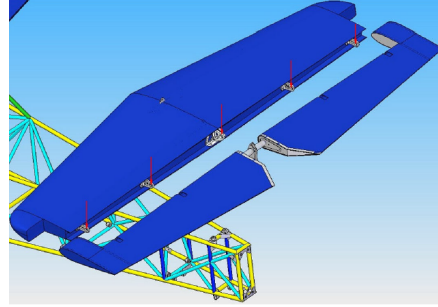
Figure 10.5: Modularity of elevator
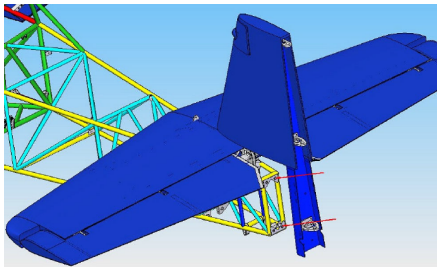
Figure 10.6: Modularity of vertical tailplane
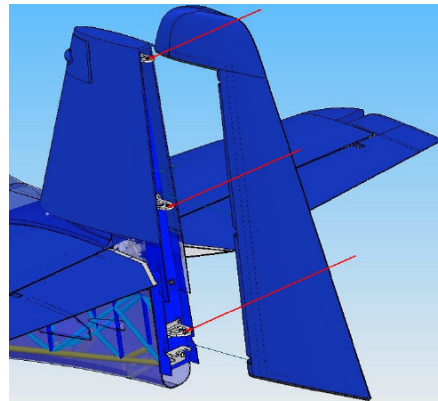
Figure 10.7: Modularity of rudder

10.2 Mass & Cost Budget Breakdown

Table 10.1 shows the contribution to the total race mass of the different aircraft components. The Class II weight estimation is updated with the output values from the detailed design phase. In addition, the mass of the components that were designed into detail are given and completed with existing parts to come to a more detailed mass breakdown. As can be seen in the table, the total race mass is 681.1 kg. This is lower than the requirement of a minimal race mass of 698 kg [5]. Ballast can be added at a convenient location to ensure compliance with the minimal required race mass. The unit cost requirement of the FX-15 is a driving requirement. Therefore a market analysis has been performed to ensure that the unit cost limit is not exceeded. The aircraft is broken down into several subsystems for the budget estimate. These subsystems and their estimated cost range are shown in table 10.2.

Table 10.1: Mass budget breakdown

Class II	mass [kg]	Detailed design	mass [kg]	Source
Wing group	106	Wing group	106	
		Spar	60	Section 4.3.6
		Skin and ribs	46	Section 10.2
Surface control group	20.2	Surface control group	20.2	Section 10.2
Tail group	32.1	Tail group	32.1	Section 10.2
Landing gear group	37.3	Landing gear group	19	
		Main gear strut	5.2	Section 7.4.2
		Main gear wheel kit	5.6	[56]
		Main gear tire	6	[57]
		Tail gear	2.2	[58]
Fuselage group	76.7	Fuselage group	81.9	
		Structure	48.8	Section 5.3.3
		Structural joints	4.9	Estimate
		Skin	28.2	Section 5.3.3
Propulsion group	255.6	Propulsion group	255.9	
		Propeller	27.6	[7]
		Transmission	9.2	Section 8.1
		Air intake and cooling	2	Section 8.2.4
		Engine	212.2	[7]
		Propeller pitch control	0.1	[79]
		Exhaust system	3	[7]
		Transmission casing	1.8	Estimate
Safety systems	16.5	Safety systems	4.3	
		Harness	2	[7]
		Firewall	2.3	Section 8.6
Equipment	41.2	Equipment	37.2	
		Fuel tank	9.5	[82]
		CCT box	12.1	[5]
		Smoke generator	7	[90]
		Battery	3	[80]
		Cockpit instruments	4.1	[91]
		Exterior lighting	0.1	[92]
		Pilot seat	1.3	[93]
Empty mass	**585.6**		**556.6**	
Fuel mass	59.6		59.6	Section 8.6
Payload mass	204.4		233.4	
Take-off mass	**849.6**		**849.6**	
Fuel mass race	36		36	[11]
Payload mass race	88.5		88.5	[5]
Ballast mass			16.9	
Race mass	**710.1**		**698**	

Table 10.2: Estimated subsystem and total unit cost ranges

Subsystem	Minimum cost [€]	Maximum cost [€]
Fuselage group	9 600	12 300
Wing group	10 800	14 100
Control surfaces group	900	2 200
Propulsion group	85 500	87 000
Tail group	2 500	5 000
Avionics group	4 000	9 000
Landing gear group	3 400	5 100
Safety systems group	1 400	1 400
Production & assembly	42 000	49 000
Paint job	2 500	4 500
Miscellaneous	2 000	2 500
Total unit cost	**164 600**	**192 100**

Table 10.2 is based on the cost estimation from the baseline report [24]. However, some values have been updated. The main difference is that the wing cost has increased significantly in comparison with the previous estimation. This is because the previous estimate accounted for a metal wing while a carbon fiber wing is used for the FX-15. The fuselage price also increased due to the CFRP skin. Also the production & assembly cost has been estimated to increase because the FX-15 is a more complex aircraft compared to reference aircraft, thus 500 additional working hours have been taken into account for production and assembly. A paint job has been taken into account together with miscellaneous parts. Among these are fuel lines, electrical wires, lights, and more. Note that when the FX-15 participates in the RBAR, the €39 000 propeller will be sponsored by Hartzell, thus reducing the unit cost. It is also possible to add a turbocharger to the FX-15. This turbocharger will add €18 775 to the total unit cost.

10.3 Compliance Matrix

This section shows the compliance matrix of the FX-15, in which the requirements which are stated by FlashCo. are compared with the actual performance of the FX-15.

Table 10.3: Compliance matrix

Requirement	Required	Obtained	Requirement met?
Aerobatic aircraft	-	-	yes
Crew	1 pilot	1 pilot	yes
Design cruise speed	450 km/h	440 km/h	no/yes[1]
Service ceiling	5000 m	$\approx$ 6000 m	yes
Rate of climb	18 m/s	25.9 m/s	yes
Maximum load factor	12g	12g	yes
Start gate speed	370 km/h	440 km/h	yes
Wing span	max 8.50 m [5]	8.5 m	yes[2]
Unit cost	max €275 000	max €192 10	yes
First flight	2017	TBD	-[3]
Transport	modular	modular	yes
End − of − life disposal plan	yes	yes	yes
Production facilities	home-built	home-built	yes
Comply with CS23 regulations	checked where applicable	checked where applicable	yes
Comply with RBAR regulations	checked	checked	yes

[1] The design cruise speed requirement could not be met with the 315 hp engine, however, the FX-15 fitted with the 350 hp turbocharged engine can achieve a maximum speed of 450 km/h. This has been brought to FlashCo.'s attention.

[2] Project guide states that the wing span should not be higher than 7.6 m, however, the RBAR regulations allow a maximum wing span of 8.5 m. After a discussion with FlashCo., the requirement was dropped.

[3] Can not be determined at this stage of the project.

11 Sustainable Development

This chapter outlines the appraoch regarding sustainable development. First, the influence on society will be discussed in section 11.1. Second, the environmental impact will be outlined in section 11.2. Finally, the economic sustainability will be discussed in section 11.3.

11.1 Society

Aeronautical design has been characterized by gradual evolution over the past decades. This causes many aircraft to be depressingly similar in terms of appearance, configuration, and performance. Yet once in a while an aircraft appears that breaks this habit. One of these aircraft was the SR-71. The SR-71 was a true marvel of engineering and perhaps one of the most inspiring aircraft ever built. Thousands upon thousands of young engineers and aviators were inspired by the radically different design and capabilities of the SR-71.

Needless to say, there is no comparison between the SR-71 and the FX-15. However, the FX-15 was deliberately designed to be an innovative and extraordinary aircraft. It will easily stand out at any race it flies. The design is meant to show the world that one does not always have to adhere to proven lay-outs and that thinking out of the box can be rewarding in the long run. It will inspire a new generation of engineers and aviators to think out of the box and come up with new ideas, just like the SR-71 did. New ideas are needed to push the state of the art of aeronautical engineering forward and thereby enable new aircraft designs with superior efficiency and performance to today's aircraft. It is important to win a race, but it is equally important to inspire the audience.

11.2 Environment

An important aspect of sustainability is the impact of a product on its environment. This section outlines the reduction of environmental impact throughout the lifecycle of the FX-15.

11.2.1 CO_2 footprint

CO_2 emissions of aviation gasoline amount to 2.2 kg/L [94]. The engine of the FX-15 burns 95 L/h at a velocity of 440 km/h. This results in fuel burn of 0.22 L/km which amounts to 0.475 kg of CO_2 emissions per km. To put this number into perspective, a round trip of an Airbus A380 between London and Sydney results the same amount of carbondioxide emissions as during 6000 hours of flying the FX-15 [95, 96]. This illustrates how negligible the total contribution of the FX-15 to the earth's greenhouse gases really is.

11.2.2 Modular Design

One of the features of the FX-15 is a modular design. This allows for components to be replaced by better performing components as the aircraft matures. The advantage of this feature is postponement of aircraft replacement, thereby reducing waste of resources.

11.2.3 End-of-Operations Plan

Despite modular improvements, the day will come when the FX-15 becomes obsolete as newer aircraft surpass its performance. It was decided to donate the FX-15 to the Deltion College in Zwolle, the Netherlands, when that day comes. The Deltion College is a renowned institution for aircraft maintenance training. The FX-15 can be studied and used by students for many decades even after its last flight, thereby increasing the longevity of the aircraft. Hopefully some of these students will be inspired by the FX-15 to come up with new innovations for future aircraft.

11.2.4   End-of-Life Plan

The materials and components of the FX-15 will be recycled as much as possible. Here follows a brief description of the recycling plan ordered by material:

Steel. The truss structure of the FX-15 is made of steel. The truss structure will be melted to reuse the steel in other applications.
Aluminum. The engine which is made of aluminum will be melted to recycle the aluminum.
Plastics. Any components made of plastics (such as the canopy, pilot seat and instrument panel) will be melted so the plastic can be cast or extruded again.
Composites There is no sustainable process to recycle composites at the current state of technology. However, a lot of research is being done in this area and it is not unreasonable to expect new sustainable solutions to appear during the lifetime of the FX-15.
Instruments and electronics. Instruments and avionics will be refurbished and reused in other aircraft.

11.3   Finance & Economy

The FX-15 will generate a lot of publicity for FlashCo. Furthermore, it will improve the brand image as an innovative market leader. This will cause a sustained increase in FlashCo.'s sales.

The budget allocated for the FX-15 is almost fully utilized. This can be seen in section 12.3.1. The remainder of the budget will be used for sustainable purposes. The aircraft will win the RBAR and generate large returns in the form of publicity. The aircraft will subsequently be donated to an aircraft maintenance school and thereby have a positive impact on the public relations of FlashCo. Each part will be refurbished or recycled at the end of the aircraft's lifecycle. This means that usage of the aircraft is maximized in every possible way throughout the FX-15's lifecycle.

12 Project Design & Development Logic

This chapter describes the steps that must be taken to continue the development of the FX-15. The manufacturing, assembly & integration plan discusses the production of all the subsystems and the assembly of the entire aircraft. The aircraft life and procedures regarding emergencies, maintenance and transportation are presented next. The business plan is elaborated on after this, including an analysis of the market and return on investment. The chapter is concluded with a risk assessment.

12.1 Manufacturing, Assembly & Integration Plan

The manufacturing, assembly and integration of the FX-15 is the phase starting after the detailed design where the parts have been designed and the materials used have been designed. The main materials that are used in the FX-15 are AISI 410S steel, HexPly 8552 IM7 (layered into a laminate), Divinycell HT131, CFRP (for the skins) and AL2014-T6. The steel, CFRP and AL2014-T6 can be purchased at multiple suppliers. HexPly 8552 IM7 will be ordered at Hexcel and Divinycell HT131 will be ordered at DIAB.

The production of each of the main FX-15 subsystems is discussed below. All of the mentioned production processes can be performed at TU Delft in The Netherlands.

- The fuselage structure will be produced by welding the AISI 410S steel tubes into a truss structure.
- The wing main spar will be produced by winding the HexPly 8552 IM7 prepreg around a mold of the spar and using an autoclave to cure it. The exact curing process is described at Hexcel [30]. After curing, the carbon fiber spar shell will be joined with the Divinycell HT131 foam by adhesive bonding. The Divinycell HT131 foam will be milled into the right shape.
- The fuselage skin, wing skin and tail skin will be produced by winding the CFRP prepreg around molds of the fuselage, wing and tail and curing them in an autoclave.
- The landing gear will be produced by forming the AL2014-T6 into the right shape.

To avoid unnecessary waste, lean manufacturing is applied. An overview of the manufacturing, assembly & integration process is shown in fig. 12.1.
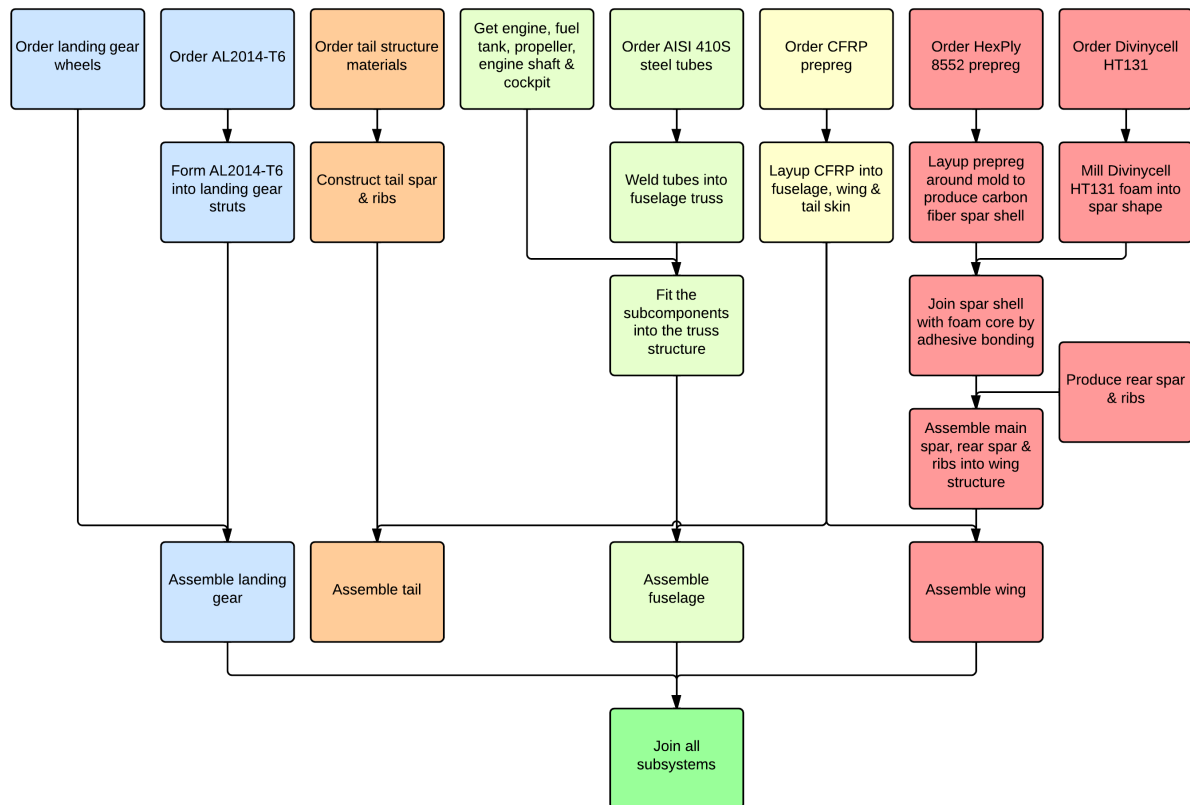
Figure 12.1: Overview of the manufacturing, assembly & integration process

12.2 Operations & Logistics

This section describes the operations and logistics of the FX-15. The focus lies on special operations surrounding the races, such as certain procedures in case of emergencies, maintenance and transportation. It does not lie on aircraft control, because flying the race itself is relatively straightforward and explained in flight school.

12.2.1 Operations

During the operating life of the aircraft, the pilot and mechanics still have a lot to do with and around the aircraft. The pilot has to be safe when flying the aircraft and the mechanics will have to perform maintenance in order to keep it operable.

Safety

In case of an emergency the pilot has to be able to save at least himself and if possible the aircraft. No standard procedure exist for handling an emergency because every emergency is different. The following sections will explain what design choices have been made in order for the pilot be safe during a calamity. The Red Bull Air Race regulations [5] and the emergency procedures as described in the 3rd chapter of the Extra 300S Information Manual [50] are used as reference.

According to the RBAR Technical regulations the cockpit has to be designed as such that the pilot can easily escape the cockpit in case of an emergency, even if the aircraft is submerged under water. The regulations state that "the respective Race Pilot shall be able to demonstrate exiting the cockpit within 10 seconds." Using the Extra 300S as a reference, the following bail-out procedure has been defined [50]:

1. Reduce speed to 100 Kts

2. Pull mixture to lean

3. Open canopy

4. Take off headset

5. Open seat belt

6. Leave aircraft

7. Try to avoid wing and tail

8. Open parachute

During the procedure described above, the low pressure on top of the fuselage will suck the canopy away from the fuselage, after which the pilot can easily climb out. When entering and exiting the aircraft on ground, the canopy should open to one side, but in order to facilitate this bail-out, the canopy will be able to come off completely.

In order to keep the pilot safe from fire, a firewall is placed between the cockpit and the engine. This firewall should be padded with a fire resistant material. The design of the firewall is explained in detail in section 8.6. In case of fire, the following procedure should be followed:

1. Shut off fuel valve

2. Turn off master switch

3. Land as soon as possible

4. If landing is not possible or aircraft has become uncontrollable, start bail-out procedure as described above.

A firewall will protect the cockpit in case of fire, RBAR Technical Regulations [5] state that if the aircraft "is manufactured of steel tube [it] should be padded with at least 0.02 m of appropriate fire resistant materials, applied where possible." As the fuselage of the FX-15 is a truss structure, this will be applied as pilot safety is a very important aspect of the aircraft design.

Maintenance

Maintenance is a very important aspect of the aircraft operations and has to be taken into account to ensure that the aircraft can be operated safely. Due to the racing schedule, time is a very important factor. Maintenance should be thorough, but not time-consuming. To meet these requirements, two aspects will be discussed. The first is accessibility and the second is the time aspect.

Every part of the aircraft has be designed in such a way that it is possible to repair or replace it without having to take the entire aircraft apart. This is important because parts that are not easily accessible are more likely to be overlooked during quick maintenance. This could lead to dangerous situations if small cracks or other failures are not detected. This is also one of the reasons the FX-15 is a modular aircraft.

Time is very important in the racing world and not only during races. All aspects of aircraft operations should be as efficient as possible. This means that the maintenance and replacement of parts is taken into account during the design of the FX-15. Especially parts that are more likely to fail are designed in such a way that they can be replaced quickly. The fact that it takes less time to replace parts is another reason a modular design was chosen.

12.2.2 Logistics

In between races all the aircraft and crew and entire Red Bull Air Race stage need to be transported. The transportation and logistics are all managed by Red Bull. This section will focus on the logistics of the FX-15 in between races during the 2017 season. In this section, it is explained how the logistics in between races will be managed during the 2017 season.

As the RBAR organization facilitates the transport of the aircraft, the FX-15 should be designed to fit in the transportation aircraft used by Red Bull. This means that the aircraft has to be modular. The wing and empennage are disassembled from the fuselage, and these three parts are then transported individually.

The fuselage is wrapped with a protective foil and the wing and tail are transported in cases. In fig. 12.2 it is shown how Chambliss' team approaches the logistics problem.

(a) Fuselage

(b) Wing

Figure 12.2: Transportation method applied by Team Chambliss

The FX-15 has a detachable wing, and the structure of the empennage is designed for modularity. The wing is located on the bottom side of the aircraft. After races, the wing can be lowered out of the fuselage structure which facilitates easy disassembly. The modularity has already been explained in detail in section 10.1.2.

12.3 Business Plan

The business plan of the FX-15 is elaborated on in this section by explaining the market analysis and analyzing the return on investment.

12.3.1 Market Analysis

A market analysis has been done in order to see whether the FX-15 has a healthy future. Because the FX-15 is designed for a very specific purpose (winning the RBAR), the market analysis differs from market analyzes that are performed for general aviation aircraft.

The aerobatic racing aircraft market is relatively small, but the exceptional performance of the FX-15 may lead to a relatively big marketshare. Twelve pilots fly in the master class, so there are 12 possible customers for the RBAR. Furthermore, the FX-15 can be used by other aerobatics pilots to fly airshows. Reference aircraft like the Corvus CA-41, the MSX-R, the Extra 300S and the Zivko Edge 540 all have a unit cost ranging from €240 000 to €280 000 [97] [51] [98] [99]. This means that the FX-15 is cheaper than its competition (although this may be because development costs of the FX-15, estimated to be around 72000 euro, are not included in this estimate) (section 10.2). It is also expected that the FX-15 will need more maintenance than its competitors because it is a more complex aircraft. The total market for the FX-15 is estimated to be 18 customers. If now an average price for an aerobatics racer is set at 260 000 euro, the market volume can be determined to be around 4 680 000 euro.

12.3.2 Return on Investment

The current market mainly consists of aircraft like the Corvus CA-41, the MSX-Rand the Zivko Edge 540. These aircraft are aerobatic aircraft which participate in the RBAR. The FX-15 is designed as a racing aircraft which can perform aerobatic maneuvers. From the performance analysis chapter 9, it turned out that the FX-15 is slightly faster than the competition, and thus has a decent chance to win the RBAR. For a company like FlashCo., a victory in a race hosted by the main rival (Red Bull), would ensure a lot of

publicity. This publicity will be beneficial for their sales. Another strong aspect of the FX-15 is its innovative design. Even when the FX-15 will not win the race, FlashCo. will get publicity because of this eye-catching design. Furthermore the (design of the) FX-15 will be published in the Leonardo Times magazine, which also provides publicity for FlashCo..

It is clear that the return on investment will mainly be dependent on the publicity that the FX-15 will gather. This publicity will ensure more sales for FlashCo. because new target groups and sales markets can be reached worldwide. However, the determination of this sales increase is beyond the knowledge of this group and will need to be analyzed by FlashCo. itself.

A part of the investment can be recuperated with the end-of-life plan, which is described in chapter 11.

12.4 Risk Assessment

Since the design phase of the FX-15 has been concluded and this report is the final report written by the design team of the FX-15, the risk analysis will be focused on the phases that will follow after the design phase. The risk assessment in this section is meant as a tool for risk mitigation and control for the different groups and individuals that will work on the (further development,) production and operations of the FX-15 in order to ensure victory for the FX-15 at the RBAR World Championship 2017 for FlashCo.

Some risks regarding production and operation have already been identified in the baseline report [24]. These risks will be revised and analyzed. The Delphi technique was used to find an unbiased opinion of each individual member of the design team of the FX-15 regarding the consequences and probabilities of occurrence of these risks. The risks are stated and summarized:

- **M1: A delay occurs during production.** The design of the FX-15 does contain some complex and complicated components and subsystems to fabricate, however, it is not expected that this poses great risks for the project. The consequence of short delays could be significant, but the probability is assumed low.

- **M2: Supplier default.** The used subsystems and materials for the design are widely used and available. The probability and consequence are assumed low, since alternative suppliers are available.

- **M3: Miscommunication 3rd party.** The used components and materials for the design are hardly complex or complicated, ensuring low probability and low consequences of miscommunications.

- **M4: Production error.** The risk of a production error is assumed low from a design point of view, with a low probability and a marginal to significant impact.

- **M5: Assembly error.** The risk of assembly error from a design point of view is assumed significant, the assembly of the unusual engine configuration could pose problems.

- **S1: Engine failure due to underdesigned propulsion system.** The usage of a transmission system from engine to propeller increases the risk of engine failure due to the increase of the number of intermediate subsystems/components that can fail.

- **S2: Damage during transport caused by wrongly designed transport system.** The FX-15 is easy to disassemble ensuring minimal probability for errors.

- **S3: Aircraft design does not perform well enough to assure victory at RBAR.** The design of the FX-15 is highly innovative and expected to be very fast. However, without actual flight tests chances are that the aircraft design will not assure victory. Medium probability and catastrophic consequences.

- **S4: Control surface failure due to under designed steering system.** The risk of failing control surfaces is existent, the control surfaces have been extensively investigated, however, stick forces have not been analyzed in this report. It is expected that the probability is low, and the consequences marginal.

- **S5: Small modifications required affecting aircraft performances.** The detail design of the FX-15 is as complete as possible all aspects of the aircraft have been analyzed. The chances of required modifications are low, the consequences could be significant.

- **S6: Undetectable structural damage.** The RAMS analysis for the different structures reduces the chances of this and the strong design ensures that consequences will not be critical.

- **S7: Poorly performed maintenance.** A service manual remains to be written. However, at this stage there are no indications that maintenance will be more complicated or complex than any other aerobatic racing aircraft.

The results of the risk analysis are plotted in a risk map, see fig. 12.3.
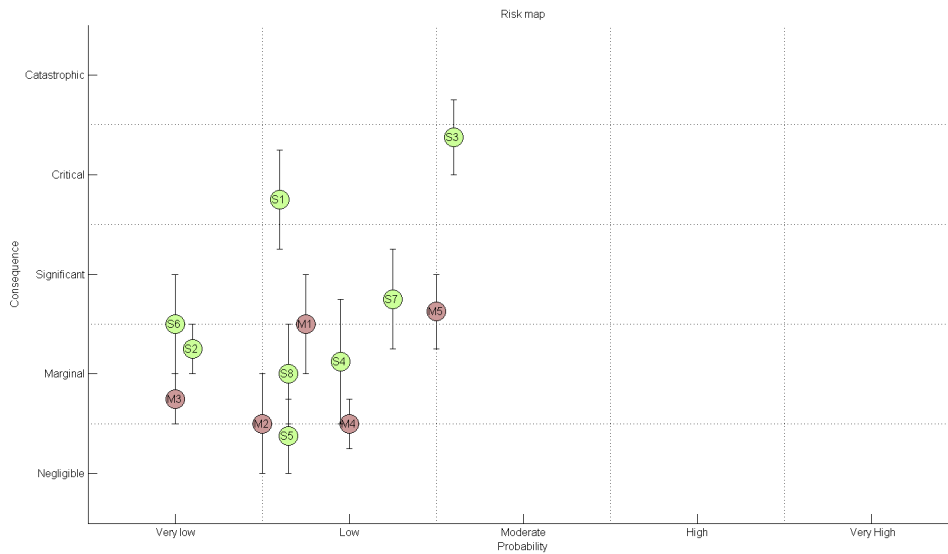
Figure 12.3: Risk map

Risk Mitigation and Control

Appendix B in the Baseline report [24] provides an extensive and detailed risk mitigation strategy for each of the risks. For risk mitigation and control these guidelines for risk mitigation should constantly monitored, updated and improved throughout the entire production and operations phase. If risk mitigation and control are performed well, nothing will stand in the way of a successful performance of the FX-15 at the 2017 edition of the RBAR.

13   Conclusion & Discussion

The design of the FX-15, a modular aerobatic race aircraft designed to win the 2017 Red Bull Air Race Championship, has been presented in this report.

The aircraft's 9.3 m^2 wing generates a lift coefficient of up to 2.07 using the custom designed NACA 0011-61MOD airfoil. The wing span was set to 8.5 m, the upper bound of the allowable range, to reduce drag to a minimum. In the event of a stall, separation will safely start at the root of the wing as a result of the taper ratio of 0.6. The aerodynamic loads are carried by a custom HexPly 8552 IM7 laminate spar filled with Divinycell HT131 foam. The engine was placed in the center section of the fuselage to permit a smooth and streamlined fuselage shape with a zero-lift drag coefficient of merely 0.0063. A truss structure made of AISI 410S stainless steel tubes bears fuselage loads of up to ±12g. A system of shafts, sprockets, and chains ascertains a reliable transmission of the 315 horsepower generated by the Lycoming Thunderbolt AEIO-540-D engine to the 3-bladed Hartzell 7690 composite propeller. The FX-15's maximum roll rate of 440 °/s is achieved by large ailerons spanning more than half of the wing. The empennage was designed for sufficient stability and control, resulting in a horizontal stabilizer area of 2.1 m^2 and a vertical stabilizer area of 1.7 m^2. The aircraft's empty mass amounts to only 556 kg despite unconventional and innovative features. The aircraft's ability to carry a payload of 233 kg and and a fuel load of 60 kg results in a maximum take-off weight of 850 kg. However, the race mass amounts to 698 kg because it is neither necessary to fly a race with full fuel nor maximum payload. The weight is carried by an undercarriage consisting of two main gears and a small tail wheel in a taildragger configuration.

Designing the FX-15 was certainly not a trivial task. The applied aerodynamic solver was unable to compute viscous drag for complex wing geometries, forbidding the design of proper wingtips or even winglets. However, it is certainly recommendable to look into wingtip devices in the future. The fiber layout of the spar could not be optimized due to time constraints. Optimizing the fiber layout could yield significant improvements of the wing structure in the future. It was a challenge to fit the transmission system in the confined space of the fuselage and to protect the pilot from fast moving components in the event of a failure. Aerodynamic design of the undercarriage was troubled by vast amounts of time necessary to run a CFD simulation. A particularly challenging aspect of the design of the empennage was to ascertain the ability to quickly recover from a spin.

The FX-15 meets all requirements set by FlashCo. The service ceiling of approximately 6000 meters exceeds its requirement by 1000 meters. The required climb rate of 18 m/s is surpassed by more than 50%. The wing is designed to generate the large amounts of lift necessary to fly maneuvers at load factors of up to 12, as set per requirement. A positive side effect caused by this particular wing design is a very low stall speed, undercutting the required 31 m/s by 7 m/s even at its maximum takeoff weight of 850 kg. The required cruise speed of 450 km/h is met with an optional turbocharger. Red Bull Air Race regulations exclude turbochargers but the largest velocity reached during a race is 370 km/h at the start gate, a velocity easily attained with an unmodified engine. The aircraft can be produced at a unit cost of €192 100, well below the allocated budget of €275 000.

The FX-15 supports sustainable development by inspiring the next generation with its unique design. It will inspire them to come up with new ideas that are needed for solutions to a more sustainable world. Continuing this line of thought, it was decided to donate the FX-15 to an aircraft maintenance school at the end of its flying career to serve its last purpose as training material for a new generation of aviators and engineers.

Bibliography

[1] C. Liem. *Trajectory Optimization of an Aerobatic Air Race*, 2009.

[2] DSE Group 15, Kluyverweg 5. *Aerobatic Racing Aircraft Design Midterm Report*, May 2014.

[3] Ir. Joris A. Melkert. AE3021 Aircraft Design - Preliminary Sizing of Aircraft.

[4] European Aviation Safety Agency, Brussels, Belgium. *Certification Specifications for Normal, Utillity, Aerobatic & Commuter Category Airplanes*, November 2003.

[5] Red Bull Air Race, Race Committee, Petersbrunnstrasse 17, Salzburg, Austria. *Red Bull Technical Regulations*, March 2010.

[6] Aviation Gasoline 100LL. `http://www.etc-cte.ec.gc.ca/databases/Oilproperties/pdf/WEB_Aviation_Gasoline_110LL.pdf`. [Online; accessed 08-06-2014].

[7] Corvus Aircraft, 6035 Ballószög II. Körzet 35. *Corvus CA-41 Racer Information Manual*, May 2010.

[8] Dr. J. Roskam. Part I: Preliminary sizing of airplanes.

[9] D.P. Raymer. *Aircraft Design: A Conceptual Approach*. AIAA Education Series. American Institute of Aeronautics & Astronautics, 2006.

[10] Standard Atmosphere Computations. `http://aero.stanford.edu/stdatm.html`. [Online; accessed 20-05-2014].

[11] Red Bull Air Race, Race Committee, Petersbrunnstrasse 17, Salzburg, Austria. *Red Bull Technical Regulations*, March 2014.

[12] Delft University of Technology. *Project Guide Design Synthesis Exercise*, April 2014.

[13] Dr. J. Roskam. *Airplane Design Part III*. Roskam Aviation & Engineering Corporation, 1st edition, 1986.

[14] Dr.ir. G. La Rocca. Aerospace design & systems engineering elements II.

[15] E. Torenbeek. *Synthesis of Subsonic Airplane Design*. Delft University Press, 1st edition, 1982.

[16] JavaFoil — Analysis of Airfoils. `http://www.mh-aerotools.de/airfoils/javafoil.htm`. [Online; accessed 29-05-2014].

[17] D. Howe. *Aircraft Conceptual Design Synthesis*. Professional Engineering Publishing Limited, 1st edition, 2000.

[18] Lycoming - Engine Data. `http://www.lycoming.com/Lycoming/PRODUCTS/Engines/Certified/540Series/EngineData.aspx`. [Online; accessed 09-05-2014].

[19] Ir. Joris A. Melkert. AE3021 Aircraft Design - Improved Drag Prediction.

[20] Mark Drela. XFOIL: An Analysis and Design System for Low Reynolds Number Airfoils. 1988.

[21] A. Elham. Weight Indexing for Multidisciplinary Design Optimization of Lifting Surfaces. `http://repository.tudelft.nl/view/ir/uuid%3A253459bb-e20b-4165-b093-81b1a8cf3a79/`. [Online; accessed 17-06-2014].

[22] H. Abbott, Albert E. von Doenhoff. *Theory of Wing Sections*. Dover Publications, 2nd edition, 1958.

[23] Mark D. Maughmer. The Design of Winglets for Low-Speed Aircraft. `http://www.mandhsoaring.com/Why%20Winglets/WL-IT.pdf`. [Online; accessed 18-06-2014].

[24] DSE Group 15, Kluyverweg 5. *Aerobatic Racing Aircraft Design Project Plan Group 15*, April 2014.

[25] A.C. in 't Veld. *AE3202, Flight Dynamics Lecture Notes*, 2013.

[26] Mohammed H. Sadraey. *Aircraft Design, A Systems Engineering Approach*. Wiley, 1st edition, 2013.

[27] Frank Versteegh, personal communication, May 14, 2014.

[28] Air Race Planes 2009. `https://www.youtube.com/watch?v=DS_AhPoe_oU`. [Online; accessed 21-06-2014 (on topic from 1:04)].

[29] Kolibri - Composite Conceptual Design and Analysis Tool. `http://www.lightweight-structures.com/kolibri-composite-conceptual-design-and-analysis-tool/index.html`. [Online; accessed 11-06-2014].

[30] Hexcel HexPly 8552 IM7. `http://www.hexcel.com/Resources/DataSheets/Prepreg-Data-Sheets/8552_eu.pdf`. [Online; accessed 17-06-2014].

[31] Divinycell HT Technical Data. `http://www.diabgroup.com/~/media/Files/Products/Core-material-pdf/HT%20March%202014%20rev11%20SI.pdf`. [Online; accessed 10-06-2014].

[32] Divinycell HT Cost Data. `https://www.google.nl/url?sa=t&rct=j&q=&esrc=s&source=web&cd=5&ved=0CFEQFjAE&url=http%3A%2F%2Fforum.canardaviation.com%2Fattachment.php%3Fattachmentid%3D6862%26d%3D1353978378&ei=l8OWU82RN8GdO4abgKgI&usg=AFQjCNFLzv85drqMJSPV6i_63EM5mQO8-Q&bvm=bv.68445247,d.ZWU&cad=rja`. [Online; accessed 10-06-2014].

[33] Recycling Aerospace Composites for Recovery of High Value Carbon Fibres & Resin Chemicals. `http://users.ox.ac.uk/~pgrant/Recycling%20aerospace%20composite.pdf`. [Online; accessed 23-04-2014].

[34] CES EduPack 2013. `http://www.grantadesign.com/education/edupack/`. [Online; accessed 11-06-2014].

[35] F. T. Wallenberger, N. Weston. *Natural Fibers, Plastics and Composites*. Kluwer Academic Publishers, 1st edition, 2004.

[36] Divinycell HT Sustainability Data. `http://www.diabgroup.com/en-GB/Products-and-services/Core-Material/Divinycell-HT`. [Online; accessed 12-06-2014].

[37] Fuselage Loads. `http://itlims.meil.pw.edu.pl/zsis/pomoce/BIPOL/BIPOL_9A.pdf`. [Online; accessed 18-06-2014].

[38] Norman S. Currey. *Aircraft Landing Gear Design: Principles and Practices*. American Institute of Aeronautics and Astronautics, Inc., 3rd edition, 1988.

[39] CATIA V5 Finite Element Reference Guide. `http://www.mech.upatras.gr/~papado/CAD/catia/catpdffemrg_C2/femrg.pdf`. [Online; accessed 23-06-2014].

[40] Edge 540 Pilot's Operating Handbook and Flight Manual. `http://www.kfva.ch/fileadmin/images/downloads/Edge-Manual.pdf`. [Online; accessed 13-06-2014].

[41] Aviation News Edge 540 Technical Data. `http://www.air-races.com/the-planes/zivko-edge-540/`. [Online; accessed 13-06-2014].

[42] Besenyei's Corvus Racer Wins Approval for Windsor. `http://www.redbull.com/cs/Satellite/en_air/Article/Besenyei%E2%80%99s-Corvus-Racer-wins-approval-for-Windsor-021242856631006`. [Online; accessed 13-06-2014].

[43] Extra 300 Service Manual. `http://www.extraaircraft.com/docs/tech-manuals/MM300/CH53.pdf`. [Online; accessed 13-06-2014].

[44] Prof. A. Rothwell, personal communication, May 16, 2014.

[45] AISI Type 410S Stainless Steel, tempered at 233°C. `http://matweb.com/search/DataSheet.aspx?MatGUID=d62692f42c0046a48bd54dc91c0f9655&ckck=1`. [Online; accessed 18-06-2014].

[46] P-63 Kingcobra. `http://www.militaryfactory.com/aircraft/detail.asp?aircraft_id=263`. [Online; accessed 22-06-2014].

[47] Dr. J. Roskam. *Airplane Design Part III*. Roskam Aviation & Engineering Corporation, 1st edition, 1986.

[48] Hartzell Propeller Inc., Piqua, Ohio 45356-2634, U.S.A. *Hartzell Apllication Guide*, February 2014.

[49] Red Bull Air Race, Race Committee, 502 Airport Road, Guthrie. *Edge 540-T Pilot's Operation Handbook*, October 2001.

[50] Extra Flugzeugproduktions- und Vertriebs- GmbH, 46569 Hunxe, Federal Republic of Germany. *Extra 300S Information Manual*, April 2002.

[51] Janes MX, MX2 & MXS. `https://janes.ihs.com/CustomPages/Janes/DisplayPage.aspx?DocType=Reference&ItemId=+++1344683&Pubabbrev=JAWA`. [Online; accessed 08-05-2014].

[52] XFLOW CFD. `http://xflowcfd.com/`. [Online; accessed 16-05-2014].

[53] Aluminum 2024-O. `http://asm.matweb.com/search/SpecificMaterial.asp?bassnum=ma2024o`. [Online; accessed 17-06-2014].

[54] APM - 2024 Aluminum Alloy Distributor. `http://www.aeroprecisionmetals.com/article/apm-2024-aluminum-alloy-distributor`. [Online; accessed 17-06-2014].

[55] R.C. Hibbeler. *Mechanics of materials*. Pearson, 8rd edition, 2012.

[56] Grove Aircraft Landing Gear Systems Inc. `http://www.groveaircraft.com/5series.html`. [Online; accesses 16-06-2014].

[57] Aircraft Tire Data Book. `http://www.goodyearaviation.com/resources/pdf/db_airdatabook.pdf`. [Online; accessed 16-06-2014].

[58] Matco T6 Solid 6" Tailwheel. `http://www.aircraftspruce.com/catalog/lgpages/matcoT6.php`. [Online; accessed 19-06-2014].

[59] Heat Impact On V-Belt Life. `http://www.emersonindustrial.com/en-US/documentcenter/PowerTransmissionSolutions/Other/Belt%20Drive%20Monthly's/Form_9804E.pdf`. [Online; accessed 10-06-2014].

[60] Couplings and Universal Joints. `http://www.sdp-si.com/D757/couplings3.htm`. [Online; accessed 18-06-2014].

[61] Triathlon HT Chain Specifications. `http://www.wippermann.com/data-live-wippermann/docs/Dokumente-2013/en/downloads/produkt-broschueren/triathlon-chains-ht-wippermann-bro-2013-en.pdf`. [Online; accessed 10-06-2014].

[62] Chain Drive Design. `http://www.rexnord.eu/fileadmin/Rexnord_Kette/PDF/Catalogue_Flyer/Auslegung_Kettentrieb_E.pdf`. [Online; accessed 10-06-2014].

[63] Aluminum 6061-T6; 6061-T651. `http://asm.matweb.com/search/SpecificMaterial.asp?bassnum=MA6061t6`. [Online; accessed 10-06-2014].

[64] AISI 4130 Steel, normalized at 870°C (1600°F). `http://asm.matweb.com/search/SpecificMaterial.asp?bassnum=m4130r`. [Online; accessed 10-06-2014].

[65] Bicycle Chain Efficiency. `http://web.archive.org/web/20060206210227/http://www.hw.ac.uk/mecWWW/research/mdk/res.htm`. [Online; accessed 16-06-2014].

[66] Motor Vehicle Exhaust Emissions. `http://www.volkspage.net/technik/ssp/ssp/SSP_230.pdf`. [Online; accessed 11-06-2014].

[67] Cengel-Boles. *Thermodynamics: An Engineering Approach Chapters 1-9*. Custom edition for TUDelft. McGraw-Hill Custom Publishing, 2010.

[68] Shell Avgas 100LL. `http://s03.static-shell.com/content/dam/shell-new/local/country/aus/downloads/aviation/avgas-100ll-pds.pdf`. [Online; accessed 10-06-2014].

[69] Calculating the Stoichiometric Air-Fuel Ratio. `http://www.brighthubengineering.com/machine-design/15235-the-stoichiometric-air-fuel-ratio/`. [Online; accessed 18-06-2014].

[70] Subsonic Wind Tunnel Tests of Various Forms of Air Intake Installed in a Fighter-Type Aircraft. `http://naca.central.cranfield.ac.uk/reports/arc/rm/3134.pdf`. [Online; accessed 06-06-2014].

[71] Air Extractor. `http://www.jonkersailplanes.co.za/airextractor.htm`. [Online; accessed 12-06-2014].

[72] Sky Smoke FAQ. `http://www.skysmoke.com/faq.htm`. [Online; accessed 19-06-2014].

[73] Aircraft Turbo System & Parts Price List. `http://www.hartzellenginetech.com/catalog/Turbo-Price-List-HET-2013.pdf`. [Online; accessed 15-05-2014].

[74] Dr. A. Gangoli Rao, personal communication, June 10, 2014.

[75] Aircraft Supercharging. `http://www.g3ignition.com/Supercharging.html`. [Online; accessed 15-05-2014].

[76] Will a New Era of Turbocharging Bring Back Old Problems? `http://www.autoguide.com/auto-news/2012/06/will-a-new-era-of-turbocharging-bring-back-old-problems.html#more-140644`. [Online; accessed 11-06-2014].

[77] Turbo'd for Fuel Economy. `http://www.autospeed.com/cms/article.html?&A=109931`. [Online; accessed 11-06-2014].

[78] Communication systems. `http://www.aircraftspruce.com/catalog/avpages/beckerar6201.php`. [Online; accessed 13-06-2014].

[79] Hitec Servos. `http://www.servocity.com/html/hs-5645mg_digital_torque.html#.U5re5vmSzLc`. [Online; accessed 13-06-2014].

[80] Varley Red Top Battery. `http://www.varleyredtop.com/pdf/11_vrt8.pdf`. [Online; accessed 13-06-2014].

[81] Communication System. `http://www.sea-avionics.com/lc/cart.php?target=productDetails&model=618M-3&substring=618m3`. [Online; accessed 13-06-2014].

[82] Fluorocell 600 Series. `http://atlinc.com/pdfs/Racing/ATL-2014-Catalog-Page6.pdf`. [Online; accessed 16-06-2014].

[83] Fluorocell 600 Series Prices. `http://www.atlinc.com/pdfs/Racing/ATL-2014-Pricing-for-web-pg2.pdf`. [Online; accessed 17-06-2014].

[84] Bicycle Chain Efficiency. `http://www.aircraftspruce.com/catalog/appages/flopetube.php`. [Online; accessed 16-06-2014].

[85] Legal Information Institute Firewall Regulations. `http://www.law.cornell.edu/cfr/text/14/23.1191`. [Online; accessed 13-06-2014].

[86] Zircoflex Flexible Ceramic Heat Shield. `http://www.zircotecwebstore.com/ZircoFlex%C2%AE-Flexible-Ceramic-Heat-Shield/dp/B009DC0GQE?childAsin=B009CQAK8U&class=quickView&field_availability=-1&field_browse=2143876031&field_keywords=*&field_subjectbin=3809648031&id=ZircoFlex%C2%AE+Flexible+Ceramic+Heat+Shield&ie=UTF8&refinementHistory=subjectbin%2Cprice%2Csize_name&searchBinNameList=subjectbin%2Cprice%2Csize_name&searchKeywords=*&searchNodeID=2143876031&searchPage=1&searchRank=salesrank&searchSize=12`. [Online; accessed 13-06-2014].

[87] Pyrogel XT-E. `http://www.aerogel.com/products-and-solutions/pyrogel-xt-e/`. [Online; accesses 17-06-2014].

[88] Titanium Sheet Specifications. `http://www.titaniumjoe.com/index.cfm/products/sheet-plate/`. [Online; accessed 17-06-2014].

[89] Truss Structure Joints. `http://www.google.com/patents/US3783573`. [Online; accessed 19-06-2014].

[90] Smoke systems. `http://www.aircraftspruce.com/catalog/appages/smokes.php?clickkey=10725`. [Online; accessed 19-06-2014].

[91] Extra Flugzeugproduktions- und Vertriebs- GmbH, 46569 Hünxe, Federal Republic of Germany. *Extra 300L Information Manual*, March 2009.

[92] Wing Tip Navigation Light. `http://www.aircraftspruce.com/catalog/elpages/wingtipnavlight.php`. [Online; accessed 30-06-2014].

[93] tillet t10 kart racing seats. `https://www.tillett.co.uk/T10-racing-car-seat.asp`. [Online; accessed 30-06-2014].

[94] Voluntary Reporting of Greenhouse Gases Program - Fuel and Energy Source Codes and Emission Coefficients. `http://www.eia.gov/oiaf/1605/coefficients.html`. [Online; accessed 20-06-2014].

[95] Emissions of the Airbus A380. `http://www.airbus.com/aircraftfamilies/passengeraircraft/a380family/environment/emissions/`. [Online; accessed 20-06-2014].

[96] Specifications of the Airbus A380. `http://www.airbus.com/aircraftfamilies/passengeraircraft/a380family/specifications/`. [Online; accessed 20-06-2014].

[97] Janes Corvus CA-41 Racer 540. `https://janes.ihs.com/CustomPages/Janes/DisplayPage.aspx?DocType=Reference&ItemId=+++1345303&Pubabbrev=JAWA`. [Online; accessed 08-05-2014].

[98] Janes Extra EA-300 & EA-330. `https://janes.ihs.com/CustomPages/Janes/DisplayPage.aspx?DocType=Reference&ItemId=+++1342465`. [Online; accessed 30-04-2014].

[99] Janes Zivko Edge 540. `https://janes.ihs.com/CustomPages/Janes/DisplayPage.aspx?DocType=Reference&ItemId=+++1343761&Pubabbrev=JAWA`. [Online; accessed 08-05-2014].

A Aircraft Parameters

Table A.1: Summary of aircraft parameters

Parameter	Value	Unit	Source	Description
Wing Planform & Aerodynamics				
Airfoil	NACA 0011-61MOD	$[-]$	Section 4.1.3	Wing airfoil
A	7.77	$[-]$	Table 4.7	Wing aspect ratio
b	8.50	$[m]$	Table 4.7	Wing span
$C_{D_{0_{wing}}}$	$7.048(10^{-3})$	$[-]$	Table 4.7	Zero-lift drag coefficient of the wing
$C_{L_{design}}$	0.31	$[-]$	Table 4.7	Design lift coefficient of the wing
$C_{L_{max}}$	2.07	$[-]$	Table 4.7	Maximum lift coefficient of the wing
C_{L_α}	4.47	$[rad^{-1}]$	Table 4.7	Wing lift slope
C_r	1.37	$[m]$	Table 4.7	Wing root chord
C_t	0.82	$[m]$	Table 4.7	Wing tip chord
i_w	4.05	$[°]$	Table 4.7	Angle of incidence of the wing
S	9.30	$[m^2]$	Table 4.7	Wing area
$(\bar{x}_{ac})_w$	0.25	$[-]$	Table 3.10	Location of the wing AC
x_{cg}	2.85	$[m]$	Table 5.1	Location of the wing CG
α_{stall}	26.5	$[°]$	Table 4.7	Angle of attack of the wing at stall
λ	0.60	$[-]$	Table 4.7	Wing taper ratio
Λ_{LE}	0.00	$[°]$	Table 4.7	Wing leading edge sweep angle
$\Lambda_{0.25c}$	-1.84	$[°]$	Table 4.7	Wing quarter chord sweep angle
$\Lambda_{0.5c}$	-3.68	$[°]$	Table 4.7	Wing half chord sweep angle
Ailerons				
b_A/b	0.51	$[-]$	Table 4.9	Aileron span to wing span ratio
C_A/C	0.25	$[-]$	Table 4.9	Aileron chord to wing chord ratio
$C_{l_{\delta_A}}$	0.16	$[-]$	Table 4.9	Roll moment derivative for aileron deflection
y_i	1.84	$[m]$	Table 4.9	Inner aileron location (from mid wing)
y_o	4.0	$[m]$	Table 4.9	Outer aileron location (from mid wing)
δ_A	30	$[°]$	Table 4.9	Maximum elevator deflection
Wing Structure				
Material 1	HexPly 8552 IM7 (65%) [45, -45, 90, 0]s epoxy matrix layup	$[-]$	Section 4.3.3	Carbon fiber used for main wing spar
Material 2	Divinycell HT131	$[-]$	Section 4.3.3	Foam used for main wing spar
b_{max}	$25(10^{-2})$	$[m]$	Section 4.3.3	Maximum spar width
b_{min}	$5(10^{-2})$	$[m]$	Section 4.3.3	Minimum spar width
$m_{main\ spar}$	30	$[kg]$	Section 4.3.3	Mass of the main spar (one wing)
t_{max}	$7.336(10^{-3})$	$[m]$	Section 4.3.3	Maximum carbon fiber laminate thickness
t_{min}	$1.048(10^{-3})$	$[m]$	Section 4.3.3	Minimum carbon fiber laminate thickness
Fuselage Aerodynamics & Geometry				
Material	CFRP	$[-]$	Section 5.2.2	Carbon fiber used for fuselage skin
C_{D_0}	$6.3(10^{-3})$	$[-]$	Section 3.15	Refined drag estimation for the fuselage
b_f	1.04	$[m]$	Table 5.2	Maximum fuselage width
h_f	1.30	$[m]$	Table 5.2	Maximum fuselage height

L_f	7.14	$[m]$	Table 5.2	Fuselage length
m_{skin}	28.2	$[kg]$	Section 5.2.2	Fuselage skin mass
S_f	16.0	$[m^2]$	Table 5.2	Total surface area of the fuselage
S_{fp}	5.40	$[m^2]$	Table 5.2	Projected area of the fuselage
t/c	0.20	$[-]$	Table 5.2	Thickness over chord ratio of the fuselage
x_{cg}	2.61	$[m]$	Table 5.1	Location of the fuselage CG

Fuselage Structure

Material	AISI 410 stainless steel (tempered at 233 °C	$[-]$	Section 5.3.3	Steel used for fuselage truss structure
m_{truss}	48.8	$[kg]$	Section 5.3.3	Fuselage truss structure mass
r_o	$9(10^{-3})$	$[m]$	Section 5.3.3	Inner radius of fuselage truss structure tubes
r_o	$10(10^{-3})$	$[m]$	Section 5.3.3	Outer radius of fuselage truss structure tubes
σ_{max}	$890(10^6)$	$[Pa]$	Table 5.5	Maximum Von Mises stress (critical design point)
σ_{min}	$-772(10^6)$	$[Pa]$	Table 5.5	Minimum Von Mises stress (critical design point)
δ_{max}	$7.88(10^{-2})$	$[m]$	Table 5.5	Maximum deflection (critical design point)

Horizontal Stabilizer

Airfoil	NACA 0009	$[-]$	Section 6.1.3	Horizontal stabilizer airfoil
A_h	3.00	$[-]$	Table 6.3	Horizontal stabilizer aspect ratio
b_h	2.52	$[m]$	Table 6.3	Horizontal stabilizer span
$C_{D_{0_{h,emp}}}$	$2.6(10^{-3})$	$[-]$	Table 3.15	Refined drag estimation for the horizontal stabilizer
c_{h_r}	1.09	$[m]$	Table 6.3	Horizontal stabilizer root chord
c_{h_t}	0.58	$[m]$	Table 6.3	Horizontal stabilizer tip chord
C_{L_h}	0.085	$[-]$	Table 6.3	Horizontal stabilizer lift coefficient
$C_{m_{\alpha_f}}$	0.011	$[-]$	Table 6.6	Pitching moment coefficient due to fuselage
i_h	4.51	$[°]$	Table 6.3	Horizontal stabilizer incidence angle
S_h	2.12	$[m^2]$	Table 6.3	Horizontal stabilizer surface area
S_h/S	0.23	$[-]$	Table 6.3	Horizontal stabilizer to wing surface ratio
$x_{ac,total}$	2.41	$[m]$	Table 6.6	Distance nose to AC of entire aircraft
$x_{cg,total}$	2.56	$[m]$	Table 6.6	Distance nose to CG of entire aircraft
x_{cg}	6.18	$[m]$	Table 5.1	Location of the horizontal stabilizer CG
x_{LE}	2.14	$[m]$	Table 6.3	Distance nose to LEMAC
α_h	4.51	$[°]$	Table 6.3	Horizontal stabilizer angle of attack
λ	0.55	$[-]$	Table 6.3	Horizontal stabilizer taper ratio
$\Lambda_{h_{0.25c}}$	8.98	$[°]$	Table 6.3	Horizontal stabilizer sweep at 25% chord

Vertical Stabilizer

Airfoil	NACA 0012-93	$[-]$	Table 6.5	Vertical stabilizer airfoil
A_v	1.50	$[-]$	Table 6.9	Vertical stabilizer aspect ratio
b_{eff_s}	0.89	$[m]$	Table 6.9	Effective vertical stabilizer span during spin
b_v	1.58	$[m]$	Table 6.9	Vertical stabilizer span
$C_{D_{0v,emp}}$	$4.7(10^{-4})$	$[-]$	Table 3.15	Refined drag estimation for the vertical stabilizer
$C_{n_{\beta_{tot}}}$	0.144	$[-]$	Table 6.9	Yawing moment coefficient due to sideslip
$C_{n_{\beta_{fus}}}$	-0.076	$[-]$	Table 6.5	Yaw derivative due to sideslip contribution fuselage
$C_{n_{\beta_{prop}}}$	-0.020	$[-]$	Table 6.5	Yaw derivative due to sideslip contribution propulsion
$C_{n_{\beta_v}}$	0.126	$[-]$	Table 6.9	Yaw derivative due to sideslip contribution

C_{r_v}	1.500	[m]	Table 6.9	Vertical stabilizer root chord
$C_{Y_{\beta_v}}$	-0.417	[−]	Table 6.5	Sideforce sideslip coefficient slope
S_{eff_s}	0.90	[m²]	Table 6.9	Effective vertical stabilizer surface during spin
S_v	1.65	[m²]	Table 6.9	Surface area
x_{cg}	6.18	[m]	Table 5.1	Location of the vertical stabilizer CG
λ	0.40	[−]	Table 6.5	Vertical stabilizer taper ratio
$\Lambda_{0.5}$	0.00	[°]	Table 6.5	Half-chord sweep angle

Rudder

C_{rudder}/C	0.60	[−]	Table 6.9	Rudder chord to wing chord ratio
δ_r	30.00	[°]	Table 6.9	Maximum rudder deflection
$c_{n_{\delta_{r_{SR}}}}$	0.033	[−]	Table 6.9	Yawing moment derivative for rudder spin recovery
τ_r	0.79	[−]	Table 6.9	Angle of attack effectiveness parameter rudder

Elevator

C_E/C_h	0.40	[−]	Table 6.7	Elevator to tail chord ratio
$C_{L_{h_{max}}}$	0.786	[−]	Table 6.7	Maximum horizontal stabilizer lift
$C_{L_{h_{min}}}$	-0.567	[−]	Table 6.7	Minimum horizontal stabilizer lift
τ_{max}	0.597	[−]	Table 6.7	Maximum angle of attack effectiveness

Flight Dynamics

C_{l_p}	-0.35	[−]	Table 6.11	Moment derivative about X-axis due to angular velocity about the X-axis
C_{l_r}	0.10	[−]	Table 6.11	Moment derivative about X-axis due to angular velocity about the Z-axis
$C_{L_{des}}$	0.31	[−]	Table 6.11	Design Lift coefficient
C_{m_q}	-7.88	[−]	Table 6.11	Moment derivative about Y-axis due to angular velocity about the Y-axis
$C_{m_{alpha}}$	-0.22	[−]	Table 6.11	Moment derivative about Y-axis due to angle of attack
$C_{m_{\dot{\alpha}}}$	-4.83	[−]	Table 6.11	Moment derivative about Y-axis due to change in angle of attack
C_{n_r}	-0.08	[−]	Table 6.11	Moment derivative about Z-axis due to angular velocity about the Z-axis
$C_{n_{\beta}}$	0.12	[−]	Table 6.11	Moment derivative about Z-axis due to sideslip angle
C_{X_u}	-0.051	[−]	Table 6.11	Force derivative about X-axis due to velocity along the X-axis
$C_{Y_{\beta}}$	-0.63	[−]	Table 6.11	Force derivative about Y-axis due to sideslip angle
C_{Z_q}	-3.69	[−]	Table 6.11	Force derivative about Z-axis due to angular velocity about the Y-axis
C_{Z_u}	-0.60	[−]	Table 6.11	Force derivative about Z-axis due to velocity along the X-axis
C_{Z_0}	-0.02	[−]	Table 6.11	Dimensionless force about Z-axis in steady flight
$C_{Z_{\alpha}}$	-4.48	[−]	Table 6.11	Force derivative about Z-axis due to angle of attack
$C_{Z_{\dot{\alpha}}}$	-1.57	[−]	Table 6.11	Force derivative about Z-axis due to change in angle of attack
K_X^2	0.015	[−]	Table 6.11	Non-dimensional radius of gyration about X-axis
K_Y^2	0.021	[−]	Table 6.11	Non-dimensional radius of gyration about Y-axis
K_Z^2	0.032	[−]	Table 6.11	Non-dimensional radius of gyration about Z-axis
μ_b	8.27	[−]	Table 6.11	Relative density, asymmetric
μ_c	62.90	[−]	Table 6.11	Relative density, symmetric
Aperiodic roll	-0.705	[−]	Table 6.12	Aperiodic roll eigenvalue
Dutch roll	$-0.0576 \pm 0.5850i$	[−]	Table 6.12	Dutch roll eigenvalue

Phugoid	$-2.146(10^{-4}) \pm 8.439(10^{-4})i$	[$-$]	Table 6.12	Phugoid eigenvalue
Short period	-1.872 ± 1.251	[$-$]	Table 6.12	Short period eigenvalue
Spiral	0.4082	[$-$]	Table 6.12	Spiral eigenvalue

Landing Gear

Airfoil fairing	NACA 64-020	[$-$]	Section 7.5	Airfoil fairing for the double landing gear
$C_{D_{uc}}$	$3.1(10^{-3})$	[$-$]	Section 7.8	Scaled drag coefficient of double landing gear
$m_{equipment}$	13.78	[kg]	Section 7.8	Mass of double landing gear equipment
m_{strut}	5.18	[kg]	Section 7.8	Mass of double landing gear strut
m_{total}	18.96	[kg]	Section 7.8	Total mass of double landing gear
x_{cg}	1.96	[m]	Table 5.1	Location of the landing gear CG
x_e	0.60	[m]	Section 7.1	Lateral distance between wheel and CG
y_e	0.80	[m]	Section 7.1	Vertical distance between wheel and CG

Transmission System

F_{chain}	$21.08(10^3)$	[N]	Table 8.2	Maximum applied force on the chain
m_{total}	9.24	[kg]	Table 8.2	Mass of the complete transmission system
n	26	[$-$]	Table 8.2	Number of teeth of a sprocket
r_{final}	$65.7(10^{-3})$	[m]	Table 8.2	Radius of a sprocket
v_{chain}	18.57	[m/s]	Table 8.2	Speed of the chain
$\theta_{mainshaft}$	3.31	[$°$]	Table 8.2	Maximum angular deflection of the main shaft
$\theta_{propshaft}$	3.44	[$°$]	Table 8.2	Maximum angular deflection of the propeller shaft
$\tau_{mainshaft}$	$98.0(10^6)$	[Pa]	Table 8.2	Maximum shear stress in the main shaft
$\tau_{propshaft}$	$320.4(10^6)$	[Pa]	Table 8.2	Maximum shear stress in the propeller shaft
τ_{tooth}	$39.8(10^6)$	[Pa]	Table 8.2	Maximum applied shear stress on a sprocket tooth

Air Intake & Cooling System

$A_{safe,\ one\ intake}$	$2.75(10^{-2})$	[m^2]	Table 8.5	Required safe intake area of one intake
$\dot{m}_{cooling\ required}$	3.29	[kg/s]	Table 8.5	Required mass flow to cool the engine
$\dot{m}_{intake\ required}$	0.31	[kg/s]	Table 8.5	Required mass flow to run the engine
$\dot{m}_{total\ required}$	3.60	[kg/s]	Table 8.5	Total required mass flow to operate the engine
$\dot{m}_{total\ safe}$	5.40	[kg/s]	Table 8.5	Total required mass flow to operate the engine (with safety factor)
$T_{cooling\ exit}$	408.15	[K]	Table 8.5	Exit temperature of the cooling air
η	0.28	[$-$]	Table 8.5	Engine efficiency

Electrical System

$t_{all\ systems}$	20	[min]	Table 8.9	Time that all systems can be powered by the battery (when generator fails)
$t_{vital\ systems}$	221	[min]	Table 8.9	Time that only vital systems can be powered by the battery (when generator fails)

Aircraft Performance

L/D_{max}	16.7	[$-$]	Table 9.2	Maximum lift over drag ratio
P	315	[hp]	Table 9.1	Power of the engine at race conditions
RC_{max}	25.9	[m/s]	Table 9.2	Maximum rate of climb (at an airspeed of 33.7 m/s)
R_{50l}	184	[km]	Table 9.2	Range with 50l of fuel (with 10 l reserve) at maximum cruise speed
R_{83l}	337	[km]	Table 9.2	Range with 83l of fuel (with 10 l reserve) at maximum cruise speed
s_{land}	398	[m]	Table 9.2	Landing distance
$s_{takeoff}$	145	[m]	Table 9.2	Take-off distance
V_{max}	122.3	[m/s]	Table 9.2	Maximum (cruise) speed
V_{stall}	24.1	[m/s]	Table 9.2	Stall airspeed

Isometric view
Scale: 1:100

Top view
Scale: 1:75

Right view
Scale: 1:75

This drawing is our property. It can't be reproduced or communicated without our written agreement.		EAD			
DRAWN BY	DATE	DRAWING TITLE			
Alex	23-6-2014	FX-15 Final Design			
CHECKED BY	DATE	SIZE	DRAWING NUMBER		REV
		A4	10.1		X
DESIGNED BY	DATE	SCALE 1:75	WEIGHT(kg) 680.9	SHEET	1/2
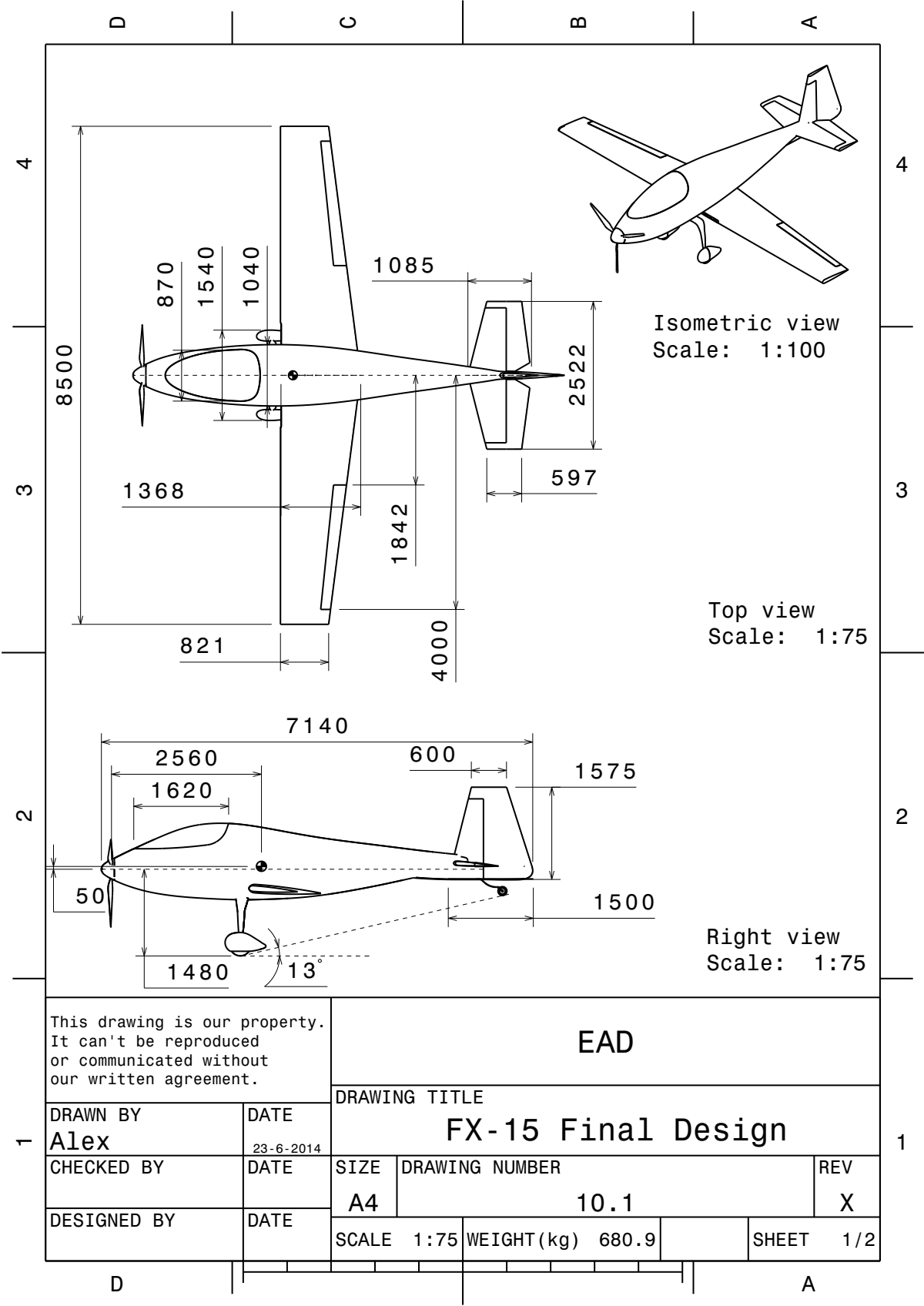
C Reference Aircraft

Table C.1: Reference aircraft parameters

Name	Source	Empty weight [kg]	MTOW [kg]	(W/S)_TO [kg/m2]	(W/P)_TO [kg/kW]	CLmax	Take off length [m]	Vstall [m/s]	S [m2]	TOP	W/S_TO [N/m2]	W/P_TO [kg/W]
XtremeAir Sbach 342	[102]	670	850	75.6	3.3	1.51	400	28.3	11.25	15.7	741.64	0.032
Zivko Edge 540	[102]	531	703	77.2	3.2	1.78	90	26.4	9.10	13.5	757.33	0.032
Dyn'Aero CR100	[102]	550	760	71.5	5.7		351		10.65		701.42	0.056
CAP 10	[102]	540	780	71.9	5.8	1.52	395	27.5	10.85	26.5	705.34	0.057
Sukhoi S u -31	[102]	750	1050	82.0	3.3	1.64	110	29.4	11.83	15.6	804.42	0.032
Mylius My-103 Mistral	[102]	620	950			2.09		26.4	10.45			
Terzi T30 Katana	[102]	658	880					27.2				
Slick 360	[102]	465	625	67.2	3.2	1.39	351	28.9	8.60	15.2	659.23	0.032
Laser Z-300	[102]	522	658	70.8	2.9	1.69	304	25.9	9.30	11.5	694.55	0.028
Slick 540	[102]	550	716	83.0	3.3	1.43	351	30.6	8.60	18.2	814.23	0.032
MX2	[102]	584	839	88.6	4.3	1.57		30.0	9.48	23.3	869.17	0.042
Rud RA-3	[102]	499	816		6.1			25.8				0.06
Extra EA300S	[102]	585	820	83.6	3.7	1.43	248	30.6	9.81	20.7	820.12	0.036
Extra EA300L	[102]	672	820	76.6	3.7	1.53	248	28.3	10.70	17.7	751.45	0.036
Van's RV-14	[102]	562	862	79.4	5.9	2.07		23.9	11.70	21.8	778.91	0.058
Corvus CA-41 Racer 540	[102]	545	700	77.8	2.7	1.79		26.4	9.00	11.5	763.22	0.027
Extra EA-500	[102]	1445	2130									
Rud Aero RA-2	[102]	612	855									
Rud RA-2L	[102]	454	771									
Pilatus PC-9	[102]	1725	2350									
Extra EA-200	[102]	562	700									
Embraer EMB-314 Super Tucano	[102]	2420	3190									
Enaer (ECH-51) T-35 Pillán	[102]	930	1315									
Cessna T240 TTX	[102]	1179	1633									
Cirrus SR22-G3	[102]	1009	1542									
Lancair Super ES	[102]	862	1451									
Solaris Sigma 310	[102]	1051	1587									
Mooney M20R	[102]	1025	1528									
Ravin 500	[102]	850	1620									
Bellanca Super Viking	[102]	1043	1508	100.5	6.8	1.63	433	31.4	15.00	39.9	985.91	0.066
Van's RV10	[102]	726	1225	89.1	6.3	1.78		28.3	13.70	30.5	874.07	0.062
Lancair IV-P	[102]	998	1610	176.8	6.2	2.43	549	34.2	9.10	43.5	1734.41	0.061
Cessna 172R Skyhawk	[102]	771	1111	68.7	9.3	1.58	514	26.4	16.20	38.8	673.95	0.091
Piper PA-28R-201 Arrow	[102]	816	1247	79.0	8.4	1.33	488	30.8	15.80	47.8	774.99	0.082
Piper PA-28-181 Archer III	[102]	766	1156	73.2	8.6	2.15	491	23.3	15.80	28.4	718.09	0.085
Hensley H-1 Wolf	[102]	953	1587	142.4	6.5	2.95		27.8	11.15	29.8	1396.94	0.063
Commander 115TC	[102]	976	1499	106.2	7.5	1.46	678	34.2	14.12	52.1	1041.82	0.073
Socata TB 20	[102]	800	1400	117.6	7.5		595				1153.66	0.074
Cessna 182 Skylane	[102]	893	1406	86.2	8.2	1.76	462	28.1	16.30	38.4	845.62	0.08
Diamond DA42 Twin Star	[102]	1250	1785	109.6	8.2	1.66	458	32.5	16.29	51.8	1075.18	0.08
Glasair III	[102]	737	1098	144.1	4.9	1.89		35.0	7.60	35.9	1413.62	0.048

D Output Values of the Preliminary Design Phase

Table D.1: Output values of the preliminary design phase

Parameter	Value	Unit	Source	Description
Wing Planform				
S	9.70	$[m^2]$	Section 3.4	Wing surface area
b	8.50	$[m]$	Section 3.5	Wing span
A	7.45	$[-]$	Section 3.5.1	Aspect ratio
λ	0.50	$[-]$	Section 3.5.2	Taper ratio
$\Lambda_{0.25}$	-1.48	$[°]$	Section 3.5.3	Quarter chord sweep
$\Lambda_{0.50}$	-2.96	$[°]$	Section 3.5.3	Half chord sweep
C_r	1.76	$[m]$	Section 3.5.5	Root chord
C_t	0.88	$[m]$	Section 3.5.5	Tip chord
$\bar{c}$	1.37	$[m]$	Section 3.5.4	Length of the MAC
Fuselage Geometry				
b_f	0.90	$[m]$	Section 3.7	Fuselage width
h_f	1.25	$[m]$	Section 3.7	Fuselage height
l_f	6.90	$[m]$	Section 3.7	Fuselage length
Aerodynamic Properties				
C_{D_0}	0.0216	$[-]$	Section 3.8	Zero-lift drag coefficient
e	0.839	$[-]$	Section 3.8	Oswald factor
Weight Estimation				
W_w	114	$[kg]$	Section 3.9	Mass of the wing
W_t	25	$[kg]$	Section 3.9	Mass of the tail
W_{uc}	38	$[kg]$	Section 3.9	Mass of the undercarriage
$W_{surf,control}$	21	$[kg]$	Section 3.9	Mass of the surface controls
W_{prop}	255	$[kg]$	Section 3.9	Mass of the propulsion system
W_{fus}	100	$[kg]$	Section 3.9	Mass of the fuselage
W_{eq}	42	$[kg]$	Section 3.9	Mass of the equipment
W_{safety}	17	$[kg]$	Section 3.9	Mass of the safety systems
OEW	605	$[kg]$	Section 3.12	Operative empty weight
W_{fuel}	51.6	$[kg]$	Section 3.9	Mass of the fuel
$W_{payload}$	186	$[kg]$	Section 3.9	Mass of the payload
$MTOW$	849.6	$[kg]$	Section 3.12	Maximum take-off weight
$W_{fuel,race}$	36	$[kg]$	Section 3.12	Mass of the fuel for the race
$W_{payload,race}$	88.5	$[kg]$	Section 3.12	Mass of the payload for the race
W_{race}	735.5	$[kg]$	Section 3.12	Race mass
Stability				
S_h	1.77	$[m^2]$	Section 3.10	Horizontal tail surface area
X_{LEMAC}	2.19	$[m]$	Section 3.10	Location of the leading edge of the MAC
Refined Drag Estimation				
$C_{D_{0_{fus}}}$	$6.30(10^{-3})$	$[-]$	Section 3.11	Zero-lift drag coefficient of the fuselage
$C_{D_{0_{wing}}}$	$13.10(10^{-3})$	$[-]$	Section 3.11	Zero-lift drag coefficient of the wing
$C_{D_{0_{tail}}}$	$3.10(10^{-3})$	$[-]$	Section 3.11	Zero-lift drag coefficient of the tail
$C_{D_{0_{gear}}}$	$2.20(10^{-3})$	$[-]$	Section 3.11	Zero-lift drag coefficient of the landing gear
C_{D_0}	$24.70(10^{-3})$	$[-]$	Section 3.11	Total zero-lift drag coefficient
$C_{D_{induced_{fus}}}$	$0.00(10^{-3})$	$[-]$	Section 3.11	Induced drag coefficient of the fuselage
$C_{D_{induced_{wing}}}$	$1.40(10^{-3})$	$[-]$	Section 3.11	Induced drag coefficient of the wing
$C_{D_{induced_{tail}}}$	$0.00(10^{-3})$	$[-]$	Section 3.11	Induced drag coefficient of the tail
$C_{D_{induced_{gear}}}$	$0.00(10^{-3})$	$[-]$	Section 3.11	Induced drag coefficient of the landing gear
$C_{D_{induced}}$	$1.40(10^{-3})$	$[-]$	Section 3.11	Total induced drag coefficient

E Gannt Chart

ID	Task Mode	Task Name			Sun 1 Jun		Wed 4 Jun		Sat 7 Jun	
			7	8	9	10	11	12	13	14	15
0		**Final Report**									
1		Structure report									
2		Track analysis									
3		**Preliminary design**									
4		Class I weight estimation									
5		Wing/Power Loading									
6		Class II weight estimation									
7		Refined drag estimation									
8		Wing planform									
9		Tail sizing and wing location									
10		**Wing detail design**									
11		Wing structure									
12		Wing aerodynamics									
13		**Fuselage detail design**									
14		Fuselage structure									
15		Fuselage aerodynamics									
16		Subsystem location									
17		**Tail detail design**									
18		Horizontal stabilizer									
19		Vertical stabilizer									
20		Control surfaces									
21		Aircraft flight dynamics									
22		**Propulsion detail design**									
23		Transmission									
24		Engine cooling and air intake									
25		Engine tuning									
26		Propeller pitch control & electrical power sizing									
27		Fuel tank & firewall									
28		**Aircraft performance analysis**									
29		FX-15 performance analysis									
30		**Landing gear detail design**									
31		Landing gear location									
32		Trade-off									
33		Structural optimization									
34		Dimensional optimization									
35		Equipment									
36		**Final Design**									
37		Description of final design									
38		Mass & cost breakdown structure									
39		Compliance matrix									
40		**Sustainable development**									
41		**Project design & design development logic**									
42		Manufacturing, assembly & integration plan									
43		Operations & logistics									
44		Business plan									
45		RAMS									
46		Risk assessment									
47											
48		N2 chart									
49		Systems engineering approach									
50		Quality check									
51		Final Report Deadline									

Task		Inactive Task		Start-only	⊏	
Split	··········	Inactive Milestone	◇	Finish-only	⊐	
Milestone	◆	Inactive Summary	▽	Deadline	⬇	
Summary	▬▬	Manual Task		Critical	▬▬	
Project Summary	▽▽	Duration-only		Critical Split	······	
External Tasks	▬▬	Manual Summary Rollup	▬▬	Progress	▬▬	
External Milestone	◆	Manual Summary	▬▬	Slack	▬▬	

Project: Final Report
Date: Tue 24-6-14

24-6

Task		Inactive Task		Start-only	⊏
Split		Inactive Milestone	◇	Finish-only	⊐
Milestone	◆	Inactive Summary		Deadline	↓
Summary		Manual Task		Critical	
Project Summary		Duration-only		Critical Split	
External Tasks		Manual Summary Rollup		Progress	
External Milestone	◆	Manual Summary		Slack	

Project: Final Report
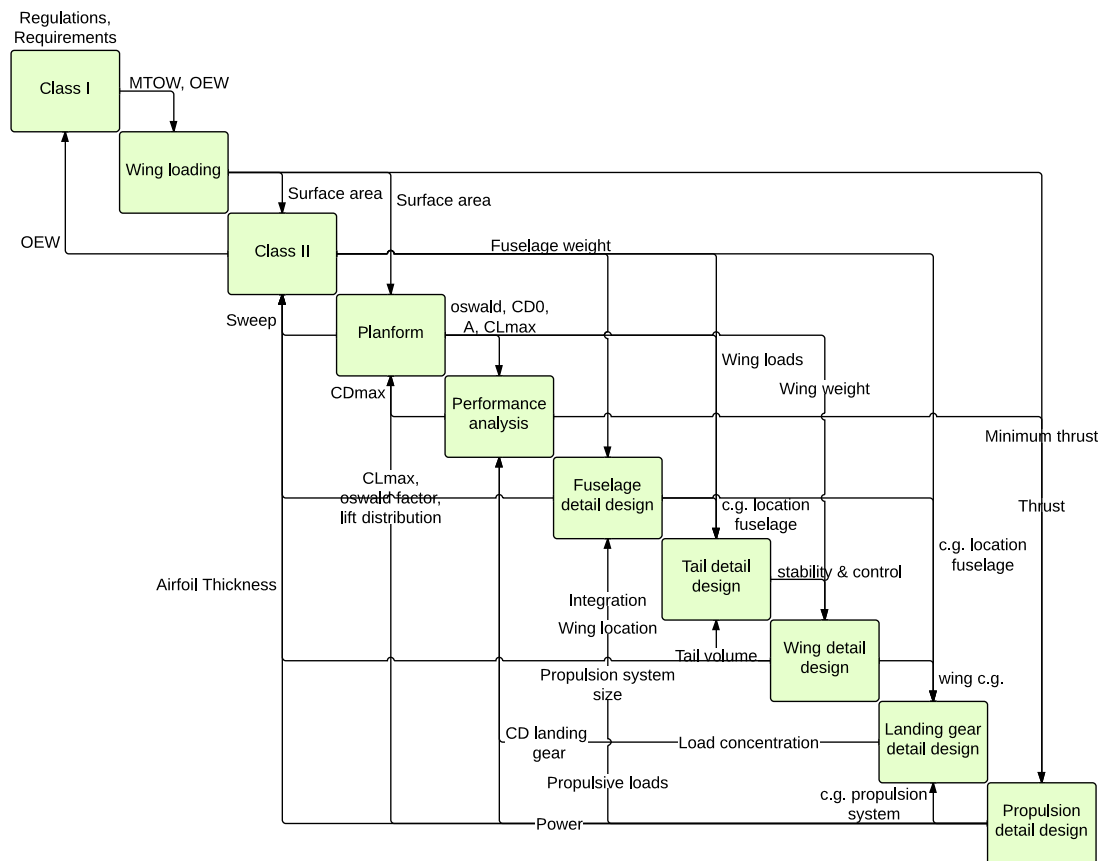Date: Tue 24-6-14

IX

F N2 Chart

Figure F.1: N2 chart

G Systems Engineering Approach

During the DSE project, the systems engineers were responsible for the collaboration of different departments, the planning, and the consistency of the design. This section describes the approach used to assure a qualitative execution of the aforementioned tasks.

To ensure a good collaboration between different departments multiple measures are taken. One measure is to have all the departments come up with information that they needed from all other departments. This creates awareness within the departments, as well as it gives insight into the collaboration. A second measure is to share daily updates with the entire group. Every department states their progress and their issues. This ensures that every department has up-to-date knowledge about other departments, furthermore problems between departments can be spotted and dealt with on time.

The planning for every department is initially made by the departments themselves. They are finalized by the systems engineers. The departments set internal deadlines apart from the overall deadlines that are set by the systems engineers or the tutors. During the daily updates, the progress with respect to the deadlines was checked. If departments show signs of falling behind, actions are taken to ensure that the deadlines will be met.

To ensure consistency of the design, the systems engineers create a file with parameters that can be viewed by every member of the group, but only altered by the systems engineers. If values are updated or new values are determined, they are given to the systems engineers, who in turn put them in the shared file. Furthermore, if one department needs information from another department, the question is asked through the systems engineers. They are responsible for the consistency and can therefore give the right answer or redirect the question to the corresponding department.

Lastly, risks per department are determined. The risks act as a guide for the systems engineers, who have a clear overview of what to specifically focus on in every department.